Spin Chemistry of Guest@Host Systems: $H_2@C_{60}$ and Nitroxide@Octa Acid

Judy Y.-C. Chen

Submitted in partial fulfillment of the
Requirements for the degree
of Doctor of Philosophy
in the Graduate School of Arts and Sciences

COLUMBIA UNIVERSITY

2012

© 2012
Judy Y.-C. Chen
All Rights Reserved

ABSTRACT

Spin Chemistry of Guest@Host Systems: H_2@C_{60} and Nitroxide@Octa Acid

Judy Y.-C. Chen

This thesis describes the nuclear and electronic spin chemistry of incarcerated guest molecules to form a guest@host complex in conjunction with the utility of nuclear magnetic resonance (NMR) and electron paramagnetic resonance (EPR) spectroscopy.

The first chapter describes the background and motivation of our scientific pursuit. Chapters 2-4 describe the nuclear spin chemistry of the two allotropes of elemental hydrogen, *para*-H_2 and *ortho*-H_2, incarcerated in C_{60}, open-C_{60} and C_{70} fullerenes to form endofullerene guest@host complex, symbolized as *p*H_2@fullerene and *o*H_2@fullerene, respectively.

Chapter 2 presents experimental results of the temperature dependence of the equilibrium of the interconversion of *o*H_2@fullerene and *p*H_2@fullerene and the use of different paramagnetic spin catalysts for this interconversion.

Chapters 3 and 4 presents the spin-lattice relaxation (T_1) and the paramagnet-enhanced relaxation, relaxivity (R_x) of $o^{1,2}H_2$@fullerene ($^{1,2}H_2$ = ^{1}H-NMR-active H_2 and HD) as well as the introduction of a new system for magnetic exploration: H_2O@fullerene.

Chapter 5 describes the electron spin chemistry of a paramagnetic nitroxide molecule incarcerated inside a capsule (nitroxide@octa acid) and presents supramolecular effects on paramagnetic interaction between the nitroxide incarcerated inside the capsuleplex with the nitroxide in bulk aqueous media studied by electron paramagnetic resonance (EPR) spectroscopy.

Table of Contents

List of Figures

Chapter 1

Chapter 2

Chapter 3

Chapter 4

Chapter 5

List of Charts

List of Equations

List of Schemes

List of Tables

Chapter 2

Chapter 3

Chapter 4

Acknowledgements

It is not possible to acknowledge in detail my sincerest gratitude for the apprenticeship with Professor Nicholas J. Turro at Columbia University, and the illuminating discussions and constructive criticisms so many friends and colleagues, especially members of the Turro group, and our visitors from abroad have afforded me over the past five years. I would like to thank particularly, Professor Mervat Zewail from Cerritos College for getting me to the starting line of pursuing a degree in Chemistry. Dr. John D. Roberts from Caltech for being my coach and mentor throughout the past nine years and to this day, I know you will always be there. Finally, Professor Nicholas J. Turro here at Columbia University for running alongside me these past five years, demonstrating first-hand the proper form of a professional scientist and letting me absorb all that I can. These mentors have had the greatest influence in my scientific career and are the reason for where I am today. I will always be indebted to their intellectual generosity.

Thank you to the members of my dissertation committee: Professor Ann McDermott, Professor Louis Brus, Professor George Flynn, and Professor Ron G. Lawler for reviewing this thesis and for the suggestions to improve this work.

Thank you Sandy Turro for proofreading my entire thesis line-by-line and for showing me the meaning of perseverance, resilience and how to cross the finish line with grace and style.

Thank you to the Turro group 2006-2011 with special mention, love and gratitude to: Dr. Xuegong Lei, Dr. Arunkumar Sundaresan (Arun), Dr. Steffen Jockusch, Dr. Alberto Moscatelli, Dr. Angel Marti, Dr. Mike Frunzi, Dr. Yongjun Li, Xia Li, Professor Sivaguru Jayaraman, Dr. Ellane Park, Professor José Paulo Da Silva and Professor Massimo Bietti. You have been my colleagues, friends and family. Thank you for being there during the tough times, not unlike those middle miles in a marathon where I can't see the finish line and begin to doubt my purpose

and question my motivation. All of you are what I will miss most about New York City (besides Central Park and the fast-paced environment) but thanks to Skype and Google chat, not all will be lost. I am also greatly indebted to Arun and the family members of Dr. Xuegong Li and wife of Dr. Yongjun Li, Jing Wang for fueling me with homemade authentic cuisines throughout my graduate student life. It brought me a taste of home and a feeling of care. Thank you.

Thank you, in no particular order, Dr. Chien-Yang (Frank) Chiu, Dr. Kuo-Ying (Penny) Huang, Teresa Jacques, Tania Cabrera, Miguel Hernandez, Dr. Rohitha SriRamaratnam, Dr. Kristy Tran, Dr. Teresa Fazio, Professor Uttam Tambar, Dr. Daniel Caspi, Natalie Mak-Pudlowski, and Dr. Shirley Chen for your genuine friendship and also for fuel from time-to-time.

Thank you Chemistry department: Socorro Lugo (Socky), Daisy Melendez, Danielle Farrell (Dani), Alix Lamia, Emilia Warlinski-Tokiwa, Chris Cecilio, Song Yu, Rati Jebashvili, and Jay Kirschenbaum for the foundation and support, and for making my time with the department memorable.

Thank you Columbia Center for New Media Teaching and Learning (CCNMTL): Dan Beeby, Michael Cennamo, Brian O'Hagan, Stephanie Ogden, Gerard Zoehfeld, and Steve Welsh for providing your expertise in technology-supported teaching as well as tools to facilitate virtual research collaborations in the Turro group.

The planning of this thesis and the writing of many chapters have benefited from the help and advice of Professor Turro and Professor Ronald G. Lawler. Those familiar with their work will have no difficulty in discerning their influence. Let them be assured of my deep gratitude.

I would also like to thank those that were involved in my project by chapters:

Chapter 2. Thank you Dr. John Decatur for all your help related to NMR, and thank you to the $H_2@C_{60}$ team: Professor Ron Lawler, Dr. Steffen Jockusch, Dr. Xuegong Lei, Dr. Angel Marti, Dr. Mike Frunzi, Dr. Yongjun Li, Dr. Salvo Mamone, Dr. Alberto Moscatelli.

Chapter 3. I would like to thank our collaborator, teacher and friend, Professor Ronald G. Lawler for his unwavering patience and enthusiasm in explaining and unraveling the abstract mathematic formulations behind relaxation mechanisms and bringing forth a model (cartoon) that can be visualized.

Chapter 4. Thank you Dr. Elena Sartori and Professor Ron Lawler for their time in helping me sort out all the data. Thank you Boss for teaching me how to systematically approach a problem and where to look for possible solutions (see first sentence). Most importantly, for not letting me fixate on the problem and keeping the project moving forward.

Chapter 5. Thank you to Dr. Francesca Ottaviani for the EPR tutorial in January of 2008, for translating the experimental EPR data through simulation to provide physical information and a more in-depth understanding about the system studied above, and for her hospitality during my visit to Italy in the summer of 2008.

Thank you Dr. Nithyanandhan Jayaraj for running the NMR part of the project and a fun week in the Turro lab including our excursion to The Empire State Building. Thank you Professor Ramamurthy for sending him.

Thank you Dr. Steffen Jockusch for helping with the details involved in the experiments, especially at the beginning of my graduate student career. Thank you Boss for bringing all the resources to one place.

Last but most importantly, just as one never runs the full 26.2 miles during marathon training and being able to complete the full course on the actual day takes much more than preparation, I

want to thank my family – mom, dad and my sisters Angela and Eileen Chen; and my best friend, Shunte Yllera, for providing me with the unconditional love and support that has strengthened and nourished me through the years.

Thank you New York City running community and my team mates from Greater New York Racing Team. Go Speedchicks!

To The Boss and Sandy

"If it were not for time, everything would happen at once; if it were not for deadlines, nothing would happen at all."

Chemical Structures and Nomenclatures for All The Players

List 1: C_{60} Family

C_{60} fullerene derivatives nomenclature

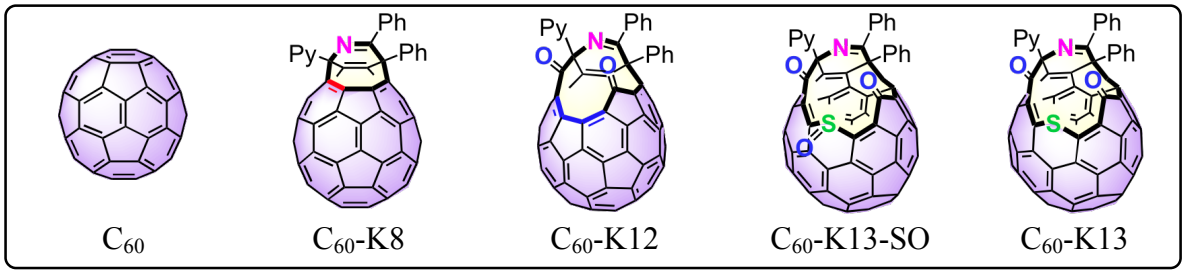

C_{60} endofullerenes

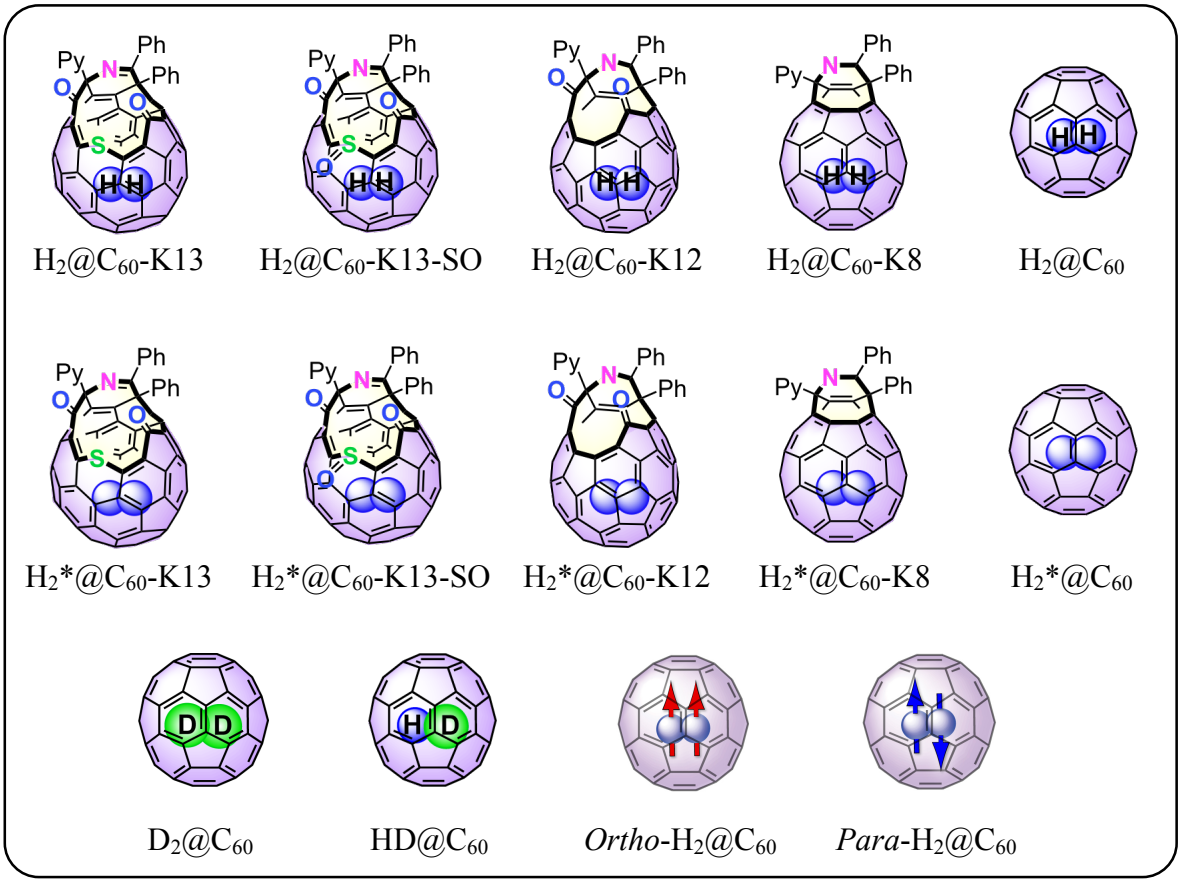

H_2* = mixtures of H_2, HD and D_2 hydrogen molecules

List 2: C_{70} Family

C_{70} fullerene derivatives nomenclature

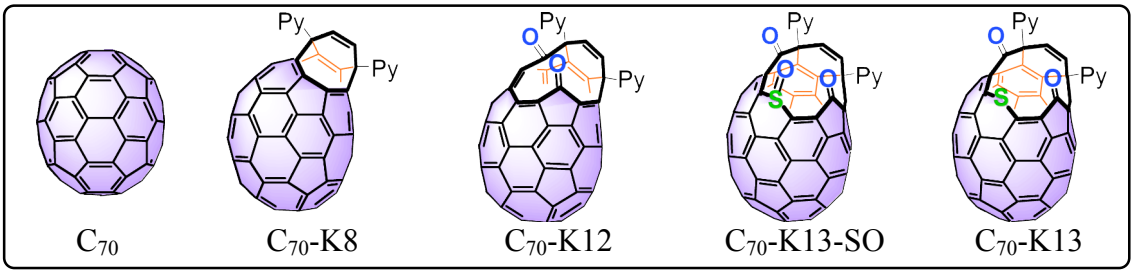

H_2 containing C_{70} endofullerenes

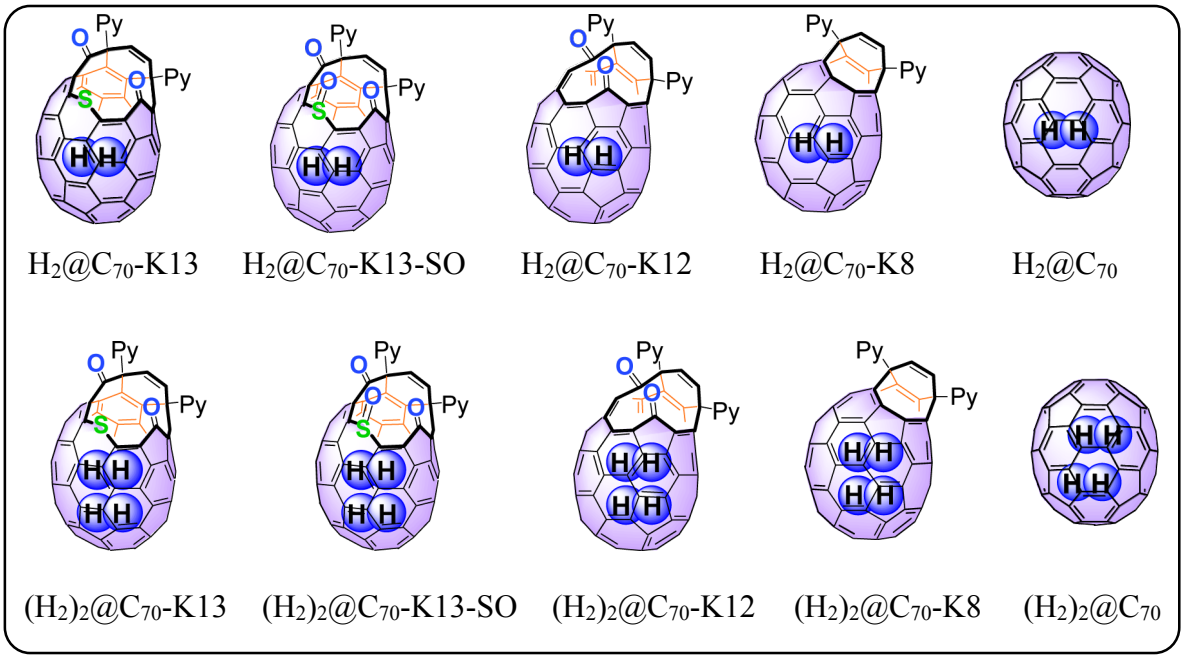

H_2* containing C_{70} endofullerenes

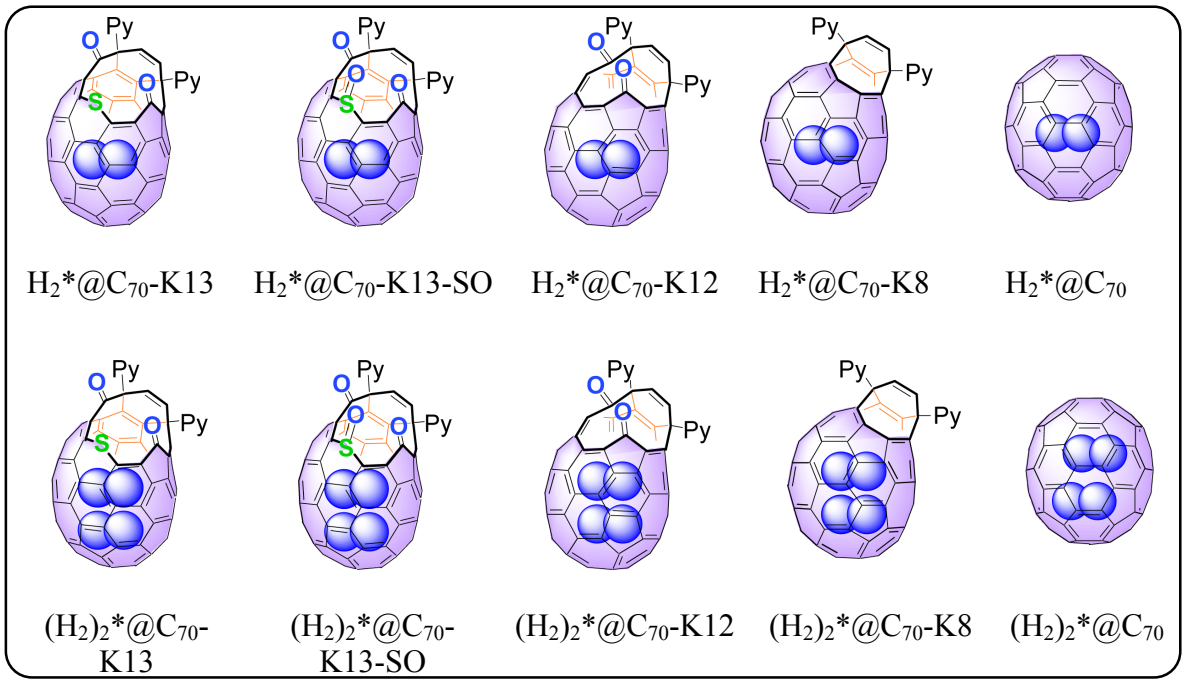

List 3: Water-encapsulating Fullerenes

Iwamatsu Fullerenes[a]

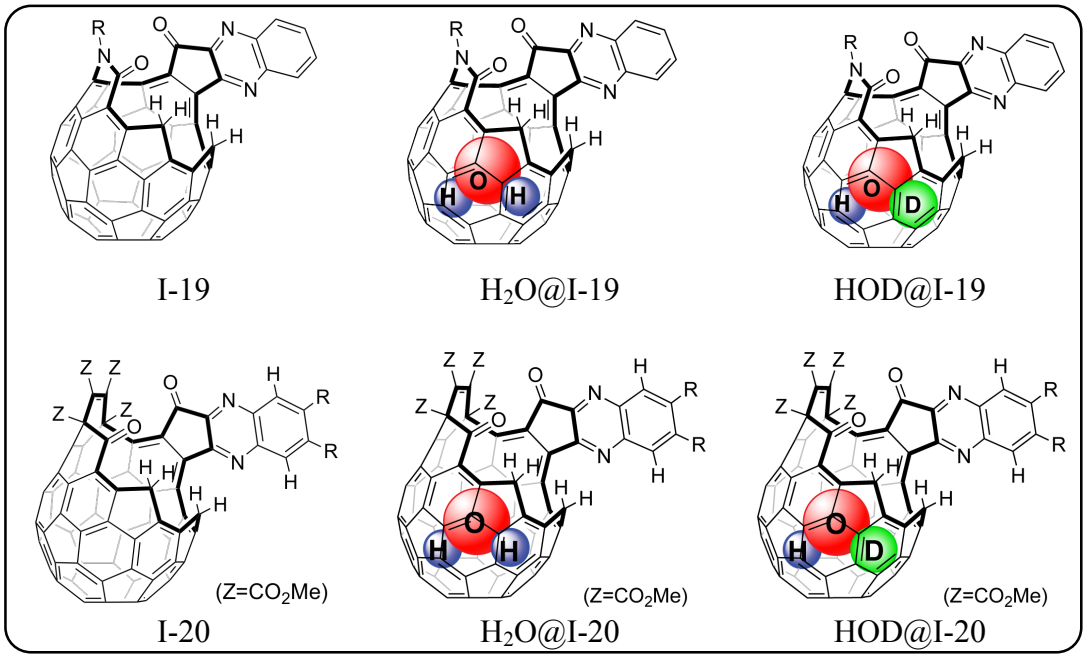

[a] Denoted with "I-" followed by number corresponding to ring size

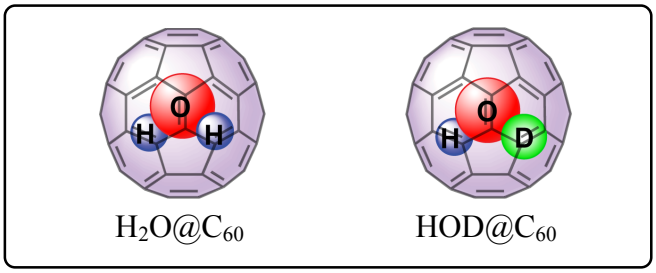

$H_2O@C_{60}$ $HOD@C_{60}$

List 4: $H_2@C_{60}$ derivatives covalently linked to nitroxide radical(s) nomenclature and its calculated distances based on 1/T values[a]

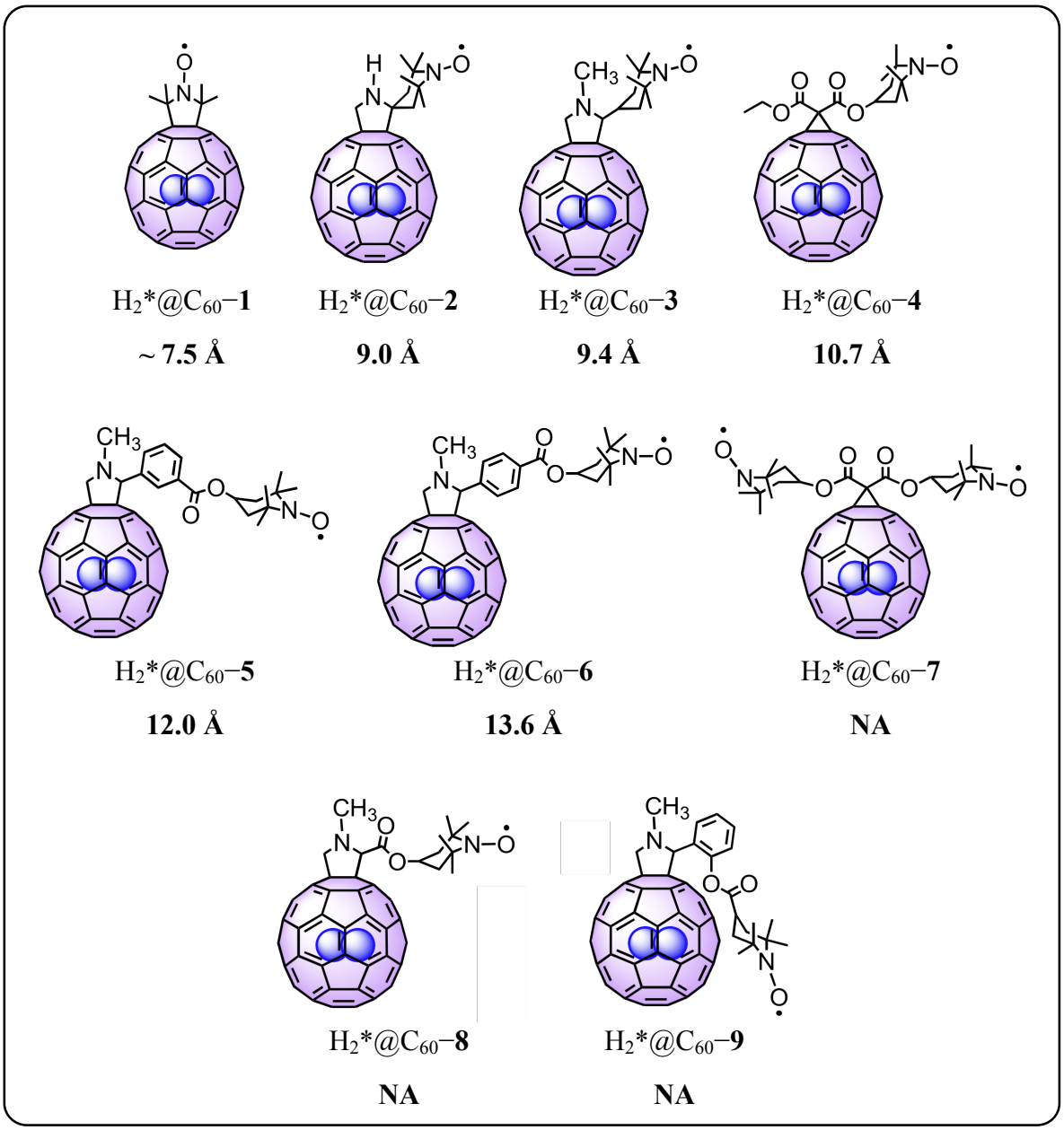

[a] *J. Phys. Chem. Lett.* **2010**, 1, 2135-2138

1 Introduction to Supramolecular Guest@Host Systems

In molecular chemistry, the structure and dynamics are controlled by the covalent chemical bonds between two atoms or groups of atoms and a single molecular structure is sufficient to understand the system. In supramolecular chemistry, the structures and dynamics are controlled by the non-covalent chemical bonds between two atoms or groups of atoms and this can be (1) the inclusion of small guest molecules within suitable host compounds, termed guest@host complex, resulting in constrained systems that imbue unique properties upon the incarcerated organic substrate[1], and (2) the study of basic feature of highly selective interactions occurring between two or more non-covalently linked molecules and with their implementation in specially designed non-natural systems[2]. For example, for many years attempts to isolate cyclobutadiene in solution at room temperature failed because one diene undergoes a very rapid Diels-Alder reaction with a second diene molecule (dimerization). Dr. Donald Cram was able to "tame" and isolate cyclobutadiene by synthesizing it in a host system that would provide supramolecular steric hindrance to prevent dimerization.[3] In the case of (2), targeted delivery of active pharmaceutical ingredients can be facilitated *in vivo*. In natural or synthetic systems, binding can result from any combination of hydrogen bonding, ion pairing, van der Waals interactions cation/anion - π interactions and solvophobic effects. So, supramolecular tactics are becoming widely employed and therefore, the knowledge gained from constructing such assemblies, in which two or more distinct molecules are held together by non-covalent forces to form a supramolecule (guest@host complex), including the understanding of their new properties and interactions with its immediate surroundings can be applied to the design and development of innovative devices.

The guest@host complex can be generalized into five main classes as shown in Figure 1.1. In general, a host molecule can be classified based on the differences in their skeleton (Chart 1.1) and are by itself referred to as a cavitand, carcerand or a capsule. When the host(s) forms a guest@host complex with a guest (denoted by G in Figure 1.1)

Name of guest@host Complex	Definition (Refers to Solution)	Schematic Structure (Large Spheres Represent Solvent)
Micelleplex	Guest@micelle complex. Examples: DBK@SDS (DBK = dibenzyl ketone), cylopentenone@deconate	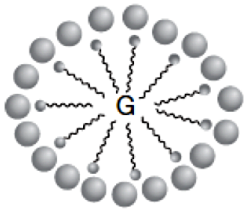
Cavitandplex	Guest@cavitand complex. Examples: cinnamic acid@CB	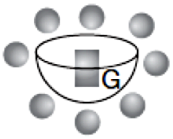
Capsuleplex (Hemicapsulplex)	Guest@capsule complex. Examples: DBK@OA_2, $anthracene_2$@OA_2	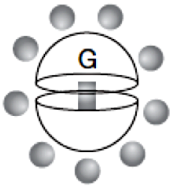
Hemicarceplex	Guest@carcerand complex (portals are large enough for guests to exit (ex) or enter the host cavity). $k_{ex} > k_{photo}$ Examples: biacetyl@Cram's carcerand	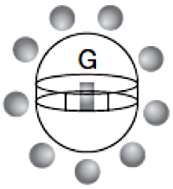
Carceplex	Guest@carcerand complex (portals are too small for guest to exit or enter the host cavity). $k_{ex} < k_{photo}$ Examples: cyclobutadiene@Cram's carcerand	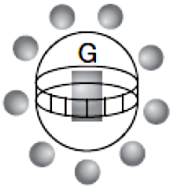

Figure 1.1: Name of guest@host complex and their definition accompanied by a schematic cartoon representation. Figure adopted from Nick Turro's Supramolecular Chemistry lecture notes.

then the whole unit is referred to as a cavitandplex, carceplex, or a capsuleplex. The difference between a hemicarceplex and a carceplex is that the guest, G can enter and exit the host of a hemicarceplex but is completely incarcerated in a carceplex.

An alternate method in supramolecular chemistry called self-assembly overcomes the limitations of carcerands and hemicarcerands. Self assembly describes the spontaneous construction of defined structural non-covalent arrays from smaller engineered building blocks, where weak interactions such as hydrogen bonding, ion pairing or hydrophobic interactions drive two host molecules to self assemble in an organized manner while including the guest.[4] Unlike carcerands, self-assembled molecules are dynamic in nature. Hydrogen bonds, hydrophobic forces, salt bridges, and metal/ligand interactions, have been used to create spaces that act as hosts for a range of guests.[5] Their association/disassociation rates can be controlled by the variation of conditions like pH, solvent environment, e.g., protic, aprotic and temperature.

Two main classes will be discussed in this thesis: a capsuleplex (Figure 1.1) and a carceplex (Figure 1.1) in which the former invokes self-assembly and the latter is man-made.

1.1 Capsuleplex: nitroxide@octa acid

The host molecule featured in the capsuleplex is a synthetic resorcinarene derivative (Chart 1.1) capable of forming dimeric capsular structure by self-assembly in an aqueous medium, and its structures and details are discussed in Chapter 5. The guest molecules are all derivatives of an organic free radical, nitroxide (Figure 1.2). The nitroxide is a

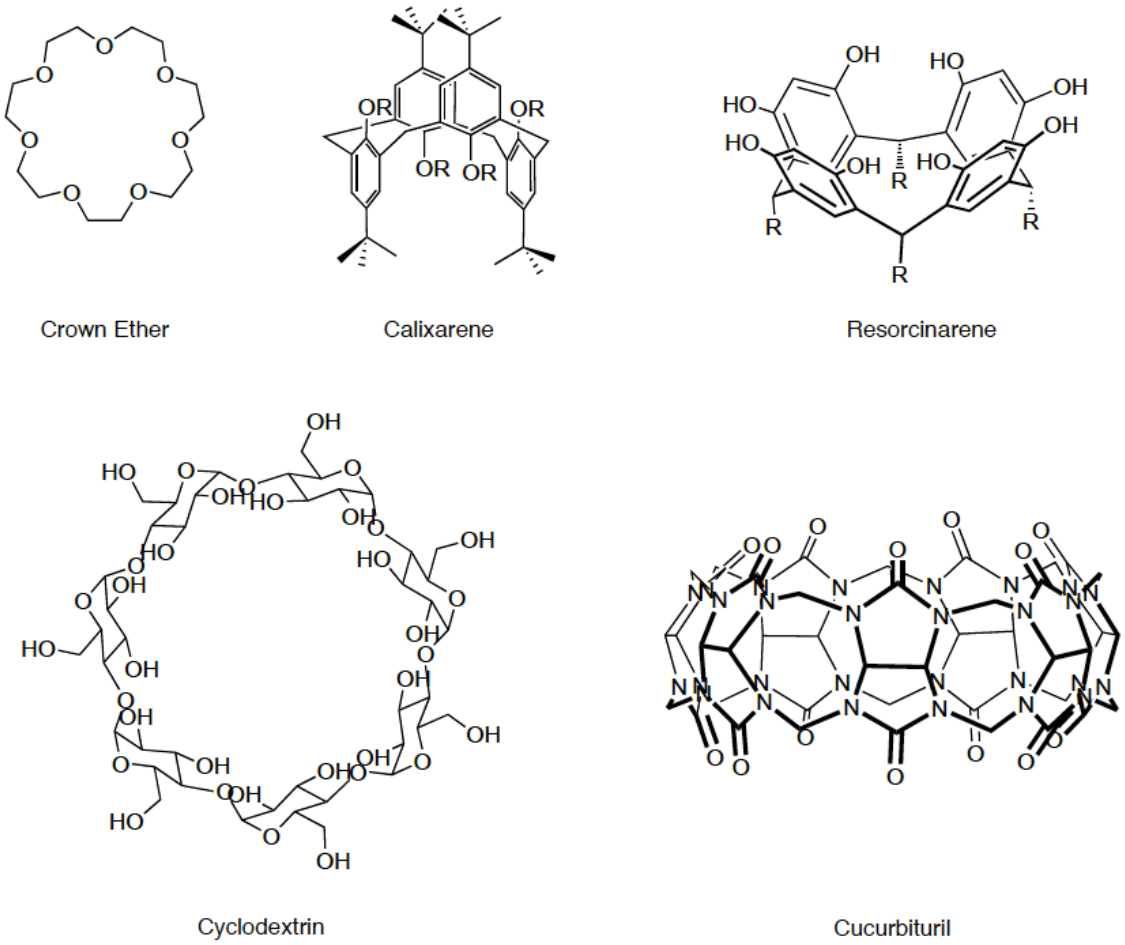

Chart 1.1: Structures of some organic host molecules: Crown ether, calixarene, resorcinarene, cyclodextrin and cucurbituril. These can be represented topologically as cavitands in **Figure 1.1**

stable paramagnetic species with one unpaired electron (S=1/2). The N-O bond is sp^3- hybridized so the π-electron is localized exclusively on the N-O group. Its stability is attained by steric hindrance of two *t*-butyl groups on the N site. These localized

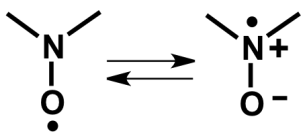

Figure 1.2: Resonance structures of nitroxide.

nitroxides are excellent probes for changes in the local environment. For example, the structural resonance in nitroxide radical as illustrated in Figure 1.2 shows that the ionic structure is hydrophilic and soluble in water and in polar solvents, whereas in a typical organic solvent, the neutral form may dissolve more easily; thus, the resonance equilibrium will change depending on the surroundings and whether the nitroxides are in polar or non-polar environments. The unpaired electron density (called the "spin density") is localized on the oxygen atom in the nonpolar structure and shifts towards the nitrogen atom as the equilibrium transfers to the right (Figure 1.2). In another words, the more the polar structure contributes, the more spin density on the nitrogen atom is observed. This effect is ascertained from electron paramagnetic resonance (EPR), also referred to as electron spin resonance (ESR) spectroscopy by measuring the nitrogen hyperfine coupling constant. Hyperfine coupling constant, denoted as A_N/a_N where the subscript denotes a nitroxide or A_{ii} expressed as tensor, is the interaction between the magnetic moment of an electron with the magnetic moment of the nucleus in its vicinity, in this case the nitrogen atom. As the polarity of the environment increases, the resonance shifts to the right (Figure 1.2) and the strength of the hyperfine interaction between the electronic spin and nitrogen nuclear spin increases; therefore the hyperfine coupling constant measures the polarity of the environment.[6] Both the hyperfine coupling in EPR and the spin-spin splitting or *J* coupling in NMR give information about the immediate surrounding of the electron or proton of interest. In EPR, the g-factor or g_{ii} expressed as tensor, is analogous to the chemical shift in NMR. For a free electron, $g_e = 2.002319$ and usually does not vary much for nitroxides. Additionally, the motion of the nitroxide radical is greatly influenced by the molecular dynamics of the surrounding molecule and

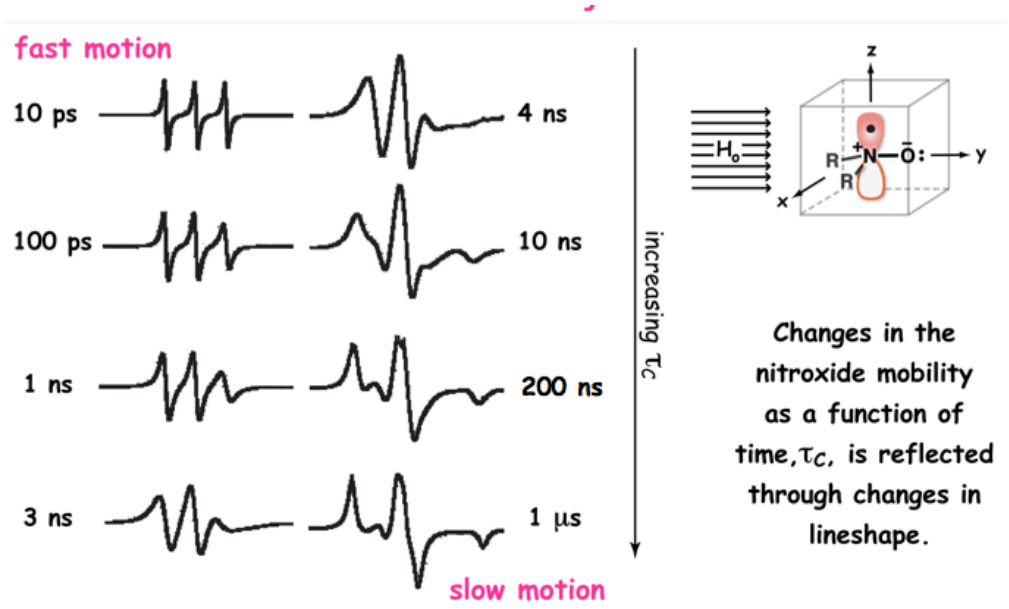

Figure 1.3: EPR spectra of changes in the nitroxide mobility as a function of time, τ_c as reflected through changes in line shape.

is reflected in the line shape of the EPR spectra (Figure 1.3), and the corresponding EPR parameter characterizes the molecular motion of nitroxide and is the rotational diffusion correlation time, τ.[7] There is a correlation between the correlation time and the viscosity of the solution and this can be extracted from the line shape of the EPR/ESR spectra. The specific guest molecules and the information extracted from their interaction with the host molecule are discussed in detail in Chapter 5.

1.2 Carceplex: $H_2@C_{60}$

The host molecule featured in the carceplex (Figure 1.1) is a specific carbon allotrope made up of sixty carbon atoms. The guest molecule is a proton allotrope. An allotrope is one of two or more different structural forms for an element with different physical and chemical properties. The following sections describe each of the carbon and proton allotropes in detail.

1.2.1 Carbon allotropes

Carbon exists in many allotropic forms including graphite, graphene, hollow tubules of graphite sheets called carbon nanotubes (CNTs), diamond and fullerene-like structures.[8] The focus of the carbon allotropes in this study are C_{60} and C_{70} and, as Hirsch[9] describes it, the C_{60} is a soccer ball shaped molecule and C_{70} is his bigger brother the "American football". It's an international project.

The 1996 Nobel Prize in Chemistry was shared by Robert F. Curl Jr., Sir Harold Kroto and Richard E. Smalley for their discovery of fullerenes, a new form of carbon atoms arranged in closed shells. The discovery of the unique structure of C_{60} was published in *Nature*[10] but neither physicists nor chemists had expected carbon to form such a symmetrical form! Since then, an entire new branch of chemistry was born. There is now a vast collection of literature about fullerenes.[9,11] I will point out those of interest as they become relevant in the discussion. In brief, we are interested in the physical properties of, and the differences between, C_{60} and C_{70} fullerenes as host molecules.

C_{60} and C_{70} fullerenes can be synthesized via (1) combustion with premixed laminar benzene-oxygen-argon flames and, depending on the pressures, temperatures and carbon-to-oxygen ratio, different C_{70}:C_{60} ratios of the fullerenes along with soot, polyaromatic hydrocarbons (PAHs) are formed. The amount of C_{60} and C_{70} produced is in the range of 0.003-9% of the soot mass. The C_{70}:C_{60} ratio varies from 0.26 to 5.7. Fullerenes can also be obtained by (2) pyrolysis of hydrocarbons, preferably aromatic hydrocarbons. The fullerenes are formed by dehydrogenation reactions. The products include both C_{60} and C_{70} in yields <0.5%; the side products are hydrofullerenes. The first example of a systematic and stepwise assembly of C_{60}

was the pyrolysis of naphthalene at 1000 °C in an argon stream.[12,13] Fullerene synthesis by laser pyrolysis has also been done using benzene and acetylene as the carbon source.[14]

1.2.2 Guest: Proton Allotopes

Following the discovery of proton spins, it has been realized that H_2 as well as H_2O have two distinct isomers (allotropes) with respect to their spin orientations, *ortho* (where the proton spins are parallel ↑↑) and *para* (where they are antiparallel ↑↓).[15] Since the two protons are confined to a single wave function, *para*-H_2 has two indistinguishable opposite configurations, both singlets (similar to two electrons in the same orbital). *O*rtho-H_2, on the other hand, has three degenerate configurations (similar to two electrons in the triplet state).

1.2.3 Pauli nuclear spin isomers of H_2

The components of the H_2 wave function, responsible for *ortho* and *para* states, involve both the rotational and nuclear spin degrees of freedom ψ_{rot} and ψ_{spin}, as shown in Figure 1.4. In principle, the conversion between *ortho* and *para* states can be brought via perturbations that mix either the rotational states or the nuclear spin states of different symmetries (Figure 1.4). However, quantum mechanics dictates a strict correlation between the nuclear spin states, *I,* and rotational states, J*,* of the symmetric molecule H_2. The overall molecular wavefunction, Ψ, of indistinguishable fermions (protons are fermions) has to be antisymmetric in exchange of the nuclei, $\psi_{rot} \times \psi_{spin}=\Psi(A)$ as shown in Figure 1.4. The symmetric spin isomer, *ortho*-H_2 (↑↑) is restricted to antisymmetric rotational states (J=1) and the antisymmetric spin isomer, *para*-H_2 (↑↓) is restricted to

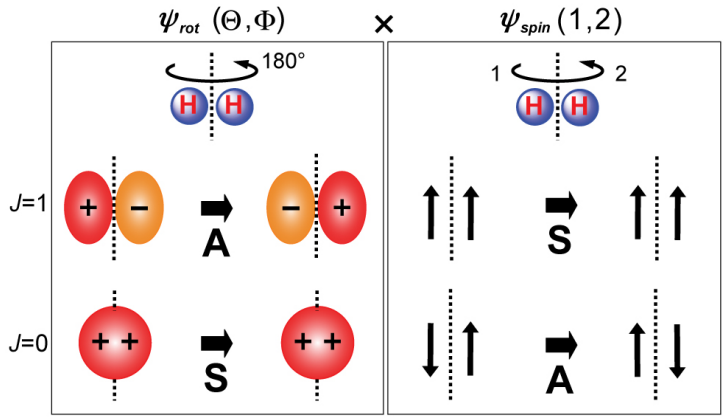

Figure 1.4: Schematic description of the effect on rotation about the H−H axis on the symmetry. (**A**, asymmetric or **S**, symmetric) of the rotational wave function ψ_{rot} of H_2 (left) and the spin wave function ψ_{spin} (right) for the two lowest rotational levels, J=0 and J=1 of H_2.

symmetric rotational states (J=0). Therefore, these spin state isomers have different energies (Figure 1.5).

1.2.4 Energy differences between the proton spin isomers

Figure 1.5 illustrates the energies between the two spin isomers of a hydrogen molecule. The *ortho*-H_2 (oH_2, triplet state) is at a higher energy level than the *para*-H_2 (pH_2, singlet state) isomer. The energy separation is 120 cm^{-1} (360MHz, 173K). It follows statistically that the oH_2:pH_2 ratio is 3:1. Macroscopically speaking, 75% of the H_2 gas molecules are in the *ortho* configuration. Furthermore, physical properties of these allotropes are different, e.g., oH_2 has a magnetic moment and pH_2 does not.

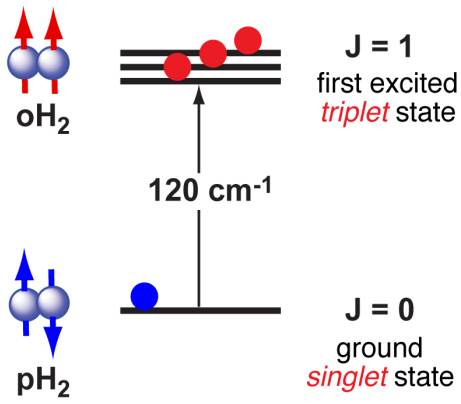

Figure 1.5: Energy level for the ground and first excited rotational state of H_2. The ground state (J=0) is a nuclear singlet state (*para*-H_2) and the first excited rotational state (J=1) is a nuclear triplet state (*ortho*-H_2).

1.2.5 Temperature dependence on equilibrium distribution of proton spin isomers

Maxwell[16] observed that the specific heat (J/Kg•K) of H_2 derailed from that of a diatomic gas below room temperature, and began to resemble that of a monoatomic gas at cryogenic temperatures. The quantum interpretation of this result is that energy spacing of the rotational levels for H_2 is much larger relative to other heavy atoms because of its low mass. At low temperature, the heat energy unequally distributes into the rotational motion of the hydrogen molecule.

It follows that there is a temperature dependence on the equilibrium of spin distributions. In the case of H_2, as shown in Figure 1.6, at temperatures above 150 K, the distribution between *ortho* and *para* hydrogen is statistical, 3:1 oH_2:pH_2, and at temperatures below 30 K, almost all are *para*hydrogens, e.g., ~99.8% at 20 K. Water molecule, H_2O also exists in two forms of spin isomers, *ortho*-H_2O (oH_2O) and *para*-H_2O (pH_2O). The energy difference is reduced to a tiny

level,[17] about 40 cm-1, and these isomers were found to be stable while the exchange between them is highly spin-forbidden and very slow,[18] similar to the forbidden transition between singlet and triplet states of electrons. The 3:1 ratio of oH_2O:pH_2O occurs at temperatures above 40 K. The 50:50 ratio of oH_2O:pH_2O occurs at 15 K and almost all are *para*water at 5 K and below.[17]

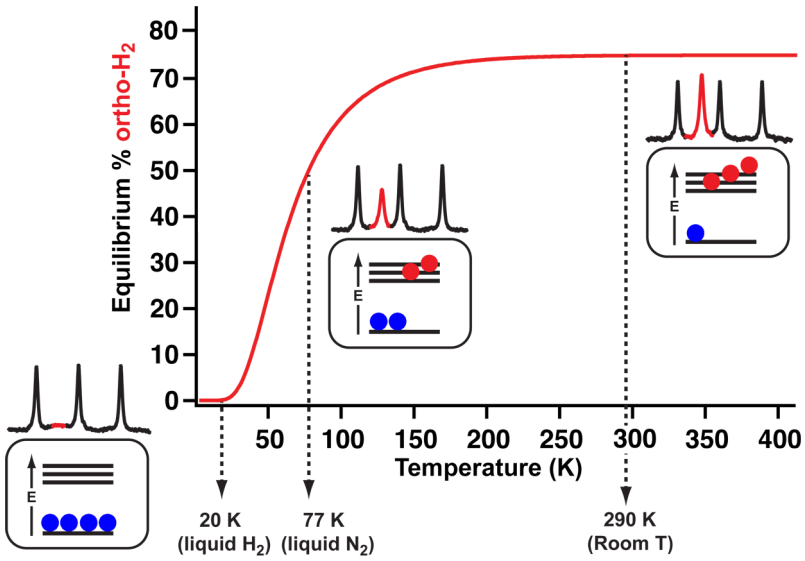

Figure 1.6: Temperature dependence of the population of *ortho*- and *para*-hydrogen (oH_2 and pH_2). At low temperature limit, e.g. liquid hydrogen, the population of oH_2 to pH_2 approaches zero. The high temperature limit the oH_2/pH_2 approaches 3. In the absence of a paramagnetic catalyst, the conversion between $oH_2 \leftrightarrow pH_2$ is extremely slow. With a catalyst, the thermodynamic equilibrium at any temperature is reached within minutes.

1.2.6 *Ortho* ↔ *para* conversion between the proton spin isomers

In the gas phase, the *ortho-para* conversion due to collisions and radiation processes is highly improbable.[19] The valuable factor of conversion is magnetic interactions. In the absence of magnetic impurities, the estimated lifetime of the gaseous *ortho* and *para* molecules is many months.[20] Thus, the hydrogen molecule and water vapor is a true mixture of two gaseous

ensembles consisting of magnetic (*ortho*) and nonmagnetic (*para*) molecules. This means that the *ortho* and *para* ensembles can be, in principle, spatially separated.

The "magnetic catalyst" mechanism, first treated by Wigner[21], invokes a magnetic field gradient across the ^{1}H spins that mixes the I=0 (*para*) and I=1 (*ortho*) states. In addition, the perturbation also affects the "overlap" of the otherwise orthogonal rotational state functions for *ortho* and *para*. The result is a non-zero probability of transitions between the states.

As will be discussed in Chapter 2, in which we used the classic Wigner theory[21], to explain our $oH_2 \leftrightarrow pH_2$ conversion rates for covalently attached nitroxides and also the effects of external nitroxide (Figure 1.2) or O_2 as the magnetic catalyst, the perturbation is the dipole-dipole interaction between the two ^{1}H spins and an electron spin. In the case of biradicals or the triplet states of C_{70} there are two electron spins, or one net electron spin of S=1. Ilisca[22] has invoked other mechanisms, including interactions of the nuclei with orbital electron magnetism; however, the role of this "spin orbit effect" involving nuclear spin of light atoms such as the hydrogen molecule is negligible. In fact, conversion can take place via the Wigner mechanism under the influence of a magnetic field of any type as long as it is not exactly the same at both ^{1}H nuclei all the time.

1.2.7 Application and Motivation

There is an extensive amount of information on diatomic molecules, specifically the hydrogen molecule. If one opens a physical chemistry or physics textbook where one learns about Pauli's Principal and Aufbau's Rule in quantum mechanics, surely, one always find examples using hydrogen molecules, the simplest molecules with discrete energy levels. One might also learn that the hydrogen molecule has two allotropic forms, *ortho*-hydrogen and *para*-hydrogen and the only difference between these two allotropes is the orientation of their nuclear

spins which results in remarkable physical property and spectroscopy. This is especially of interest for physicists and theoreticians because of its symmetry.

For H_2, an important application in chemistry of these quantum mechanical symmetry effects is called "Para Hydrogen Induced Polarization"(PHIP). If hydrogen gas is kept at low temperatures it converts after some time into the energetically favorable *para*-hydrogen, but only in the presence of a spin catalyst (by contact with paramagnetic species or adsorption to nuclear spins).[23] The increase in population of the *para* state leads to the hyperpolarization of the H_2 molecule. These *para*-enriched hydrogen molecules are in a pure nuclear singlet state, also the lowest rotational state according to the Pauli exclusion principle and they remain stable in liquid solutions for days in the absence of a paramagnetic catalyst.[24,25] Proton spin polarization can then be transferred to the reaction products of *para*hydrogen, yielding the characteristic *para*-H_2 effects in the NMR spectra as discovered in 1986 by Weitekamp and Eisenberg.[26,27,28] Since then, other systems have been investigated in order to better understand the fate of the hydrogen in catalytic hydrogenation reactions and utilizing it as a diagnostic tool.[29,30,31,32,33,34] Generally, the PHIP method depends on adding *para*-H_2 across a double or triple bonds in the substrate molecule e.g. an alkyne R_1-C≡C-R_2 with $R_1 \neq R_2$. This transforms an A_2 (*ortho*-H_2) system into an AX system (hydrogenated double bond). In a normal situation, the ^{1}H NMR signal corresponding to *ortho*-H_2 is a single line. Scheme 1.1 shows the energy levels for a two spin system for the A_2 and AX situation of strong coupling of the nuclear spins and it corresponds to what is expected of *para*-H_2 if it were added to a double or triple bond and it produced two non-equivalent protons A and X.

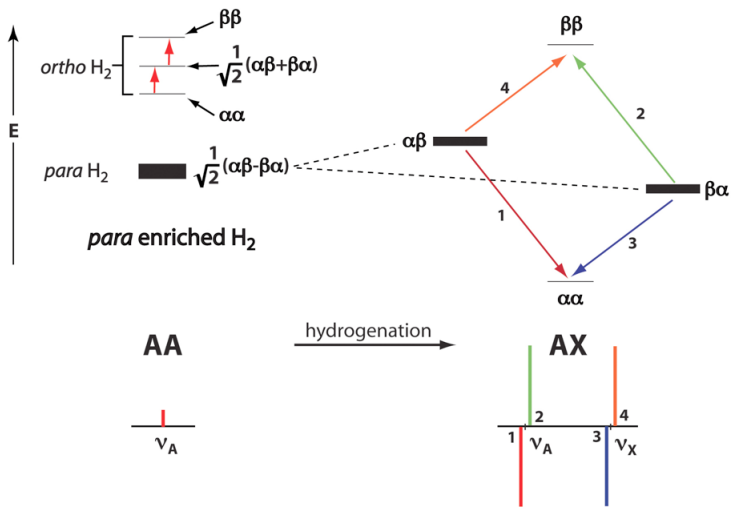

Scheme 1.1: Energy level of *para* enriched H_2 in the presence of magnetic field. Left: The AA spin system; Right: an AX spin system resulting from hydrogenation reaction from the two hydrogen atoms of the initial AA system.

Also it is necessary that the *para*-H_2 be transferred pair-wise to the substrate and the symmetry of *para*-H_2 has to be broken, in other words, to go from an AA system to an AX system. If this is not the case then transition between populated state, $1/\sqrt{2}(\alpha\beta - \beta\alpha)$ and the vacant states $\alpha\alpha$ or $\beta\beta$ are symmetry forbidden. Now consider the hydrogenation reaction such that the two protons of the hydrogen molecule, initially an AA system, are added pair-wise into the substrate molecule and evolve towards an AX system. This means that these two protons are now hydrids and become magnetically nonequivalent in the final molecule. Only those nuclear spin energy levels in the product molecule become populated having corresponding symmetry properties of the initial *para*-H_2. Specifically, if the chemical shift frequency difference, $\Delta\nu$ between the protons of the product molecule is greater than its J coupling between each other, then the new states corresponds to $\alpha\beta$ and $\beta\alpha$ in the product. This is shown Scheme 1.1 in which the population of $1/\sqrt{2}(\alpha\beta - \beta\alpha)$, corresponding to *para*-H_2, maps into $\alpha\beta$ and $\beta\alpha$ states

of the product, shown with a dotted line. With normal H_2 (a mixture of 25% *para*-H_2 and 75% *ortho*-H_2), the NMR signal of *ortho*-H_2 is a singlet and after hydrogenation, the NMR is a typical doublet of doublets. In the case of *para*-enriched H_2, NMR signal from the *ortho*-H_2 is largely reduced because most of the population is redistributed to the *para*-H_2 after *para*-enrichment at low temperature (Figure 1.6). Upon hydrogenation, each $\alpha\beta$ and $\beta\alpha$ states receives one half of the population from the *para*-enriched H_2 and four intense NMR transitions are possible from these initial states to the unoccupied states of $\alpha\alpha$ and $\beta\beta$ (Scheme 1.1). And since either spin can undergo absorption or emission with equal probability, the spectrum at each chemical shift consists of two lines of equal, but opposite amplitude separated by J (Scheme 1.1). This is the basic underlying principle and Bower and Weitekamp named it PASADENA (Parahydrogen And Synthesis Allowed Dramatically Enhanced Nuclear Alignment). Examples are the ^{1}H NMR of ethylbenzene formed by the addition of *para*-H_2 to styrene,[35] and ^{13}C-labeled succinic acid in its application for MRI.[36] The polarization effect disappears once the thermodynamic equilibrium population is reestablished. Thus, effects are limited by the spin-lattice relaxation time, T_1 of the product molecule. In theory, the extraordinary enhancements in the NMR signal may reach values as high as 10^5-times the signal intensity of the corresponding derivatives produced with normal H_2,[27,37,38,39] allowing the detection of species which are present in solution in very low concentrations. This is one of the holy grails and motivations to study the hydrogen molecule. There is also the ALTADENA effect in which $\Delta\nu << J$, the opposite of the PASADENA effect, and this aspect is beyond the scope of the thesis.

1.2.8 The birth of the $H_2@C_{60}$ project in the Turro Group

Our research group has studied spin chemistry of guest@host complexes of singlet and triplet radical pairs for several decades.[40] The existence of the two molecular hydrogen spin isomers

was also of interest. We were fascinated with the seminal reports of the endofullerenes,[41,42,43] structures for which atoms and molecules were incarcerated in fullerenes (carceplex of Figure 1.1). However, there was no apparent connection between H_2 and endofullerenes of guest@host systems. This changed in 2005 when Professor Nicholas Turro (Boss) had a conversation with Professor Martin Saunders of Yale University, a pioneer[41] in the synthesis and study of atoms and molecules inside fullerenes. Saunders pointed out the elegant synthesis of $H_2@C_{60}$ by Professors Koichi Komatsu and Yasujiro Murata of Kyoto University[44] which inspired Boss to initiate a collaboration that began after a meeting with Professor Komatsu and Murata at the ACS PacifiChem meeting in December of 2005 to investigate the physical properties of H_2 inside C_{60} namely its spin chemistry and magnetic spectroscopy. I came to Columbia in the Fall of 2006 and began with comparing the relaxation times, T_1 of H_2 and HD in toluene and C_{60} (Chapter 2). In July of 2008, Boss sent a graduate student, Jeremiah Johnson (JJ) to spend 3 months in the laboratory of Professor Yasujiro Murata in Japan to learn the synthesis of $H_2@C_{60}$. It was a fruitful experience for both parties because they figured out how to control and quantitatively insert different ratios[45] of H_2:HD:D_2 inside C_{60} and we were able to scale up the production of $H_2@C_{60}$ to open doors for different types of synthetic modifications and spectroscopic studies.[46] Soon after JJ's return, scientists and theoreticians interested in/working on $H_2@C_{60}$ and any other endofullerene related compounds gathered at Columbia University for a two day $H_2@C_{60}$ Symposium. Figure 1.7 is a representative photo of the 2008 $H_2@C_{60}$ Symposium put together by The Boss. Since then, the $H_2@C_{60}$ project has blossomed.[46,47] This international collaboration also opens up a whole other venue in how research is done in our group. We utilize Internet tools, e.g., Skype and Google Docs to facilitate virtual discussions, presentations and seminars on a regular basis!

Figure 1.7: Group photo in 209 Havemeyer of the $H_2@C_{60}$ Symposium at Columbia University on August 14th and 15th, 2008.

1.2.9 Generation of endofullerenes, $H_2@C_{60}$

The synthesis[44,48,49] of $H_2@C_{60}$ is outlined schematically in Scheme 1.2 along with their nomenclature[50] just below the structure in bold. Each step (1 through 8) described in the text below corresponds to the number in parenthesis over the synthesis arrow in Scheme 1.2.

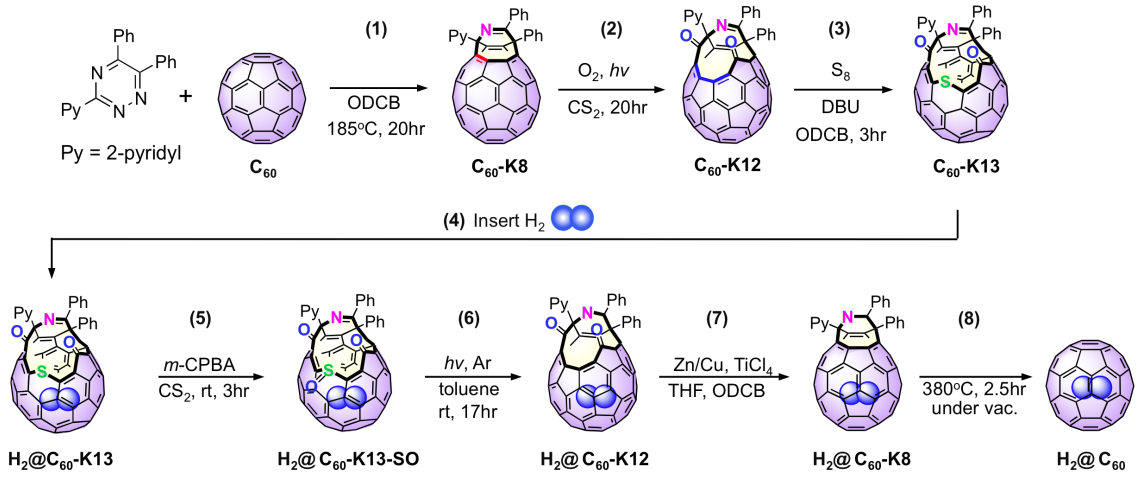

Scheme 1.2: The synthesis of $H_2@C_{60}$. Please refer to text for details.

$H_2@C_{63}NO_2SPh_2Py$ ($H_2@C_{60}$-K13) (Scheme 1.2 second row, most left structure) was synthesized by (1) thermal reaction of C_{60} with 3-(2-pyridyl)-5,6-diphenyl-1,2,4-triazine under argon to form C_{60}-K8: an aza-open-cage fullerene derivative having an eight-membered-ring orifice on the fullerene cage. (2) C_{60}-K8 undergoes oxidative ring-enlargement reactions with singlet oxygen under photo-irradiation to give azadioxo-open-cage fullerene derivative, C_{60}-K12, which has a 12-membered-ring orifice. (3) Thermal reaction of C_{60}-K12 with elemental sulfur in the presence of 1,8-diazabicycloundec-7-ene (DBU) resulted in further ring enlargement to give azadioxothia-open-cage fullerene derivative, C_{60}-K13, which has a 13-membered-ring orifice. (4) Insertion of molecular hydrogen into C_{60}-K13 to give $H_2@C_{60}$-K13 in 100% yield was accomplished by treating a powder of C_{60}-K13 with high pressure of hydrogen gas (800 atm) at 200 °C in an autoclave for 8 hours.

$H_2@C_{60}$ (Scheme 1.2) was synthesized by removal of the sulfur atom on the rim of the orifice followed by chemical closure of the orifice of $H_2@$ C_{60}-K13. High temperature must be avoided to prevent significant loss of encapsulated hydrogen. (5) The sulfur atom of $H_2@C_{60}$-K13 was oxidized by *m*-CPBA at room temperature to give the sulfoxide $H_2@C_{60}$-K13-SO. (6)

The sulfinyl group was removed by photoirradiation with visible light under argon also at room temperature to give $H_2@C_{60}$-K12, a 12-membered-ring orifice. (7) The two carbonyl groups in $H_2@C_{60}$-K12 were reductively coupled by using Ti(0) at 80°C to give $H_2@C_{60}$-K8 with eight-membered-ring. (8) Finally, complete closure of the orifice was achieved by heating the powder of $H_2@C_{60}$-K8 in a glass tube under vacuum at 380°C for 2.5 hours. The crude product was dissolved in carbon disulfide and passed through silica-gel column to give $H_2@C_{60}$.

1.3 Scope of this work

The story and results presented in this thesis are as follows: Chapter 1 describes the background and motivation of our scientific pursuit. Chapters 2-4 pertains to the carceplex (Figure 1.1) $H_2@C_{60}$ and Chapter 5 pertains to the capsuleplex (Figure 1.1) nitroxide@octa acid.

Chapter 2 presents experimental results of the *ortho*-H_2 ↔ *para*-H_2 conversion of $H_2@C_{60}$ and stable intermediates of H_2 inside open forms of fullerene ($H_2@openC_{60}$) isolated during the synthesis steps (Scheme 1.2) as well as *ortho*-H_2 ↔ *para*-H_2 conversion of $H_2@C_{70}$ and $(H_2)_2@C_{70}$ fullerenes. The spin-lattice relaxation (T_1) and paramagnetic relaxivity (R_x) of $^{1,2}H_2$, $^{1,2}H_2@C_{60}$, $^{1,2}H_2@openC_{60}$, $^{1,2}H_2@C_{70}$, $(H_2)_2@C_{70}$ and H_2O@fullerene are presented in Chapters 3 (T_1) and Chapter 4 (R_x).

Chapter 5 presents supramolecular effects on paramagnetic interaction between nitroxide incarcerated inside the capsuleplex with nitroxide in bulk aqueous media studied by electron paramagnetic resonance (EPR) spectroscopy.

1.4 References

(1) Cram, D. J. Cavitands: organic hosts with enforced cavities. *Science* **1983**, *219*, 1177-83.

(2) Lehn, J. M. Supramolecular chemistry. *Science* **1993**, *260*, 1762-3.

(3) Cram, D. J. Tanner, M. E.; Thomas, R. The Taming of Cyclobutadiene. *Angew. Chem. Int. Ed. Engl.* **1991**, *30*, 1024-1027.

(4) Jasat, A.; Sherman, J. C. Carceplexes and Hemicarceplexes. *Chem. Rev.* **1999**, *99*, 931-968.

(5) Barrett, E. S. Dale, T. J.; Rebek, J. Self-assembly dynamics of a cylindrical capsule monitored by fluorescence resonance energy transfer. *J. Am. Chem. Soc.* **2007**, *129*, 8818-24.

(6) Dodd, G. Barratt, M.; Rayner, L. Spin probes for binding site polarity. *FEBS Lett.* **1970**, *8*, 286-288.

(7) Freed, J. H. In *Theory of Slow Tumbling ESR Spectra for Nitroxides*; Academic Press, Inc.: New York, **1976**; pp. 53-130.

(8) Ebert, L. Science of fullerenes and carbon nanotubes By M. S. Dresselhaus, G. Dresselhaus and P. C. Eklund, Academic Press, **1996**, 965 pages.

(9) Hirsch, A.; Brettreich, M. *Fullerenes*; Wiley-VCH Verlag GmbH & Co. KGaA: Weinheim, FRG, **2005**.

(10) Kroto, H. W. Heath, J. R. O'Brien, S. C. Curl, R. F.; Smalley, R. E. C60: Buckminsterfullerene. *Nature* **1985**, *318*, 162-163.

(11) Bakry, R. Vallant, R. M. Najam-ul-Haq, M. Rainer, M. Szabo, Z. Huck, C. W.; Bonn, G. K. Medicinal applications of fullerenes. *International Journal of Nanomedicine* **2007**, *2*, 639-649.

(12) Taylor, R. Langley, G. J. Kroto, H. W.; Walton, D. R. M. Formation of C_{60} by pyrolysis of naphthalene. *Nature* **1993**, *366*, 728-731.

(13) Tayler, R.; Langley, G. J. In *Proceedings of the Symposium on Recent Advances in the Chemistry and Physics of Fullerenes and Related Materials*; San Francisco, CA, **1994**; p. 68.

(14) Armand, X. Fullerene synthesis by laser pyrolysis of hydrocarbons. *J. Phys. Chem. Solids* **1997**, *58*, 1853-1859.

(15) Farkas, A. In *Orthohydrogen, Parahydrogen and Heavy Hydrogen*; Cambridge University Press, **1935**; pp. 1-205.

(16) Yates, J. T.; Johnson, K. J. In *Molecular Physical Chemistry for Engineers*; University Science Books, **2007**; pp. 293-346.

(17) Stephenson, C. C.; McMahon, H. O. The Rotational Partition Function of the Water Molecule. *J. Chem. Phys.* **1939**, *7*, 614.

(18) Tikhonov, V. I.; Volkov, A. a Separation of water into its ortho and para isomers. *Science* **2002**, *296*, 2363.

(19) Oka, T. Collision-Induced Transitions between Rotational Levels. *Adv. Atomic and Mol. Phys.* **1974**, *9*, 127-206.

(20) Curl, R. F. Nuclear Spin State Equilibration through Nonmagnetic Collisions. *J. Chem. Phys.* **1967**, *46*, 3220.

(21) Wigner, E. P. Concerning the Paramagnetic Conversion of para-ortho Hydrogen. III. *Phys. Chem.* **1933**, *B23*, 28-32.

(22) Ilisca, E. Theory of ortho-para hydrogen conversion catalyzed by "d" electrons. *Chem. Phys. Lett.* **1990**, *168*, 289-292.

(23) Buntkowsky, G. Walaszek, B. Adamczyk, a; Xu, Y. Limbach, H.-H.; Chaudret, B. Mechanism of nuclear spin initiated para-H_2 to ortho-H_2 conversion. *Phys. Chem. Chem. Phys.* **2006**, *8*, 1929-35.

(24) Silvera, I. The solid molecular hydrogens in the condensed phase: Fundamentals and static properties. *Rev. Mod. Phys.* **1980**, *52*, 393-452.

(25) Kranendonk, J. van *Solid hydrogen : theory of the properties of solid H_2, HD, and D_2*; Plenum Press: New York, **1983**; pp. 1-306.

(26) Bowers, C.; Weitekamp, D. Transformation of Symmetrization Order to Nuclear-Spin Magnetization by Chemical Reaction and Nuclear Magnetic Resonance. *Phys. Rev. Lett.* **1986**, *57*, 2645-2648.

(27) Bowers, C. R.; Weitekamp, D. P. Parahydrogen and synthesis allow dramatically enhanced nuclear alignment. *J. Am. Chem. Soc.* **1987**, *109*, 5541-5542.

(28) Eisenberg, R. Parahydrogen-induced polarization: a new spin on reactions with molecular hydrogen. *Acc. Chem. Res.* **1991**, *24*, 110-116.

(29) Duckett, S. B.; Sleigh, C. J. Applications of the parahydrogen phenomenon: A chemical perspective. *Progress in Nuclear Magnetic Resonance Spectroscopy* **1999**, *34*, 71-92.

(30) Duckett, S. B. Newell, C. L.; Eisenberg, R. Observation of New Intermediates in Hydrogenation Catalyzed by Wilkinson's Catalyst, $RhCl(PPh_3)_3$, Using Parahydrogen-Induced Polarization. *J. Am. Chem. Soc.* **1994**, *116*, 10548-10556.

(31) Atkinson, K. D. Cowley, M. J. Elliott, P. I. P. Duckett, S. B. Green, G. G. R. López-Serrano, J.; Whitwood, A. C. Spontaneous transfer of parahydrogen derived spin order to pyridine at low magnetic field. *J. Am. Chem. Soc.* **2009**, *131*, 13362-8.

(32) Bargon, J. Kandels, J.; Kating, P. Nuclear magnetic resonance studies of homogeneous catalysis using parahydrogen: Analysis of nuclear singlet–triplet mixing as a diagnostic tool to characterize intermediates. *J. Chem. Phys.* **1993**, *98*, 6150.

(33) Aime, S. Gobetto, R.; Canet, D. Longitudinal Nuclear Relaxation in an A_2 Spin System Initially Polarized through Para-Hydrogen. *J. Am. Chem. Soc.* **1998**, *120*, 6770-6773.

(34) Aime, S. Dastrù, W. Gobetto, R. Russo, a; Viale, a; Canet, D. A Novel Application of para H_2 : the Reversible Addition/Elimination of H_2 at a Ru_3 Cluster Revealed by the Enhanced NMR Emission Resonance from Molecular Hydrogen. *J. Phys. Chem. A* **1999**, *103*, 9702-9705.

(35) Bowers, C. R. Carson, P. J. Norris, D. J.; Weitekamp, D. P. In *25th Congress AMPERE on Magnetic Resonance and Related Phenomenon*; Springer, Berlin, **1990**; Vol. 148, p. 148.

(36) Chekmenev, E. Y. Hövener, J. Norton, V. a; Harris, K. Batchelder, L. S. Bhattacharya, P. Ross, B. D.; Weitekamp, D. P. PASADENA hyperpolarization of succinic acid for MRI and NMR spectroscopy. *J. Am. Chem. Soc.* **2008**, *130*, 4212-3.

(37) Bargon, J. Kandels, J.; Kating, P. Nuclear magnetic resonance studies of homogeneous catalysis using parahydrogen: Analysis of nuclear singlet–triplet mixing as a diagnostic tool to characterize intermediates. *J. Chem. Phys.* **1993**, *98*, 6150.

(38) Bargon, J. Kandels, J.; Woelk, H. Boosting the Sensitivity of NMR Spectroscopy using Parahydrogen. *Z. Phys. Chem.* **1993**, *180*, 65-93.

(39) Eisenschmid, T. C. Kirss, R. U. Deutsch, P. P. Hommeltoft, S. I. Eisenberg, R. Bargon, J. Lawler, R. G.; Balch, A. L. Para hydrogen induced polarization in hydrogenation reactions. *J. Am. Chem. Soc.* **1987**, *109*, 8089-8091.

(40) Turro, N. J.; Kraeutler, B. Magnetic field and magnetic isotope effects in organic photochemical reactions. A novel probe of reaction mechanisms and a method for enrichment of magnetic isotopes. *Acc. Chem. Res.* **1980**, *13*, 369-377.

(41) Saunders, M. Cross, R. J. Jimenez-Vazquez, H. A. Shimshi, R.; Khong, A. Noble Gas Atoms Inside Fullerenes Noble Gas Atoms Inside Fullerenes. *Science* **1996**, *271*, 1693-1697.

(42) Rubin, Y. *Fullerenes and Related Structures*; Hirsch, A., Ed. Springer Berlin Heidelberg: Berlin, Heidelberg, **1999**; Vol. 199, pp. 67-91.

(43) Iwamatsu, S.-ichi; Murata, S. Open-Cage Fullerenes: Synthesis, Structure, and Molecular Encapsulation. *Synlett* **2005**, 2117-2129.

(44) Komatsu, K. Murata, M.; Murata, Y. Encapsulation of molecular hydrogen in fullerene C_{60} by organic synthesis. *Science* **2005**, *307*, 238-40.

(45) Sessions Jr, H. T. *Analytical Method for Measuring Total Protium and Total Deuterium in a Gas Mixture Containing H2, D2, and HD via Gas Chromatography*; **2007**;WSRC-STI-2007-00416.

(46) Mamone, S. Chen, J. Y.-C. Bhattacharyya, R. Levitt, M. H. Lawler, R. G. Horsewill, A. J. Rõõm, T. Bačić, Z.; Turro, N. J. Theory and spectroscopy of an incarcerated quantum rotor: The infrared spectroscopy, inelastic neutron scattering and nuclear magnetic resonance of $H_2@C_{60}$ at cryogenic temperature. *Coord. Chem. Rev.* **2011**, *255*, 938-948.

(47) Turro, N. J. Chen, J. Y.-C. Sartori, E. Ruzzi, M. Martí, A. A. Lawler, R. Jockusch, S. López-Gejo, J. Komatsu, K.; Murata, Y. The spin chemistry and magnetic resonance of $H_2@C_{60}$. From the Pauli principle to trapping a long lived nuclear excited spin state inside a buckyball. *Acc. Chem. Res.* **2010**, *43*, 335-45.

(48) Ã, K. K.; Murata, Y. A New Route to an Endohedral Fullerene by Way of -Framework Transformations. *Chem. Lett.* **2005**, *34*, 886-891.

(49) Murata, M. Murata, Y.; Komatsu, K. Synthesis and properties of endohedral C_{60} encapsulating molecular hydrogen. *J. Am. Chem. Soc.* **2006**, *128*, 8024-33.

(50) Chai, Y. Guo, T. Jin, C. Haufler, R. E. Chibante, L. P. F. Fure, J. Wang, L. Alford, J. M.; Smalley, R. E. Fullerenes with metals inside. *J. Phys. Chem.* **1991**, *95*, 7564-7568.

2 Ortho/para Nuclear Spin Conversion

Before the story of *ortho*/*para* nuclear spin conversion begins, it is necessary to define some notations that will be referred to throughout the chapter. The two allotropes of hydrogen, *ortho*-H_2 and *para*-H_2 will be denoted *o*H_2 and *p*H_2, respectively. The equilibrium mixture at any given temperature is termed *e*H_2. At room temperature (RT), *e*H_2 = 75% *o*H_2/25% *p*H_2. At 77 K, *e*H_2 = 50% *o*H_2/50% *p*H_2 (Figure 1.6). Later in the chapter the H_2 sample will be enriched in *p*H_2 at RT, meaning at nonequilibrium % *p*H_2 rather than the equilibrium 25% *p*H_2, it will be denoted **p*H_2. This not to be confused with H_2* which represents a mixture of ^{1}H-NMR-active H_2 and HD isotopomers.

For Guest@Host notations, H_2 incarcerated inside the fullerenes C_{60} or C_{70} are denoted H_2@C_{60} or H_2@C_{70}, respectively. H_2 incarcerated inside open form fullerenes, these are the stable intermediates in the synthesis steps to making H_2@C_{60} (Scheme 1.2) will be denoted H_2@open-C_{60} in general unless a specific structure is being discussed and their corresponding notation is shown in **Chart 2.1**. Finally, H_2 incarcerated inside open, closed and any fullerene derivatives altogether, is termed H_2@fullerene.

2.1 Intermolecular spin conversion

Figure 2.1 is a generalized cartoon illustrating the overall picture of what we aim to accomplish. We termed the direction of nuclear spin conversion from *o*H_2 to *p*H_2 (*o*H_2 → *p*H_2) "forward conversion" and the nuclear spin conversion from *p*H_2 to *o*H_2 (*p*H_2 → *o*H_2) "back conversion" (Figure 2.1). The *o*H_2 triplet spin (red arrows, ↑↑) and *p*H_2 singlet spin (blue arrows, ↑↓) are shown in a simplified energy diagram (two rectangular boxes in Figure 2.1) as well as part of the H_2 molecule (inside the black circle in Figure 2.1). The black circle enclosing the *o*H_2 and *p*H_2

spins is a host molecule, e.g., C_{60}, C_{70} or any fullenerene derivatives. We took advantage of the NMR active, oH$_2$, to experimentally observe and monitor the progress of spin conversions.

Chart 2.1: Structures of endofullerenes pertaining to Chapter 2.

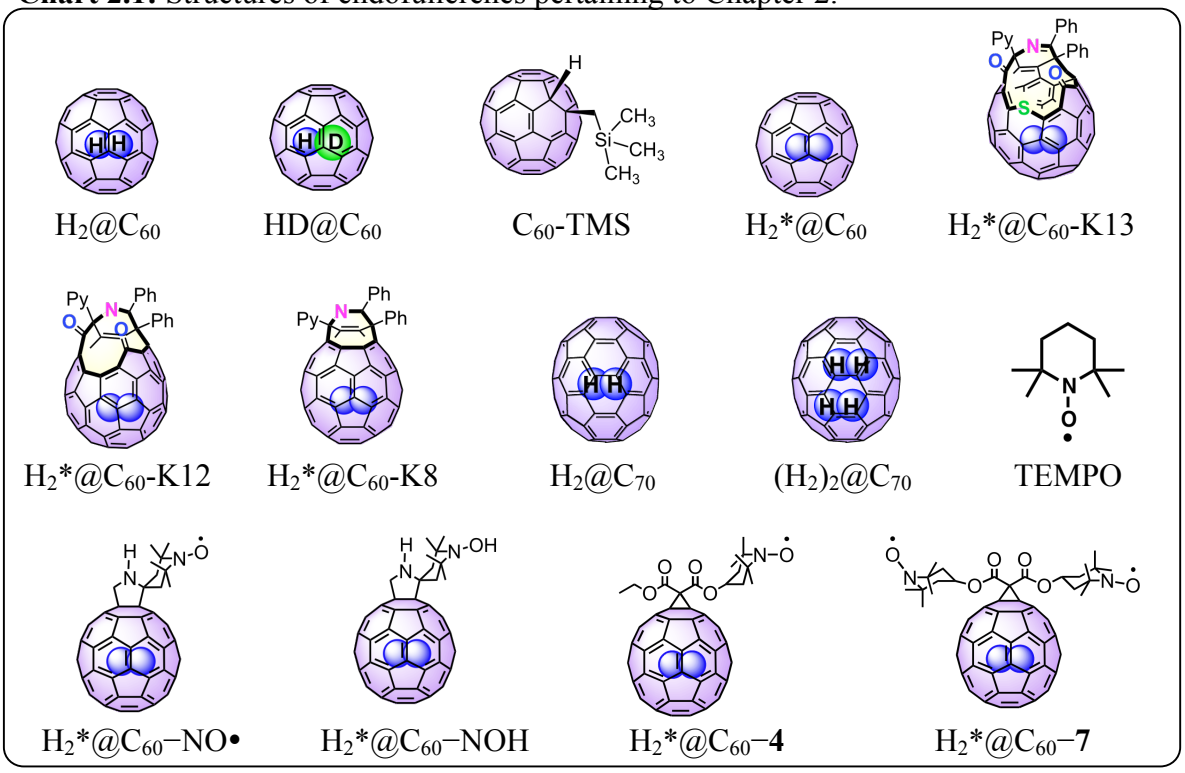

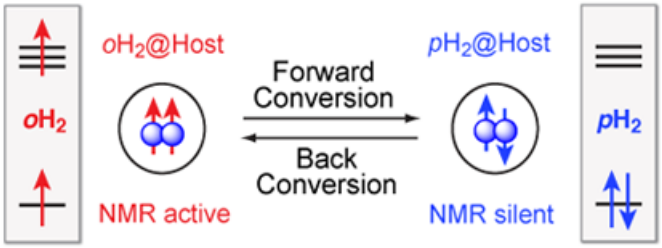

Figure 2.1: The nuclear spin conversion from oH$_2$ → pH$_2$ is termed "forward conversion" and the nuclear spin conversion from pH$_2$ → oH$_2$ is termed "back conversion". oH$_2$ is NMR active and pH$_2$ is NMR silent.

2.1.1 Results

2.1.1.1 Lifetimes of $H_2@C_{60}$ back conversion in vacuum, air, oxygen saturated solution and in the presence of nitroxides

We determined that the lifetime of back conversion in vacuum at room temperature is (8 ± 1) days. In comparison with the lifetimes for free H_2 in different solvents (Table 2.1), it is clear that pH$_2$ in the C_{60} cage is substantially more "magnetically isolated" than dissolved H_2 itself in the absence of paramagnetic catalysts.[1] In addition, the timescale of the back conversion of pH$_2$@C$_{60}$ to oH$_2$@C$_{60}$ is closer to that of the gas phase (days) than in liquid (several hours). This was further reinforced by comparing the bimolecular catalytic rate constant, k_{po}, determined by adding different spin catalysts to the *pH$_2$@C$_{60}$

Table 2.1: Time Constants for *para* to *ortho* back conversion of free H_2 as a function of solvent

Solvent	T_{po} (hr)[a]	T_{po} ($H_2@C_{60}$[b] /H_2)
Acetone-*d6*	11.1	15
Acetonitrile-*d3*	15.0	11
Methanol-*d4*	5.3	31
Ethanol-*d6*	6.0	27
Isopropanol-*d8*	15.4	11
Bromomethane-*d5*	12.9	13
Carbon disulfide	15	11

[a] Ref. [1]. at ambient temperature
[b] T_{po} for $H_2@C_{60}$ corresponds to conversion lifetime in air in ODCB, (6.8 ± 0.7) days.

with what is known for free H_2 in solution (Table 2.2). Specifically, in an oxygen saturated solution of *pH$_2$@C$_{60}$, the sample underwent back conversion with a lifetime of ca. 100 hr, corresponding to a value of the second-order rate constant for catalysis, $k_{po(O2)}$, of ca. 5 X 10^{-4} $M^{-1}s^{-1}$, based on an estimated solubility of oxygen in aromatic solvents. The rate constant for the nitroxide spin catalyzed back conversion was found to be 4 X 10^{-5} $M^{-1}s^{-1}$. These rates as compared with those for catalysis of the conversion for

Table 2.2: Bimolecular catalytic rate constant, k_{po} for $pH_2 \rightarrow oH_2$ back conversion

Catalyst	pH_2 k_{po} ($M^{-1}s^{-1}$)	$pH_2@C_{60}$ k_{po} ($M^{-1}s^{-1}$)	k_{po} ($H_2/H_2@C_{60}$)
O_2	2×10^{-1} in H_2O	5×10^{-4} in ODCB	400
Nitroxides	8×10^{-2} in $CDCl_3$	4×10^{-5} in ODCB (TEMPO)	2000

solutions of free pH_2: 2 X 10^{-1} $M^{-1}s^{-1}$ (O_2 in H_2O) and 8 X 10^{-2} $M^{-1}s^{-1}$ (nitroxide in $CDCl_3$) are orders of magnitude slower (Table 2.2).

The conventional mechanism for the $oH_2 \leftrightarrow pH_2$ conversion requires an induced inhomogeneous magnetic field that causes the two nuclear spins to become nonequivalent thus undergoing nuclear singlet-triplet transitions through dipole-dipole coupling. In the case of incarcerated H_2 inside C_{60} fullerene, the conversion between $oH_2@C_{60}$ and $pH_2@C_{60}$ in the presence of oxygen and nitroxides can also be explained in terms of this mechanism. However, an alternative mechanism in which a collision of oxygen or nitroxide with $oH_2@C_{60}$ or $pH_2@C_{60}$ forms a weak attractive complex, which is absent in the case of free H_2, and with a significant lifetime, enhancing the time scale of the inhomogeneous magnetic field, cannot be ruled out as a plausible mechanism for conversion.

2.1.1.2 $oH_2@C_{60} \leftrightarrow pH_2@C_{60}$ conversions with ^{129}Xe gas

Xenon + $H_2@C_{60}$ presents a new system for catalyzing the conversion between *ortho* and *para*hydrogen. ^{129}Xe is a spin-1/2 nucleus (25% abundance) that can potentially interact magnetically with another spin system which could catalyze spin conversion. In comparison with the conventional forward conversion at 77 K with oxygen, xenon is a solid at 77 K with negligible vapor pressure so it cannot be removed via vacuum like O_2. However, catalysis should be slower and removal at higher temperature may be permissible with minimal back conversion which is attractive for very low temperature conversion (below 77 K). Because xenon is

essentially either a gas or solid, we used a gas mixture with N_2 serving as the carrier gas in order to facilitate intimate contact between xenon and $H_2@C_{60}@NaY$ at 77 K.

Part I. Forward conversion.[2] A mixture of 90:10 N_2/Xe gas was condensed into a sample tube containing 2 g $H_2@C_{60}@NaY$. The same experiment was repeated with just N_2 gas, no xenon. The sample was held at 77 K via an external dewar and immersed in liquid N_2/Xe solution for ~ 7 days. Since the vapor pressure of N_2 is 1 atm at 77 K, the cryogen was removed without raising the temperature via vacuum. The removal of N_2 took 3 hours instead of 30-60 minutes (see Part II of section 2.5.7.1), presumably due to N_2 absorption inside the NaY zeolite supercages. The workup was normal (see Part III of section 2.5.7.1), the NMR tube was not degassed or flame sealed, no additional spin catalysts were added.

Figure 2.2 corresponds to the ^{1}H NMR spectrum of the time-dependence $*pH_2*@C_{60} \rightarrow oH_2*C_{60}$ back conversion after immersion in xenon solution described above. The forward conversion was observed in the Xe/N_2 + $H_2*@C_{60}$ spin system at 77 K and not in the N_2 only + $H_2*@C_{60}$ control. The pH_2 was enriched to 35-40% with xenon in 7 days instead of 50% in > 30 minutes by O_2 at 77 K corresponding to ~3000X slower kinetics. The lifetime for back-conversion in air at 300 K was ~4.8 days. However, we still need to rule out the possibility that the conversion in the xenon sample was not due to small amount of O_2 contaminant in the Xe.

Part II. Back conversion. The cartoon to the left of Figure 2.16 from section 2.5.2 shows how the sample was prepared for the back conversion experiment with xenon. An 800 μL CS_2 solution containing 6 mg of $H_2*@C_{60}$ was prepared. 100 μL aliquot was

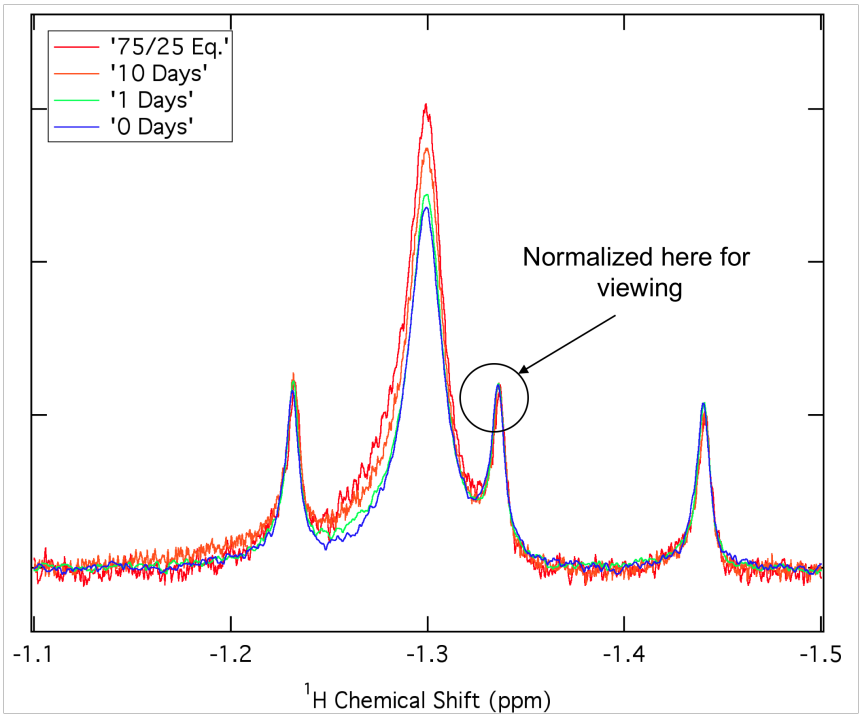

Figure 2.2: 500 MHz ^{1}H NMR spectrum of *pH$_2$*@C$_{60}$→oH$_2$*@C$_{60}$ back conversion after xenon solution in ODCB at 300 K.

saved for absorption spectroscopy. The remaining 700 μL was dissolved in ~30 mL hexane and stirred with NaY until the H$_2$*@C$_{60}$ was adsorbed on the surface. Forward conversion was carried out in the conventional way with O$_2$ at 77 K (See Part I and II of section 2.5.7.1) and after the workup (Part III of section 2.5.7.1), the *para*-enriched H$_2$*@C$_{60}$ solid was (1) dissolved in 800 μL CS$_2$, (2) the second 100 μL aliquot was removed for absorption spectroscopy, (3) the remaining 700 μL CS$_2$ solution was dried by blowing argon and (4) redissolved with 1.2 mL ODCB. This solution is divided into two 0.6 mL samples in a J. Young NMR tube, one saturated with argon (control) and the other xenon.

Figure 2.3 is the line width comparison for argon and xenon saturated (0.12 M) solutions of H$_2$*@C$_{60}$ with zero line broadening. **Figure 2.4** is the time dependence of back conversion in ODCB of xenon (red) and argon (blue) saturated solutions at 300 K. The xenon solubility was

calculated based on known values for cholorbenzene[3] and the data were plotted based on Method 2 of Figure 2.25. The lifetime in xenon saturated

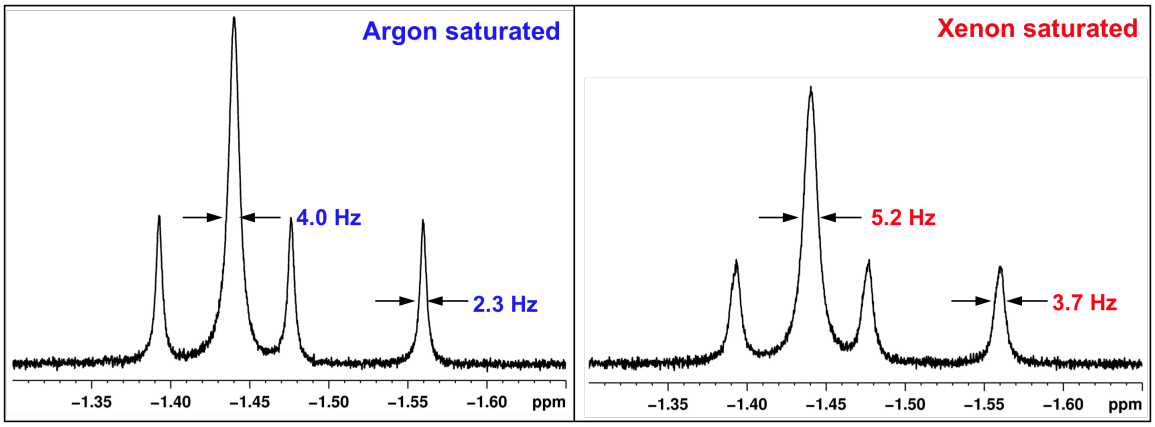

Figure 2.3: Line width comparison for argon and xenon saturated solutions of H_2*@C_{60}. 500 MHz ^{1}H NMR in ODCB at 300 K. LB = 0 Hz. TD = 40960. NS = 64. AQ = 5.11 sec. FIDRES = 0.0978 Hz. RG = 64. P1 = 7.6 μs. D1 = 0.

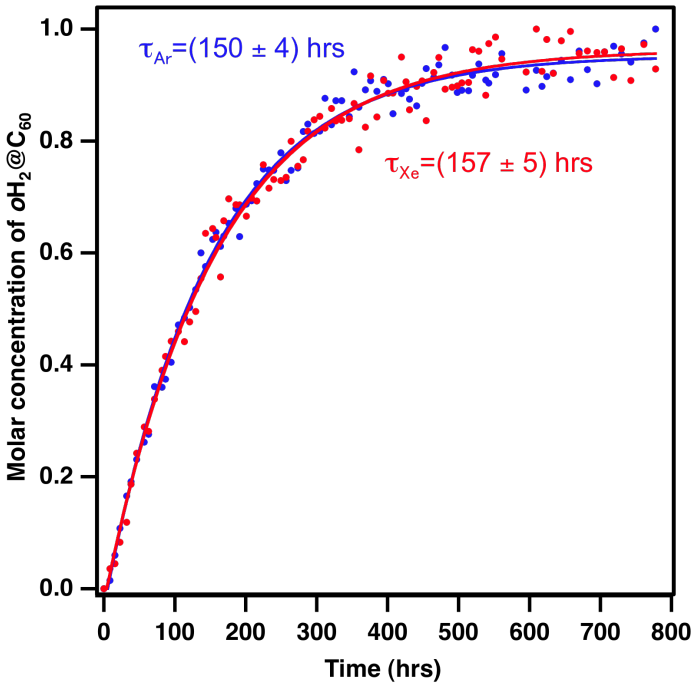

Figure 2.4: Time dependence of back conversion in ODCB of 0.12 M Xenon (red) and argon (blue) saturated solution at 300K. Xenon solubility was calculated based on known values for chlorobenzene. Data were plotted based on Method 2 of Figure 2.25.

solution, τ_{po}(Xe) was determined to be (157 ± 5) hrs / (6.5 ± 0.2) days and the lifetime in argon saturated solution, τ_{po}(Ar) was determined to be (150 ± 4) hrs / (6.3 ± 0.2) days. The τ_{po}(Xe) was determined on a different occasion to be (6.2 ± 0.6) days and for τ_{po}(Ar) = (148 ± 4) hrs / (6.2 ± 0.2) days. These results indicated that there was not a significant heavy atom effect from Xe.

Table 2.3 is a compilation of the average lifetimes, τ_{po} for $H_2@C_{60}$ in the presence of different catalysts.

Table 2.3: Lifetimes, τ_{po} for $pH_2@C_{60} \rightarrow oH_2@C_{60}$ back conversion

Catalyst	τ_{po} (days) [a]
48 mM TEMPO	0.6 ± 0.3
33 mM TEMPO	2 ± 1
5 mM TEMPO	4.6 ± 0.4
O_2 sat. (8.8 mM[b])	4.2
Ar sat.	6.3 ± 0.2
Xe sat. (0.12 M[3])	6.5 ± 0.2
Vacuum	7.5

[a] 1,2-dichlorobenze, 300 K
[b] based on solubility in cholorobenzene

2.1.1.3 H_2@open-C_{60} conversions

Samples of H_2@open-C_{60} stable intermediates from the synthetic precursors to $H_2@C_{60}$ can also be subjects for examination of *ortho*/*para* conversion. Komatsu and coworkers indexed a correlation between relative orifice sizes and calculated effective areas based on experimental hydrogen release rates.[4] We were interested in indexing the orifice sizes based on how the rate of back conversion at room temperature was affected when the H_2@open-C_{60} was partially exposed to the environment and how this lifetime was also affected by the magnitude of exposure, namely the size of the orifice (Figure 1.11, Section 1.2.9 of Chapter 1). **Figure 2.5** shows the ^{1}H NMR of each of these species in one single mixture. Each of the species was well separated from each other and the chemical shift moved downfield from -7.25 ppm ($H_2@C_{60}$-K13), -5.8 ppm

(H_2@C_{60}-K12), -2.95 ppm (H_2@C_{60}-K8) to -1.44 ppm (H_2@C_{60}) as the size of the orifice decreased. In addition, the HD triplet that accompanied each of the H_2 signals was also well resolved. Since the chemical shift of

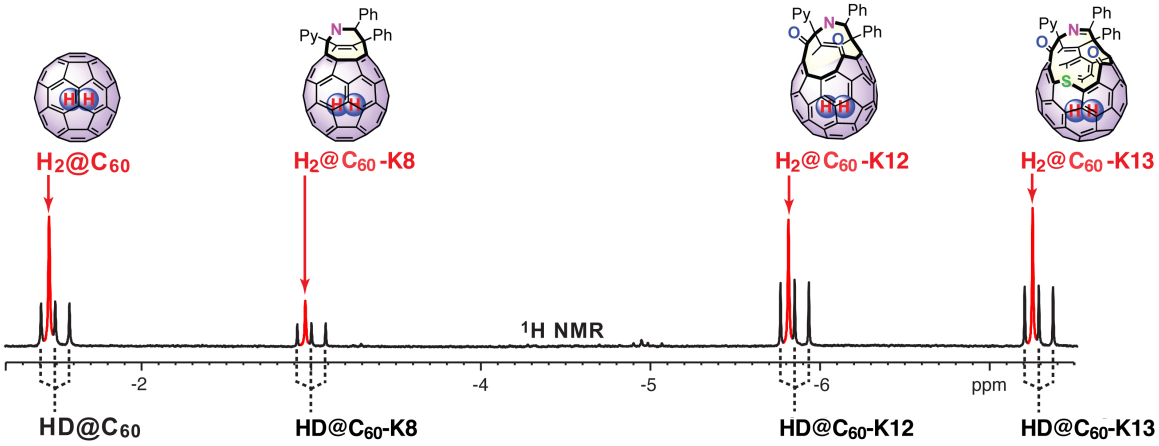

Figure 2.5: 500 MHz ^{1}H NMR spectrum of isotopomeric mixture of $^{1,2}H_2$ inside C_{60}, C_{60}-K8, C_{60}-K12 and C_{60}-K13 in 1,2-dicholorbenzene-d_4 at 300K. The singlet in red corresponds to H_2 and the triplet in black corresponds to HD.

each of the open forms were distinctive, it would be ideal to run the experiments with all the fullerenes in one sample mixture with all else being equal. We mixed the samples of H_2@open-C_{60} with 8, 12 and 13 member rings together with H_2@C_{60} as control, and conversion was carried out at 77 K in the conventional way (section 2.5.7.1). Our experimental criteria were limited by the solubility of C_{60} and open C_{60} fullerene in CS_2, specifically 7.7 mg/mL C_{60} and less so with open C_{60}. For this reason, the initial mixture contained only 1 mg each of the fullerenes. Also because of the danger of handling liquid O_2, our reaction vessel was kept small and limited to 2 g NaY Zeolite for each conversion experiment. In addition, the open fullerenes have a much higher affinity for the NaY zeolite than C_{60}; it was necessary to add small amounts of methanol during extraction with CS_2 after conversion. However, adding too much methanol

would destroy the zeolite and transform it into an opaque gel in which centrifugation would not result in a distinct solid liquid phase and one could no longer extract the fullerenes.

Once the converted sample was successfully extracted and redissolved in ODCB for NMR measurements, the sample was split into three equal parts to obtain lifetimes in air, O_2 saturated solution and with light. However, the results were less than ideal because the signal to noise suffered from sample loss during transfer, extraction and dilution. Another consequence of the experimental procedure, in general, was that the actual concentrations could not be determined.

With this failure, we designed another experiment in which we mixed $H_2@C_{60}$ and $H_2@open\text{-}C_{60}$ with $H_2*@C_{60}$ to obtain a much higher S/N ratio for the H_2 of interest. We prepared two samples in which one contained a mixture of ~1.5 mg of each H_2 only containing C_{60} and open-C_{60} and the other ~1 mg of $H_2*@C_{60}$; then we dissolved them in ~1 mL CS_2, mixed with 35 mL hexane. Forward conversion at 77 K with O_2 was carried out in the conventional way (section 2.5.7.1) and the extraction in Part III of 2.5.7.1 from zeolite also involved addition of methanol to displace the open-C_{60}'s from the surface of the zeolite. The sample was dried, redissolved in ODCB and divided into four 600 μL solutions and to each was added 5 mM, 10 mM, 15 mM or 20 mM TEMPO. ^{1}H NMR sample spectra of $H_2*@C_{60}$ and $H_2@open\text{-}C_{60}$ at each concentration of TEMPO (**Chart 2.1**) at time = 0 and time= 13 days are shown in Figure 2.30-Figure 2.37.

Figure 2.6 shows the time dependence of the back conversion of (a) $H_2*@C_{60}$, (b) $H_2@C_{60}$-K8, (c) $H_2@C_{60}$-K12 and (d) $H_2@C_{60}$-K13 in 5mM TEMPO ODCB solution at 300 K. The x-axes are times in minutes and the y-axes are normalized oH_2 intensities based on HD. The lifetimes, τ_{po} (days) were determined by analyzing NMR data with both Method 2 (black) and

Method 3 (red) for comparison. Table 2.4 is a compilation of the lifetimes for each H_2*@C_{60} and H_2@open-C_{60} at each nitroxide concentration using

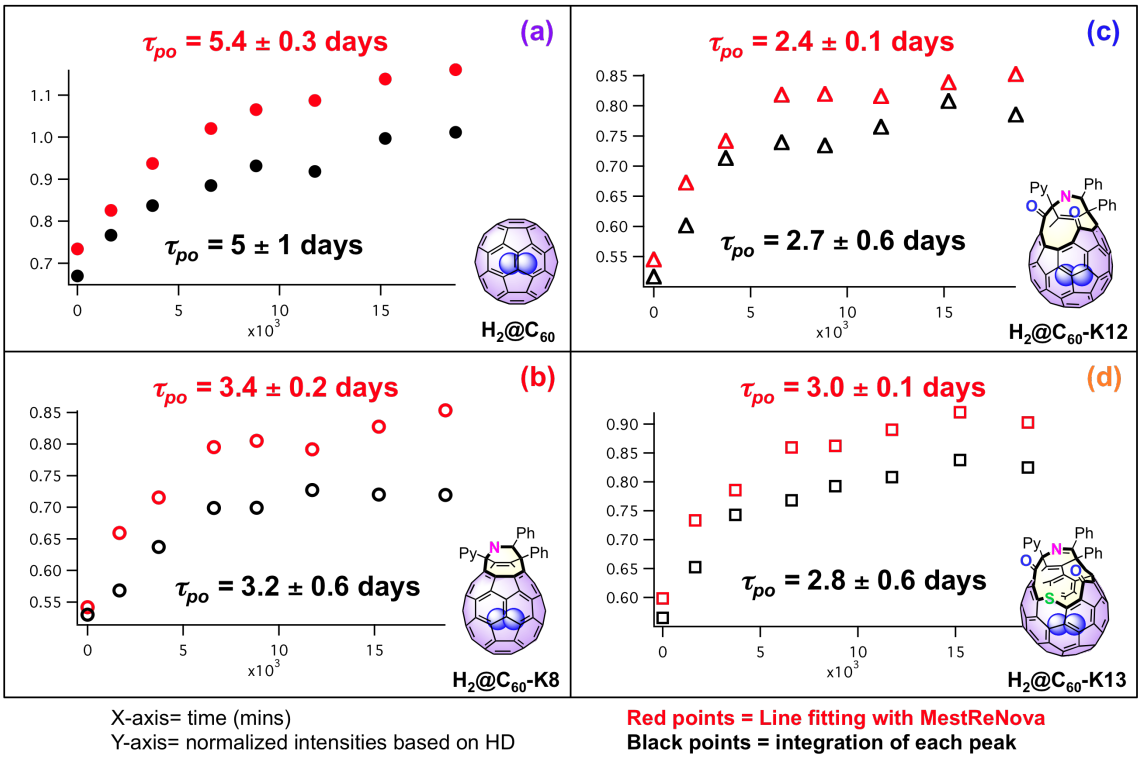

Figure 2.6: Time dependence of the *p*H_2 → *o*H_2 conversion of (a) H_2@C_{60}, (b) H_2@C_{60}-K8, (c) H_2@C_{60}-K12 and (d) H_2@C_{60}-K13 in ODCB 5mM TEMPO solution at 300 K.

Method 3. The final second-order rate constant for catalysis, k_{po} for conversion calculated based on the data in Table 2.4 with different concentrations of TEMPO is shown in Figure 2.7. Based on results in Figure 2.7 the k_{po} for H_2*@C_{60} (a) is indistinguishable from previous published results[5] and in the case of H_2@open-C_{60}, results from Figure 2.7 suggest that while the lifetimes at different concentrations of TEMPO are shorter than H_2*@C_{60}, the ratio of lifetimes is about the same as for all the open forms, at all four of the TEMPO concentrations in Table 2.4.

Table 2.4: Lifetimes, τ_{po} of $H_2@C_{60}$ and $H_2@open\text{-}C_{60}$ as a function of concentration of nitroxide, TEMPO

[TEMPO]	5 mM	10 mM	15 mM	20 mM
	Lifetimes, τ_{po} (days)			
H_2*@C_{60}	5.4 ± 0.3	5.8 ± 0.5	4.9 ± 0.3	3.6 ± 0.4
$H_2@C_{60}$-K8	3.4 ± 0.2	3.9 ± 0.4	3.8 ± 0.3	3.8 ± 0.3
$H_2@C_{60}$-K12	2.4 ± 0.1	2.9 ± 0.2	2.3 ± 0.1	2.8 ± 0.2
$H_2@C_{60}$-K13	3.0 ± 0.1	3.7 ± 0.3	2.9 ± 0.2	3.3 ± 0.2

Given that information, we know for the future, we can use a representative open form, e.g., H_2*@C_{60}-K13 (**Chart 2.1**) and mix it with H_2*@C_{60} to obtain a good S/N ratio. Table 2.5 shows the *para* to *ortho* lifetimes of the H_2*@C_{60}-K13 as compared with $H_2@C_{60}$ in air.

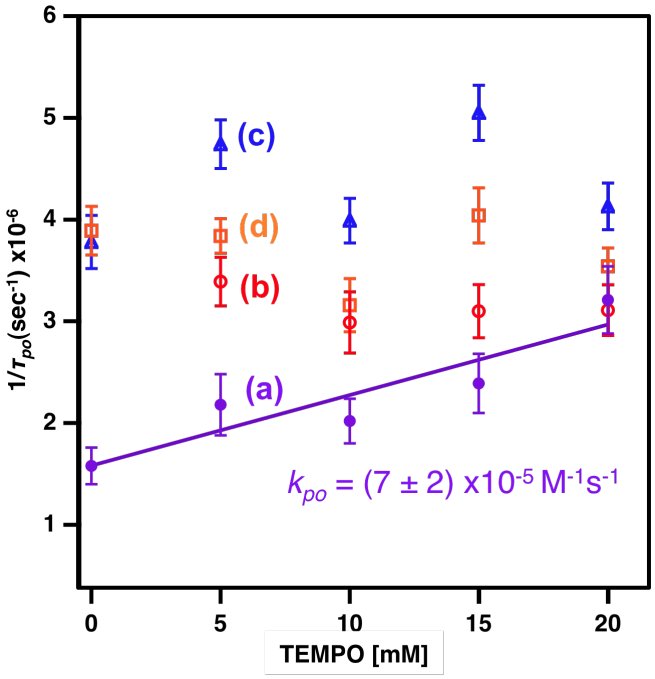

Figure 2.7: Rate for the back conversion ($1/\tau_{po}$) in presence of various concentrations of the nitroxide TEMPO at 300 K. Points labeled (a)-(d) corresponds to results shown in **Figure 2.6**.

Table 2.5: Lifetime, τ_{po} (hr) of *para* to *ortho* Conversion H_2*@C_{60} and H_2*@C_{60}-K13 in air at 300 K

Condition	H_2*@C_{60} τ_{po} (hr)	H_2*@C_{60}-K13 τ_{po} (hr)	τ_{po} (H_2@C_{60}/H_2@C_{60}-K13)
1.8 mM O_2	164 ± 21	103 ± 13	1.6

2.1.1.4 H_2@C_{70} and $(H_2)_2$@C_{70} conversion

Representative ^{1}H NMR spectra of *ortho*/*para* conversion of H_2@C_{70} and $(H_2)_2$@C_{70} (**Chart 2.1**) are shown in Figure 2.8. H_2*@C_{60} was added to the mixtures to

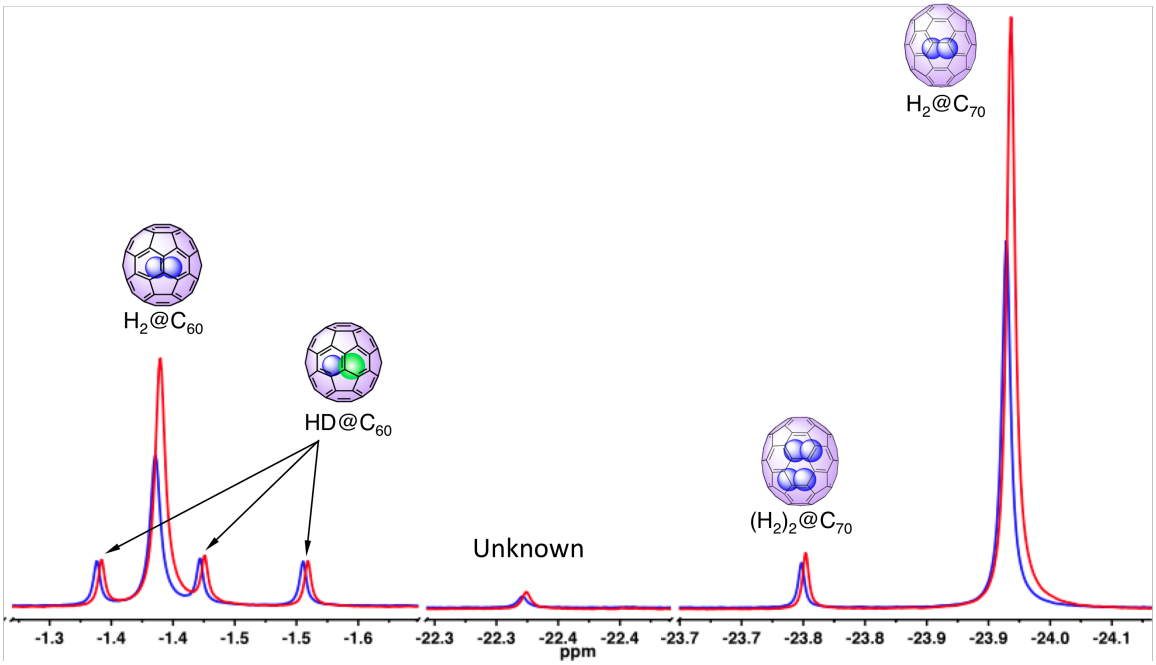

Figure 2.8: Superposition of ^{1}H NMR spectra at time = 0 (blue spectrum, t=0 indicates first spectrum taken after *para*-enrichment at 77K with O_2 catalyst) and time =11 days (red offset spectrum) of a mixture of H_2*@C_{60}, H_2@C_{70} and $(H_2)_2$@C_{70} in ODCB at 300 K.

serve as the control and HD@C_{60} was used as the internal standard. The forward conversion was carried out via standard procedure (see section 2.5.7.1). The blue spectrum in Figure 2.8 was taken after workup from *para*-enrichment at 77 K in liquid O_2 and represents time = 0 (t=0). The offset red spectrum that is superimposed on the blue was acquired after 11 days (t=11 days). An

unknown H_2 species was present at -22.35 ppm. Figure 2.9 shows the time dependence $pH_2 \rightarrow oH_2$ back conversion for $H_2@C_{60}$ (purple), $H_2@C_{70}$ (red) and $(H_2)_2@C_{70}$ (dark red) and its corresponding lifetimes, τ_{po} in

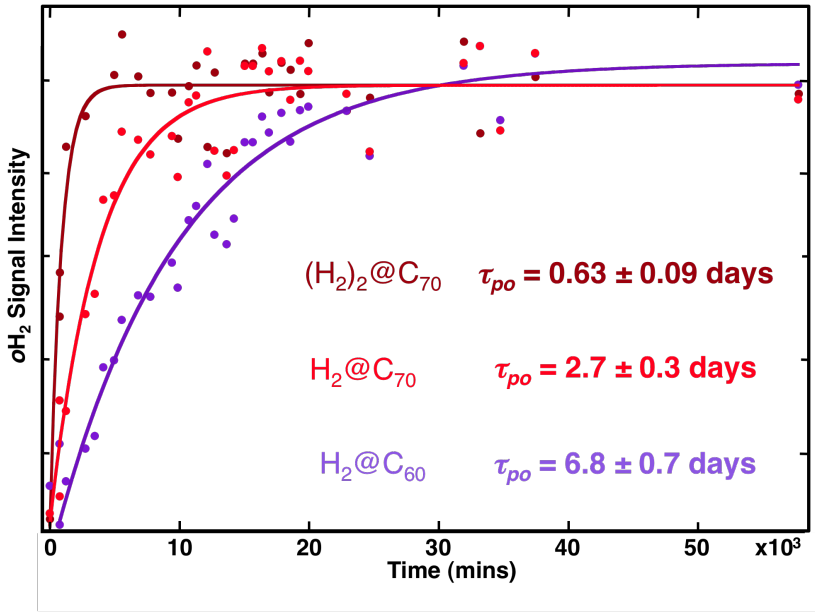

Figure 2.9: Time dependence of the pH_2 to oH_2 back conversion lifetimes for $H_2@C_{70}$, $(H_2)_2@C_{70}$ and $H_2@C_{60}$ in ODCB at 300 K in air.

ODCB at 300 K in air. The back conversion lifetime of $H_2@C_{70}$ is 3X faster than $H_2@C_{60}$. In addition, the doubly encapsulated H_2 is an order of magnitude faster than $H_2@C_{60}$ and 4X faster than the single $H_2@C_{70}$. Mechanism for the rapid back conversion is unknown but it is possible that if one of the H_2 of the $(H_2)_2$ is oH_2 then it might catalyze the spin-flip of the other pH_2 thus speeding up the back conversion.

Table 2.6 is a compilation and comparison of lifetimes, τ_{po} (days) of *para* to *ortho* conversions of H_2*@C_{60}, $H_2@C_{70}$, $(H_2)_2@C_{70}$ and H_2*@C_{60}-K13 in air and for H_2*@C_{60} in the following additional conditions: vacuum, oxygen saturated solution, argon and xenon saturated solutions as well as 22.4 mM TEMPO in ODCB solvent.

Table 2.6: Compiled lifetimes, τ_{po} (days) of *para* to *ortho* conversions of H_2*@C_{60}, H_2@C_{70}, $(H_2)_2$@C_{70} and H_2*@C_{60}-K13 in different conditions at 300 K

	Air	Vacuum	O_2 Sat.	Ar Sat.	Xe Sat.	22.4 mM TEMPO
	τ_{po} (days)					
H_2*@C_{60}	6.8 ± 0.7	8 ± 1	4.2	6.2 ± 0.2	6.2 ± 0.6	5 ± 2
H_2@C_{70}	2.7 ± 0.3					
$(H_2)_2$@C_{70}	0.63 ± 0.09					
H_2*@C_{60}-K13	4.3 ± 0.5					
Unknown solvent: ODCB	1.8 ± 0.3					

2.2 Intramolecular spin conversion

Thus far, the forward conversion with liquid O_2 at 77 K has been reliable; however, it takes extra precaution and also the entire process takes eight working hours. Further, the back conversion at RT takes days using all the aforementioned intermolecular spin catalysts. We reasoned that if we can covalently link a nitroxide to the skin of the C_{60}, then we could optimize the system by using the nitroxide as the catalyst for forward and back conversion. No liquid O_2, no extraction, no sample loss! Our synthetic expert Xuegong Lei synthesized a nitroxide covalently linked to H_2@C_{60} (H_2*@C_{60}–NO•) to do just that. Initial EPR and NMR measurements are consistent with those expected for paramagnetic H_2@C_{60}- NO•. ^{1}H NMR spectrum showed that the line shape was broad

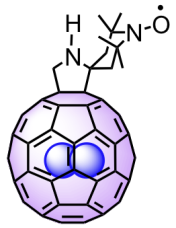

H_2*@C_{60}–NO•

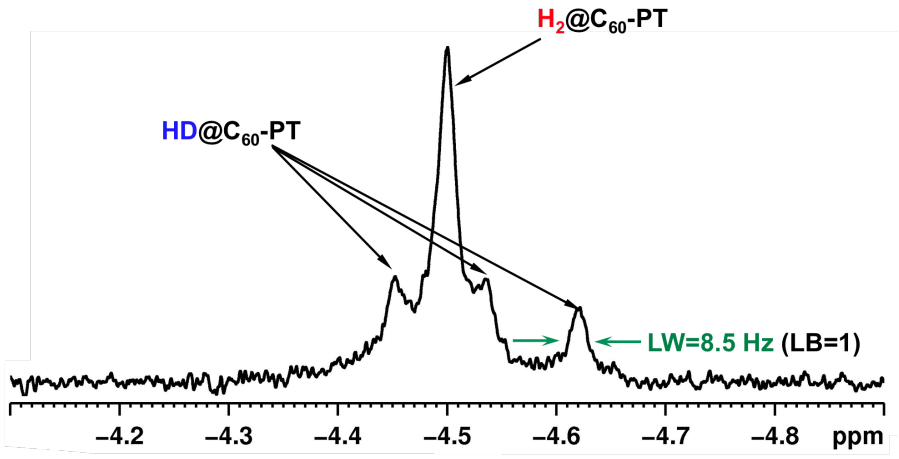

Figure 2.10: ^{1}H NMR spectrum of H_2*@C_{60}-NO• in toluene-d_8 at 300 K. The notation, PT = NO•

and the two downfield HD peaks were buried underneath the H_2 peak; however, the most upfield HD peak was broad (8-9Hz) but well resolved for use as the standard (Figure 2.10). We dissolved ~1mg H_2*@C_{60}−NO• in 600 mL ODCB and submerged it in liquid N_2 for 4 days, the line shape changed but there was no apparent conversion. We suspect that the timescale of the back conversion occurred much faster than the time required for removing the sample from liquid N_2 to taking the NMR measurement. We practiced and took NMR as quickly as possible after the sample was warmed to RT. Still, within the fastest workup possible (90 sec), no *para*-enrichment was observed, the ^{1}H signals of the before and after are indistinguishable. To test our hypothesis that the *para*-enrichment does occur but is rapidly reversed to equilibrium distribution at RT during work up, we modified the H_2*@C_{60}−NO• system by synthesizing a diamagnetic version (H_2*@C_{60}−NOH) by reduction with phenylhydrazine which we can rapidly switch back to and regenerate the paramagnetic analog by oxidation with $Cu(OAc)_2$ creating a reversible magnetic switch for interconverting incarcerated nuclear spin isomers. The actual synthesis of the switch compound and conversion was carried out by one of our postdocs, Dr. Yongjun Li.

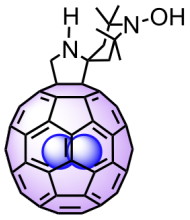

H_2*@C_{60}–NOH

Prior to executing the magnetic switch conversion we determined the effect of substitution on the forward and back conversion of the incarcerated spin isomers of H_2. A diamagnetic derivative that is very similar in structure to H_2*@C_{60}–NO• was put through the conventional enrichment procedure and the results showed that the substitution by itself does not significantly modify the rate of the back conversion.[6]

Then we tested our hypothesis concerning the lack of *para*-enrichment when H_2*@C_{60}–NO• was cycled to 77 K and back to RT. First we treated the hydroxylamine diamagnetic derivative under the conventional forward conversion conditions (NaY/77 K/Liquid O_2). Then we treated the *para*-enriched H_2*@C_{60}–NOH with $Cu(OAc)_2$ at RT. The ^{1}H NMR showed an overlap of H_2*@C_{60}–NOH with the portion of the sample that was oxidized to H_2*@C_{60}–NO•. In addition, the ^{1}H NMR signal showed that the H_2*@C_{60}–NOH was enriched in *para*-H_2 while H_2*@C_{60}–NO• was not. The results demonstrated that the system can act as a switch interconverting the incarcerated *ortho*-H_2 / *para*-H_2 nuclear spin isomers.[6]

We also executed and published further studies on the distance dependent pH_2/oH_2 conversion in H_2@C_{60} derivatives convalently link to nitroxide radical(s).[7]

2.3 Photochemical spin conversion

2.3.1 Attempts in photo-induced back conversion of $H_2@C_{60}$

In all the conversion experiments discussed above, the catalysts used for the back conversion at room temperature were either in the form of an electronic or nuclear spin, e.g., O_2, Xe and nitroxides, that could interact with one of the nuclear spins of H_2 and induce a selective flip of one spin, and the timescales for re-establishing equilibrium at RT were on the order of days in solution and hours or minutes when the nitroxide radicals were covalently linked to C_{60}.[6,7] However, these catalysts are weak and very difficult to remove following the reaction. An ideal method would be a process that rapidly establishes spin equilibrium at any temperature without a cumbersome or convalently-linked spin catalyst.

There have been extensive magnetic resonance studies of the triplet ^{1}H nuclear spin states of *o*H_2 and of the triplet electronic state spin state of C_{60}. For example, the electronic triplet state of C_{60} ($^3C_{60}$) has been investigated by both time-resolved ESR (TR ESR) spectroscopy[8] and by triplet-triplet absorption (TTA) spectroscopy[9]. It has been reported[10] that the steady state and TR ESR and TTA spectra of $H_2@^3C_{60}$ and $^3C_{60}$ are experimentally indistinguishable and therefore provide no evidence for spin-spin interactions of the unpaired electron spins and $^3C_{60}$ and the unpaired nuclear spins of *o*H_2. Although conventional spectroscopy does not reveal any evidence for the aforementioned interactions, we want to investigate this weak spin-spin interaction ^{1}H-$^3C_{60}$ hyperfine coupling by using *p*$H_2@C_{60} \rightarrow$ *o*$H_2@C_{60}$ conversion as a spin probe for spin-spin interactions on the nuclear spins of *o*H_2 with the electron spins of $^3C_{60}$. The idea is to use this photoactive paramagnetic "cage" triplet state to catalyze a spin transformation of the "guest" inside, generating *o*H_2 or *p*H_2.

Absorption spectra were taken first of our samples of C_{60}, $H_2^*@C_{60}$ and $H_2^*@C_{60}$-K13 (**Chart 2.1**) in benzene (Figure 2.11). There was no difference between C_{60} and $H_2^*@C_{60}$ absorption bands (sharp absorption at 335 nm and broad absorption at 544, 600 and 625 nm). In the case of $H_2^*@C_{60}$-K13S, the absorptions are blue-shifted to 320 and 450 nm and only one signal was present for the broad absorption at 450 nm.

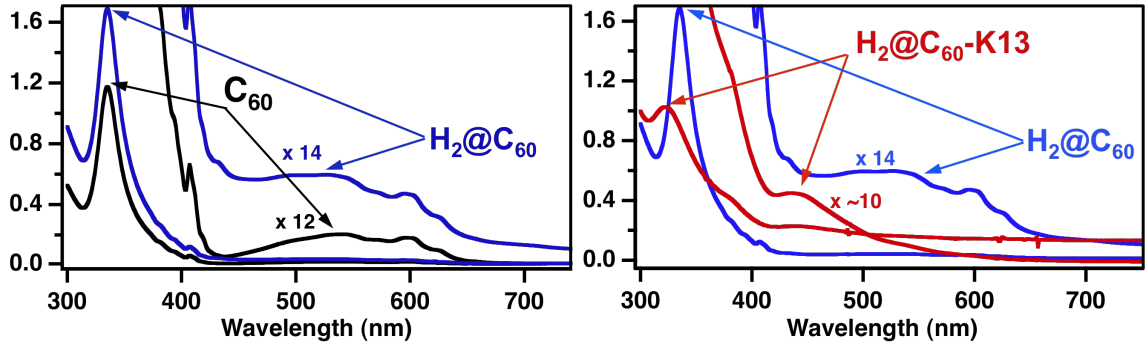

Figure 2.11: Absorption spectrum of C_{60} (0.34 mM and 0.028 mM C_{60} (x12)), $H_2@C_{60}$ (0.37 mM and 0.026 mM (x14)), $H_2@C_{60}$-K13 (0.3 mM and 0.03 mM (x~10)).

In our photochemical back conversion at room temperature experiment, we first enriched the $H_2@C_{60}$ via the conventional method, conversion performed on NaY zeolite surface, in liquid O_2 at 77 K (see section 2.5.7.1). After the workup, the solid was redissolved in ODCB, split into three samples and each sample was subjected to twelve cycles of freeze-pump-thaw followed by flame seal. Accurate concentration of the endofullerenes was unable to be determined due to the incomplete recovery during extraction of the converted sample from the zeolite surface. However, independent experiments show that $H_2@C_{60}$ and $HD@C_{60}$ sticks to the NaY Zeolite surface with the same affinity; therefore, incomplete extraction with CS_2 still preserved the initial H_2:HD ratio. Sample one was kept in the dark and served as our control. It should have a significantly longer lifetime then the photo-irradiated samples. Sample two was kept in the dark after 50 hours of irradiation and sample 3 received continuous irradiation. We used a Xe lamp

(380-700nm). The result was disappointing to say the least. All three samples had the same lifetime for back conversion.

In another photochemical back conversion experiment, we used a mixture of ~1 mg $H_2@C_{60}$ and ~1 mg $H_2^*@C_{60}$-K13. After *para*-enrichment via the conventional method at 77 K with O_2, the sample was split into two, one received continuous irradiation and the other was kept in the dark.

^{1}H NMR signals of oH_2, inside both open and closed C_{60} were simultaneously observed at δ= -7.2 and -1.4 ppm, respectively (Figure 2.12). The pre-converted oH_2 spectrum is shown on the top and its corresponding post-converted NMR spectrum is shown on the bottom. As previously mentioned, the integrated HD signal does not vary in intensity under these conditions; therefore, it functioned as the ideal internal standard.

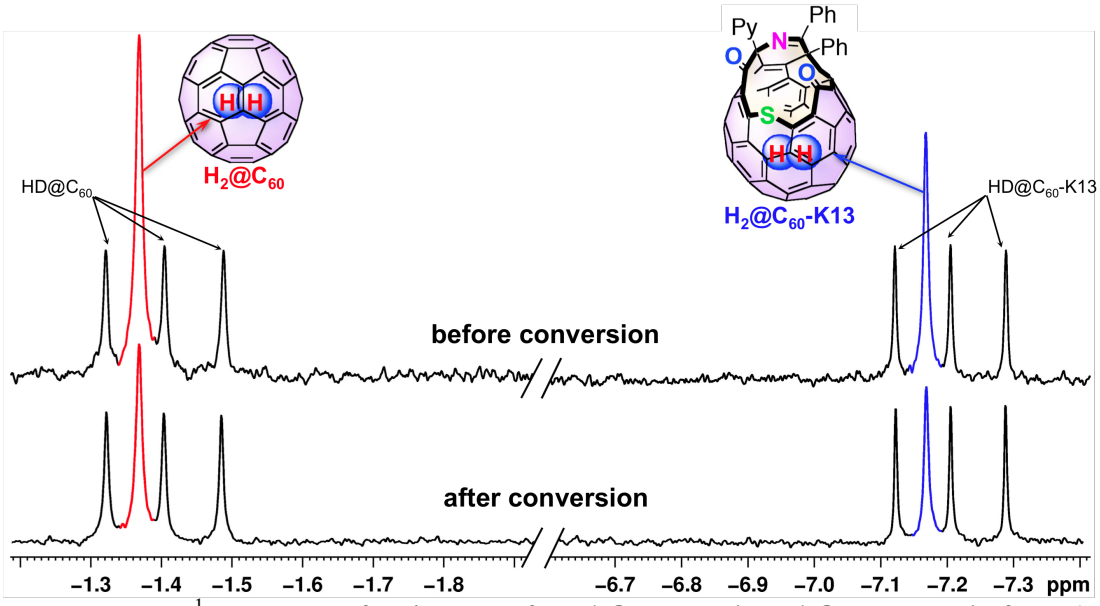

Figure 2.12: ^{1}H NMR of mixture of H_2*@C_{60} and H_2*@C_{60}-K13 before (top spectrum) and after (bottom spectrum) conversion at 77 K with O_2.

The apparent reduction of oH$_2$ intensity relative to its corresponding HD internal standard for both the closed and open C$_{60}$ system demonstrated successful forward conversion with O$_2$ at 77 K.

The time course in reestablishing equilibrium population at room temperature in air, or the back-conversion from pH$_2$ → oH$_2$ inside both closed and open C$_{60}$ upon irradiation at 380-700nm demonstrated that pH$_2$ in the closed and open C$_{60}$ cage back-converts independently of the ^{3}C$_{60}$. The pH$_2$ → oH$_2$ lifetimes, τ_{po} between the open and closed C$_{60}$ was different, as was discussed before; however, the lifetime was the same for both the samples in the dark and with application of hv for both open and closed C$_{60}$. The ratio of the integrated HD signals between closed and open C$_{60}$ throughout the back conversion were practically constant which indicated that H$_2$ and HD did not escape from the open C$_{60}$. This further pointed out that photo-induced conversion via ^{3}C$_{60}$ did not work and we suspected that the triplet lifetime for C$_{60}$ may be too short or quenched via TT annilation in solution to allow its paramagnetism to induce measurable conversion.

2.3.2 Photo-induced forward conversion of H$_2$@C$_{70}$ and why H$_2$@C$_{60}$ failed

In experiments with H$_2$@C$_{70}$ run by Mike Frunzi, ^{3}C$_{70}$ was generated from H$_2$@C$_{70}$ for photochemical conversion. A mixture of ~ 0.2 mg H$_2$*@C$_{60}$ and H$_2$*@C$_{70}$ were dissolved in 300uL of toluene-d_8 and added to quartz ampoules. Toluene was the solvent of choice because (1) it is a convenient NMR solvent, and (2) it is known to form transparent glasses at low temperature which later we found to be crucial for the photochemical experiment to work since light needs to be able to penetrate the sample. Then O$_2$ was removed by free-pump-thaw technique to prevent quenching of the triplet state of the fullerenes and the ampoule was flame-sealed. Next the ampoule was placed in a quartz optical dewar filled with liquid N$_2$ and irradiated

via a 300 W xenon lamp fitted with a water filter which filtered out IR to prevent formation of organic radicals which

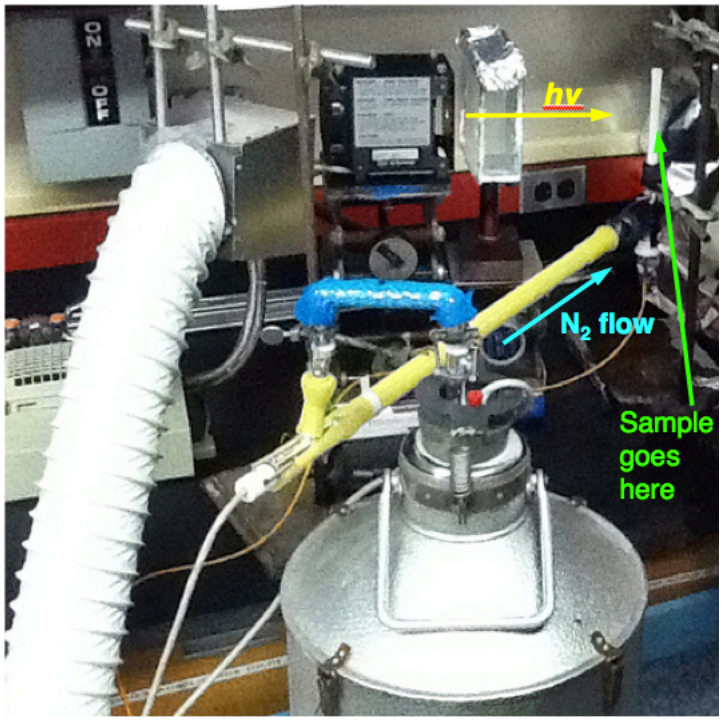

Figure 2.13: Experimental setup for photoinduced *ortho*/*para* $H_2@C_{70}$ conversion.

may participate in the reaction (Figure 2.13). The ^1H NMR spectra of the $H_2*@C_{60}$ and $H_2*@C_{70}$ mixture normalized to the $HD@C_{70}$ NMR lines taken before and after four hours of irradiation at 77 K showed that while the resonances for $oH_2@C_{60}$, $HD@C_{60}$ and $HD@C_{70}$ were essentially unchanged after irradiation, the resonance for oH_2 inside C_{70} was significantly reduced! Additional irradiation at 77 K of $H_2*@C_{60}$ showed no change while further irradiation of $H_2*@C_{70}$ showed a 33% oH_2 signal reduction denoting the full conversion (50:50 ratio of the equilibrium mixture of oH_2:pH_2 nuclear spin isomers at 77 K) at this temperature.

To ensure that the signal depletion of $oH_2@C_{70}$ was indeed the result of pH_2 enrichment inside C_{70}, the thermal-induced spin conversion method with NaY/77 K/Liquid O_2 was carried out in the conventional way (see section 2.5.7.1) with approximately 3 mg each of $H_2@C_{70}$ and

H_2*@C_{60}. The *o*H_2 signal inside both C_{60} and C_{70} reduced in intensity relative to the HD triplet of HD@C_{60}, which indicated that, the thermal-induced spin conversion method was effective for both H_2@C_{60} and H_2@C_{70} whereas the photo-induced spin conversion was not. The sample was monitored regularly via ^{1}H NMR as the *o*H_2 / *p*H_2 ratio slowly increased and returned to 3:1 over the course of a month with lifetimes of 6.8±0.7 and 2.7±0.3 days for H_2@C_{60} and H_2@C_{70}, respectively. The irradiated sample of H_2*@C_{70} was also monitored in the same way and with the *o*H_2 returning to equilibrium at RT with a lifetime of 2.6±0.5 days indicating that in both the thermal- and photo-induced case, there was *para* enrichment of H_2 inside C_{70} fullerene and both returned to equilibrium at RT at the same rate.

The difference between the H_2*@C_{60} and H_2*@C_{70} systems under photoinduced conversion, specifically, why the H_2@C_{60} sample did not undergo conversion upon photolysis whereas the H_2*@C_{70} sample did, although both samples do undergo thermally induced conversion to the expected 50:50 equilibrium mixtures of spin isomers using the previously established method was to others intriguing and to me comforting. Comforting to me because I spent months trying photoconversion with H_2@C_{60} and for the longest time I thought it was my lack of skills and experimental design as a scientist that the photoconversion with H_2*@C_{60} and H_2*@open-C_{60} failed. The fact that with similar implementation of experimental design for photo-induced conversion with H_2*@C_{70} yielded positive results showed that there was a different reason that it did not work with C_{60} and those reasons have to do with the difference between the C_{60} and C_{70} fullerene and not me. So the question was what is the difference between the two systems under photoinduced conversion?

The selection rule for the *ortho*/*para* catalysis requires a magnetic field gradient from the spin-catalyst to induce the nuclear spin flip. However, the spin-density, or spin distribution of the

triplet states for both C_{60} and C_{70} do not clearly suggest that one fullerene has a more asymmetric excited state electron density distribution that could be responsible for the magnetic field gradient necessary to induce conversion.[11] In addition, H_2*@C_{60}-K13 yielded a negative result for conversion which further indicated that the asymmetric electron density distribution is ruled out as the mechanism for spin conversion.

The triplet lifetime reported in the literature for C_{70} is two orders of magnitude longer than C_{60} at RT in toluene[12]. We speculated that the ~100-fold longer lifetime for triplet C_{70} relative to triplet C_{60} allowed the paramagnetism of the former to operate as a spin catalyst more effectively with respect to the conversion of the nuclear spin isomers. We therefore measured the triplet lifetimes of H_2*@C_{60} and H_2*@C_{70} at 77 K to confirm the triplet lifetimes of our systems under our photoinduced conversion conditions (Table 2.7). Dr. Steffen Jockusch prepared the samples in decalin/cyclohexane (3:1; v/v) glass at concentration of 100 μM and the triplet absorption decay was measured, probing at 785 nm. Indeed, results in Table 2.7 agree favorably with the values for C_{60} and C_{70} at RT and we concluded that the 219X longer triplet lifetime of triplet C_{70} of H_2*@C_{70} allowed the paramagnetism to act as spin catalyst for the nuclear spin conversion. Triplet C_{70} also exhibited effective triplet self-quenching in toluene ($k= 1.2 \times 10^8$ $M^{-1}s^{-1}$) via short-lived triplet excimers[12]; therefore, we speculated that as long as C_{70} is in a glassy state this

Table 2.7: H_2@C_{60}, H_2@C_{60}-K13 and H_2@C_{70} Intrinsic Triplet Lifetimes[a] at 77 K

	T_1 lifetime (ms)[b]	Relative lifetime
H_2@C_{60}	0.21 ± 0.01	1
H_2@C_{60}-K13	3.2 ± 0.2	15
H_2@C_{70}	46 ± 2	219

[a] Measurements by Steffen Jockusch
[b] In decalin/cyclohexane (3:1; v/v) glass at 100 μM and 785 nm.

self-quenching mechanism is not active and does not cause measurable spin-conversion. To explore the possibility that the glassy state could be achieved at higher temperature, Mike prepared *para*-enriched H_2*@C_{70} by irradiation at 77 K in toluene glass (Figure 2.13). Then the sample was warmed to 300 K and the solution was irradiated again. No change in the H_2 intensity was observed in the NMR between the measurements taken at 300 K before the irradiation and again after irradiation. The same *para*-enrichment procedure was repeated again with fresh H_2*@C_{70} at 77 K except this time the sample was only warmed up to 155 K and irradiated while it was still a toluene glass. At 155 K, the *ortho*:*para* ratio was 72:28 upon irradiation an increase in the *o*H_2 signal relative to the HD internal standard was observed. This result showed that photochemical spin-conversion could be driven in either the forward or back directions as long as C_{70} is in a glassy state during irradiation. This result also supports our hypothesis that the photo-induced triplet state of C_{70} acted as the spin catalyst for *ortho*/*para* conversion. For more details on the photo-induced *o*/*p* conversion, please refer to the Frunzi, et al., manuscript.[13]

2.4 Ortho/para conversions below 77 K

The limitations of the conventional method of spin transformation for *para*-enrichment of the encapsulated or "endohedral" hydrogen involves dispersing H_2@C_{60} on a NaY zeolite and immersing it in liquid O_2 at 77 K (section 2.5.7.1). While effective, it is dangerous, time-consuming and only effective at temperatures where O_2 is liquid, limiting enrichment to ~50:50 *o*H_2:*p*H_2. Work has been done by Dr. Michael Frunzi in the *para*-enrichment of Dr. Yongjun Li's covalently attached nitroxides, H_2*@C_{60}–**4** and H_2*@C_{60}–**7** (**Chart 2.1**) and utilizing the phenylhydrazine/$Cu(OAc)_2$ magnetic switch system[6] for intramolecular conversion at a much lower temperature regime (5-20K) in liquid He. Figure 2.14 is the ^{1}H NMR spectra of the *o*H_2 →

pH_2 forward conversion by covalent nitroxomalonate H_2*@C_{60}–**4** at 4 K with a forward conversion rate estimated to be 26 days.[2] The solid samples were flame sealed and placed in low temperature inserts in a helium Dewar. Each NMR spectrum was taken immediately after the sample was removed from the helium Dewar and dissolved in ODCB at different times, as indicated in Figure 2.14.

In summary, I have illustrated the evolution of spin catalysts for the *ortho*/*para* H_2 nuclear spin isomer conversions from intermolecular nuclear spin isomers of H_2 conversion with triplet oxygen (Section 2.1) to intramolecular nuclear spin conversion with covalently link nitroxides (Section 2.2) and finally to intraelectronic (ground state, S_0 vs. first excited triplet state, T_1) nuclear spin conversion with a pristine system in which the triplet state of the host, C_{70} is the spin catalyst (Section 2.3).

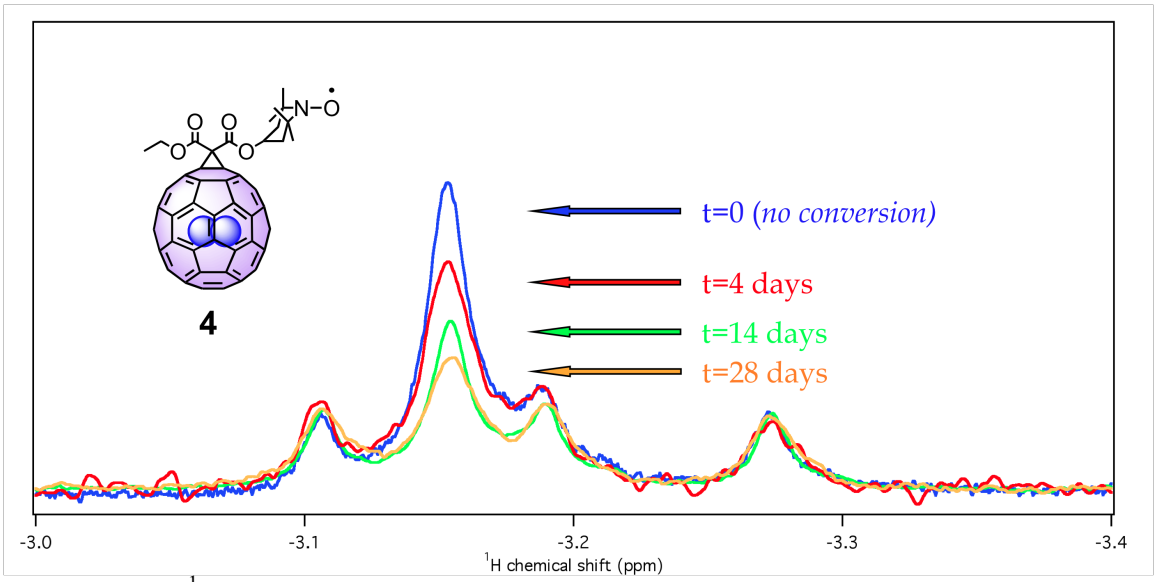

Figure 2.14: ^{1}H NMR of the *o*H_2→*p*H_2 forward conversion over time by covalent nitroxomalonate **4** at 4 K. The solid samples were flame sealed and placed in low-temp inserts in helium dewar. Each NMR spectrum was taken immediately after the sample was removed from the dewar and dissolved in ODCB at different **t** as indicated in the figure.

2.5 Experimental Sections

2.5.1 Determination of encapsulation ratio or "purity" of the H_2@fullerene

We routinely take ^{1}H NMR and check the integrated peak area of up-field region corresponding to the encapsulated H_2 and HD. Absolute encapsulation ratio is determined by comparison of the integrated peak area of pyridyl-H (+8.38 ppm in ODCB-d_4) and encapsulated H_2 (-7.25 ppm for H_2@C_{60}-K13, **Chart 2.1**). It is found that the absolute encapsulation ratio seems to depend on NMR machines and their parameters (error range would be ca. 10%). The final encapsulation ratio of H_2@C_{60} is determined by taking ^{13}C NMR and comparing the peak area of C_{60} cages as shown in Figure 2.15.

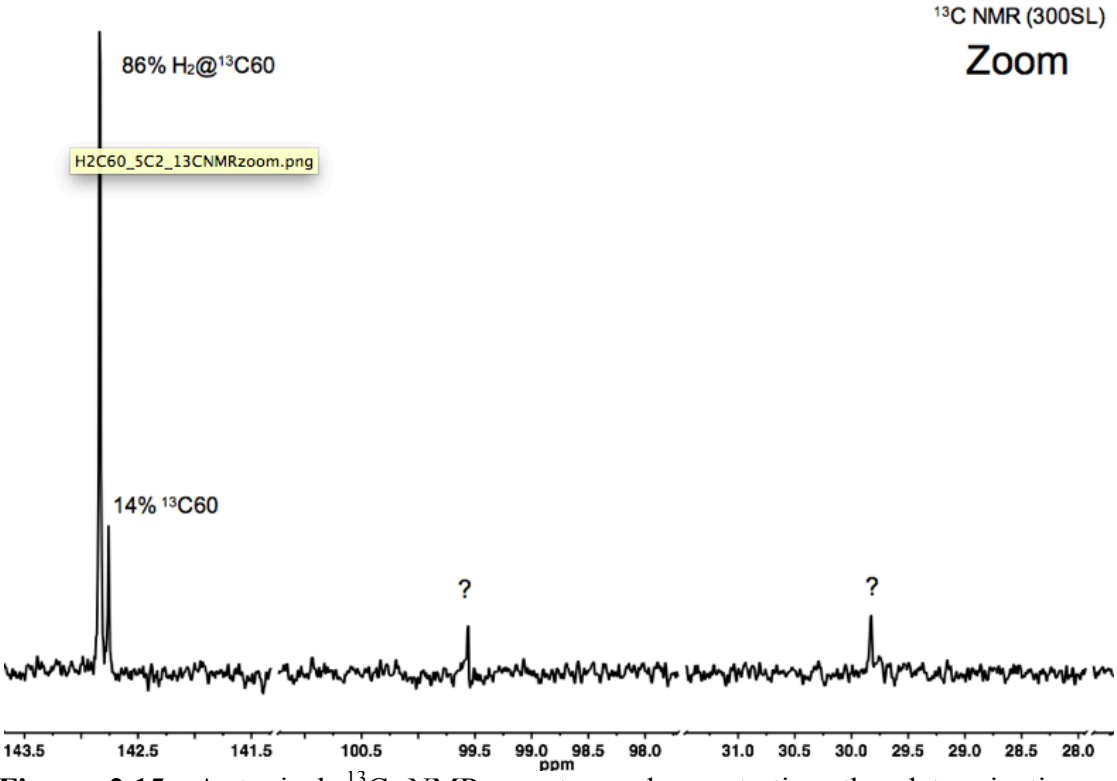

Figure 2.15: A typical ^{13}C NMR spectrum demonstrating the determination of percentage encapsulation of H_2 inside C_{60} fullerene relative to empty fullerene. The two singlets upfield to resonance of interest are due to impurities in the sample.

2.5.2 Determination of sample loss after extraction of $H_2@C_{60}$ upon forward conversion from NaY zeolite surface by absorption spectroscopy

In the determination of sample loss during forward conversion on the zeolite surface, two samples were collected at different times as shown in Figure 2.16 (Left). The first 100 μL aliquot, **A** was collected from the CS_2 solution containing $e$$H_2$*@$C_{60}$ mixture at RT (eH_2=75% $o$$H_2$/25% $p$$H_2$) prior to mixing with hexane and adsorbing onto the zeolite. Then **A** was dried and redissolved in 2.5 mL of spectroscopic grade toluene for absorption measurement. The remaining CS_2 solution containing the $e$$H_2$*@$C_{60}$ was dispersed on the zeolite surface and underwent $o$$H_2$ → $p$$H_2$ forward conversion at 77 K with liquid O_2 (Section 2.5). The second aliquot, **B** was taken after the enrichment process, once the *para*-enriched H_2*@C_{60} (*$p$$H_2$*@$C_{60}$) was extracted from the zeolite surface (see section 2.5 Part III). It was first dissolved in the same amount of CS_2 from the initial sample preparation for forward conversion (see section 2.5 Part I). Then 100 μL aliquot (same amount as **A**) was taken from the $p$$H_2$*@$C_{60}$ in CS_2 solution, dried and diluted with the same dilution factor as **A** in toluene and its absorption was measured. The dilution factor was determined based on (1) the extinction coefficients, ε of C_{60} in toluene at 515 nm and 570 nm are 866 mol^{-1}•l•cm^{-1} and 774 mol^{-1}•l•cm^{-1}, respectively (previously measured by Steffen Jockusch). (2) 1 cm path length, and (3) in order for the optical density, A to be 0.5 or below (corresponding to >32% transmittance) the concentration of H_2*@C_{60} must be < 0.65 mM. Results from the absorbance measurement are shown in Figure 2.16 (Right). Both spectra were subtracted by the background spectrum of toluene. The initial concentration of H_2*@C_{60} was 0.42 mM with absorption of 0.356. The final absorption after extracting the H_2*@C_{60} from the zeolite surface was 0.235 which corresponds to 0.28 mM and a 33% loss.

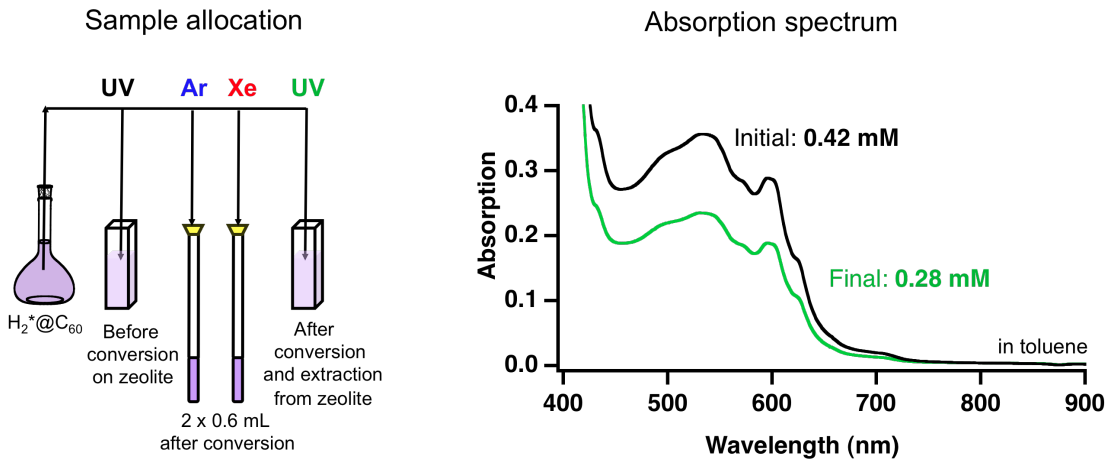

Figure 2.16: Sample preparation for the determinations of (1) lifetime back conversion with Xe and (2) 33% sample loss during forward conversion on NaY zeolite.

2.5.3 Solid-state NMR Measurements

Because of the considerable amount of sample loss determined by UV during *o*H_2@C_{60} to *p*H_2@C_{60} forward conversion from the surface of a NaY zeolite (see section 2.5.2), we attempted NMR measurements of H_2@C_{60}@NaY without the extraction step to follow the extent of conversion back conversion and to avoid sample loss. We dissolved H_2@C_{60}@NaY in CCl_4 with D_2O internal standard insert. The solution became slurry because the solvent molecules migrated into the supercages of the zeolite resulting in the formation of a gel. With Dr. John Decatur at our NMR facility, a NMR spectrum was obtained via spin echo with water suppression and showed no sign of H_2 singlet at -1.44 ppm (Figure 2.17). Next, we tried dry H_2@C_{60}@NaY powder but still no H_2@C_{60} signal was observed (Figure 2.18). Finally, we tried solid state NMR with dry H_2@C_{60}@NaY. Magic angle spinning at 3348 Hz gave sharper lines for hexane (Figure 2.19) than static measurement (**Figure 2.20**); however in both cases the endohedral H_2 signal was nowhere to be seen. We also took solid-state NMR (ssNMR) measurements with magic angle spinning at 2180 Hz of the slurry (Figure 2.21). The hexane lines were even sharper and a very

small singlet for endohedral H_2 was observed at -1.44 ppm; however, this occurred after 3625 scans and the signal is basically buried in the noise for meaningful measurements. We abandoned that idea and moved onto modifying the catalyst within the framework of the zeolite itself.

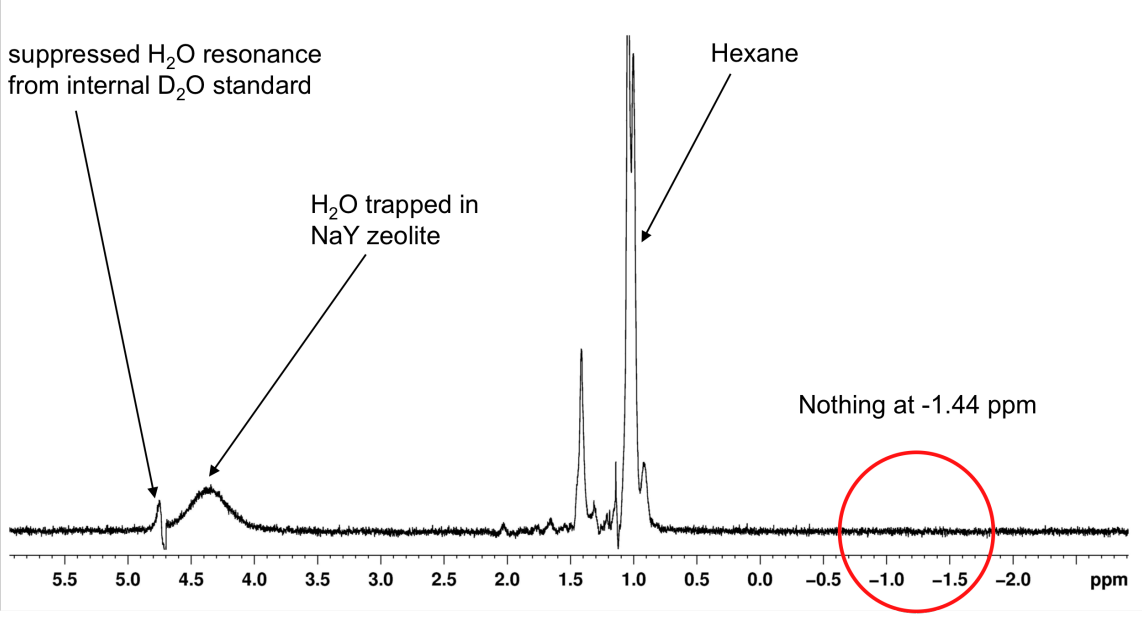

Figure 2.17: Liquid ^1H NMR of $H_2@C_{60}@NaY$ slurry in CCl_4 with internal D_2O standard. ECHO with water suppression pulse technique. 500 MHz, ns = 12,378.

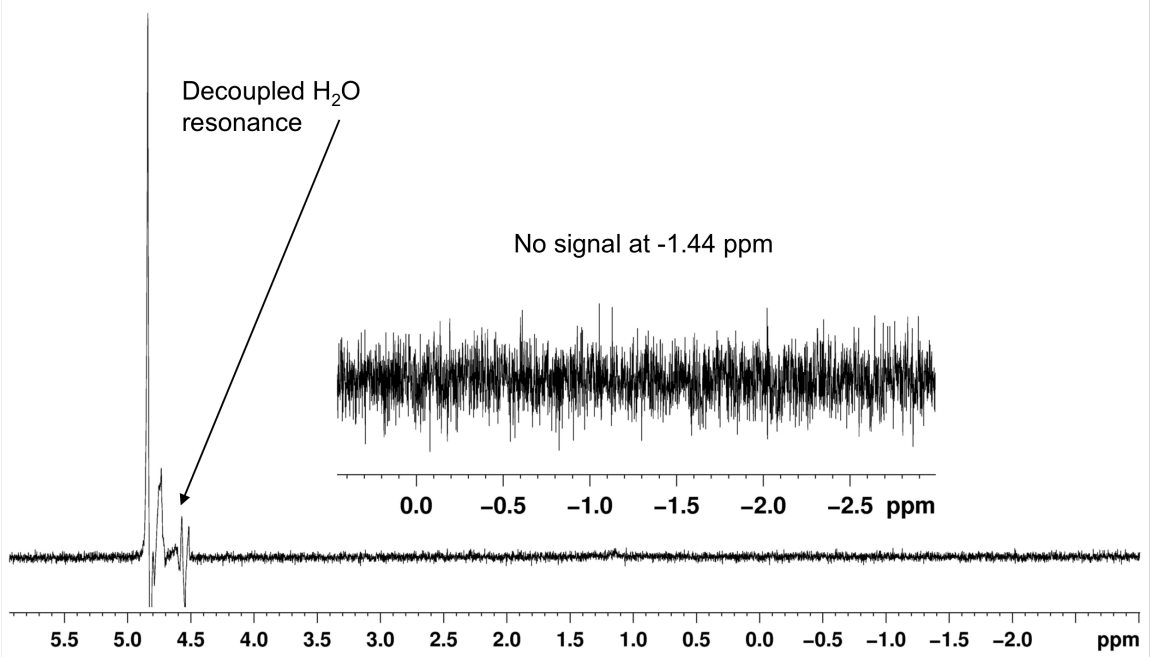

Figure 2.18: Liquid ^{1}H NMR of $H_2@C_{60}@NaY$ dry powder with internal D_2O standard. Spin echo with water suppression pulse technique. 500 MHz, ns = 809.

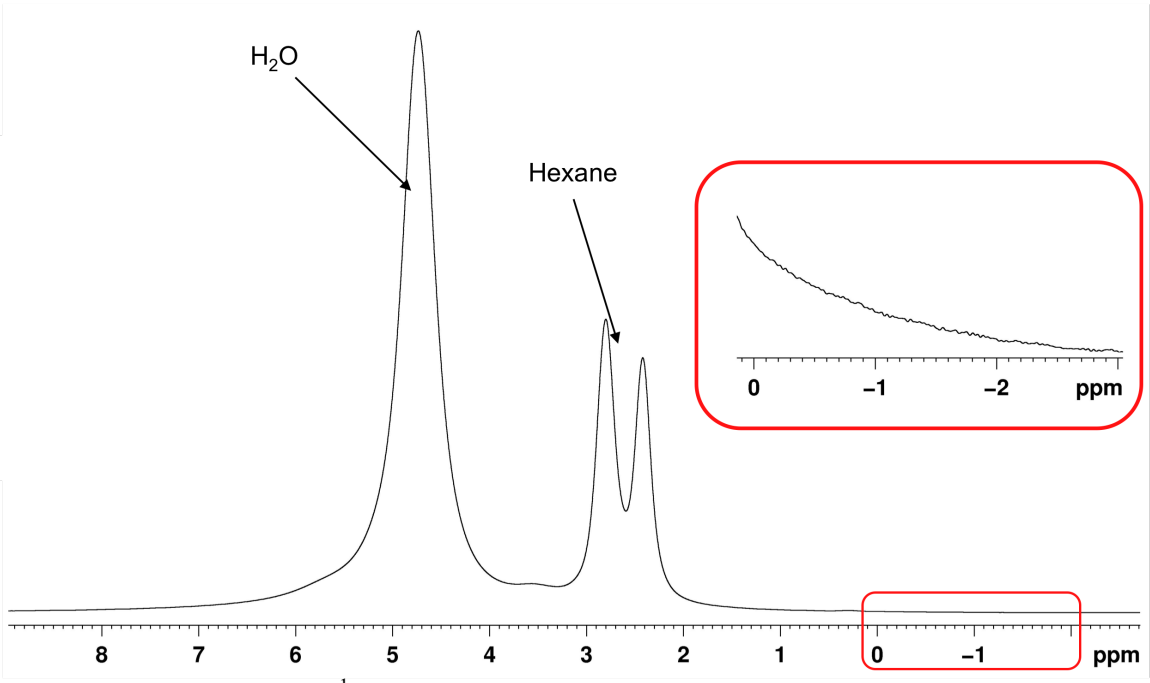

Figure 2.19: Solid-state ^{1}H NMR of $H_2@C_{60}@NaY$ dry powder with magic angle spinning @ 3348 Hz. 300 MHz, ns = 8,192.

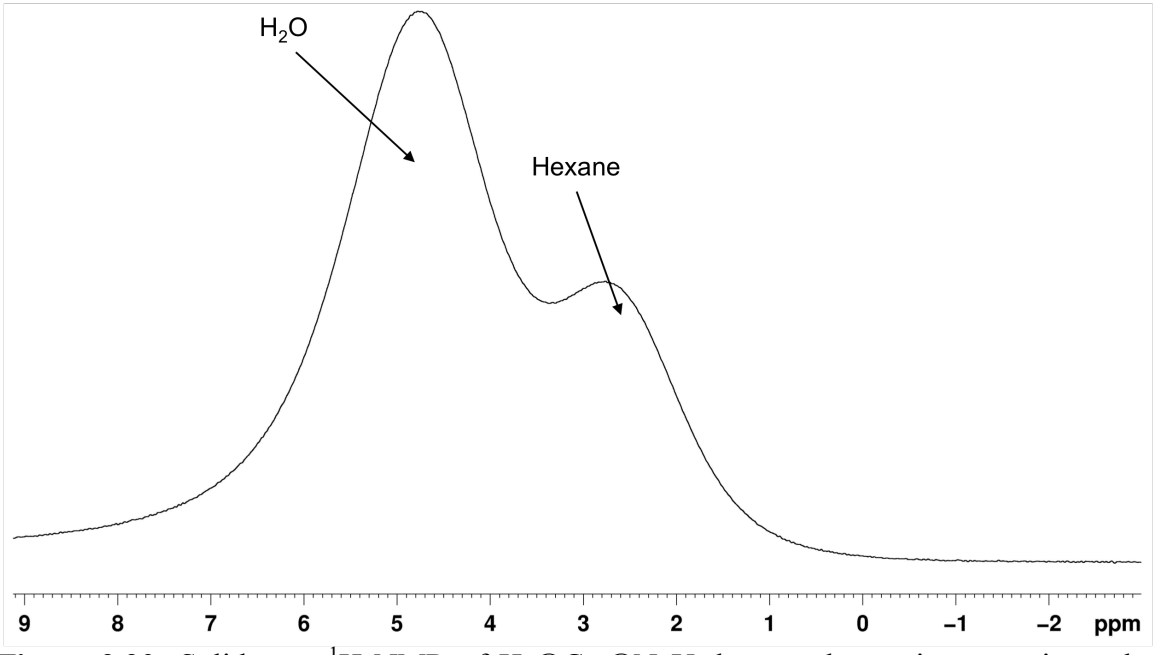

Figure 2.20: Solid-state ^{1}H NMR of $H_2@C_{60}@NaY$ dry powder static at magic angle. 300 MHz, ns = 92.

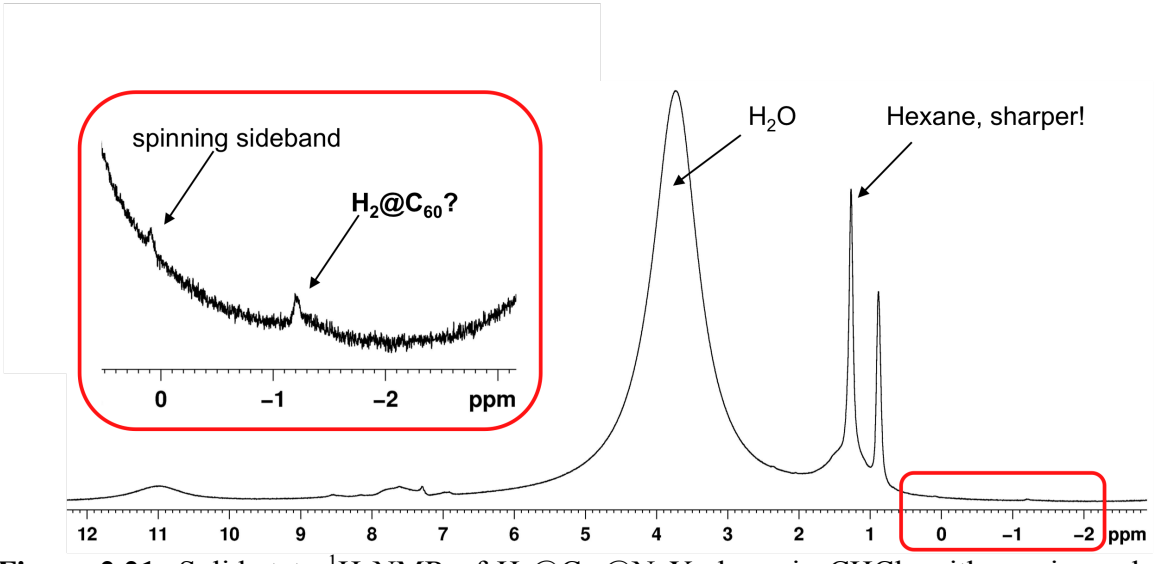

Figure 2.21: Solid-state ^{1}H NMR of $H_2@C_{60}@NaY$ slurry in $CHCl_2$ with magic angle spinning @ 2180 Hz. 300 MHz, ns = 3,625.

2.5.4 Ion exchanged zeolites

3*d* transition metal and lanthanides complexes as catalysts are known to cause interconversion between pH_2 and oH_2.[14] Therefore, we tried NaY zeolites in which the sodium

ion was exchanged with the heavy atom thallium (Tl) as well as a sample that is exchanged with a polarizable atom, cesium (Cs) as possible built-in *ortho*/*para* converters to investigate the spin-orbit induced and heavy atom effect on *ortho*/*para* conversion, respectively. A preliminary result on a small scale using 0.2 mg C_{60} (no H_2) and 122 mg TlY (1:600 of C_{60} : CsY or TlY) in mostly hexane with a control experiment without C_{60} showed that the C_{60} does not adsorb on the surface of the zeolite. The CS_2/hexane solution remained purple after stirring for two hours and a brown precipitate was present in both the experimental and control round bottom flask. The same negative result occurred for the CsY and the solution remained purple after stirring for two hours. We did not pursue this any further.

2.5.5 Internal Standards for *ortho*/*para* nuclear spin conversion

As mention in Section 2.1, nuclear magnetic resonance (NMR) spectroscopy is a convenient method to measure *ortho*/*para* conversion for the $H_2@C_{60}$ system. In addition, the proton resonance for $H_2@C_{60}$ is a prominent singlet at -1.44 ppm, shifted upfield, away from all the solvent peaks and possible impurities. However, since $H_2@C_{60}$ is a pristine system with no other protons other than the incarcerated H_2, we needed to find an internal proton standard that will not convert between *ortho* and *para* allotropes under our conditions. Below are a few things we tried and failed at different times and for different reasons.

We tried using a coaxial insert, a capillary that fits snugly into a 5 mm NMR tube and tapers to a smaller diameter stem in the lower 50 mm and filled the insert with a convenient deuterated solvent to serve as lock and standard. The advantages with this are (1) the insert can be reused, and (2) we are not limited to only solvents for NMR measurements and are free to use solvents with a higher solubility for the fullerene, e.g., toluene (2.8 mg ml^{-1}) vs. CS_2 (7.9 mg ml^{-1}). However, the $H_2@C_{60}$ samples are very precious and with the insert, samples are always lost

during transfer. The Lock and Shim were also very difficult with the insert especially when having the best line shape for integration is of prime importance. In addition, CS_2 is very volatile and with conversion experiments in which measurements are taken over a period of a month, the concentration changes gave false results. We eventually came to rely on a very convenient *internal* standard, HD@C_{60} which does not have *ortho/para* allotropes and therefore will not interconvert under our conditions. We also did find a more suitable solvent, 1,2-dichlorobeneze-d_4 (ODCB), that has a high solubility (27 mg ml^{-1}) and low volatility. The only draw back was the price, currently it runs $82/5g through Fisher Scientific with Columbia discount, otherwise it runs for about $167/5g.

On a different occasion, we synthesized C_{60}-TMS (**Chart 2.1**) as an alternative internal standard to HD; however, C_{60}-TMS gave very scattered data in itself over the course of $p$$H_2$ → $o$$H_2$ conversion time. This set of experiment is described below.

The motivation behind trying a different internal standard was because we have H_2 endofullerenes that do not contain hydrogen HD isotope and we would have more options if we were not limited to the HD as standard. In addition, we wanted to minimize any errors in the ^{1}H NMR measurements as a result of line broadening caused by the presence of paramagnetic catalysts, especially nitroxides in the determination of the rate of $p$$H_2$ to $o$$H_2$ back conversion at room temperature after *para*-enrichment at 77 K. The error also increased with increasing concentration of paramagnetic species because of significant broadening of the overlapping H_2 singlet with the HD triplet. So, we want an alternative internal standard that has a chemical shift (1) upfield away from the solvent peaks and (2) does not overlap with the H_2 peak at -1.44 ppm. To test out the viability of the C_{60}-TMS, two samples each with a mixture of H_2*@C_{60}, an H_2*@open-C_{60} and C_{60}-TMS were prepared for the conversion. One mg each of H_2*@C_{60} and

H_2*@open-C_{60} was dissolved in 1 mL CS_2 and then mixed with 35 mL of hexane. This solution was poured into a 50 mL round bottom flask containing 1.5 g of dried NaY zeolite and stirred for an hour or until brownish-red supernatant becames clear and colorless and the zeolite becames colored (Figure 2.27 of Section 2.5). The solvent was evaporated and the sample cooled to 77 K and immersed in liquid oxygen for 30 minutes (Figure 2.28 and Figure 2.29 of Section 2.5). Then the sample was rapidly worked up and fullerenes were extracted from the zeolite surface with CS_2 and methanol and dried under argon. The sample was redissolved in ODCB and *at this point, quantitative amount of C_{60}-TMS was added to the solution* right before the NMR measurement. Figure 2.22 and Figure 2.23 are ^{1}H NMR spectra of two sets of experiments both

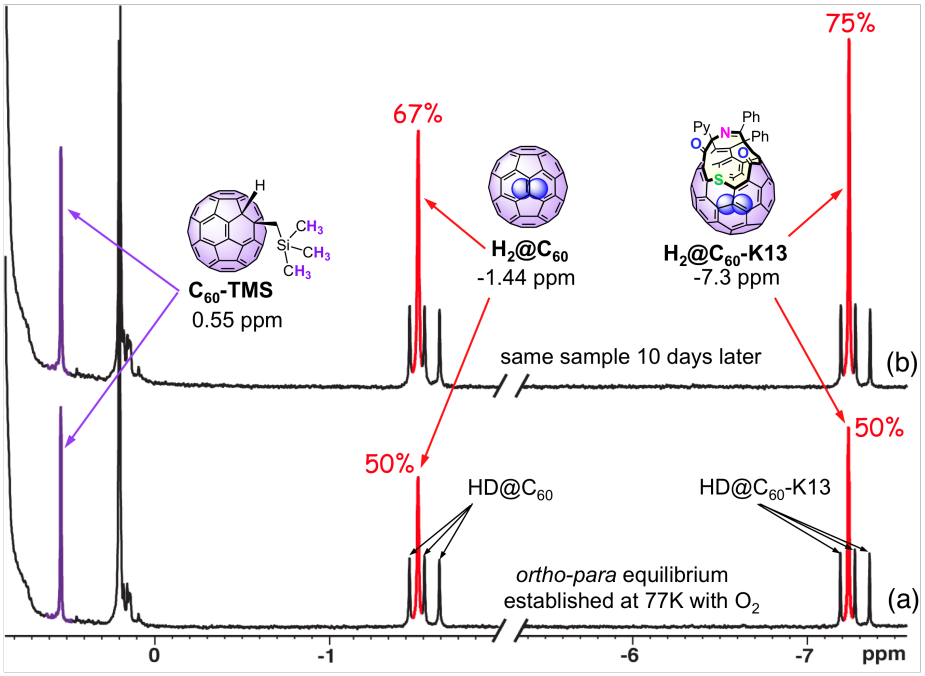

Figure 2.22: 500 MHz ^{1}H NMR spectra of isotopomeric mixture of $H_2@C_{60}$ and $H_2@C_{60}$-K13 with C_{60}-TMS internal standard in 1,2-dicholorobenze-d_4 at 300 K. Spectrum (a) corresponds to the *ortho*/*para* equilibrium distribution immediately after workup from 77K with O_2. Spectrum (b) corresponds to the *ortho*/*para* equilibrium established ten days later in air. HD triplets served as the control.

using C_{60}-TMS as internal standard and HD@fullerene as control. Spectrum (a) for both figures was taken at 300 K and corresponds to the *ortho*/*para* equilibrium established immediately after workup from 77 K. Spectrum (b) corresponds to the *ortho/para* equilibrium of the same samples ten dayslater in air. Figure 2.22 is the ^{1}H NMR that contained a mixture with H_2*@C_{60}-K13 (**Chart 2.1**) and Figure 2.23 corresponds to the mixture with H_2*@C_{60}-K12 (**Chart 2.1**). Qualitatively, the intensity of H_2 (red singlet) in (a) and (b) for both figures grew significantly over the course of ten days while the HD triplets (black) and C_{60}-TMS singlet (purple) remained unchanged. It was also apparent that the baseline for C_{60}-TMS was not flat and may contribute to errors in integration.

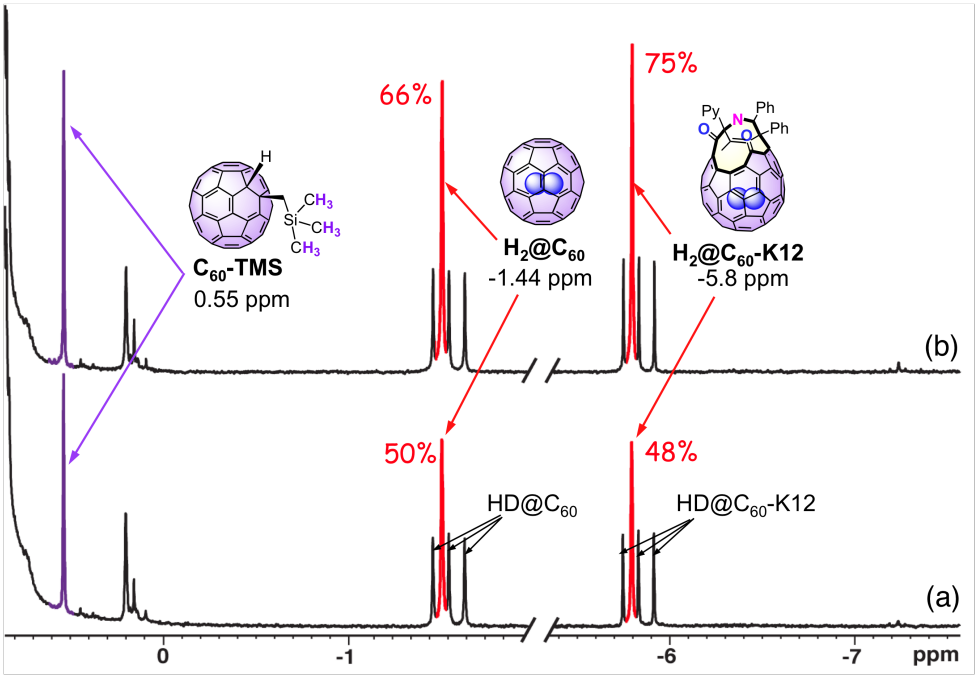

Figure 2.23: 500 MHz ^{1}H NMR spectra of isotopomeric mixture of H_2@C_{60} and H_2@C_{60}-K12 with C_{60}-TMS internal standard in 1,2-dicholorobenze-d_4 at 300 K. Spectrum (a) corresponds to the *ortho*/*para* equilibrium distribution immediately after workup from 77K with O_2. Spectrum (b) corresponds to the *ortho*/*para* equilibrium established ten days later in air. HD triplets served as the control.

A quantitative analysis of the standards: HD@C_{60}, HD@C_{60}-K13 and C_{60}-TMS was monitored over ten days. It was clear from the results that there was a lot more scatter from C_{60}-TMS (± 0.3) as compared to HD@C_{60} (± 0.1) and HD@C_{60}-K13 (± 0.1). Thus, C_{60}-TMS is not suitable for conversion experiments. However, either HD@C_{60} or HD@open-C_{60} can serve as internal standards for *p*H_2 to *o*H_2 conversion for any H_2@fullerene species. In other words, there is no constraint that one has to use HD@C_{60} for H_2@C_{60} or HD@C_{60}-K12 for HD@C_{60}-K12, so on and so forth, any combination of HD@fullerene to H_2@fullerene will give reliable results.

2.5.6 Methods of ^{1}H NMR data analysis for *ortho*/*para* conversion

In the cases where the *p*H_2 to *o*H_2 back conversion rates were enhanced (more readily measurable rates) by the addition of external spin catalyst, e.g., with the addition of nitroxides, we need to first determine the working range of concentration for ^{1}H NMR measurements.

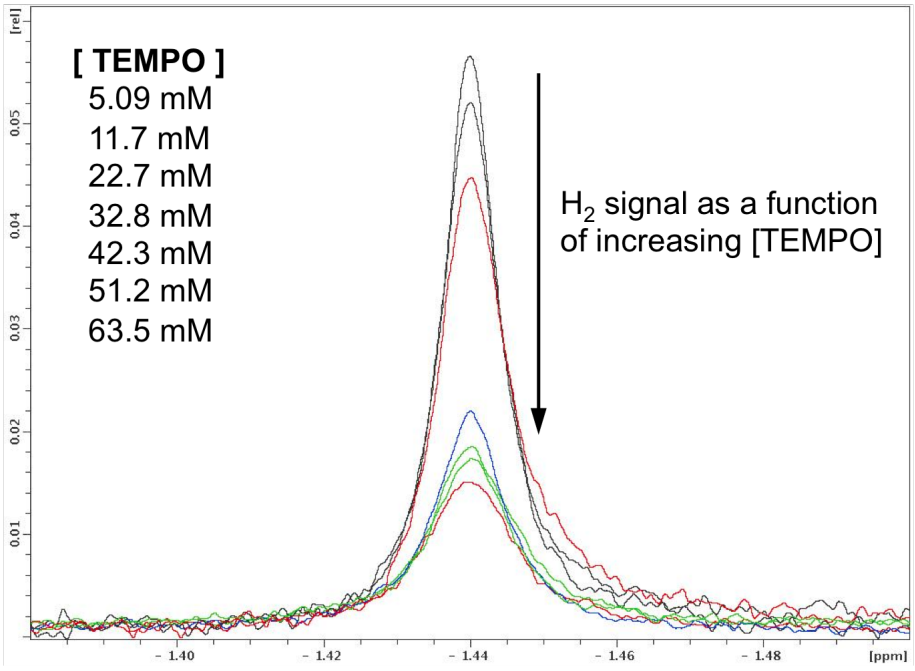

Figure 2.24: ^{1}H NMR of H_2@C_{60} as a function of different concentrations of TEMPO in determining the working range for conversion and relaxivity experiments.

Different concentrations of TEMPO (**Chart 2.1**) from 5 mM to 64 mM were added to $H_2@C_{60}$ and their line shape was monitored via ^1H NMR. There was a systematic increase in line width with increasing TEMPO concentration (Figure 2.24), thus we concluded that the upper limit of the concentration of nitroxide for NMR measurement is 20-25 mM, which corresponds to (6.0 −7.5) × 10^{21} spins.

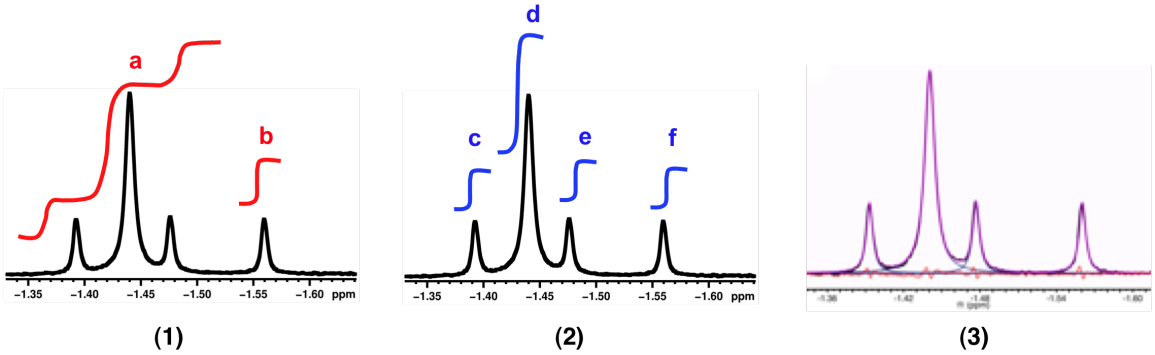

Figure 2.25: Method for the determination of oH_2 using HD as control: (1) Normalized the integral of **b** to one and take the integral of **a** and divide by three. (2) Divide the integral of **d** by the sum of the integrals **c**, **e** and **f** divided by three. (3) Line fitting, deconvolution by varying the Lorentzian/Gaussian (L/G) ratio.

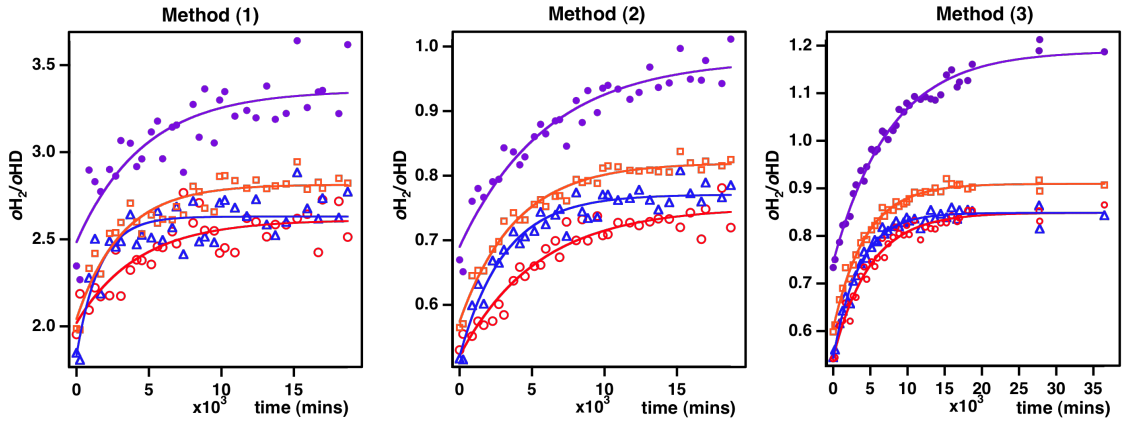

Figure 2.26: The same set of pH_2 to oH_2 conversion data for mixture of $H_2@$fullerenes are analyzed by each of the three methods described in **Figure 2.25**. ●$H_2@C_{60}$, □ $H_2@C_{60}$-K13, △ $H_2@C_{60}$-K12, ○$H_2@C_{60}$-K8 in 1,2-dichlorobenzene at 300 K with 5 mM TEMPO. Method (3) shows the complete conversion with endpoint at 24 days.

The lifetimes of *p*H_2 to *o*H_2 back conversion at room temperature were determined based on the time-dependent ratio of the area of H_2 singlet relative to the control, HD triplet, and was monitored frequently until the H_2/HD ratio plateaued or reached a constant value. Each data point as a function of time corresponds to the normalized *o*H_2 via the ratio of H_2/HD with HD being the average value of the triplet. The calculated lifetimes were determined via simple first order exponential fit.

Three methods were employed to determine the area of H_2 (and HD) peaks (Figure 2.25) In method (1) the integral of b (in red) was normalized to one, then subtract 2xb from the integral of a (in red) and divide a (in red) by three. In method (2), integral d (in blue) was divided by the average of the sum of integrals c, e and f (in blue). Method (3) used the line-fitting program in MestReNova by varying the Lorentzian/Gaussian (L/G) ratio to fit the selected area of the spectrum.

Figure 2.26 shows the results of analysis via the three different methods described in Figure 2.25 for the same set of *p*H_2 to *o*H_2 back conversion data for a mixture of *para*-enriched H_2@fullerene, specifically ●H_2@C_{60}, □H_2@C_{60}-K13, △H_2@C_{60}-K12, and ○H_2@C_{60}-K8 in ODCB with 5 mM TEMPO. The H_2@open-C_{60}'s were all from the same batch while the H_2@C_{60} was from a different batch of the synthesized material, thus the different starting/endpoints. ^{1}H NMR measurements were taken at 300 K over a span of 24 days. The area for integration and line fitting were the same for each point for each of the species. The most scattered points were observed for Method (1) then (2) with Method (3) having the snuggest fit.

2.5.7 General procedure for forward conversion with O_2 at 77 K

2.5.7.1 What works

The very first successful experiment of the *ortho*/*para* conversion was carried out by dissolving 2 mg of the mixture of $H_2@C_{60}$, $HD@C_{60}$ and $D_2@C_{60}$ ($H_2^*@C_{60}$) in the minimum amount of CS_2. Then we added 30 mL of cyclohexane and dispersed the mixture on the external surface of 1g of Sodium Y Zeolite (NaY), a white powder, by stirring.[15,16] This is shown in (1) of Figure 2.27 where a 50 mL round bottom flask

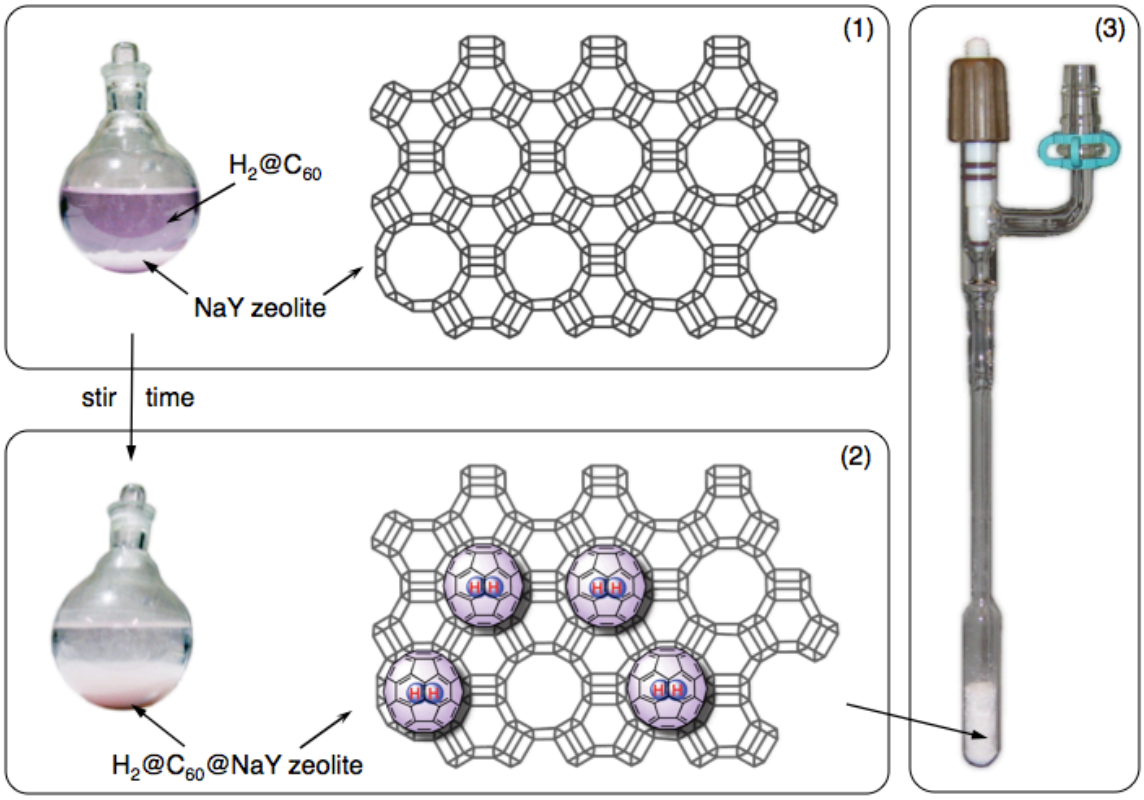

Figure 2.27: Schematics of adsorption process. (1) Initial appearance of the purple $H_2@C_{60}$ solution and white NaY mixture. Cartoon to the right of the round bottom flask depicts the NaY external surface prior to adsorption. (2) Appearance of the mixture after stirring for approximately one hour. The solution is now clear and the color is transferred to the NaY indicating successful dispersion. Cartoon to the right now shows $H_2@C_{60}$ molecules adsorbed on the surface of the NaY. The solution in flask (2) is removed and the remaining powder is transferred to a glass tube (custom made Schlenk tube) shown in (3).

contained a purple solution of H_2*@C_{60} in CS_2/cyclohexane mixture and sitting on the bottom of the flask is NaY and a magnetic stirring bar. The cartoon to the right of the flask depicts the NaY zeolite external surface prior to adsorption. After approximately an hour of stirring, the colored solution becomes clear, indicating that the fullerenes have been transferred from the liquid phase to the surface of the zeolite (2) in Figure 2.27. Then we rotovapped away the solvent and was left with a colored NaY, light purple for C_{60} and light red for C_{70} and open-$C_{60,}$ a very good visual indication to quickly determine that the fullerenes have been successfully dispersed onto the surface. This allows contact between each individual fullerene molecule with the liquid paramagnetic catalyst necessary for spin conversion. We decided to conduct the conversion experiment at 77 K because liquid nitrogen is convenient and cheap. With regards to the spin catalyst of choice, several criteria need to be met. First we need a reagent that is liquid at 77 K to efficiently make collisional contact with each dispersed H_2@C_{60} and cause forward spin conversion from *o*H_2 to *p*H_2. Second, we need to be able to quickly and easily remove this catalyst in order to prevent back conversion from *p*H_2 to *o*H_2 during the workup so that we have a chance to monitor and calculate its conversion lifetime. Both nitric oxide (NO) and oxygen (O_2) are liquid at 77 K and its ground state triplets thus can serve as a paramagnetic spin catalyst. We chose O_2 because NO is too expensive and we were not sure if the experiment would work and thus worthy of a huge investment from the very start.

The dried NaY was transferred to a glass tube shown in (3) of Figure 2.27. The transfer was done using a glass funnel with a long stem that fit inside the tube such that all the zeolite fell directly to the bottom, wider part of the tube (bulb). This is very important because any H_2@C_{60}@NaY powder that is stuck on the walls of the tube will not be submerged in liquid O_2 and *o*H_2 to *p*H_2 conversion will not occur. Then the glass bulb containing the sample was placed

under the vacuum line (Figure 2.28). The sidearm that connects the glass tube to the vacuum line was stuffed with some glass wool to prevent the zeolite from getting sucked into the manifold of the vacuum line during evacuation and grease was applied to seal.

Part I. Condensing Oxygen. First, residual solvent molecules trapped inside the NaY and air were pumped out via the vacuum line by first opening valve 4 in Figure 2.28 to start the vacuum and then open valve 2 in Figure 2.28. Then very, very slowly and carefully open valve 1. While you are opening valve 1, keep your eyes on the zeolite because this is where the zeolite will jump out of the tube and into the manifold.

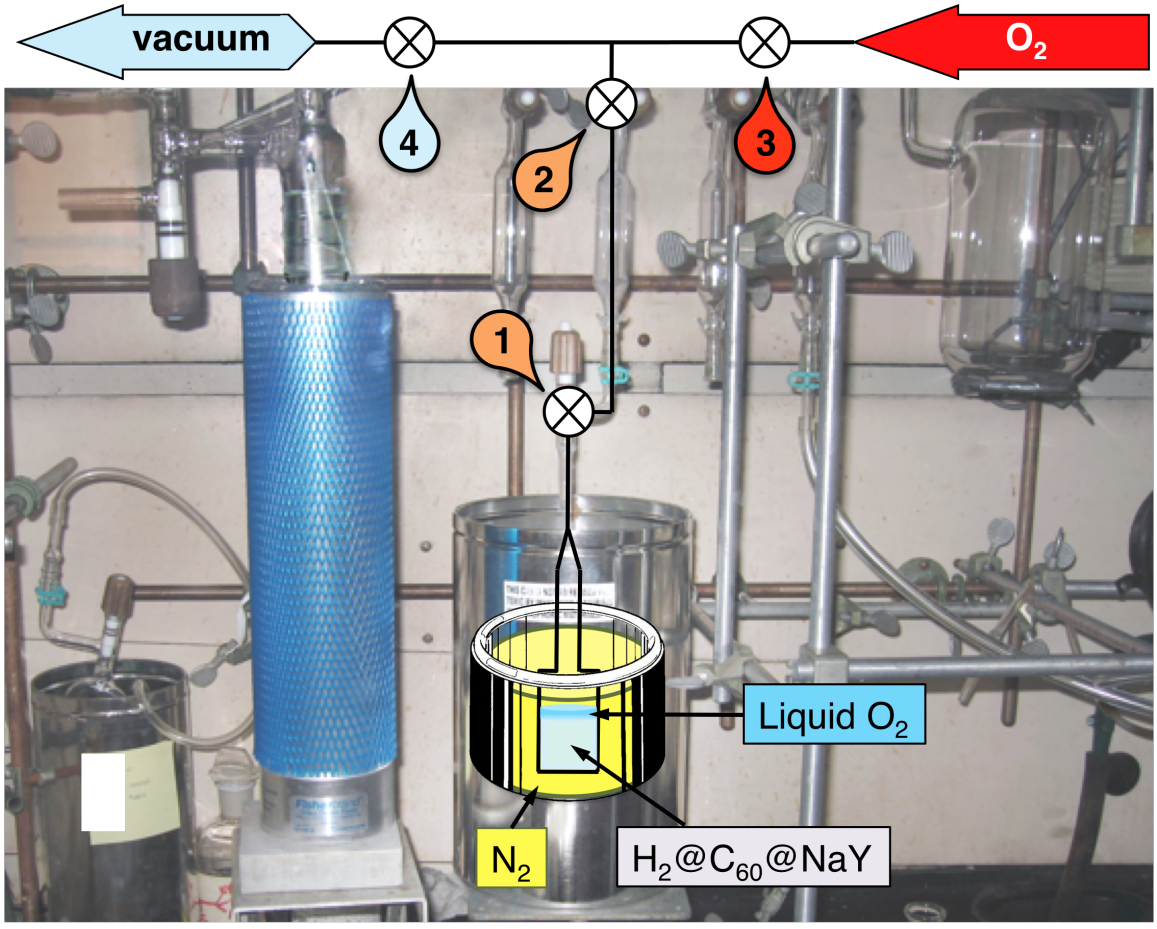

Figure 2.28: Experimental setup for thermally-induced oH$_2$ to pH$_2$ conversion.

Valve 3 in Figure 2.28 is closed. Once the powder settled down in the bulb and the vacuum gauge reads close to zero torr then one is ready to move forward. A shallow dewer was placed inside the tin can and then filled with liquid N_2 (Figure 2.28, yellow liquid is N_2). Do not immerse the glass bulb inside the liquid N_2 yet; first the manifold needs to be flushed with O_2. Close valve 2 in Figure 2.28 and then valve 4. Open valve 3 slowly to allow O_2 to flow in and then open the valve all the way. The vacuum gauge will read close to 760 torr. Close valve 3 in Figure 2.28 once the manifold has been filled with O_2. Now open valve 4 in Figure 2.28 slowly to evacuate the O_2 and air. Once the gauge reads close to zero torr, close valve 4 and slowly open valve 3 again. Repeat flushing 3X. Once the manifold is rid of air and other impurities and filled with O_2, submerge the entire bulb into liquid N_2 by raising the lab jack. Open valve 2 in Figure 2.28 to allow O_2 to flow into the sample. The oxygen tank is set up to prevent overpressure while condensing O_2 at 77 K by inserting a Teflon tubing with a 2 cm slit between the oxygen tank and desiccant/tubing that connects to the manifold (Figure 2.29). Look for blue liquid condensing on top of the zeolite. This will take approximately 15 minutes. Once you see the blue liquid, reduce everything: the flow of oxygen and pressure, then lower the lab jack such that the meniscus of

Figure 2.29: A Teflon tubing with a 2 cm slit was inserted between the oxygen tank and desiccant that connects to the manifold. This safety prevents overpressure while condensing O_2 at 77 K.

the liquid N_2 is just above the blue O_2 (Figure 2.28 cartoon of the level of the yellow N_2 relative to the blue liquid O_2 and Figure 2.29). The first time, we waited 5 hours because we didn't know just how long it would take for forward conversion. After optimizing all the conditions, we now know that it is only necessary to immerse the $H_2@C_{60}@NaY$ in liquid O_2 for half hour at 77 K to obtain the desired conversion. Meanwhile, it was important to constantly monitor the level of liquid N_2 and make sure that it stayed just above the level of O_2. For the last 5 minutes of oH$_2$→pH$_2$ conversion, close the O_2 source completely (not from the valve, from the actual tank) and maintain some backpressure.

Part II. Removing Oxygen. Be extremely careful in this part of the experiment. Fill the shallow dewer completely with liquid N_2, raise the lab jack all the way up so the glass bulb is complete submerged in liquid N_2. Close valve 3 and keep your eyes on the vacuum gauge. Do not let it go above 1000 torr. Open valve 4 until vacuum gauge reads 0.02 torr. Lower

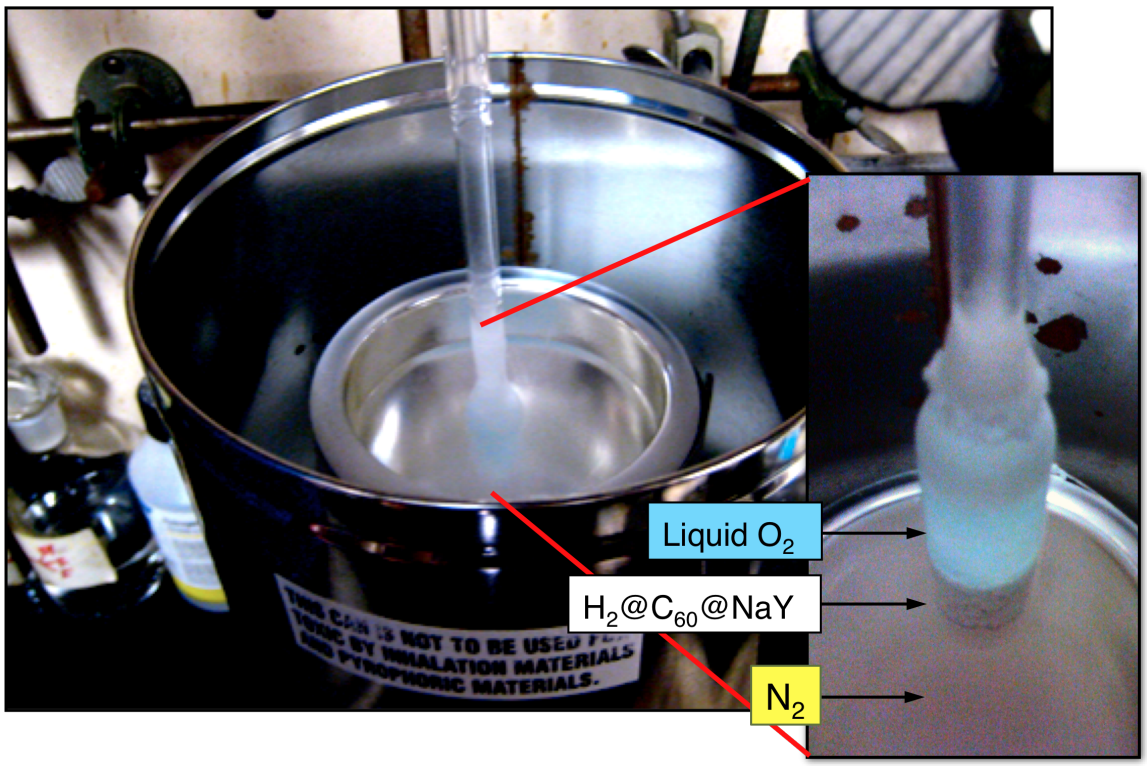

Figure 2.29: Photograph of liquid oxygen at 77 K.

fume hood. Lower the lab jack so that the liquid N_2 is at the level of the liquid O_2 and eventually at the level of NaY as the liquid O_2 gets pumped out. The key is to pump out all the liquid O_2 while the sample is still immersed in liquid N_2 and the system is maintained at 77 K. This ensures that the now *para* enriched system at 77 K does not start converting back to its *ortho* form in the presence of the O_2 spin catalyst at elevated temperature. Next, turn on the ionization gauge and monitor until it reads 10^{-2} torr, which indicates that all the O_2 has been removed. This can take 30-45 minutes or an hour. Once all the oxygen has been pumped out, lower the lab jack and close valve 2, then close valve 1. Carefully remove the sample from the vacuum line and wipe off grease and moisture on the tip of the joints.

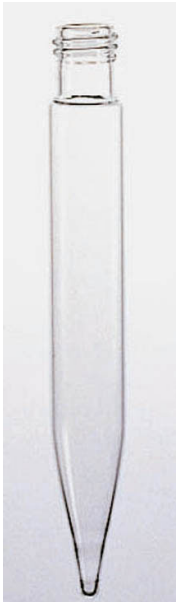

Part III. Extraction/Workup. The H_2*@C_{60}@NaY was transferred from the glass tube into a screw-top conical-bottom glass centrifuge tube (picture to the right) with CS_2 in the hood. Once all the zeolites have been transferred to the centrifuge tube, a Teflon cap (Wheaton Black Phenolic Screw Cap with PTFE-Faced Rubber Liner) was screwed on and the mixture was shaken vigorously and then centrifuged. The supernatant was carefully pipetted out and into a clean centrifuge tube. The extraction with CS_2 was repeated until the zeolite was almost colorless and the color of the supernatant was also faint. In the case of open-C_{60}, a few drops of methanol were added during each extraction because the open-C_{60}'s have a high affinity for the zeolite than C_{60} and needs methanol to displace it. Finally, the CS_2 (methanol) solution containing *para*-enriched H_2@C_{60} can either be removed by blowing with argon or rotavapped down. The solid was dissolved in ODCB for ^{1}H NMR measurement. This entire workup process could be accomplished in about an hour.

Part IV. NMR Measurements. Prior to the first NMR measurement each day, a proton spectrum was acquired for a nonconverted sample of $H_2@C_{60}$ as a standard to correct/account for daily field fluctuations.

2.5.7.2 What does not work

Prior to getting successful conversion results via dispersing the $H_2@C_{60}$ on the external surface of NaY zeolite, we tried other methods to spread out the $H_2@C_{60}$ molecules because they tended to clump together which prevented the oxygen molecules to make collisional contact with each $H_2@C_{60}$ molecule, a condition that is necessary for *ortho*/*para* interconversion. We tried coating the glass bulb with a layer of $H_2@C_{60}$ and then condensed liquid O_2, but it did not work. We also tried, on different occasions, using silica gel and glass wool as dispersing agent but the pore sizees were too large and the $H_2@C_{60}$ still clumped up together. In the case of silica gel (60Å pores), it was very easy to remove O_2 after conversion and $H_2@C_{60}$ was also easily extracted from the surface. However, only 11% of forward conversion was achieved. NaY Zeolite has external pores of 7.5 Å which hold each $H_2@C_{60}$ molecule just right (van der Waals diameter ~11 Å and nucleus to nucleus diameter is ~7.1 Å for C_{60}) and we get 30% conversion, corresponding to (45 ± 10)% *p*$H_2@C_{60}$. The drawback with NaY is that it is difficult to remove O_2 after conversion and also to extract the $H_2@C_{60}$ from the NaY surface during workup.

2.5.7.3 Unnecessary Evil

The initial workup mentioned in Part III. Extraction/Workup was performed in a bubble filled with inert gas because we were worried about back conversion in the presence of oxygen during the timescale of the workup. However, the determination of lifetimes of the back

conversion under different conditions indicated that the time it took for the workup was negligible relative to the conversion time. Thus the workup could be done in air.

2.5.7.4 Material

We purchased our fullerenes from Materials Technologies Research (MTR) at $22.50/gram for C_{60} with 99.5% purity and $260/gram for C_{70} with 98% purity.

2.5.8 Experimental ^{1}H NMR Spectrum of *para*-enriched H_2*@fullerene back conversion in TEMPO at 300 K

The spectra below showed a selective upfield shift of a broad peak between zero and one ppm as the concentration of TEMPO increased. This was likely due to an exchange between the paramagnetic and diamagnetic forms of TEMPO and hydroxylamine by hydrogen atom transfer.[17]

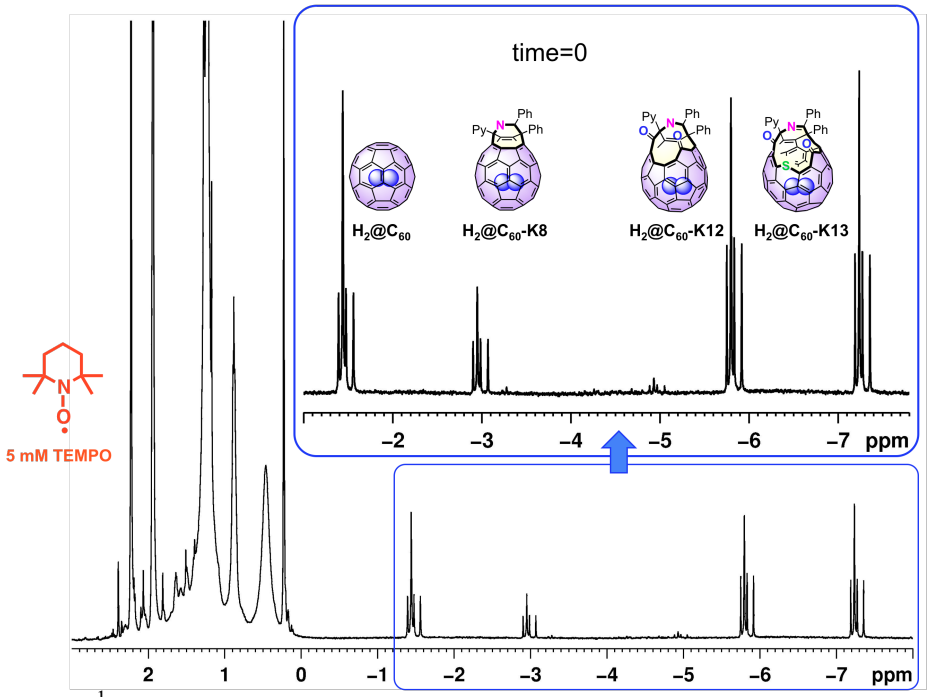

Figure 2.30: ^{1}H NMR of *para*-enriched *o*H_2*@open-C_{60} with 5 mM TEMPO in ODCB at 300 K. Time = 0

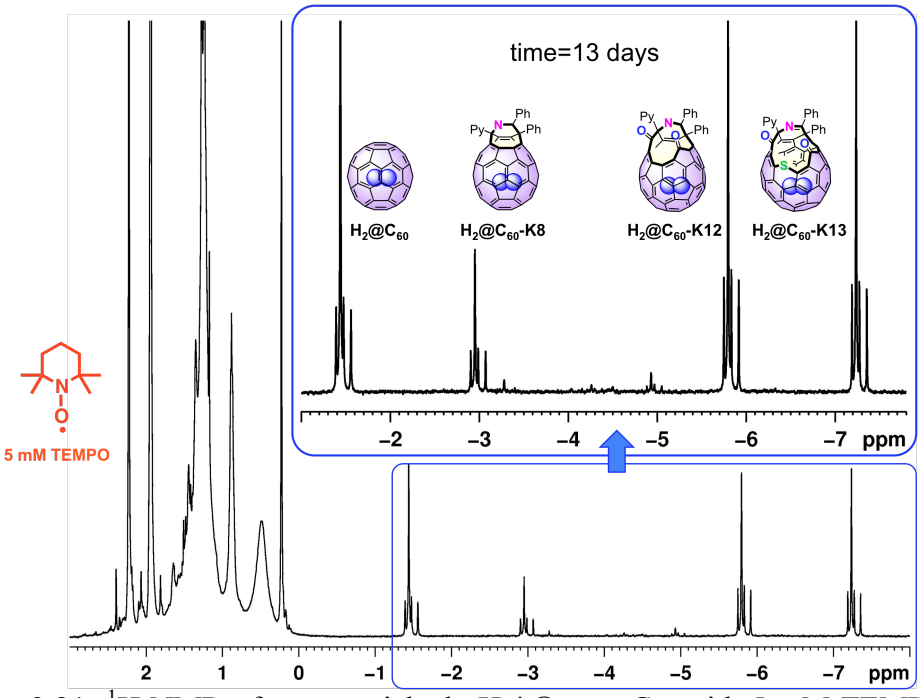

Figure 2.31: ^{1}H NMR of *para*-enriched oH$_2$*@open-C$_{60}$ with 5 mM TEMPO in ODCB at 300 K. Time = 13 days.

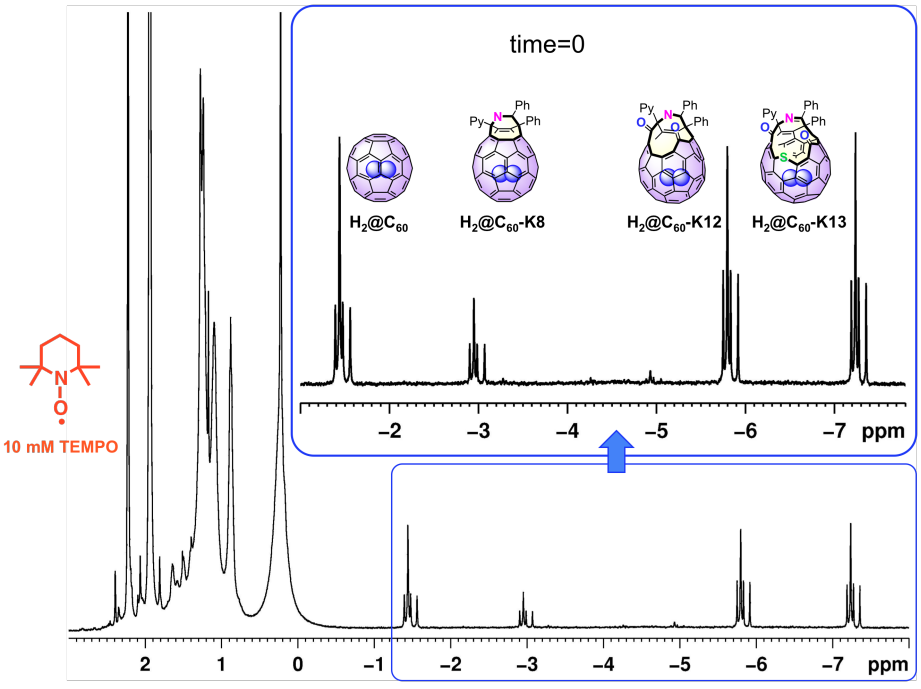

Figure 2.32: ^{1}H NMR of *para*-enriched oH$_2$*@open-C$_{60}$ with 10 mM TEMPO in ODCB at 300 K. Time = 0.

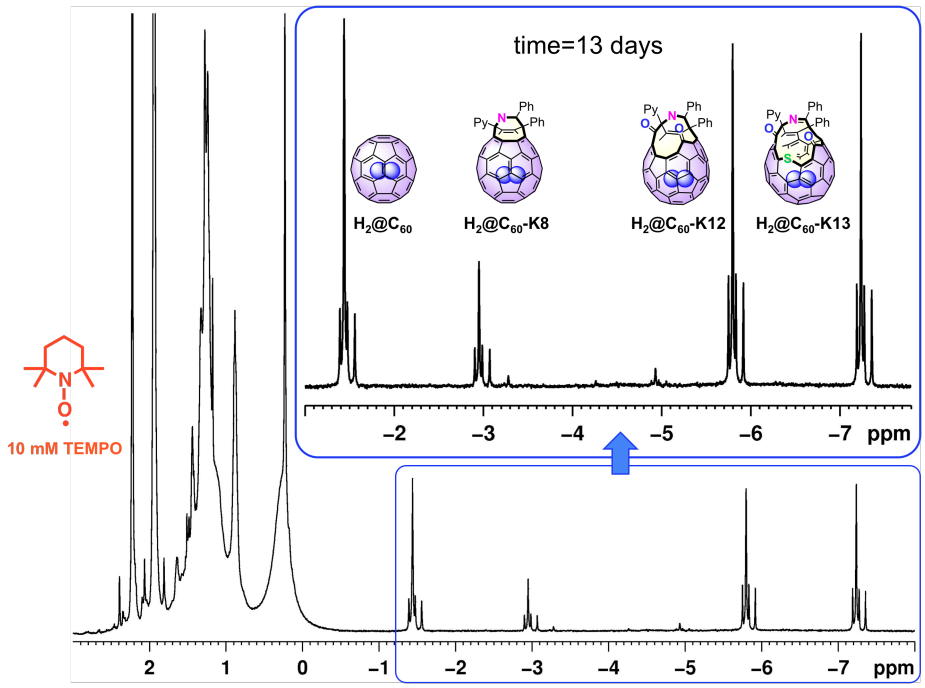

Figure 2.33: ^{1}H NMR of *para*-enriched oH$_2$*@open-C$_{60}$ with 10 mM TEMPO in ODCB at 300 K. Time = 13 days.

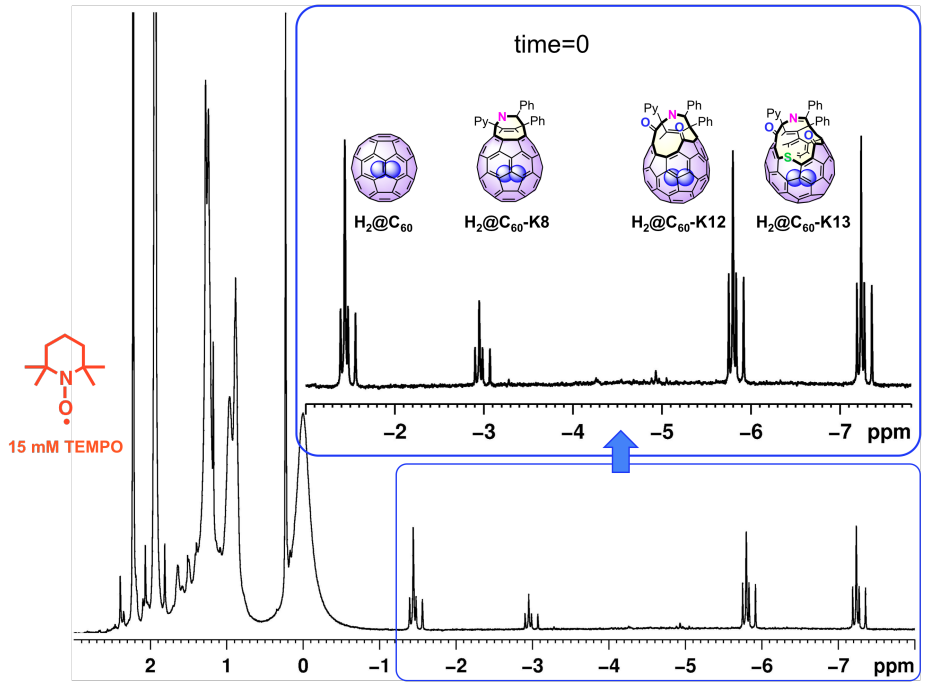

Figure 2.34: ^{1}H NMR of *para*-enriched oH$_2$*@open-C$_{60}$ with 15 mM TEMPO in ODCB at 300 K. Time = 0.

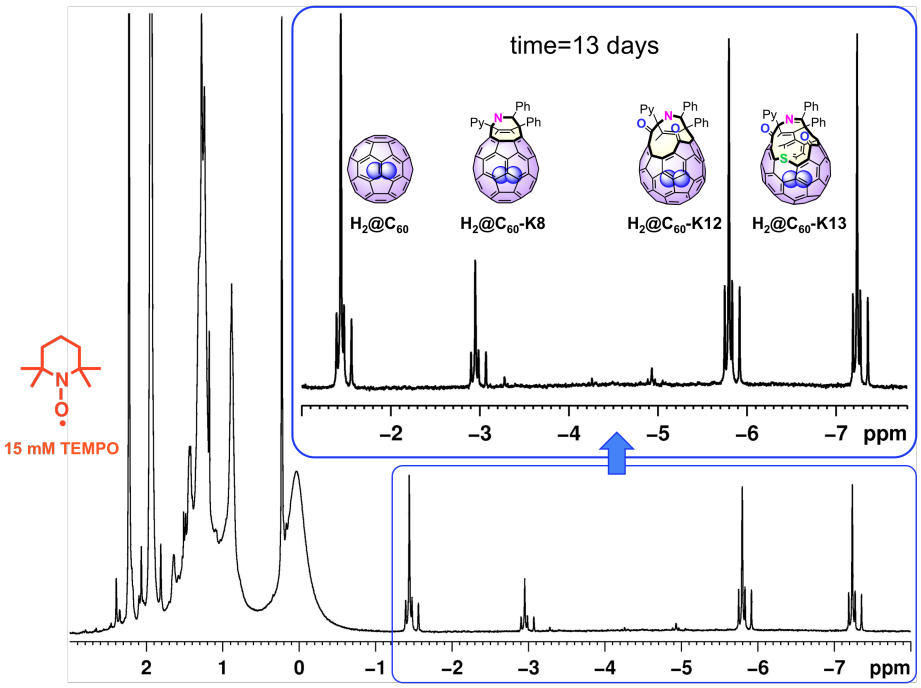

Figure 2.35: ^{1}H NMR of *para*-enriched oH$_2$*@open-C$_{60}$ with 15 mM TEMPO in ODCB at 300 K. Time = 13 days.

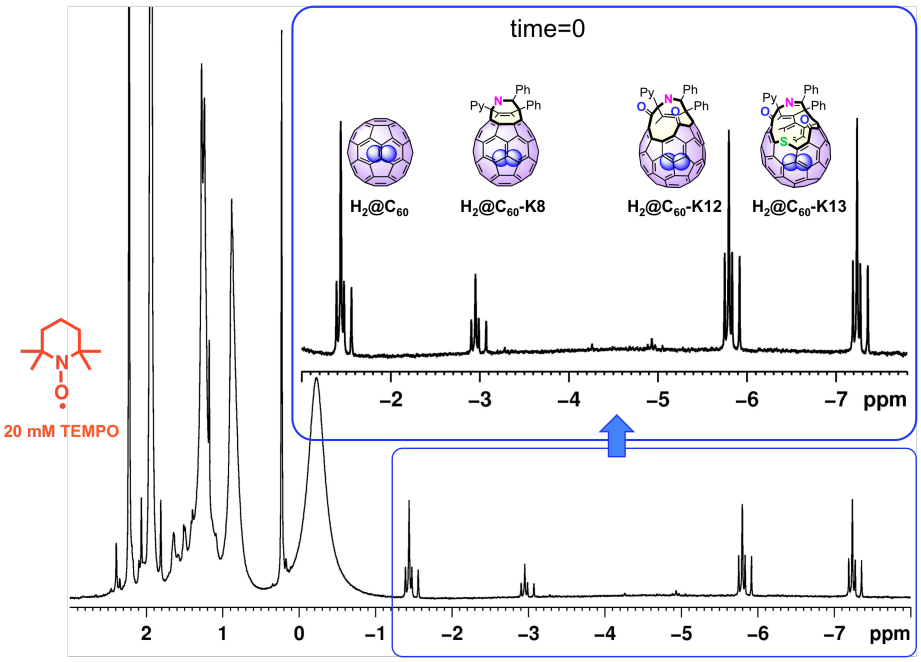

Figure 2.36: ^{1}H NMR of *para*-enriched oH$_2$*@open-C$_{60}$ with 20 mM TEMPO in ODCB at 300 K. Time = 0.

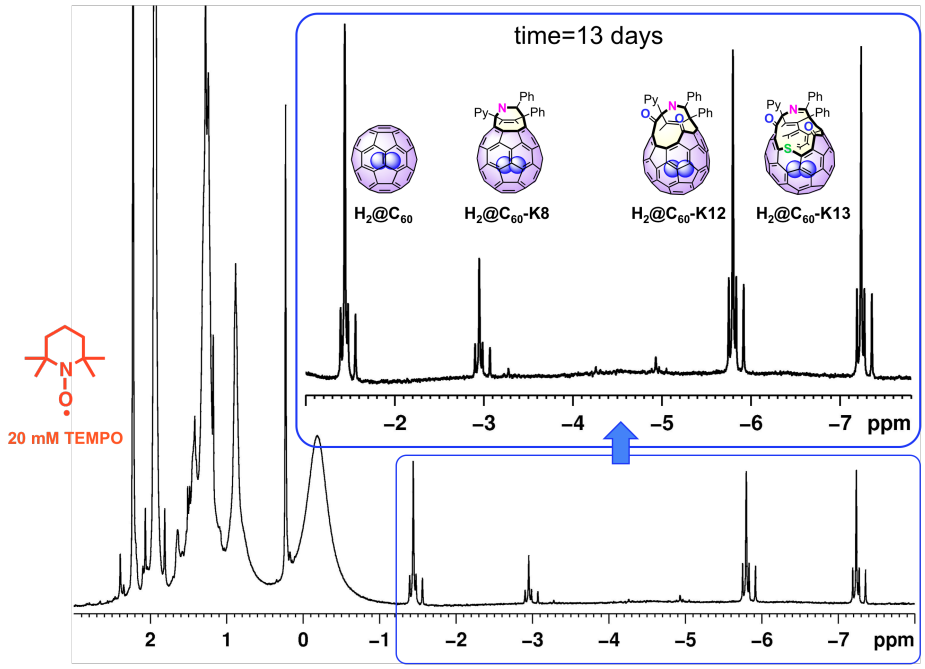

Figure 2.37: ^{1}H NMR of *para*-enriched *o*H_2*@open-C_{60} with 20 mM TEMPO in ODCB at 300 K. Time = 13 days.

2.6 References

(1) Aroulanda, C. Starovoytova, L.; Canet, D. Longitudinal nuclear spin relaxation of ortho- and para-hydrogen dissolved in organic solvents. *J. Phys. Chem. A* **2007**, *111*, 10615-24.

(2) Unpublished work by Dr. Michael Frunzi.

(3) *Solubility Data Series Vol. 2: Krypton, Xenon and Radon- Gas Solubilities*; Kertes, A. S.; Clever, H. L., Eds. Pergamon Press: Oxford OX3 0BW, England, 1979; p. 178.

(4) Chuang, S.-C. Murata, Y. Murata, M.; Komatsu, K. An orifice-size index for open-cage fullerenes. *J. Org. Chem.* **2007**, *72*, 6447-53.

(5) Turro, N. J. Martí, A. A. Chen, J. Y.-C. Jockusch, S. Lawler, R. G. Ruzzi, M. Sartori, E. Chuang, S.-C. Komatsu, K.; Murata, Y. Demonstration of a Chemical Transformation Inside a Fullerene. The Reversible Conversion of the Allotropes of H2@C60. . *J. Am. Chem. Soc.* **2008**, *130*, 10506-10507.

(6) Li, Y. Lei, X. Jockusch, S. Chen, J. Y.-C. Frunzi, M. Johnson, J. a; Lawler, R. G. Murata, Y. Murata, M. Komatsu, K.; Turro, N. J. A magnetic switch for spin-catalyzed interconversion of nuclear spin isomers. *J. Am. Chem. Soc.* **2010**, *132*, 4042-3.

(7) Li, Y. Lei, X. Lawler, R. G. Murata, Y. Komatsu, K.; Turro, N. J. Distance-Dependent para- $H_2 \rightarrow$ ortho-H_2 Conversion in $H_2@C_{60}$ Derivatives Covalently Linked to a Nitroxide Radical. *J. Phys. Chem. Lett.* **2011**, *2*, 741-744.

(8) Levanon, H. Meiklyar, V. Michaeli, A. Michaeli, S.; Regev, A. Paramagnetic states and dynamics of photoexcited fullerene C_{60}. *J. Phys. Chem.* **1992**, *96*, 6128-6131.

(9) Arbogast, J. W. Darmanyan, A. P. Foote, C. S. Diederich, F. N. Whetten, R. L. Rubin, Y. Alvarez, M. M.; Anz, S. J. Photophysical properties of sixty atom carbon molecule (C60). *J. Phys. Chem.* **1991**, *95*, 11-12.

(10) López-Gejo, J. Martí, A. A. Ruzzi, M. Jockusch, S. Komatsu, K. Tanabe, F. Murata, Y.; Turro, N. J. Can H_2 inside C_{60} communicate with the outside world? *J. Am. Chem. Soc.* **2007**, *129*, 14554-5.

(11) Gastel, M. van Zero-field splitting of the lowest excited triplet states of C_{60} and C_{70} and benzene. *J. Phys. Chem. A* **2010**, *114*, 10864-70.

(12) Ausman, K. D.; Weisman, R. B. Kinetics of Fullerene Triplet States. *Res. Chem. Int.* **1997**, *23*, 431-451.

(13) Frunzi, M. Jockusch, S. Chen, J. Y.-C. Calderon, R. M. K. Lei, X. Murata, Y. Komatsu, K. Guldi, D. M. Lawler, R. G.; Turro, N. J. A Photochemical On-Off Switch for Tuning the Equilibrium Mixture of H_2 Nuclear Spin Isomers as a Function of Temperature. *J. Am. Chem. Soc.* **2011**.

(14) Matsumoto, M.; Espenson, J. H. Kinetics of the interconversion of parahydrogen and orthohydrogen catalyzed by paramagnetic complex ions. *J. Am. Chem. Soc.* **2005**, *127*, 11447-53.

(15) Ellison, E. H. Adsorption and photophysics of fullerene C_{60} at liquid-zeolite particle interfaces: unusually high affinity for hydrophobic, ultrastabilized zeolite Y. *J. Phys. Chem. B* **2006**, *110*, 11406-14.

(16) Sastre, G. Cano, M. L. Corma, A. García, H. Nicolopoulos, S. González-Calbet, J. M.; Vallet-Regí, M. On the Incorporation of Buckminsterfullerene C_{60} in the Supercages of Zeolite Y. *J. Phys. Chem. B* **1997**, *101*, 10184-10190.

(17) Kreilick, R. W. NMR Studies of a Series of Aliphatic Nitroxide Radicals. *J. Chem. Phys.* **1967**, *46*, 4260.

3 Spin Lattice Relaxation T_1

Only the *ortho*-H_2 ($o$$H_2$) allotrope is discussed in this chapter: the ^{1}H-NMR-active H_2 and HD isotopologues. All spins discussed here are spin ½ unless otherwise specified. Relaxation is essential for the success of a spin resonance experiment otherwise the absorption line becomes completely saturated (equal population of the upper and lower states) unless the spin system can give up its excess Zeeman energy to its surrounding, "lattice" (solvent, matrix, crystalline environment). Every molecule interacts with its surroundings and that interaction limits the lifetimes of the spin states. This is reflected in the line shape in the magnetic resonance spectra.

3.1 Background

Resonance absorption can be detected only if there is a population difference between the two spin levels, so in the absence of an external magnetic field the populations, N_α and N_β of the spin states, α and β are equal; therefore, no signal will be observed. In terms of spins, there is no physical distinction between the z direction and any other direction in the absence of a field, so M_x and M_y decay to zero at the same rate as M_z [Figure 3.1 (a)].

In the presence of a magnetic field, H_0 along the z-axis, H_z [Figure 3.1 (b)] and according to Boltzmann's law, the populations of the two spins states differ by only one part in 10^5 and nuclear resonance absorption is relatively weak; however, M_z no longer vanishes in thermal equilibrium and approaches a steady value M_0. Given an rf pulse, or stimulation transition, in which the probabilities of upward and downward transitions are equal, the populations are flipped, now the excited state has an excess population that

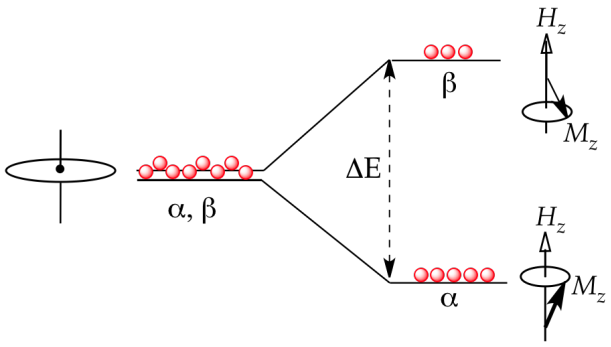

Figure 3.1: Proton spin levels and corresponding populations (red balls) and the spin net magnetic moment vector (M_z) in (a) absence of magnetic field and (b) in the presence of a magnetic field, H_z.

needs to reestablish thermal equilibrium. This requires that there are interactions between the nuclei and their surroundings which cause the spin orientation to change while the excess magnetic energy is transferred to other degrees of freedom, or its surroundings. In spin language, the changes of M_z need an exchange of Zeeman energy with the surroundings. This process of nonradiative transition between the two states, $|\alpha\rangle$ and $|\beta\rangle$ is called *spin-lattice relaxation*. The name was originated from solid state studies where nuclear spins in a solid transfer energy to other degrees of freedom, including the vibrations of the crystal lattice, each time a spin turns over. The references to lattice here refer to the physical systems which concern us or the immediate surroundings, rather than directly concerned with spin. Spin relaxation is possible because the spin system is coupled to the thermal motions of the "lattice," be it gas, liquid or solid state. The important point is that the lattice is at thermal equilibrium; this means that the probabilities of spontaneous spin transitions up and down are *not* equal, as they were for rf induced transitions and that the former has a characteristic time dependence, T_1. T_1 is called the

"spin-lattice relaxation time." It is a measure of the time taken for energy to be transferred to other degrees of freedom, that is, for the spin system to approach thermal equilibrium. Large values of T_1 are on the order of minutes or even hours for some nuclei, indicating very slow relaxation and a very long NMR experiment or none at all.

Because of spin relaxation the spin states have a finite lifetime and its corresponding line width due to spin-lattice relaxation is on the order of $1/T_1$. However, other mechanisms also contribute to line broadening which have the effect of varying the *relative energies* of the spin levels, rather than their lifetimes. These processes are irreversible and are dependent on the transverse components of the magnetic moment, M_x and M_y and are characterized by a relaxation time T_2. This decay time is generally different from T_1 because it does not alter the total Zeeman energy and is called the transverse relaxation time, homogeneous decay or spin-spin relaxation time. The reference to spin-spin relaxation is misleading because the process (transverse magnetization decay) does not require interactions between the nuclear spins. All that it requires is that the different spins experience slightly different magnetic fields so that they precess at a slightly different frequency. T_1 and T_2 are closely related because both modes of relaxation depend on the same interaction between the spins and their surroundings.

To understand the relationship between the relaxation times T_1 and T_2 and the effect of random fields, one needs to believe two things about the basic magnetic resonance experiment: (1) A field along the z direction causes spins in the x-y plane to move about the z-axis at a frequency that is proportional to the field (the "Larmor frequency"). That is true even if the field varies randomly with time. (2) Spins oriented along the z-axis can be rotated in the z-direction, ±z, by applying a field in the x-y plane. This is basically the same as (1) but with different orientations of the spin and field. More importantly, the movement of the spins in the ±z-

direction, called “spin flips” is most effective when the field in the x-y direction is varying at the same frequency as the spins are rotating about the z-axis (Larmor frequency again). This is, after all, the basic idea of magnetic resonance: absorbing radiation applied perpendicular to a static field at the frequency at which the spins are rotating about the z-axis. Relaxation comes into the picture simply because of the presence of random fields from a variety of sources. These fields may arise from magnetic dipoles (dipole-dipole interaction), magnetism due to molecular rotation (spin-rotation interaction), changes in shielding of the nuclei by electrons (chemical shift anisotropy) or other sources.[1]

The random fields affect spins in the z-direction or x-y plane differently. In particular, a distribution of fields in the z-direction will cause spins experiencing different fields to rotate at different frequencies and eventually destroy any net spin orientation in the x-y plane. This is transverse relaxation, i.e., a T_2 effect. It could be due, for example to having nuclei sit at different fixed angles relative to each other as in a solid, or even to having a distribution of external fields (magnet inhomogeneity). The result is broad lines and fast free-induction decay. A time-dependent random field in the z-direction will also contribute to T_2.

Random fields in the x-y plane will flip spins. This corresponds to longitudinal relaxation, i.e., a T_1 effect. The difference in this case, however, is that the random fields will be most effective if they are varying at the Larmor frequency. This, along with the conclusion from the last paragraph yields the oft-quoted rule that T_2 is equal to or shorter than T_1. The requirement that random fields varying at the Larmor frequency contribute most effectively to T_1 leads directly to the need for a way of describing the distribution of frequencies in a selection of random, time-dependent fields. This is where the spectral density function, or power spectrum, comes into play. A collection of randomly tumbling molecules, for example, might produce a

distribution of magnetic fields over a range of frequencies, with some average probability of having a field at a particular frequency. One can visualize this in the same way as one visualizes an NMR free-induction decay (FID): The FID consists of a distribution of frequencies with different probabilities, corresponding to each of the peaks in the NMR spectrum. As in the analysis of an FID, the process of determining the distribution of random fields at different frequencies involves taking the Fourier transform of a time-dependent function. In the case of random processes this function is called the auto-correlation function, *G*, and is given in Equation 3.1.

Equation 3.1

$$G(\tau) = \overline{f^*(t) f(t)}\; e^{-|\tau|/\tau_c}$$

Note that, just like an FID, *G* decays in time as the fields move randomly, i.e., they become "uncorrelated". The decay time in this case is called the "correlation time" denoted τ_c. The spectral density function, usually called *J*, is a function of the frequency. In the case of an NMR spectrum, the frequency spectrum is obtained by taking the Fourier transform of the FID. By analogy, *J* is obtained by taking the Fourier transform of *G* as in Equation 3.2

Equation 3.2

$$J(\omega) = \int_{-\infty}^{+\infty} G(\tau) e^{i\omega\tau} d\tau$$

In fact, a typical power spectrum $J(\omega)$ looks just like an NMR peak!

The final link is the connection between *J* and T_1. This requires that one assumes the results of perturbation theory where T_1, or more accurately the rate coefficient $1/T_1$, is described in terms of the action of an average perturbing potential, $\left|V_{\alpha\beta}\right|$ or field, H_x^*, H_y^* (depending how the equation is expressed, see Equation 3.3), over some average time. The potential or field depends on the details of the interaction, e.g. dipole field varies as $1/r^3$, it also depends on the sizes of magnetic moments and results in a corresponding rotation of the spins in the z-direction at some

perturbing frequency. The "time" part of it corresponds to the spectral density function, or for small Larmor frequencies, just the correlation time.

Equation 3.3 $\frac{1}{T_1} = \frac{2}{\hbar^2}\overline{\left|V_{\alpha\beta}\right|^2} J(\omega)$ where $J(\omega) = \frac{2\tau_c}{1+\omega^2\tau_c^2}$ and $V_{\alpha\beta} = \frac{1}{2}\gamma\hbar(H_x^* + iH_y^*)$

Note that in all cases the rate coefficient, or transition probability $1/T_1$ in see Equation 3.3 is proportional to the square of the perturbing frequency ω, i.e. how fast the spins are flipped by the field in the x-y plane, and also proportional to an average time over which the field acts. The fact that the square of the frequency is involved might be explainable if one thinks of it instead as $\omega\left(\frac{\omega}{1/t}\right)$ where 1/t corresponds to a frequency that can be compared with the perturbation ω. The larger the dimensionless ratio of ω to 1/t, the higher the probability that the perturbation will have an effect and the larger the probability per unit time of a change (the relaxation rate).

Also shown in eqn. 3, the transition probability, i.e., $1/T_1$, is proportional to J meaning that relaxation is most effective when $\omega = 2\tau_c$. As shown in Equation 3.3 the width of J is determined by $1/\tau$. So a sharp power spectrum, i.e., one that operates over a narrow frequency range, corresponds to a long τ_c. In addition, the maximum value also increases since it goes up with τ_c. This is similar to an "uncertainty principle" effect where the longer one has to look at a frequency the less uncertain its value becomes. Just the opposite holds for a broad power spectrum (Figure 3.2).

In summary, in order to have a successful relaxation, two conditions are necessary.

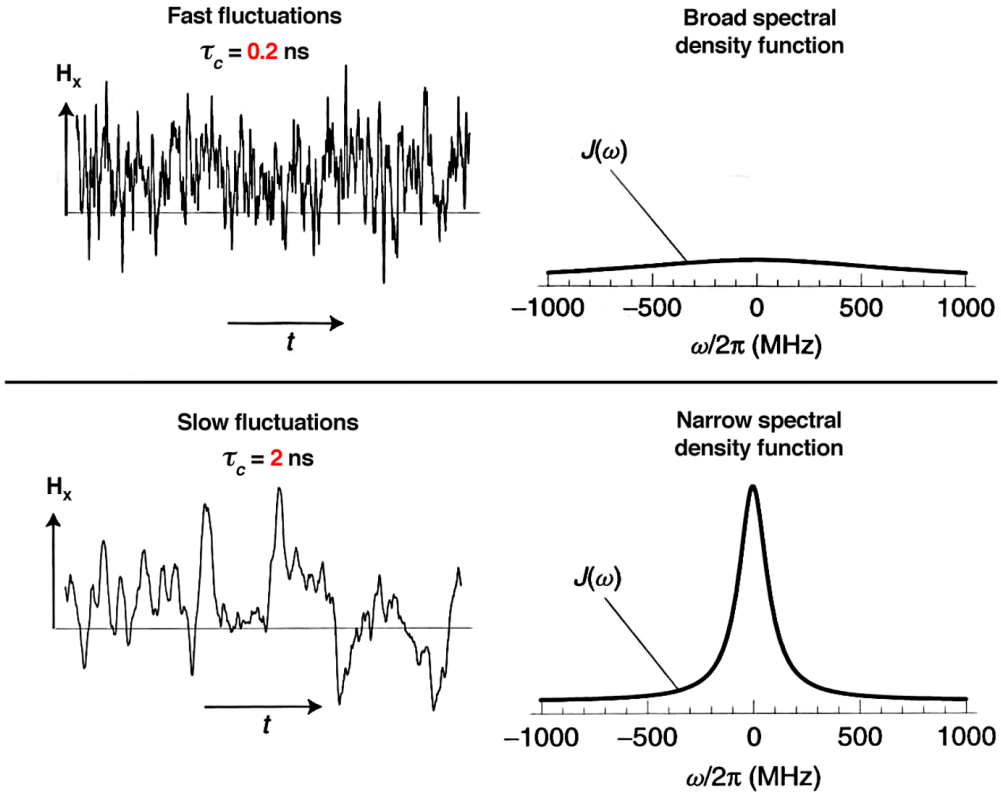

Figure 3.2: Spectral density functions. Top: A rapidly fluctuating transverse field results in short correlation time, τ_c and the spectral density function, $J(\omega)$, is broad. Bottom: A slow fluctuating transverse field results in long τ_c and $J(\omega)$ is narrow. Figure adopted from Spin Dynamics by Malcolm H. Levitt.

First, there must be some interaction which acts directly on the spin; second, it must be time-dependent. Any static interactions are simply reflected as a shift in the positions and intensities of the spectral lines without broadening them. For example, these time-dependent interactions may be as a result of (1) local magnetic fields from the spins of other nuclei moving past it, (2) from unpaired electrons, or (3) from spin-rotation interactions with which the molecular rotation itself generates magnetic fields at the nucleus. There may also be (4) chemical shielding of the nucleus as a molecule rotates and these modulate the total effective field which acts on the spin.

In addition to the aforementioned conditions, it is also essential that the molecular motions have suitable time scale. The time scale for magnetic resonance is slow and interactions at a rate much faster than the magnetic resonance frequency (10^{10} Hz for electrons and 10^{7} Hz for nuclei) have little effect on relaxation. Thus electronic motions and molecular vibrations are relatively unimportant. On the other hand, interactions that cause transitions between the α and β spin states and fluctuate strongly at the nuclear resonance frequency ω_0 produce powerful spin-lattice relaxation and line broadening. Another class of interactions contributes to the line width T_2 but not T_1 and these are random forces which modulate the spin energy levels at low frequencies without causing transitions between them.

The above description is consistent with the derivation of standard formulas for relaxation times, including this thesis and other papers that we've published on T_1 effects in the fullerenes.[2,3,4] The formulas vary mainly in variations in the types of perturbing fields (or frequencies) that are possible, or the way that the autocorrelation function (and therefore spectral density) is described.

It is now important to discuss in detail the mechanisms that gave rise to the perturbing fields resulting in the observed spin-lattice relaxation. In our study, these perturbing fields were as a result of intramolecular dipolar interactions and the spin-rotation magnetic interactions.

3.2 Dipole-dipole Interaction / Intramolecular Dipolar Interaction

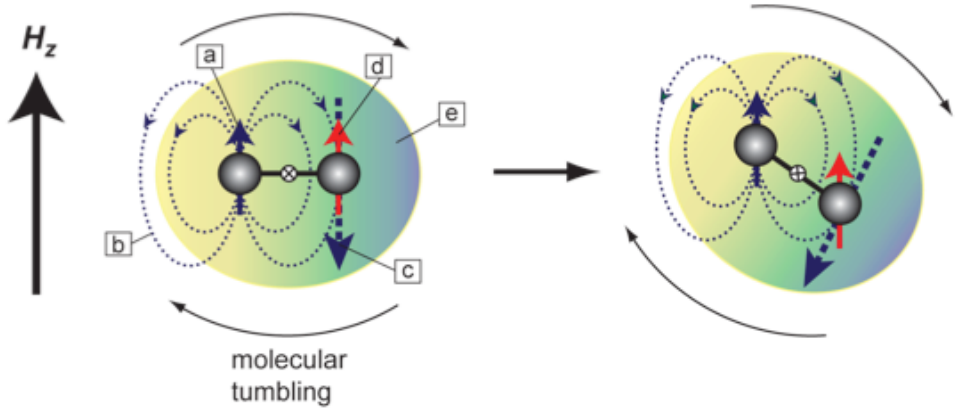

Figure 3.3: Illustration of dipole-dipole interaction. Each gray ball represents a nucleus. [**a**] source spin (blue), [**b**] magnetic field contours (dotted blue lines), [**c**] field at the detecting spin (dotted blue arrow), [**d**] detecting spin (red) and [**e**] molecule including delocalized electron cloud.

In general, a dipolar interaction involves the direct dipole-dipole coupling between two nuclear spins in the same molecule. It is the fluctuation in the magnetic field caused by the thermal motions as the molecule tumbles and changes the magnitude and direction of the magnetic field exerted by one spin on the other (**Figure 3.3**). The three aspects of the dipole-dipole (d-d) interactions as shown in **Figure 3.3** are: (1) the spin producing the field [**a**], (2) the spin detecting the field [**d**] and (3) the field itself [**c**].

3.3 Spin-rotation Magnetic Interaction

Spin-rotation magnetic interaction (s-r) is generally less important because it is a weaker interaction than the dipole-dipole interaction mentioned above. Spin-rotation interactions are wobbling in the local magnetic field felt by the proton spins as the molecules (that carries these protons) undergo constant rotational motion such that at any instance in time the orientation of

each molecule in space and its relative positions are constantly changing (**Figure 3.4**). For example, a methyl group twirls around the bond connecting it to the rest of a molecule; the nuclei and the bonding electrons circulate around the bond axis thereby generating a local magnetic field. The field will fluctuate as the result of collisions and thereby produce frequency components that can induce relaxation. The cartoon in **Figure 3.4** demonstrates another example with hydrogen molecules. The positive and negative charges rotating together about a detection spin which produces magnetic fields in opposite directions, the net result being the field due to rotation of the molecule about the detection spin (a and b in **Figure 3.4**). This is not strictly correct because the actual rotation is about the center of mass, i.e. the middle of the bond, as was indicated in **Figure 3.3** for d-d interaction. In any case, the cartoon illustrates the basic idea. In addition spin-rotation is usually important only for small molecules in nonviscous solvents.

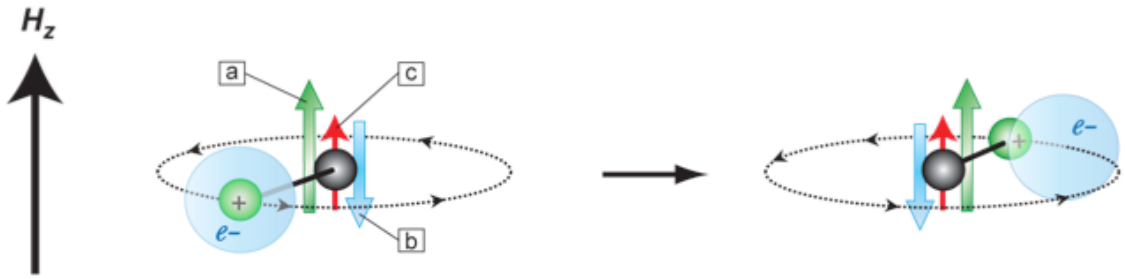

Figure 3.4: Illustration of spin-rotation magnetic interaction. [a] field from positive rotation nuclei (Green), [b] field from negative rotation electron {blue), [c] detecting spin (red).

Both of the cartoons in **Figure 3.3** and **Figure 3.4** illustrate the qualitative classical picture of the hydrogen molecule, H_2 spin relaxation mechanisms. It is important to keep in mind, however, that both relaxation mechanisms operate through the anisotropic part of the interaction, i.e., the d-d and s-r fields depend on angle and therefore fluctuate as the molecule rotates. It's the fluctuating part of the internal fields that induces the transitions corresponding to relaxation. At

the quantum mechanical level, the s-r mechanism becomes stronger at high temperatures because the higher rotational states, J, with correspondingly larger s-r fields, become more populated. The angular momentum correlation time decreases with increasing temperature, just as the reorientation time does. By itself, that would lead to a longer T_1 from the s-r mechanism as temperature increases, just as what happens with the d-d mechanism (**Figure 3.5**). Both of these two processes originate from the overall rotation of the hydrogen molecule but in our model, we assume that they are independent of each other.

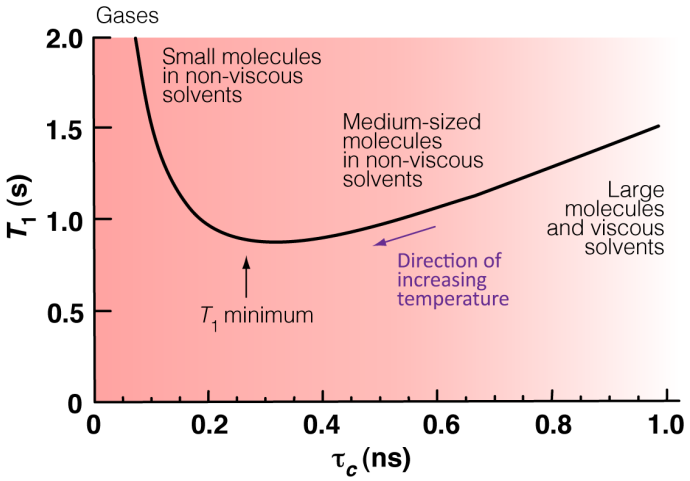

Figure 3.5: Spin-lattice relaxation time constant, T_1 as a function of correlation time, τ_c for random field fluctuations. Generally, τ_c decreases by warming the sample since an increase in temperature corresponds to more rapid molecular motion. Conversely, τ_c increases by cooling the sample. Typical ranges for τ_c are also shown.

3.4 Results and Discussion

Chart 3.1: Structures of endofullerenes pertaining to Chapter 3.

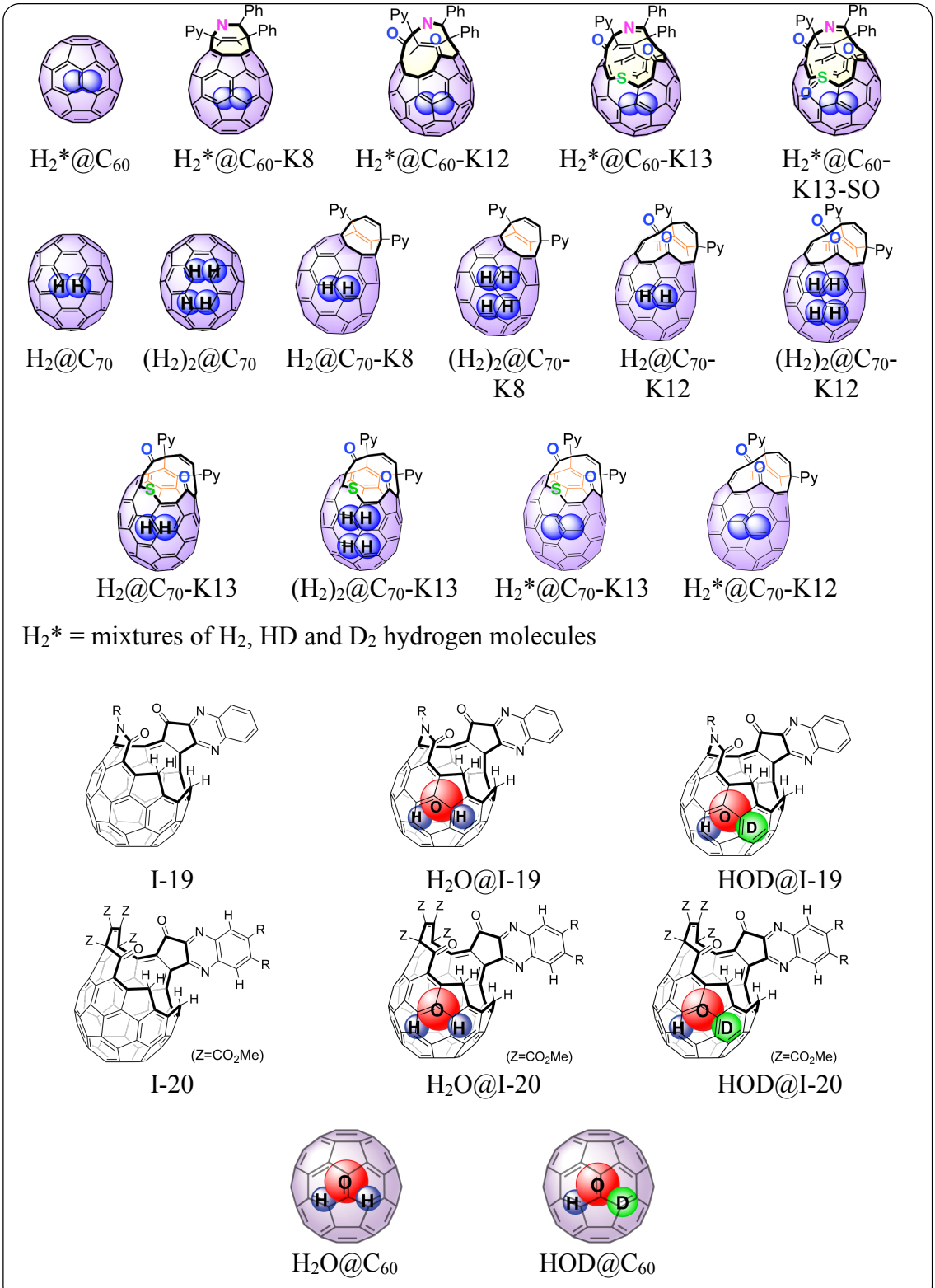

3.4.1 T_1 of $H_2@C_{60}$ and $HD@C_{60}$

In our previous work, we compared the proton spin-lattice relaxation time, T_1, for H_2 in several organic solvents with that in $H_2@C_{60}$ dissolved in the same solvents at 300 K.[5] It allowed us to compare the nature of interactions of a fleeting (transient) guest H_2 molecule confined within the walls of a solvent cavity and a permanent guest H_2 molecule that is encapsulated within the wall of the C_{60} cavity (Figure 1.1). We found that (1) the values of T_1 of H_2 and $H_2@C_{60}$ varies with solvent although a correlation between the values of T_1 and viscosity or dielectric constant of the solvent could not be found. (2) The values of T_1 are 10-20 times smaller for $H_2@C_{60}$ than for H_2 even though the ratios of T_1 for H_2 and $H_2@C_{60}$ are similar in all the solvents. (3) The T_1 values for both H_2 and $H_2@C_{60}$ do not significantly change in going from a protonated to a deuterated solvent which means that the dominating interactions determining the H_2 and $H_2@C_{60}$ nuclear relaxation mechanism must be *intra*molecular.

We also studied the temperature dependence of T_1 ranging from 200-330 K for H_2 and $H_2@C_{60}$ in toluene-d_8. The most striking feature of the data is its hyperbola shape ($-x^2$) with maximum for T_1 at ~ 240 K for both H_2 and $H_2@C_{60}$. The observation of a maximum had been reported previously for small molecules in solution[6] and in the only study of the temperature dependence of the H_2 relaxation in a homogeneous molecular solvent (D_2O), the value of T_1 was found to increase as the temperature increased in the range 283-323 K.[7] Intramolecular dipole-dipole interaction and spin-rotation interactions are known to be responsible for the relaxation of gaseous H_2; therefore it is likely that the relaxation of H_2 in solution also depends on the competition between intramolecular dipole-dipole interaction and spin-rotation interaction at temperatures below and above 240 K. Thus, the results were analyzed and explained assuming the relaxation was based on these two mechanisms at high and low

temperatures; however, we were unable to attain quantitative fit to the T_1 over the full temperature range using existing theories: Hubbard theory[8] for relaxation in liquids or the Schwinger-Bloembergen[9,10] theory of relaxation in slowly equilibrating rotational states of H_2.

In general, the characteristic shape of the spin lattice relaxation rate ($1/T_1$) as a function of temperature for H_2 and $H_2@C_{60}$ can be separated into three regions: (1) a decrease of the relaxation rate at low temperature attributed to the decrease of dipolar contribution as the temperature increases, (2) then a plateau indicating that both the dipolar and spin-rotation mechanisms offset each other, and finally (3) at high temperature, a predominance of spin-rotation with an increase in the rate of relaxation with increasing temperature.

To understand further dynamics and temperature dependence of T_1 of $H_2@C_{60}$, we introduced HD into our system. By using HD, we can investigate the assumption made before treating the two relaxation mechanisms independently operating at high and low temperatures for H_2 and $H_2@C_{60}$ by examining changes in the following properties relative to H_2: (1) the magnetic parameters of HD[11] are very different from those for H_2, deuterium has a smaller magnetic moment which will affect the magnitude of the dipolar interaction. (2) The moments of inertia between H_2 and HD are different which leads to different rotational energy spectrum and rotational state populations.[12] For example, the rotational magnetic moments of H_2, HD, and D_2 in rotational level with J=1 were found to be 0.883, 0.660 and 0.443 nuclear magnetons, respectively. These figures in the ratio of 4:3:2.[13] (3) The increase in the mass of HD and the shift of center of mass changes the average position of the proton in HD relative to H_2 in the solvent or within the fullerene cage and affects the interaction of the molecule with the surrounding medium.

First, we repeated the same experimental procedure for H_2 and $H_2@C_{60}$ in toluene-d_8 as mentioned above, their ^1H NMR signal and relaxation rates, $1/T_1$ are shown in **Figure 3.6** and colored in red. These new values are indistinguishable from those reported previously.[5]

The ^1H NMR signals and relaxation rates for HD and $HD@C_{60}$ are colored in blue (**Figure 3.6**). Column (a) of **Figure 3.6** shows a typical spectrum of the H_2/HD mixture dissolved in toluene-d_8 (top) and incarcerated inside the C_{60} cavity (bottom). **Figure 3.6** (b) shows the values of the relaxation rate, $1/T_1$, for H_2 and HD in toluene-d_8 (top graph) and in C_{60} (bottom graph) over the temperature range 200-340 K.

In the case of HD in toluene-d_8 and $HD@C_{60}$, the T_1 values determined for each signal of the HD triplet were the same within the experimental error, and only the average value is used for plots in **Figure 3.6** (b). The value of the relaxation rate for HD [left axis of **Figure 3.6** (b)] is consistently smaller than that for H_2 [right axis of **Figure 3.6** (b)] and whereas the H_2 relaxation in both media as a function of temperature passes through a shallow minimum, the relaxation rate for HD increases monotonically with temperature.

The above observations support the changes in properties mentioned in Section 3.4.1 in going from H_2 to HD and the qualitative idea that relaxation of ^1H in HD is dominated by the spin-rotation interaction over the entire temperature range studied. This is in contrast to H_2, where the dipole-dipole interaction between the protons becomes of

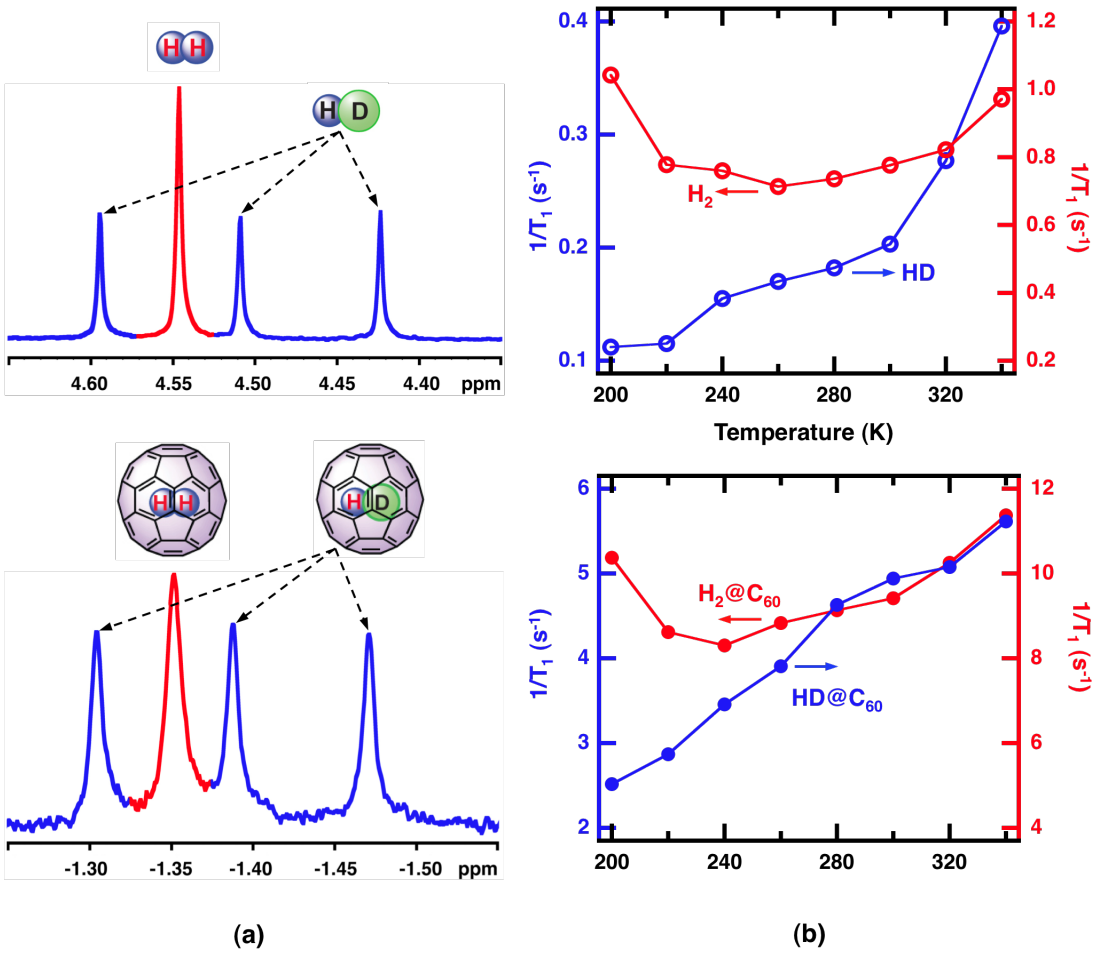

Figure 3.6: ^{1}H NMR spectra (a) and relaxation rates, $1/T_1$ (b) of toluene-d_8 solution of a H_2/HD mixture (top) and a toluene-d_8 solution of H_2/HD@C_{60} mixture (bottom). Estimated errors in relaxation rates are within the width of the symbols on the plots.

greater importance than the spin-rotation interaction at low temperatures. The observations for HD are consistent with the 6-fold decrease in the magnitude of the ^{2}H magnetogyric ratio, which greatly reduces the dipole-dipole interaction. As expected, the spin-rotation interaction becomes increasingly effective at high temperature. The substantial enhancement of the relaxation rate of HD in the C_{60} cage, parallel to that which was observed for H_2 may be similarly attributed to the reduced mobility of the incarcerated hydrogen molecule. An in-depth theoretical treatment in which the standard formula shown in Equation 3.3 is modified to reflect the types of perturbing

fields (or frequencies) that are possible, or the way that the autocorrelation function (and therefore the spectral density) is described can be found in the published manuscript.[3]

3.4.2 T_1 of H_2@open-C_{60} and HD@open-C_{60}

Since the magnitude of T_1 between free H_2, HD isotopologues ($^{1,2}H_2$) and $H_2@C_{60}$, HD@C_{60} isotopologues ($^{1,2}H_2@C_{60}$) are significantly different because of extreme degrees of confinement where in one case $^{1,2}H_2$ is loosely confined within the walls of the solvent cavity and in the other $^{1,2}H_2@C_{60}$ is permanently confined inside the walls of C_{60} cavity. We became interested in the modulation of the exposure of $^{1,2}H_2$ between these two extremes and how it affects T_1. Incidentally, in the synthesis from C_{60} to $^{1,2}H_2@C_{60}$, there are three stable hydrogen-containing open fullerene intermediates with different sized orifices. These are $^{1,2}H_2@C_{60}$-K13, $^{1,2}H_2@C_{60}$-K12 and $^{1,2}H_2@C_{60}$-K8 with 13, 12 and 8 member ring orifices, respectively (Chart 3.1). **Figure 2.5** shows the ^{1}H NMR of each of these species in one single mixture. Each of the species is well separated from the other and the chemical shift moves upfield from -7.25 ppm ($H_2@C_{60}$-K13), -5.8 ppm ($H_2@C_{60}$-K12), -2.95 ppm ($H_2@C_{60}$-K8) to -1.44 ppm ($H_2@C_{60}$) as the size of the orifice decreases. In addition, the HD triplet that accompanies each of the H_2 signals is also well resolved.

The procedure for NMR measurements to determine T_1 is the same as that mentioned in Section 3.5.1.2 for $^{1,2}H_2@C_{60}$. The typical variable delay for measuring H_2 confined inside open fullerene derivatives, denoted H_2@open-C_{60} is in the range of 0.001-2.5 s (Table 3.4. VD1-5) with d1 = 1.5 s and for HD@open-C_{60}, the typical range for variable delay is between 0.001-15 s (Table 2.1.VD4-10) with d1 = 5-15 s.

We chose toluene-d_8 as the solvent of choice because we wanted to (1) keep the data as comparable as possible to previous results and (2) toluene remains as a liquid at 200 K and does

not boil off at 340 K for temperature-dependence measurements. However, C_{60} is not very soluble in toluene (2.8 mg C_{60} / mL)[16,17] and is even less so for open forms; for example, in a mixture containing all four fullerenes, a maximum of 0.7 mg is allowed for each fullerene in a 500 μL NMR solution. The ratio of H_2:HD:D_2 is 50:36:14 and the proton resonance for HD is further split into a triplet. The initial H_2 and HD T_1 results where all the C_{60} open forms and derivatives were in one mixture had poor signal/noise and unacceptable error bars (more than 5%). Therefore, T_1 values were measured

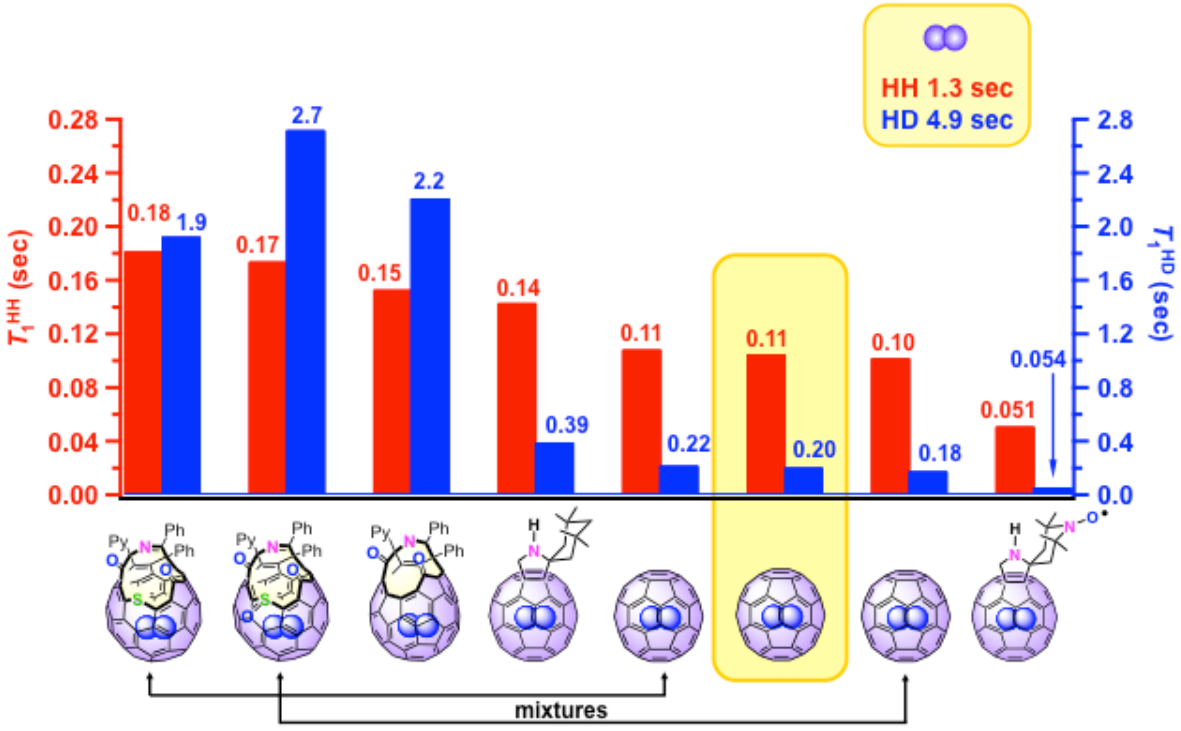

Figure 3.7: Compilation of T_1 data for H_2 (red) and HD (blue) inside open C_{60} and C_{60} derivatives. The data boxed in yellow indicates previous results and are included for comparison with current data. The black arrow on the x-axis indicates mixtures of an H_2*@open-C_{60} and H_2*@C_{60} in which the latter served as a control. All T_1 data are measured in toluene-d_8 at 300K. For nomenclature, please refer to Chart 3.1.

independently for each sample or at most with a mixture of H_2*@C_{60} as control. These results are compiled in **Figure 3.7**.

The T_1 values for $H_2@C_{60}$ (0.11 s, 0.10 s) and $HD@C_{60}$ (0.22 s, 0.18 s) for the mixtures with an open form are within the error limit as previous results (0.11 s for $H_2@C_{60}$ and 0.20 s for $HD@C_{60}$, highlighted in the yellow box); therefore, we are confident with the new values obtained for H_2@open-C_{60} and HD@open-C_{60}. There is a slight increase in T_1 for the externally modified C_{60} (0.14 s) and for the open forms, the T_1 values slightly increases with an increasing size of the orifice. The T_1 value for $H_2@C_{60}$-NO• is 2X faster than $H_2@C_{60}$ and 4X faster for $HD@C_{60}$-NO• than $HD@C_{60}$. Compounds H_2*@C_{60}-NO• and its diamagnetic analog, H_2*@C_{60}-NOH was discussed in detail in Chapter 2. In short, it turned out to be a very nice system for a regimented $o H_2 \leftrightarrow p H_2$ conversion[18] (Section 2.2) and also served as a starting point for a rich platform for studying distance-dependent intramolecular spin relaxation of H_2 by varying the lengths of spacers between the encapsulated H_2 and covalently attached TEMPO functional groups on the outer surface of C_{60} fullerene.[4,19]

3.4.3 T_1 of $H_2@C_{70}$, $HD@C_{70}$ and H_2@open-C_{70}, HD@open-C_{70}

In addition to studying the effect on $^{1,2}H_2$ as a function of the degrees of confinement inside C_{60} and its derivatives, we were also interested in how higher fullerenes affect the relaxation rate coefficient, T_1 for H_2 and HD (Chart 3.1). Our Japanese collaborators also developed the synthesis of H_2 confined inside C_{70} by a molecular surgical method, meaning, quantitative 100% encapsulation of hydrogen molecules by the fullerenes.[20] In the case of C_{70}, 3% of the final product encapsulates two molecules of H_2 per one C_{70}, denoted $(H_2)_2@C_{70}$. Previously published results showed differences in the reactivity of the C_{70} outer cage between singly and doubly incarcerated[20] H_2 as well as the observation of each individual H_2 peak in the NMR spectrum of the doubly occupied $(H_2)_2@C_{70}$-K13 fullerene (Chart 3.1) at temperatures below -80 °C.[21] However, at room temperature, only one signal is observed for $(H_2)_2@C_{70}$ because of rapid

exchange of their relative positions at the NMR time scales, it will nevertheless give us a different result from the singly occupied $H_2@C_{70}$ which will still be interesting.

3.4.3.1 T_1 at 300 K for $H_2@C_{70}$ and H_2@open-C_{70}

Samples of $H_2@C_{70}$ and H_2@open-C_{70} were prepared by dissolving ~1.6 mg of each fullerene separately in 600 μL toluene-d_8. The samples were prepared independently because C_{70} is half as soluble in toluene than C_{60} and we did not want to compromise the S/N especially for the HD triplet and the 3% $(H_2)_2@C_{70}$. However, in a separate experiment where we used ODCB as the solvent, C_{70} was much more soluble and a mixture of $H_2@C_{70}$ containing $H_2@C_{60}$ was prepared, where the latter served as the

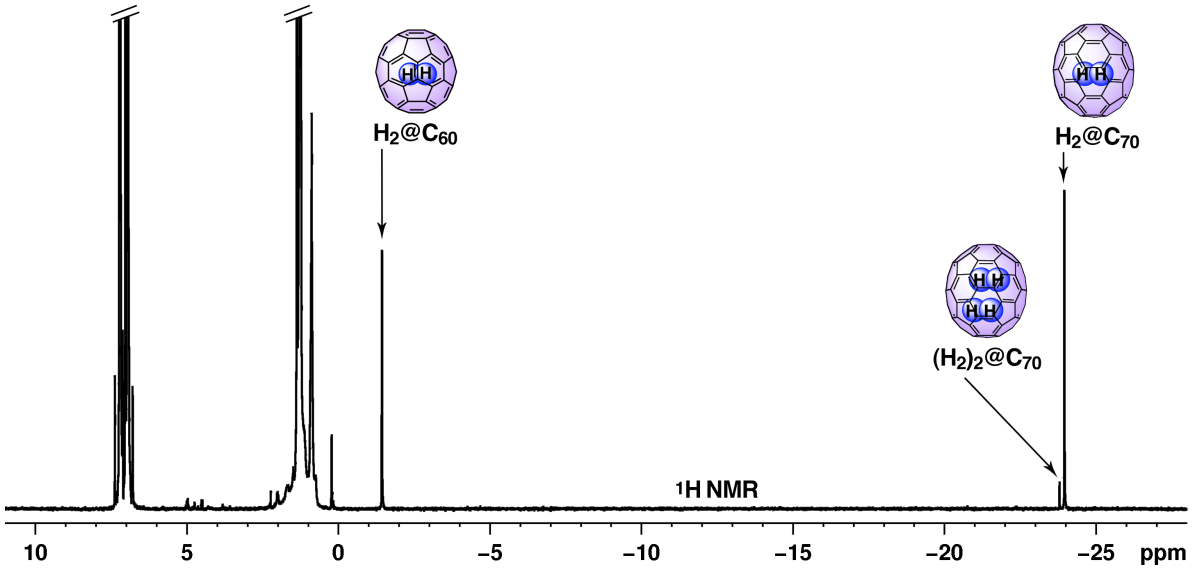

Figure 3.8: 500 MHz ^{1}H NMR spectrum of mixture of $H_2@C_{60}$ (-1.44 ppm), $(H_2)_2@C_{70}$ (-23.80 ppm) and $H_2@C_{70}$ (-23.97 ppm) in 1,2-dicholorbenzene-d_4 at 300 K.

control and T_1 values were determined to be 0.14 s and 0.10 s, respectively (**Figure 3.8**). Table 3.1 compiled some of the typical solvents used in our measurements and its corresponding solubility for C_{60} and C_{70} fullerenes.[16]

Table 3.1: Solubility of C_{60} and C_{70} in Representative Solvents

	mg ml^{-1} at RT	
Solvent	C_{60}	C_{70}
1,2-dichlorobenzene (ODCB)	27.00, 24.60	36.2
Carbon disulfide (CS_2)	7.90, 7.70	9.9
n-Hexane	0.043	0.013
Cyclohexane	0.036	N/A
Toluene	2.80, 2.90	1.4
1,2-Dichloromethane (CH_2Cl_2)	0.5	0.08

The procedure for NMR measurements to determine T_1 is the same as that mentioned in the previous sections. Typical 90° pulse calibration is in the range of 6.2-6.5 μs. The variable delay for measuring H_2 confined inside C_{70} and open-C_{70} (Chart 3.1), is between 0.001-1.5 s (Table 3.4. VD5) with d1 = 1.5-2 s. For HD confined inside C_{70} and open-C_{70}, the typical range for variable delay is between 0.001-5 s (Table 3.4.VD10) with d1 = 10 s. Each experiment time ranged from 48 minutes to 106 minutes depending on the VDLIST, D1 and NS.

Table 3.2 compares T_1 values for H_2 between C_{60}, C_{70} and open-C_{60}, open-C_{70} fullerenes. There is not a significant difference in the T_1 values between H_2 incarcerated inside C_{60}/open-C_{60} and C_{70}/open-C_{70}. For HD, there is also not a significant difference in T_1 between the open-C_{60} and open-C_{70}; however, the T_1 for HD@C_{70} is significantly longer (3.25X) than HD@C_{60}. The very last column on the right has one entry corresponding to the T_1 for doubly occupied H_2 molecules inside C_{70}. Other $(H_2)_2$@open-C_{70} were not observed because the concentrations were below the detection limit.

Table 3.2: Spin Lattice Relaxation Time, T_1 (sec) for $H_2@C_{70}$[a]

	T_1 (sec)			
	H_2	HD	HD/H_2	2 H_2
H_2*@ C_{60}	0.11	0.20	1.8	NA
H_2*@ C_{70}	0.16	0.65	4.1	0.28
H_2*@ C_{60}-K13	0.18	1.9	11	NA
H_2*@ C_{70}-K13	0.14	1.6	11	NA
H_2*@ C_{60}-K12	0.16	2.2	14	NA
H_2*@ C_{70}-K12	0.15	1.8	12	NA

[a] T = 300 K at a field of 11.7 T (500 MHz) in toluene-d_8

3.4.3.2 Temperature dependence of T_1 for $H_2@C_{70}$, HD@C_{70} and $(H_2)_2@C_{70}$

Next, we performed temperature dependence of T_1 ranging from 200-330 K for a mixture containing H_2*@C_{70} (H_2*= H_2 and HD) and $(H_2)_2@C_{70}$ (Chart 3.1) in toluene-d_8 (**Figure 3.9**). The trends shown in **Figure 3.9** indicate that the molecular motion of $^{1,2}H_2$ inside C_{70} fullerene is very different from $^{1,2}H_2$ inside both the solvent cage (toluene) and C_{60}. The dipolar relaxation mechanism appears to operate at a much wider temperature range for $^{1,2}H_2@C_{70}$ [**Figure 3.9** (a) and (b)] as well as for $(H_2)_2@C_{70}$ [**Figure 3.9** (c)] than previous results for $^{1,2}H_2$ in toluene and inside C_{60} cage. In addition, the dipolar relaxation mechanism also appears to be stronger than spin-totation relaxation mechanism for HD@C_{70} than HD in toluene and HD@C_{60} at temperatures below 240 K. At this point, further studies at temperatures below 240K and above 340 K are necessary to make any definite conclusion.

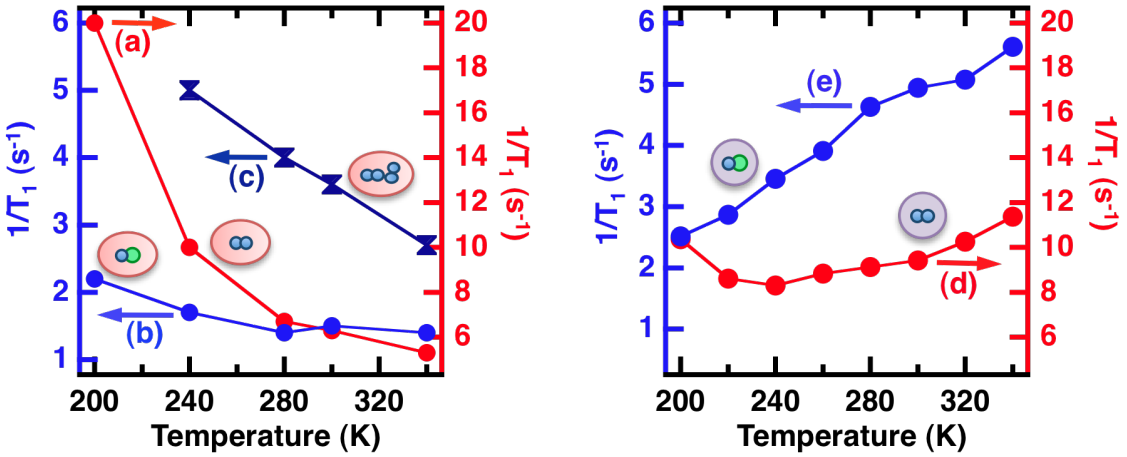

Figure 3.9: Relaxation rates, $1/T_1$ of toluene-d_8 solution as a function of temperature. Left graph: H_2/HD/$(H_2)_2$@C_{70} mixture: (a) H_2@C_{70}, (b) HD@C_{70} and (c) $(H_2)_2$@C_{70}. Right graph on the right correspond to previous results taken from **Figure 3.6** for H_2@C_{60} (d) and HD@C_{60} (e) for comparison. The directions of the arrows indicate corresponding y-axis for each of the plots.

3.4.3.3 Low temperature experiment with H_2@open-C_{70} and $(H_2)_2$@open-C_{70}

Instead of measuring the relaxation rates as a function of temperature for open-C_{70} fullerenes, we investigated its chemical shifts, δ as a function of temperature. It was observed by dynamic low-temperature NMR measurements that the proton singlet (-15.04 ppm) for $(H_2)_2$@C_{70}-K13 (Chart 3.1) at room temperature disappears at around -60°C (213 K) and then reappears as two singlets at -12.87 ppm and -17.38 ppm, respectively, at temperatures below -90°C (183 K) as a result of an exchange between the two H_2 molecules inside C_{70}-K13 [$(H_2)_2$@C_{60}-K13].[21] First we repeated this result with the addition of H_2@C_{70} and $(H_2)_2$@C_{70}. In the ^{1}H NMR spectrum shown in **Figure 3.10**, at 298 K, only one signal was observed for the two encapsulated H_2 molecules of both $(H_2)_2$@C_{70}-K13 and $(H_2)_2$@C_{70}, indicating rapid exchange of their relative positions on the NMR time scale. When the sample was cooled down to the expected temperature when the singlet corresponding to the doubly encapsulated H_2 disappeared (**Figure 3.10** middle spectrum at 193 K), the $(H_2)_2$@C_{70}-K13

behaved as expected when the initial peak at -15.22 ppm disappeared while the $(H_2)_2@C_{70}$ singlet at -23.6 ppm remained unaffected. Then at 168 K (**Figure 3.10** bottom spectrum), two new peaks with chemical shifts of -12.87 and -17.38 ppm corresponding to each of the two H_2 molecules encapsulated inside C_{70}-K13 [$(H_2)_2@C_{60}$-K13] appeared while the signal corresponding to $(H_2)_2@C_{70}$ remained unchanged still. The slight chemical shift and line broadening are expected as a result of the temperature change. From this result, we suspect that the dynamic behavior of the two H_2 molecules can only be observed when it is incarcerated inside an asymmetric fullerene; therefore we expect the doubly incarcerated H_2 inside other open C_{70} fullerene derivatives to exhibit a similar dynamic behavior.

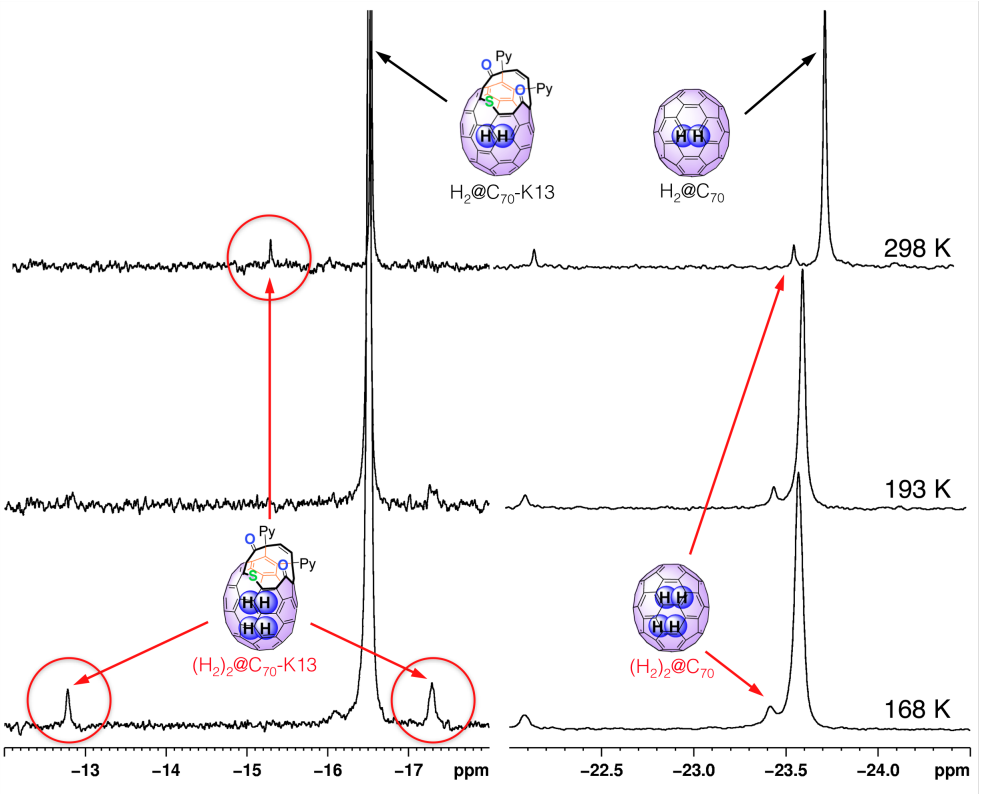

Figure 3.10: ^{1}H NMR [400 MHz, CS_2-CD_2Cl_2 (4:1)] spectra of the mixture of $(H_2)_2@C_{70}$-K13, $H_2@C_{70}$-K13 (Left) and $(H_2)_2@C_{70}$, $H_2@C_{70}$ (Right) at 298 K, 193 K and 168 K.

In a separate experiment, a mixture of H_2@C_{70}-K13, H_2@C_{70}-K12, H_2@C_{70}-K8 and each of its respective 3% of $(H_2)_2$@open-C_{70} (Chart 3.1) was dissolved in 4:1 CS_2-CD_2Cl_2. H_2@C_{70}-K13 served as the control because its thermodynamics and kinetics data are known.[21] ^{1}H NMR measurements were taken at -95°C, -75°C, -30°C and 0°C, respectively. It is clear from the ^{1}H NMR spectrum that there is a temperature dependence on the disappearance and reappearance of two singlets each corresponding to an individual H_2 of the $(H_2)_2$ species of the different open forms, $(H_2)_2$@C_{70}-K13, $(H_2)_2$@C_{70}-K12 and $(H_2)_2$@C_{70}-K8 (Chart 3.1); however, we do not have the rate constants from simulation. We do have the thermodynamic data for the chemical shifts of the two $(H_2)_2$ peaks for each of the open-C_{70}s (**Figure 3.11**). The top cartoon shows the chemical shifts at room temperature for H_2@open-C_{70} and $(H_2)_2$@open-C_{70}. The bottom cartoon shows that at -95°C, each of the H_2 of the $(H_2)_2$ are now distinct peaks with their own chemical shifts and that the difference in the chemical shifts ($\Delta\delta$) decreases as the size of the orifice gets smaller. In addition, we know from previous experiments mentioned above that the protons of $(H_2)_2$@C_{70} do not split into different chemical shifts at -95°C, $\Delta\delta$=0, which is consistent with the general trend: decrease in orifice size = decrease in $\Delta\delta$.

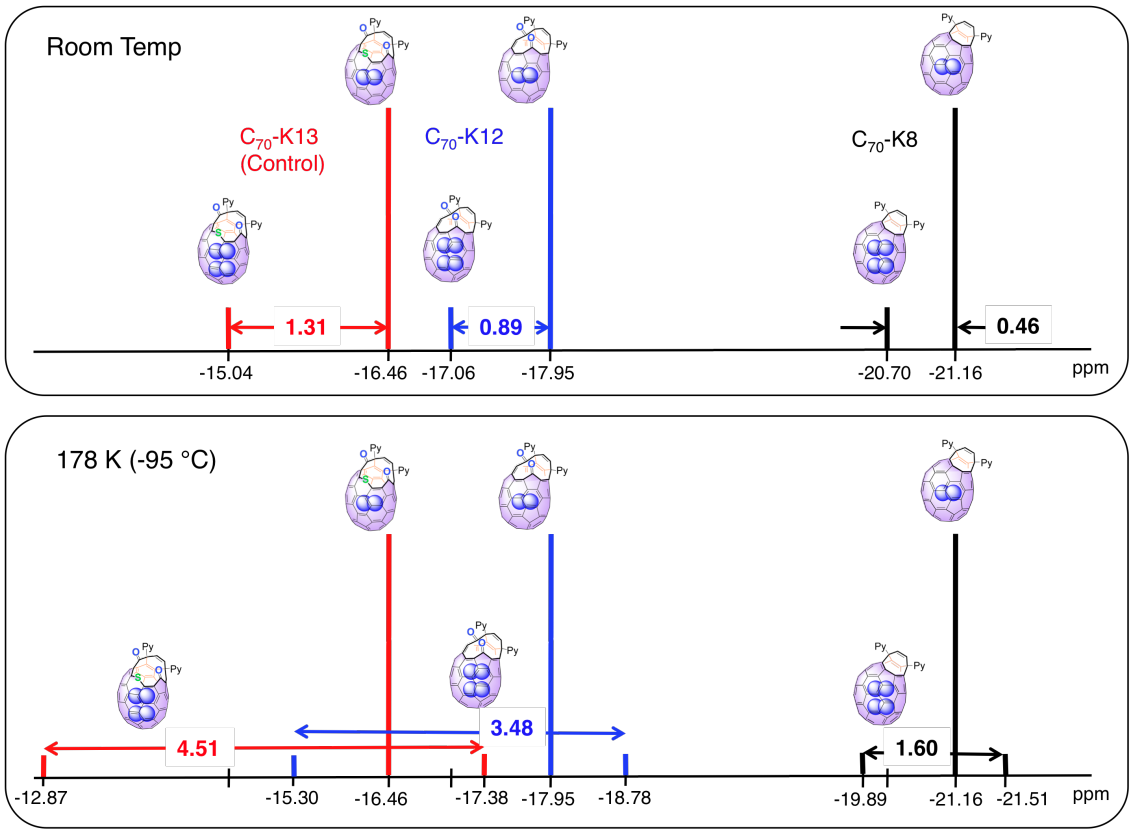

Figure 3.11: Cartoon illustrating chemical shifts of H_2@open-C_{70} and $(H_2)_2$@open-C_{70} at different temperatures, room temperature (Top) and -95°C (Bottom).

3.4.4 New system for magnetic exploration: H_2O@fullerene

We have seen how the confined motion of hydrogen molecule(s) inside both C_{60} and C_{70} fullerenes dramatically changes its spin-relaxation rate. By opening the C_{60} cage large enough to fit a H_2O molecule, one can also study its T_1 and temperature dependence as a result of confinement. This is done through a series of scissions that result in permanent 18-, 19-, or 20-atom orifices.[22,23,24,25] Most recently, our long time collaborator Professor Yasujiro Murata and his group synthesized H_2O@C_{60}.[26,27,28] We received samples of 20-atom orifice C_{60}, I-20 (Chart 3.1) from Professor Sho-ichi Iwamatsu's group and our synthetic chemist Dr. Xuegong Lei synthesized a 19-atom orifice C_{60}, I-19 (Chart 3.1). In

addition Professor Yasujiro Murata also provided us with some $H_2O@C_{60}$ to run our experiments.

I-20 has a large enough opening such that a water molecule from trace water in organic solvents will spontaneously and reversibly enter and exit the orifice at ambient temperature. I-19 encapsulates water molecule at temperature above RT by refluxing in a mixture of toluene and water for 18 h to reach 85% $^{1,2}H_2@$I-19 (Chart 3.1). This complex

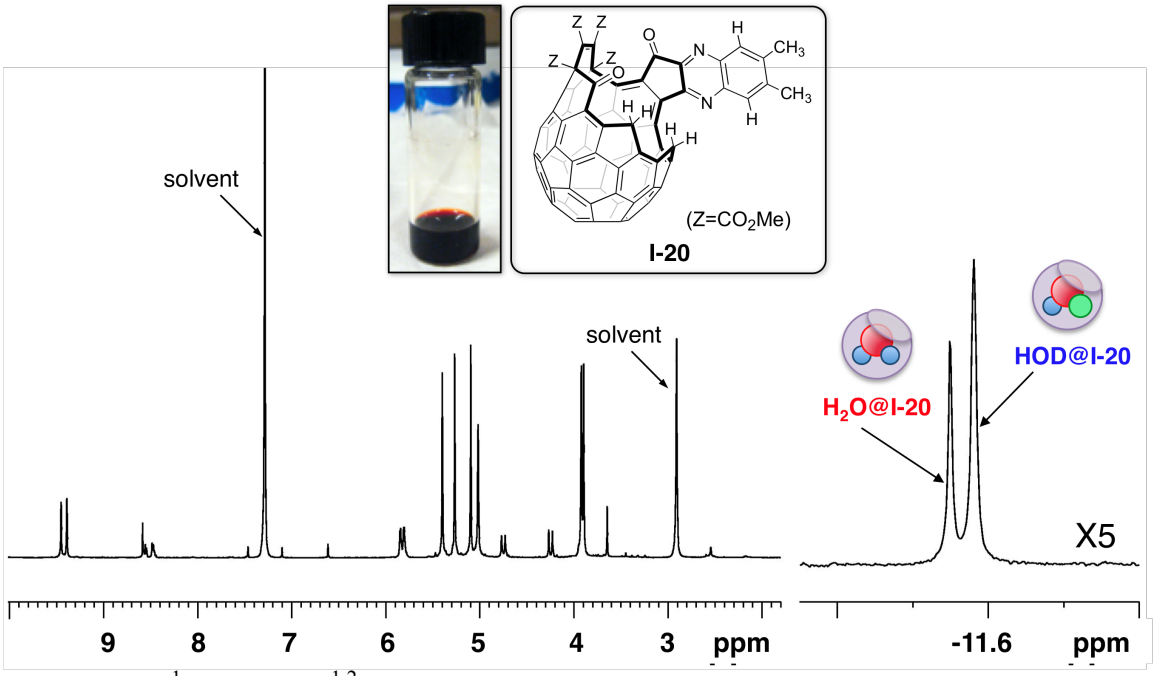

Figure 3.12: ^{1}H NMR of $^{1,2}H_2O@$I-20. I-20 = 2 mg + 5 μL 1:1 H_2O:D_2O in 600 μL TCE at 300 K.

is stable at room temperature. $H_2O@C_{60}$ is synthesized via the molecular surgery method and is used as is.

Figure 3.12 is the ^{1}H NMR corresponding to $^{1,2}H_2O@$I-20. This was prepared by dissolving 2 mg I-20 in 600 μL 1,1,2,2-Tetrachloroethane-d_2 (TCE) with the addition of 5 μL 1:1 H_2O:D_2O at 300 K. Both the H_2O (-11.40 ppm) and HOD (-11.45 ppm) peaks in **Figure 3.12** are well

resolved to measure T_1. A photo of the vial containing $^{1,2}H_2O$@I-20 in **Figure 3.12** shows that it is a very dark red solution

Figure 3.13 shows the ^{1}H NMR spectra of a mixture of $^{1,2}H_2O$@I-19 and $^{1,2}H_2O$@I-20 and illustrates the well-separated proton signals for H_2O and HDO as well as those between the two fullerenes, I-19 and I-20, respectively. T_1 values corresponding to all H_2O containing fullerenes, including $H_2O@C_{60}$ (Chart 3.1) in different solvents are compiled in Table 3.3. The solvents are arranged (from left to right) by decreasing number of chlorine atoms. Its corresponding viscosity η is also provided. However, no trend is observed that correlates the properties of the solvent to the measured T_1 values for $^{1,2}H_2O$@fullerene. What is consistent is that the T_1 for HOD > H_2O and that the average T_1 value is ~ 4X longer for $H_2O@open\text{-}C_{60}$ than for $H_2O@C_{60}$. In comparison with $H_2@C_{60}$, the T_1 value is ~26X longer for $H_2O@open\text{-}C_{60}$ than for $H_2@C_{60}$ and 6X longer for $H_2O@C_{60}$ than $H_2@C_{60}$. In the case of HD, the only available T_1 comparison is in toluene and the ratio of HOD@I-19/HOD@C_{60} = 14. Next we move to the temperature dependence in toluene-d_8 to learn more about the effect and degree of confinement on the properties of H_2O.

Since we cannot control the dynamics of the water molecules from going in and out of I-20 and the equilibrium distribution between H_2O inside/outside the fullerene is

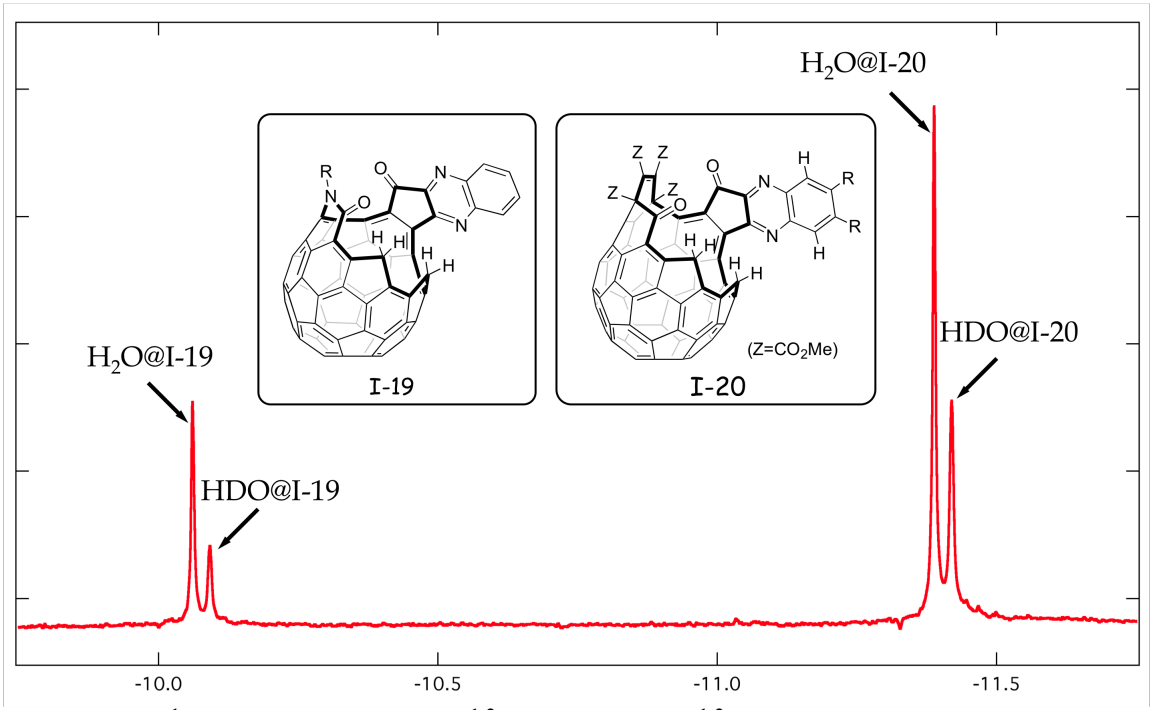

Figure 3.13: ^{1}H NMR of mixture of $^{1,2}H_2O$@I-19 and $^{1,2}H_2O$@I-20 in TCE at 300K.

Table 3.3: Spin Lattice Relaxation Time, T_1 (sec) for $^{1,2}H_2O$@fullerene[a]

Solvent →	TCE-d_6	$CDCl_3$-d_1	CD_2Cl_2-d_2	Toluene-d_8
η (cP)[b,c] →	1.629	0.539	0.423	0.548
	T_1 (sec)			
H_2O@I-19				2.6
HOD@I-19				3.0
H_2O@I-20	2.8	2.2	2.5	
HOD@I-20	3.1	2.6	3.3	
H_2O@C_{60}				0.64
H_2@C_{60}	0.108	0.082		0.104
HD@C_{60}				0.220

[a] T = 300 K at a field of 11.7 T (500 MHz)
[b] *J. Am. Chem. Soc.* **2006**, *128*, 14752-14753
[c] http://www.trimen.pl/witek/ciecze/old_liquids.html

different at different temperatures, the temperature dependence measurements were only done for $^{1,2}H_2O$@I-19 and H_2O@C_{60} (Chart 3.1). Typical 90° pulse calibration for H_2O@C_{60} is 6.6-8.7 μs. The variable delay was between 0.001-20 s (Table 3.4.VD9-VD11) with d1 = 3 s. Each experiment ranged from 34 min to ~1 hr. For H_2@I-19, the 90° pulse calibration was 6.5-7.4 μs.

The typical range for variable delay was between 0.001-15 s (Table 3.4.VD10) with d1 = 11 s. Each experiment took about 2 hours in this case.

Figure 2.16 shows the results. In the left graph, the relaxation rate, $1/T_1$ for $H_2O@C_{60}$ (a) was plot against previous results for $H_2@C_{60}$ (b) and $HD@C_{60}$ (c) for comparison. In the graph to the right, the same $H_2O@C_{60}$ plot (a) from the left was redrawn with its y-axis expanded to fit the entire graph and $1/T_1$ for $H_2O@I\text{-}19$ (b) and $HOD@I\text{-}19$ (c) were now included for comparison. Please refer to Chart 3.1 for chemical structures. Based on observation of the data alone, (1) $H_2O@C_{60}$ displayed the same trend as that of $HD@C_{60}$ with a smaller change with temperature, (2) $H_2O@I\text{-}19$ and $HOD@I\text{-}19$ behaved similarly with each other and were much less affected by temperature than $H_2O@C_{60}$. At this point, we still need to synthesize $HOD@C_{60}$ and cannot make any conclusions.

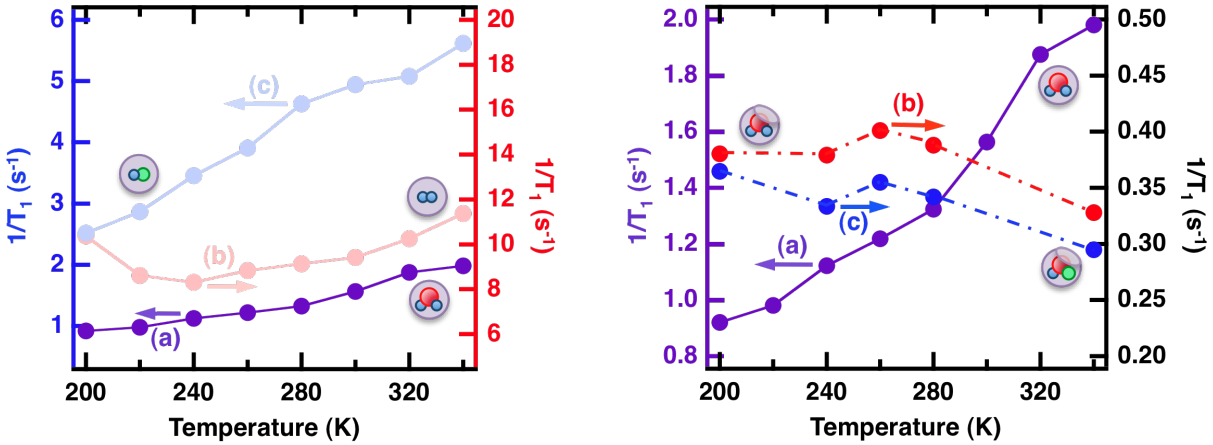

Figure 3.14: Relaxation rates, $1/T_1$ of toluene-d_8 solution of [Left] $H_2O@C_{60}$ (a). The faded plots correspond to previous results taken from Figure 2.7 for $H_2@C_{60}$ (b) and $HD@C_{60}$ (c) for comparison. [Right] The same $H_2O@C_{60}$ (a) line graph on the left is redrawn to compare with $H_2O@I\text{-}19$ (b) and $HOD@I\text{-}19$ (c). The directions of the arrows indicate corresponding y-axis for the plots. Please refer to Chart 3.1 for chemical structures

3.5 Experimental Section

3.5.1.1 Sample Preparation

To generate H_2 and HD gas dissolved in toluene-d_8, fresh calcium hydride (CaH_2) was carefully loaded into a round-bottom flask and the apparatus to generate H_2+HD gas was assembled and purged with argon for 5 minutes. Approximately five drops of fresh D_2O was carefully added dropwise with a plastic syringe into the round-bottom flask. Mixtures of the HD and H_2 gas generated were bubbled directly into a Wilmad, "J. Young Valve" NMR tube containing 600 μL toluene-d_8 that was also purged with argon prior to the addition of the HD/H_2 mixture (**Figure 3.15**). In a separate J. Young tube, 2 mg of H_2@C_{60} + HD@C_{60} mixture was dissolved in 600 μL toluene-d_8. The resulting purple solution was bubbled with argon for 5 minutes prior to measurement.

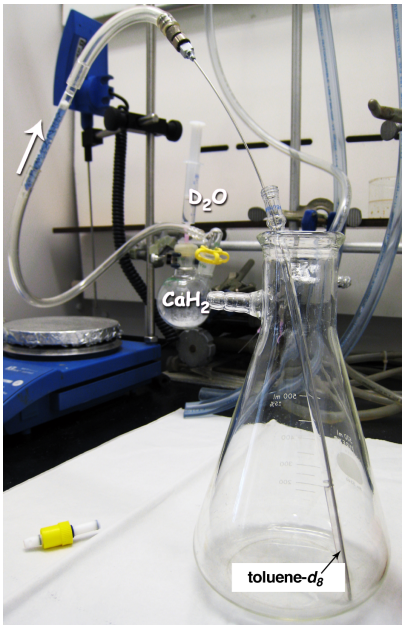

Figure 3.15: Apparatus for preparing H_2 and HD mixture in toluene-d_8.

3.5.1.2 NMR Measurements

All the spectra were obtained on a Bruker DMX-500 NMR spectrometer. The operating frequency for ^1H is 500.13 MHz. T_1 measurements were taken between 340 and 200 K with temperature increments of 20 K. The sample was allowed to equilibrate for 15 minutes or until the shimming/lock signal becomes stable prior to data acquisition at each temperature. The 90° pulse (**Figure 3.16**) was recalibrated at each temperature. T_1 measurements were performed using the inverse-recovery pulse sequence (**Figure 3.17**): relaxation delay → π → τ → π/2 → acquire, with 13 or 15 values for the variable delay τ, in the ranges 0.001-2.5 s (Table 3.4.VD5-8) and 0.001-20 s (Table 3.4.VD4-11) for H_2/HD@C_{60} and H_2/HD, respectively. A recycle delay (d1) between pulses of 2.5 s ($5\times T_1$) was used for H_2/HD@C_{60} and 25 s for H_2/HD.

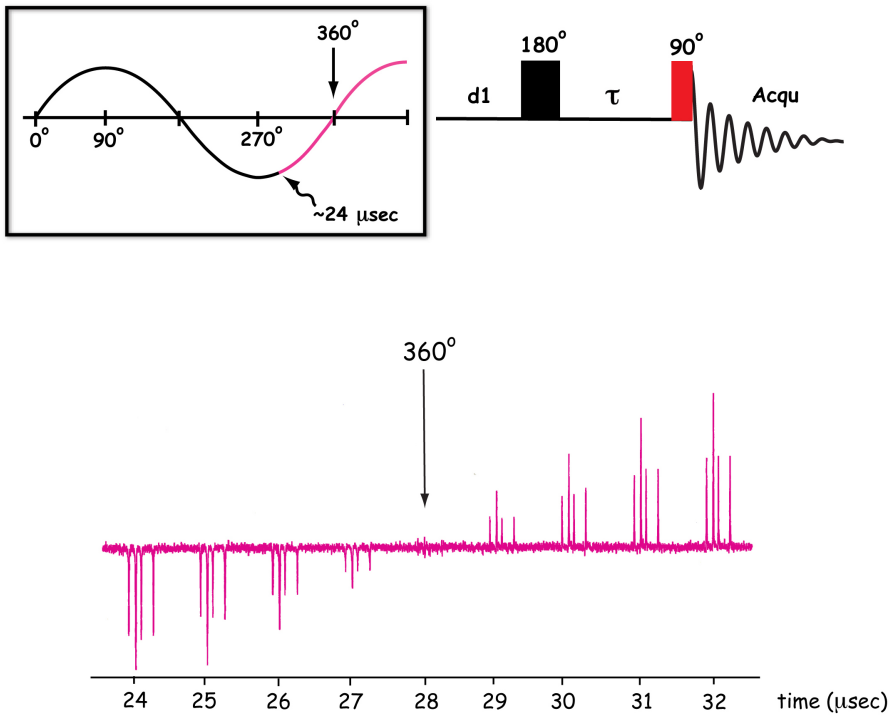

Figure 3.16: 90° pulse calibration. The value is more accurate when it crosses through zero (180° or 360°), we chose 360° and start to acquire signal at ~24µs. Finally, we take the value at 360° and divide it by 4 to get the 90° pulse.

T_1 values were calculated for the H_2 peak and each of the peaks of the HD triplet (**Figure 3.6**a) assuming first-order recovery. The digital resolution was 0.18 Hz/point. The standard deviations for fitting the H_2 and the HD data were not significantly different, which we take to imply that any nonexponential contribution to HD relaxation is undetectable in our data, which is consistent with an insignificant contribution from $^2H–^1H$ cross-relaxation.[14,15]

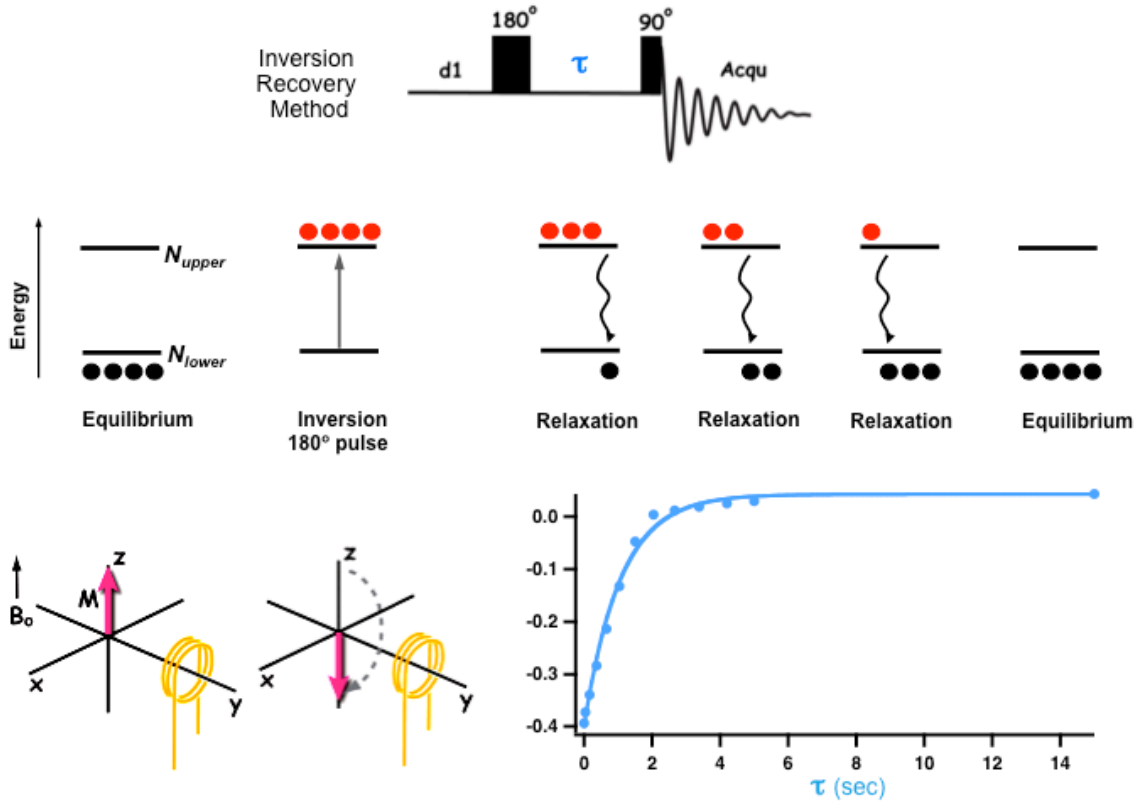

Figure 3.17: Top row: Illustration of simple pulse sequence for inversion recovery to determine T_1. Middle row: population distribution as a function of the inversion recovery method. Bottom row, left: initial state of a nuclear magnetic vector, M at equilibrium (left) and after 180° pulse (right). Bottom row, right: A sample first-order decay curve exhibited by the z magnetization as a function of time after a 180° pulse.

All solvents used in this work are commercially obtained, used without further purification and directly pipetted in to o.d. 5 mm NMR tubes fitted with J-Young valves.

Table 3.4: Compilation of Variable Delay (VD) Lists

	VD1	VD2	VD3	VD4	VD5	VD6	VD7	VD8	VD9	VD10	VD11	VD12
TD	**Judy_0.1**	**Judy_0.2**	**Judy_0.2_15**	**Salvo_0.24**	**Judy_0.3**	**Salvo_0.4**	**Salvo_0.4_32**	**Judy_0.5**	**Judy_1.0**	**Judy_3s**	**Judy_4s**	**Judy_10s**
1	0.001	0.001	0.001	0.0005	0.001	0.001	0.0005	0.001	0.001	0.001	0.001	0.01
2	0.004	0.01	0.006	0.001	0.009	0.009	0.001	0.0069	0.015	0.041	0.03	0.15
3	0.011	0.03	0.021	0.0016	0.032	0.036	0.0016	0.028	0.055	0.16	0.1	0.55
4	0.024	0.05	0.047	0.0023	0.07	0.08	0.0023	0.063	0.13	0.37	0.3	1.25
5	0.042	0.07	0.083	0.003	0.123	0.14	0.003	0.11	0.22	0.66	0.5	2.2
6	0.065	0.1	0.128	0.0045	0.192	0.22	0.0045	0.174	0.34	1.04	0.7	3.4
7	0.093	0.2	0.184	0.0065	0.276	0.32	0.0065	0.25	0.5	1.5	1	5
8	0.126	0.3	0.251	0.0075	0.376	0.43	0.0075	0.34	0.68	2.04	2	6.8
9	0.164	0.5	0.327	0.009	0.49	0.56	0.009	0.44	0.88	2.66	3	8.8
10	0.207	0.7	0.414	0.013	0.62	0.72	0.013	0.56	1.13	3.38	5	11.3
11	0.256	1	0.511	0.02	0.766	0.89	0.02	0.79	1.38	4.2	10	13.8
12	0.309		0.618	0.03	0.926	1.07	0.03	0.99	1.68	5	15	16.8
13	0.368		0.735	0.038	1.102	1.28	0.044	2.5	5	15	20	50
14	0.431		0.862	0.044	1.294	1.5	0.053					
15	0.5		1	0.053	1.5	1.74	0.064					
16				0.0547		2	0.09					
17				0.064			0.1					
18				0.073			0.13					
19				0.09			0.16					
20				0.1			0.2					
21				0.13			0.25					
22				0.16			0.3					
23				0.2			0.35					
24				0.22			0.47					
25				0.25			0.56					
26				0.3			0.72					
27				0.35			0.89					
28				0.47			1.07					
29				0.56			1.28					
30				0.72			1.5					
31				0.89			1.74					
32				1.07			2					

3.6 References

(1) Carrington, A.; McLachlan, A. D. *Introduction to Magnetic Resonance*; Harper & Rowe: New York, **1967**; pp. 1-266.

(2) Sartori, E. Ruzzi, M. Turro, N. J. Komatsu, K. Murata, Y. Lawler, R. G.; Buchachenko, A. L. Paramagnet Enhanced Nuclear Relaxation of H_2 in Organic Solvents and in $H_2@C_{60}$. *J. Am. Chem. Soc.* **2008**, 256-258.

(3) Chen, J. Y.-C. Martí, A. A. Turro, N. J. Komatsu, K. Murata, Y.; Lawler, R. G. Comparative NMR Properties of H_2 and HD in Toluene-d_8 and in H_2/HD@C_{60}. *J. Phys. Chem. B* **2010**, *114,* 14689-14695.

(4) Li, Y. Lei, X. Lawler, R. G. Murata, Y. Komatsu, K.; Turro, N. J. Distance-Dependent Paramagnet-Enhanced Nuclear Spin Relaxation of $H_2@C_{60}$ Derivatives Covalently Linked to a Nitroxide Radical. *J. Phys. Chem. Lett.* **2010**, *1*, 2135-2138.

(5) Sartori, E. Ruzzi, M. Turro, N. J. Decatur, J. D. Doetschman, D. C. Lawler, R. G. Buchachenko, A. L. Murata, Y.; Komatsu, K. Nuclear relaxation of H_2 and $H_2@C_{60}$ in organic solvents. *J. Am. Chem. Soc.* **2006**, *128*, 14752-3.

(6) Krynicki, K. Proton spin relaxation in liquid hydrogen chloride and hydrogen bromide. *Phys. Lett.* **1963**, *4*, 260-262.

(7) Gilboa, H. Spin–Lattice Relaxation Times of H_2 and D_2 in Aqueous Solutions. *J. Mag. Res., Series A* **1996**, *119*, 1-5.

(8) Hubbard, P. Theory of Nuclear Magnetic Relaxation by Spin-Rotational Interactions in Liquids. *Phys. Rev.* **1963**, *131*, 1155-1165.

(9) Bloembergen, N. *Nuclear Magnetic Relaxation*; WA Benjamin, Inc.: New York, **1961**; pp. 101-105.

(10) Abragam, A. *Principles of Nuclear Magnetism*; Oxford University Press: Oxford, **1961**; pp. 316-322.

(11) Quinn, W. Baker, J. LaTourrette, J.; Ramsey, N. Radio-Frequency Spectra of Hydrogen Deuteride in Strong Magnetic Fields. *Phys. Rev.* **1958**, *112*, 1929-1940.

(12) Farkas, A. In *Orthohydrogen, Parahydrogen and Heavy Hydrogen*; Cambridge University Press, 1935; pp. 161-166.

(13) Wheatly, P. J. *The Chemical Consequences of Nuclear Spin*; North-Holland Publishing Company: Amsterdam, 1970; p. 99.

(14) Fisher, C. Spin-lattice relaxation in HD-He gaseous mixtures. *Physica* **1973**, *66*, 1-15.

(15) Johnson, C. S.; Waugh, J. S. Nuclear Relaxation in Adulterated Hydrogen. *The J. Chem. Phys.* **1962**, *36*, 2266.

(16) Bezmel'nitsyn, V. N. Eletskii, A. V.; Okun', M. V. Fullerenes in solutions. *Physics-Uspekhi* **1998**, *41*, 1091-1114.

(17) Ruoff, R. S. Tse, D. S. Malhotra, R.; Lorents, D. C. Solubility of fullerene C_{60} in a variety of solvents. *J. Phys. Chem.* **1993**, *97*, 3379-3383.

(18) Li, Y. Lei, X. Jockusch, S. Chen, J. Y.-C. Frunzi, M. Johnson, J. a; Lawler, R. G. Murata, Y. Murata, M. Komatsu, K.; Turro, N. J. A magnetic switch for spin-catalyzed interconversion of nuclear spin isomers. *J. Am. Chem. Soc.* **2010**, *132*, 4042-3.

(19) Li, Y. Lei, X. Lawler, R. G. Murata, Y. Komatsu, K.; Turro, N. J. Distance-Dependent *para*-H_2 → *ortho*-H_2 Conversion in H_2@C_{60} Derivatives Covalently Linked to a Nitroxide Radical. *J. Phys.Chem. Lett.* **2011**, *2*, 741-744.

(20) Murata, M. Maeda, S. Morinaka, Y. Murata, Y.; Komatsu, K. Synthesis and reaction of fullerene C_{70} encapsulating two molecules of H_2. *J. Am. Chem .Soc.* **2008**, *130*, 15800-1.

(21) Murata, Y. Maeda, S. Murata, M.; Komatsu, K. Encapsulation and dynamic behavior of two H_2 molecules in an open-cage C_{70}. *J. Am. Chem .Soc* **2008**, *130*, 6702-3.

(22) Iwamatsu, S.-ichi; Murata, S. H_2O@open-cage fullerene C_{60}: control of the encapsulation property and the first mass spectroscopic identification. *Tetrahedron Lett.* **2004**, *45*, 6391-6394.

(23) Iwamatsu, S.-ichi; Uozaki, T. Kobayashi, K. Re, S. Nagase, S.; Murata, S. A bowl-shaped fullerene encapsulates a water into the cage. *J. Am. Chem .Soc* **2004**, *126*, 2668-9.

(24) Xiao, Z. Yao, J. Yang, D. Wang, F. Huang, S. Gan, L. Jia, Z. Jiang, Z. Yang, X. Zheng, B. Yuan, G. Zhang, S.; Wang, Z. Synthesis of [59]fullerenones through peroxide-mediated stepwise cleavage of fullerene skeleton bonds and X-ray structures of their water-encapsulated open-cage complexes. *J. Am. Chem. Soc.* **2007**, *129*, 16149-62.

(25) Iwamatsu, S.-ichi; Murata, S. Open-Cage Fullerenes: Synthesis, Structure, and Molecular Encapsulation. *Synlett* **2005**, 2117-2129.

(26) Kurotobi, K.; Murata, Y. A Single Molecule of Water Encapsulated in Fullerene C_{60}. *Science* **2011**, *333*, 613-616.

(27) Ramachandran, C.; Sathyamurthy, N. Water clusters in a confined nonpolar environment. *Chem. Phys. Lett.* **2005**, *410*, 348-351.

(28) Shameema, O. Ramachandran, C. N.; Sathyamurthy, N. Blue shift in X-H stretching frequency of molecules due to confinement. *J. Phys. Chem. A* **2006**, *110*, 2-4.

4 Relaxivity, R_x

As we have seen in chapter 3, T_1 is dominated by *intramolecular* dipole-dipole and spin-rotation interactions. In this chapter, we will discuss results from paramagnet-induced *intermolecular* relaxation using two stable paramagnetic species, mononitroxides TEMPO and 4-Oxo-TEMPO (Chart 4.1).

Chart 4.1: Structures pertaining to Chapter 4.

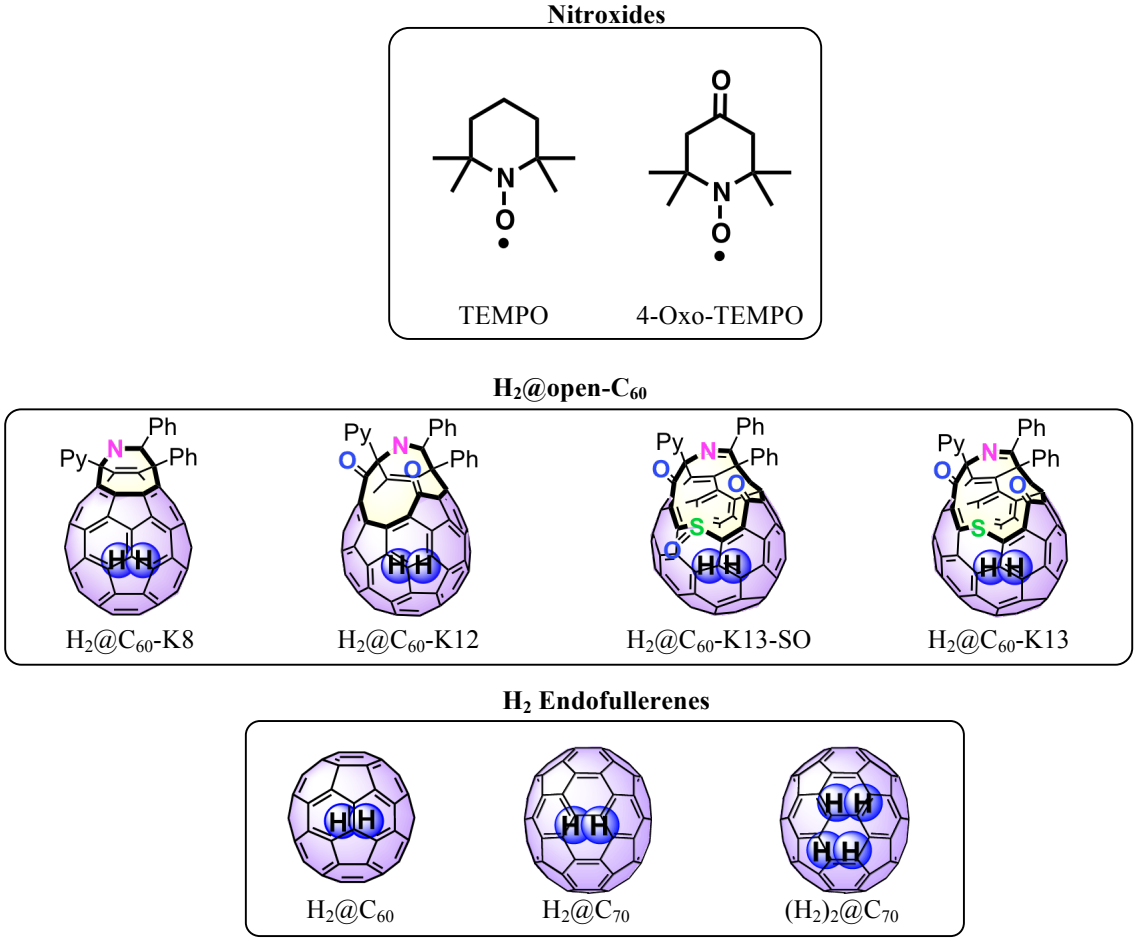

4.1 Background

Relaxivity is the ability of magnetic compounds to increase the relaxation rates of the surrounding proton and other nuclear spins. Paramagnetic enhancement of relaxation is of

fundamental importance for NMR spectroscopy and magnetic resonance imaging (MRI).[1] For example, the image intensity in ^{1}H NMR imaging, composed of the NMR signal of water protons in our tissue, is dependent on nuclear relaxation times (Chapter 3). Under normal conditions, the dominant effect of a paramagnetic relaxant/agent in NMR imaging is to increase the signal intensity of the tissue containing the relaxant. The greater decrease in T_1, dominates the relaxation effects and generates signal enhancement (with all else being equal, e.g., pulse sequence used for data acquisition and pulse sequence parameters). The pioneer work of Lauterbur et al.,[2] were first to show the feasibility of paramagnetic agents for tissue discrimination on the basis of differential water proton relaxation times.[3] The first human NMR imaging studying involving a contrast agent was performed by Young et al.;[4] in which ferric chloride was orally administered and used to enhance the gastrointestinal tract. The diagnostic potential of paramagnetic agents was first demonstrated in patients by Carr et al.[5] using Gd (III) diethylenetriaminepentaacetate [[Gd(DTPA)(H_2O)]$^{2-}$]. For these reasons, the paramagnetic relaxant is often referred to as a contrast agent or a diagnostic agent.

The most commonly used paramagnetic relaxant is gadolinium (Gd) chelates. They exhibit high relaxivities because of its high spin (7/2) metal center. Other potential alternative to Gd chelates such as the stable nitroxide free radicals has also been evaluated;[6,7] but the intrinsically low paramagnetic relaxivity of nitroxides (in part due to their low spin of ½) has interrupted their widespread application as MRI contrast agents.[8] It is, however, a perfect candidate for relaxivity measurements with our H_2@fullerene systems. Our lab has studied stable nitroxide radicals for several years as ESR or EPR probes for surfaces and supramolecular assemblies[9] and in connection with $H_2@C_{60}$, it was found more recently that the relaxation effect of the paramagnets is enhanced 5-fold in $H_2@C_{60}$ compared to H_2 under the same conditions.[10] It

makes sense to follow up on these results by first repeating the results for $H_2@C_{60}$ and then investigate the relaxivity of H_2@open-C_{60}, $H_2@C_{70}$ and $(H_2)_2@C_{70}$ (Chart 4.1).

4.2 Theory of contributions to relaxivity, R_x

The addition of a paramagnetic relaxant causes an increase in the longitudinal and transverse relaxation rates, $1/T_1$ and $1/T_2$, respective, of proton nuclei. The diamagnetic and paramagnetic contributions to the relaxation rates are additive and given by Equation 4.1, where $1/T_{1,obs}$ is the observed proton relaxation rate in the presence of a paramagnetic

Equation 4.1 $$\frac{1}{T_{i,obs}} = \frac{1}{T_{i,d}} + \frac{1}{T_{i,p}} \qquad i = 1, 2$$

species, $1/T_{1,d}$ is the diamagnetic proton relaxation rate in the absence of a paramagnetic species (Chapter 3), and $1/T_{1,p}$ represents the additional paramagnetic contribution. In the absence of electron-spin-electron-spin interactions between the nitroxides, the proton relaxation rates are linearly dependent on the concentration of these paramagnetic species ([S]); relaxivity, R_x is defined as the slope of this dependence in units of $M^{-1}s^{-1}$ (Equation 4.2).

Equation 4.2 $$\frac{1}{T_{1,obs}} = \frac{1}{T_{1,d}} + R_x[S]$$

4.3 Results

4.3.1 R_x of $H_2@C_{60}$ and H_2@open-C_{60}

Tables 4.1, 4.2 and 4.3 are representative $1/T_1$ values for $H_2@C_{60}$ and H_2@open-C_{60} (Chart 4.1) as a function of the concentration of the nitroxides TEMPO (Table 4.1) and 4-Oxo-TEMPO (Tables 4.2 and 4.3) in *ortho*-1,2-dichlorobenzene-d_4 (ODCB) at 300 K. The data collected in Table 4.1 and Table 4.2 were measured with the same batch of solvent and one mixed sample containing the following concentrations of H_2@fullerene: 0.68 mM $H_2@C_{60}$, 0.81 mM $H_2@C_{60}$-

Table 4.1: Relaxation Rate Constants for H_2@fullerene with Paramagnet TEMPO[a]

	Relaxation rate constants, $1/T_1$[b] (s^{-1})			
[TEMPO], M	$H_2@C_{60}$	$H_2@C_{60}$-K8	$H_2@C_{60}$-K12	$H_2@C_{60}$-K13
0.000	10.71	6.92	7.03	5.77
0.005	11.86	7.43	7.54	6.01
0.010	12.54	7.68	7.86	6.28
0.015	13.37	7.97	8.15	6.56
0.019	13.57	8.03	8.32	6.66
0.024	14.06	8.33	8.61	6.96
0.029	14.17	8.41	8.54	7.16

[a] 300 K, 1,2-dichlorobenzene-d_4
[b] ± 5%

Notebook II, p. 106 on 052410

Table 4.2: Relaxation Rate Constants for H_2@fullerene with Paramagnet 4-Oxo-TEMPO[a]

	Relaxation rate constants, $1/T_1$[b] (s^{-1})			
[4-Oxo-TEMPO], M	$H_2@C_{60}$	$H_2@C_{60}$-K8	$H_2@C_{60}$-K12	$H_2@C_{60}$-K13
0.000	11.31	7.19	7.25	5.78
0.005	12.74	7.87	8.06	6.25
0.010	13.40	8.00	8.20	6.41
0.015	13.64	8.33	8.13	6.54
0.019	13.79	8.13	8.20	6.58
0.024	14.35	8.26	8.40	6.80
0.029	14.20	8.13	8.40	6.85

[a] 300 K, 1,2-dichlorobenzene-d_4
[b] ± 5%

Notebook II, p. 108 on 052610

Table 4.3: Relaxation Rate Constants for H_2@fullerene with Paramagnet 4-Oxo-TEMPO[a]

	Relaxation rate constants, $1/T_1$[b] (s^{-1})				
[4-Oxo-TEMPO], M	$H_2@C_{60}$ (Avg)	$H_2@C_{60}$-K8	$H_2@C_{60}$-K12	$H_2@C_{60}$-K13	$H_2@C_{60}$-K13-SO
0.000	10.03	6.66	7.25	5.57	5.90
0.004	10.27	6.89	8.06	5.79	6.27
0.009	10.66	7.22	8.20	6.06	6.66
0.015	11.16	7.52	8.13	6.39	7.14
0.020	11.52	7.91	8.20	6.75	7.59

[a] 300 K, 1,2-dichlorobenzene-d_4
[b] ± 5%

Notebook II, p. 82 on 091109

K8, 0.70 mM $H_2@C_{60}$-K12 and 0.66 mM $H_2@C_{60}$-K13 (Chart 4.1). The data collected in Table 4.3 were from a different occasion with sample preparation as described in Section 4.5.1 and Figure 4.3.

Table 4.4 lists the calculated relaxivities based on the data in Table 4.1 and the average from Table 4.2 and Table 4.3 for various combinations of paramagnets, denoted by *S* and nuclei, denoted by *I*. Note that the relaxivity proportionality constant R_x for $H_2@C_{60}$ with 4-Oxo-TEMPO is larger in ODCB than in toluene[10] and between the two paramagnets, TEMPO and 4-Oxo-TEMPO, the former has a slightly stronger effect on $H_2@C_{60}$ than 4-Oxo-TEMPO in the same solvent.

The relaxivity value of 86 ± 9 reported in Table 4.4 for the combination of 4-Oxo-TEMPO and $H_2@C_{60}$ is based on the average of five R_x values, four of which were determined from Table 4.3 with each sample containing a mixture of $H_2@C_{60}$ and one of the open fullerenes, $H_2@C_{60}$-K8, $H_2@C_{60}$-K12, $H_2@C_{60}$-K13 and $H_2@C_{60}$-K13-SO (see sample preparation scheme in Figure 4.3 and Chart 4.1 for chemical structures) plus one more R_x value determined from Table 4.2 The individual R_x values corresponding to $H_2@C_{60}$ in the mixture are as follows: 74 ± 3 (K8), 80 ± 5 (K12), 80 ± 5 (K13), and 82 ± 1 (K13-SO). The notation in parenthesis following the R_x value indicates the open form that was associated with the $H_2@C_{60}$ in the mixture.

Table 4.4: Relaxivities for Various Combinations of Paramagnets (*S*) and Nuclei (*I*) in ODCB, 300 K

	Relaxivity, R_X ($M^{-1}s^{-1}$)	
(*I* ↓) / (*S* →)	[TEMPO]	[4-Oxo-TEMPO]
$H_2@C_{60}$	129 ± 18	86 ± 9 (avg)
$H_2@C_{60}$-K8	50 ± 5	43 ± 6
$H_2@C_{60}$-K12	54 ± 6	50 ± 4
$H_2@C_{60}$-K13	48 ± 2	45 ± 5

The relaxivities between the different open forms are very similar and the values are ~10 $M^{-1}s^{-1}$ greater in 4-Oxo-TEMPO than in TEMPO. Table 4.5 displays the data in Table 4.4 in a different way illustrating the same results. The R_x ratio of $H_2@C_{60}$ / H_2@open-C_{60} indicates that (1) the communication between TEMPO and $H_2@C_{60}$ is 2.5X stronger than TEMPO and H_2@open-C_{60}. (2) The communication between 4-Oxo-TEMPO and $H_2@C_{60}$ is 2X stronger than 4-Oxo-TEMPO and H_2@open-C_{60}. (3) The variation in the size of the orifice had no affect on the relaxivity given the same nitroxide.

Table 4.5: R_x Ratio of $H_2@C_{60}$ / H_2@open-C_{60}

	R_X Ratios	
	[TEMPO]	[4-Oxo-TEMPO]
$H_2@C_{60}$ / $H_2@C_{60}$-K8	2.5 ± 0.2	2.0 ± 0.2
$H_2@C_{60}$ / $H_2@C_{60}$-K12	2.3 ± 0.2	1.7 ± 0.2
$H_2@C_{60}$ / $H_2@C_{60}$-K13	2.6 ± 0.4	1.9 ± 0.3

4.3.2 R_x of $H_2@C_{60}$ and $H_2@C_{70}$

Relaxation rate constants for mixtures of $H_2@C_{70}$, $(H_2)_2@C_{70}$ and $H_2@C_{60}$ (Chart 4.1) as a function of the concentration of 4-Oxo-TEMPO are shown in Table 3.7. The sample tube contained 2.7 mM $H_2@C_{60}$, 3.5 mM $H_2@C_{70}$ and 0.11 mM $(H_2)_2@C_{70}$ in ODCB.

Table 4.6: Relaxation rate constants

	$1/T_1$ (s^{-1})		
[4-Oxo-TEMPO], M	$H_2@C_{60}$	$(H_2)_2@C_{70}$	$H_2@C_{70}$
0.000	9.96	3.36	7.20
0.002	NA	3.53	7.11
0.004	10.34	3.84	7.50
0.006	10.46	3.83	7.62
0.008	10.63	4.22	7.71
0.010	10.83	4.28	7.94
0.016	11.22	4.84	8.25
0.023	11.65	5.24	8.71

300 K, 1,2-dichlorobenzene-d_4

Figure 4.1 is the plot of $1/T_1$ vs. the concentration of relaxant, 4-Oxo-TEMPO obtained from Table 4.6. The relaxivity values, R_x were obtained by fitting the data to the equation $1/T_1 = 1/T_{1,0} + R_x[S]$ for (a) $H_2@C_{60}$ (b) $(H_2)_2@C_{70}$ and (c) $H_2@C_{70}$ (Chart 4.1). Based on the relaxivity values for $H_2@C_{70}$ (70 ± 5 $M^{-1}s^{-1}$), the communication between $H_2@C_{60}$ and $H_2@C_{70}$ and nitroxide are inconsequential to the shape of the fullerene. However, there is a slightly stronger communication between the doubly encapsulated H_2 inside C_{70} and nitroxide.

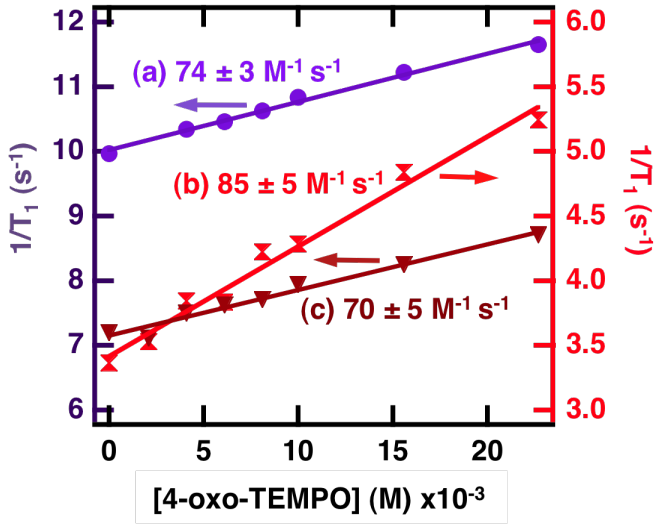

Figure 4.1. Plot of $1/T_1$ vs. the concentration of relaxant, 4-Oxo-TEMPO. The relaxivity values, R_x were obtained by fitting the data to Equation 4.2 for (a) $H_2@C_{60}$ (b) $(H_2)_2@C_{70}$ and (c) $H_2@C_{70}$. Each of the points on the plots was obtained from Table 3.7.

4.3.3 Summary of R_x values for H_2@fullerene with 4-Oxo-TEMPO

We have measured the bimolecular contribution, R_x (relaxivity), to the spin-lattice relaxation rate ($1/T_1$) for the protons of H_2@fullerene (Chart 4.1) dissolved in organic solvent, ODCB. In the presence of paramagnet 4-Oxo-TEMPO nitroxide radical the measurements showed that despite the 5-fold enhancement found in $H_2@C_{60}$ compared to dissolved H_2 under the same conditions[10], no significant difference was observed between $H_2@C_{60}$ and H_2 that are partially

exposed to the environment in the open C_{60} fullerenes and incarcerated inside a football shaped C_{70} fullerene. Figure 4.2 is a summary of all relaxivity values corresponding to different H_2@fullerene with the nitroxide 4-Oxo-TEMPO. Future experiments in determining relaxivities of HD@fullerenes will be possible with a new batch of H_2*@fullerene containing a much higher percentage of HD (Table 4.8).

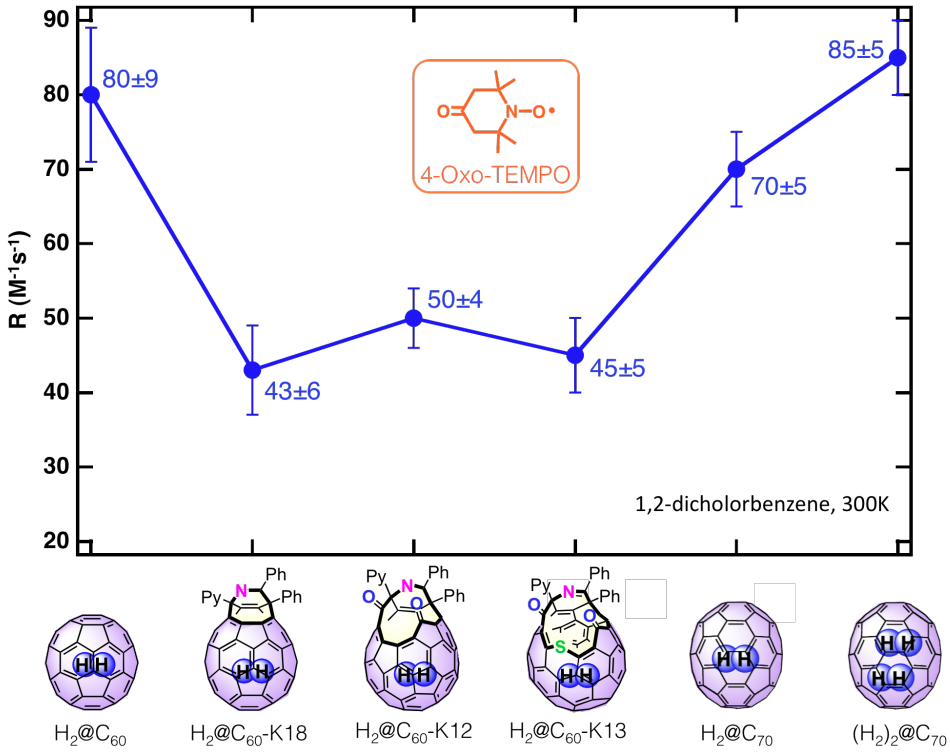

Figure 4.2: Compilation of all relaxivity values, R_x for H_2@fullerene in ODCB at 300 K.

4.4 Summary of measurements from chapters 2-4: k_{po}, $1/T_1$, and R_x for open fullerenes

Table 4.7 summarizes the ratios of the values of the parameters from chapters 2-4: (1) pH$_2$ → oH$_2$ back conversion rate constants, k_{po} (Chapter 2); (2) relaxation rate constants, $1/T_1$ (Chapter 3); and (3) relaxivities, R_x (Chapter 4) for H_2@open-C_{60} relative to those for H_2@C_{60}. A salient feature of the results is that all dynamic processes, k_{po} and R_x, occur at a faster rate for H_2@open-C_{60}'s than for H_2@C_{60} under the same conditions. However, the values of the ratio between all

the open forms are not significantly different which suggest that there is no correlation between the orifice sizes and the rate of the measured dynamic processes.

Table 4.7: Ratios of Rate Constants for H_2@open-C_{60} relative to H_2@C_{60}. (1) $pH_2 \rightarrow oH_2$ Conversion Rate Constants (k_{po}); (2) Relaxation Rate Constants ($1/T_1$); and (3) Relaxivities (R_x)

Dynamic Process	$pH_2 \rightarrow oH_2$ Conversion, k_{po}[a]		Relaxation Rate, $1/T_1$[b]	Relaxivity R_x[a]	
	Air	5 mM TEMPO		TEMPO	4-Oxo-TEMPO
H_2@C_{60} / H_2@C_{60}-K8		1.6	0.73	2.6	1.9
H_2@C_{60} / H_2@C_{60}-K12		2.3	0.73	2.4	1.6
H_2@C_{60} / H_2@C_{60}-K13	1.6	1.8	0.61	2.7	
H_2@C_{60} / H_2@C_{60}-K13-SO			0.65		

[a] ODCB
[b] Toluene-d_8
T = 300 K, at a field of 11.7 T (500 MHz)

4.5 Experimental Section

4.5.1 Sample Preparation

We used ODCB as the solvent of choice for relaxivity measurements because (1) the fullerenes are much more soluble in ODCB than in toluene (Table 3.2) thus better signal-to-noise, and (2) it is the same solvent used for $oH_2 \leftrightarrow pH_2$ conversion (Chapter 2) and we want to maintain consistency in factors that we have control over as much as possible throughout our experiments. The samples for relaxivity measurements were prepared as follows (Figure 4.3): three 2.5 mL ODCB solutions were prepared containing a mixture of 1 mM H_2@open-C_{60} and 0.5 mM H_2@C_{60} in where the latter served as control. These are represented as the green, yellow and blue boxes on the top row of Figure 4.3. Then each of the three solutions containing different open fullerenes was further divided into four smaller samples by using a Hamilton syringe to transfer the desired aliquot from the solution into a small vial. These are shown in the diagram with numbers 1-4 with colors corresponding to each mixture. At this point, the T_1 values are

determined for each of the mixtures. Then 0.5 mL of a fresh 0.2 M stock solution of the nitroxide was prepared as indicated by the orange box at the bottom of Figure 4.3. Appropriate aliquots with 5 μL increments (for convenience) of nitroxide from the stock solution were added via a Hamilton syringe to each vial containing the fullerene solution (Figure 4.3). The vial was then screwed close with a Teflon cap and the solution was shaken to mix, and then transferred into an NMR tube for T_1 measurements. The additions of the nitroxide to the fullerene solution were not done all at once, only one was prepared and after its T_1 measurement was complete, another one was prepared. Also, the mixture with nitroxides was not prepared sequentially (e.g., 5, 10, 15, 20 μL) rather it was done at random (e.g., 20, 5, 15, 10 μL) and alternating with different fullerene solutions to account for systematic errors in measurement. The stock solution was kept in the dark and stored in the refrigerator between each addition and measurement to preserve its integrity. All measurements were done in one sitting as to account for the fluctuations between days, e.g., temperature, shimming with the spectrometer.

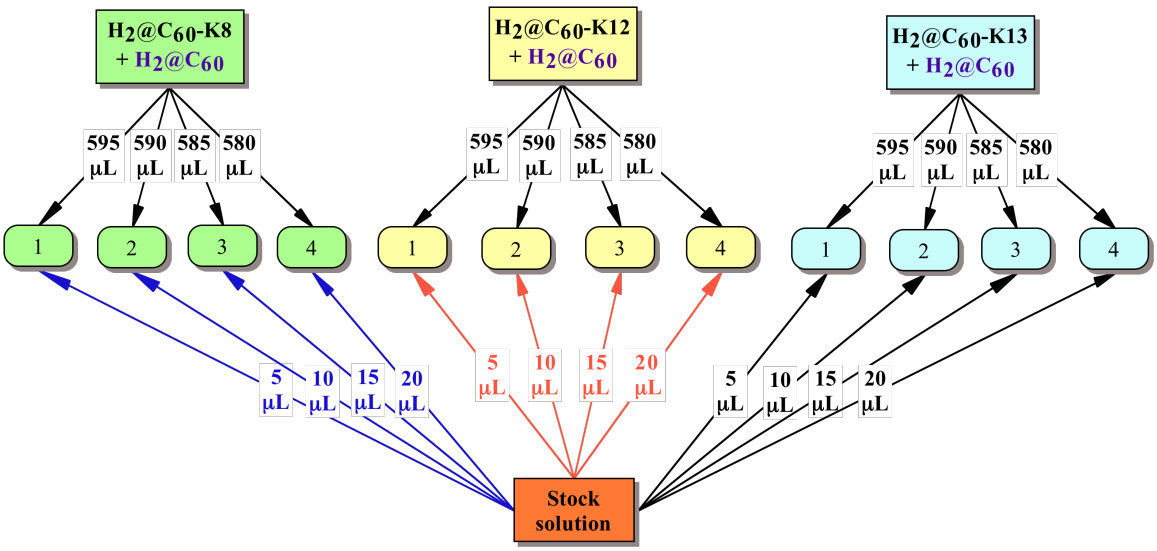

Figure 4.3: Illustration of sample preparation for relaxivity measurements. Colors are provided for clarity and not indicative of the color of the actual solution. For structures please refer to Chart 4.1.

We tried first using H*@C_{60} and H*@open-C_{60} (H*=H_2 and HD) because it made sense to also acquire relaxivity for HD inside different fullerenes with one shot; however, the broadening of the line shape because of the presence of paramagnetic species made it impossible, especially at higher nitroxide concentrations, e.g., above 20 mM. Therefore, only the relaxivity for H_2 are presented. It will be necessary to synthesize a new batch of H_2*@fullerene containing a much higher final percentage of HD (Table 4.8) and using line fit in Method 3 of Figure 2.19 of in order to obtain its R_x values.

4.5.2 NMR Measurements

All the spectra were obtained on a Bruker DMX-500 NMR spectrometer. The operating frequency for ^{1}H is 500.13 MHz. The 90° pulse was recalibrated with each sample. Typical 90° pulse (p1) was between 8.1-8.4 μsec. T_1 measurements were performed using the inverse-recovery pulse sequence (Figure 3.8): relaxation delay → π → τ → π/2 → acquire, with 15 values for the variable delay τ, in the range 0.001-1 s (Table 3.1.VD3) for H_2@C_{60} and H_2@open-C_{60}, respectively. The number of scans (NS) was increased with samples containing higher concentration of nitroxides.

Table 4.8: Insertion conditions for desired final H2 : D2 : HD ratio and its corresponding graph.

$\%H_2$ init	$\%D_2$ init	change	$\%H_2$ final	$\%D_2$ final	%HD	HD:H_2	HD:D_2
0.00	100.00	0.00	0.00	100.00	0.00	-	0.00
5.00	95.00	4.75	0.25	90.25	9.50	38.00	0.11
10.00	90.00	9.00	1.00	81.00	18.00	18.00	0.22
15.00	85.00	12.75	2.25	72.25	25.50	11.33	0.35
20.00	80.00	16.00	4.00	64.00	32.00	8.00	0.50
25.00	75.00	18.75	6.25	56.25	37.50	6.00	0.67
30.00	70.00	21.00	9.00	49.00	42.00	4.67	0.86
35.00	65.00	22.75	12.25	42.25	45.50	3.71	1.08
40.00	60.00	24.00	16.00	36.00	48.00	3.00	1.33
45.00	55.00	24.75	20.25	30.25	49.50	2.44	1.64
50.00	50.00	25.00	25.00	25.00	50.00	2.00	2.00
55.00	45.00	24.75	30.25	20.25	49.50	1.64	2.44
60.00	40.00	24.00	36.00	16.00	48.00	1.33	3.00
65.00	35.00	22.75	42.25	12.25	45.50	1.08	3.71
70.00	30.00	21.00	49.00	9.00	42.00	0.86	4.67
75.00	25.00	18.75	56.25	6.25	37.50	0.67	6.00
80.00	20.00	16.00	64.00	4.00	32.00	0.50	8.00
85.00	15.00	12.75	72.25	2.25	25.50	0.35	11.33
90.00	10.00	9.00	81.00	1.00	18.00	0.22	18.00
95.00	5.00	4.75	90.25	0.25	9.50	0.11	38.00
100.00	0.00	0.00	100.00	0.00	0.00	0.00	-

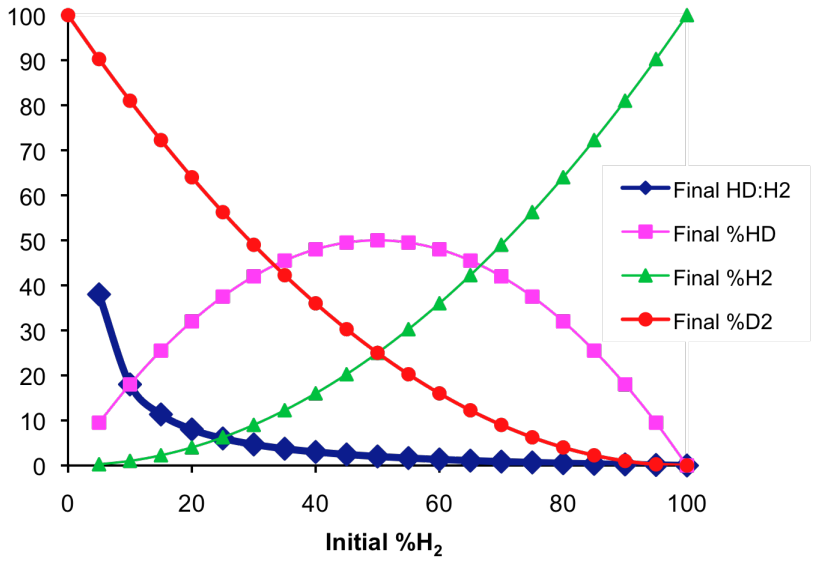

4.5.3 What to do when discrepancy arises with previous results

There have been many trials in establishing the best experimental procedure and parameters, as well as reproducing previous published/unpublished results on the relaxivity of $H_2@C_{60}$ in the

presence of the paramagnetic nitroxide radical, TEMPO. A general procedure for comparing results with those of someone else in the group is described below because this is especially important when a discrepancy remains and one has to worry about a number of subtle details. (1) See if one can find original data and plot them yourself. In my case, I had to find Dr. Elena Sartori's original data on the values of T_1 as a function of concentration of nitroxides and refit them myself. (2) Check both the T_1's at my concentrations also. This will check to see if the program or method of extracting a rate constant might lead to a different number. (3) The other possibilities include the actual concentrations that are plotted. Specifically, if Dr. Sartori or my nitroxide is not 100% pure, then the numbers on the x-axis will be different and the slope will be different. Though the actual discrepancy between Dr. Sartori and my data is not large, it was worth trying to figure out. For the short term, I focused on the purity of the nitroxides, TEMPO and 4-Oxo-TEMPO by making calibration plot with a fresh and known sample of TEMPO. The method is simple but care in accuracy of the sample preparation is necessary to obtain reliable results. Once the control solutions are prepared, EPR measurements are taken and the integral of the EPR signal of the nitroxide are plotted against the actual concentration that was prepared. From this, one can then determine/calculate the actual concentration of the nitroxide sample used in the relaxivity experiments.

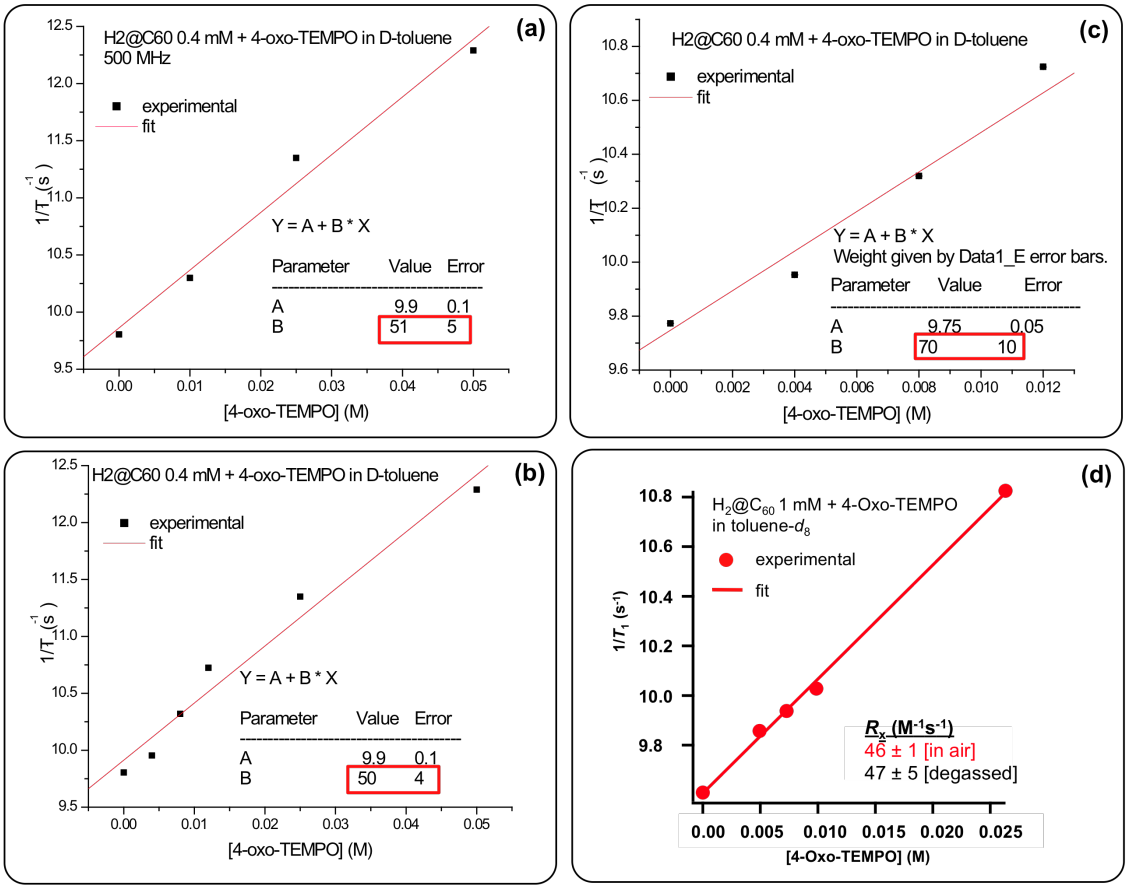

Figure 4.4: Relaxation rates as a function of the concentration of 4-Oxo-TEMPO in toluene-d_8 at 300 K. The slope from the fit corresponds to relaxivity proportionality constant R_x. Plots (a), (b) and (c) corresponds to previous results measured by Elena. The numbers enclosed in the red box, or parameter B, is the R_x value and its error from the linear regression. Parameter A corresponds to $1/T_{1,d}$ of Equation 4.2. Plot (d) is a representative graph measured by me. The R_x value in red was measured in air, the R_x value in black was obtained with a degassed sample. Note that the range in the x-axis across the four plots contributed to the discrepancy of the R_x values.

Based on Figure 4.4, Dr. Sartori and I actually had the same results for 4-Oxo-TEMPO. She and I differed in the concentrations for $H_2@C_{60}$, 0.4 mM and 1 mM, respectively. This is reasonable because at the time that she was doing all the experiments, our $H_2@C_{60}$ inventory was scarce. Elena did linear regressions with Origin (PC program) and I via Igor (Mac program). The discrepancy between our results was due to the range in which we fitted our data. Elena excluded

from linear regression the point corresponding to the highest concentration of radicals [Figure 4.4 (a) and (b)]. She noticed that those points were always a little below others and feared that at those concentrations, the radicals where relaxing themselves and were exchanging too fast. According to Elena, the T_2 and T_1 of the radical enter the relaxivity theoretical formula and under certain conditions might affect the relaxivity. We did not get to the bottom of this issue but decided to just drop those points to avoid the risks [Figure 4.4 (c)]. On the other hand, in the reported results for H_2 (R_x = 14.5 ± 0.4 with 4-Oxo-TEMPO),[10] the points corresponding to high concentrations of nitroxides were not excluded in the relaxivity measurements because the slope did not change by including or excluding those points. The bottom line is that despite the discrepancy between Dr. Sartori's and my data, the overall conclusion that communication between the $H_2@C_{60}$ and nitroxide is unexpectedly strong doesn't change.

The solvent was changed from toluene to ODCB beyond this point (once we have resolved the issue of the apparent discrepancy) because the H_2-containing open fullerenes were much less soluble than $H_2@C_{60}$ and the signal-to-noise really suffered. The T_1 values were also obtained in air with a standard 5 mm NMR tube without further degassing with argon in a J. Young tube because we found that the results were the same but with a much larger error from the degassed sample due to sample evaporation/loss during bubbling. We also found that the maximum allowed concentration before the NMR spectrum got wiped out by the paramagnetic species and the results became unreliable above 40 mM and that the best range of concentration of the nitroxides to work with in determining the proportionality constant R_x for relaxivity is between 0-25 mM with more data points between 0-15 mM.

4.6 References

(1) Lauffer, R. B. Paramagnetic metal complexes as water proton relaxation agents for NMR imaging: theory and design. *Chem. Rev.* **1987**, *87*, 901-927.

(2) Lauterbur, P. C. Image Formation by Induced Local Interactions: Examples Employing Nuclear Magnetic Resonance. *Nature* **1973**, *242*, 190-191.

(3) Lauterbur, P. C. Mendoca-Dias, M. H.; Rudin, A. M. *Frontier of Biological Energetics*; Dutton, P. L. Leigh, L. S.; Scarpa, A., Eds. Academic Press, Inc.: New York, 1978; p. 752.

(4) Young, I. R. Clarke, G. J. Bailes, D. R. Pennock, J. M. Doyle, F. H.; Bydder, G. M. Enhancement of relaxation rate with paramagnetic contrast agents in NMR imaging. *J. Comp. Tomography* **1981**, *5*, 543-7.

(5) Carr, D. H. Brown, J. Bydder, G. M. Weinmann, H.-J. Speck, U. Thomas, D. J.; Young, I. R. Intravenous Chealated Gadolinium as a Contrast Agent in NMR Imaging of Cerebral Tumours. *The Lancet* **1984**, *323*, 484-486.

(6) Keana, J. F. W. Pou, S.; Rosen, G. M. Nitroxides as potential contrast enhancing agents for MRI application: Influence of structure on the rate of reduction by rat hepatocytes, whole liver homogenate, subcellular fractions, and ascorbate. *Magn. Res. Med.* **1987**, *5*, 525-536.

(7) Bennett, H. F. Brown, R. D. Koenig, S. H.; Swartz, H. M. Effects of nitroxides on the magnetic field and temperature dependence of $1/T_1$ of solvent water protons. *Magn. Res. Med.* **1987**, *4*, 93-111.

(8) Vallet, P. Haverbeke, Y. van; Bonnet, P. A. Subra, G. Chapat, J.-pierre; Muller, R. N. Relaxivity enhancement of low molecular weight nitroxide stable free radicals: Importance of structure and medium. *Magn. Res. Med.* **1994**, *32*, 11-15.

(9) Jenks, W. S.; Turro, N. J. Exchange Effects and CIDEP. *Res. Chem. Interm.* **1990**, *13*, 237-300.

(10) Sartori, E. Ruzzi, M. Turro, N. J. Komatsu, K. Murata, Y. Lawler, R. G.; Buchachenko, A. L. Paramagnet enhanced nuclear relaxation of H_2 in organic solvents and in $H_2@C_{60}$. *J. Am. Chem. Soc.* **2008**, *130*, 2221-5.

5 Supramolecular Effects on Paramagnetic Interaction between a Nitroxide Incarcerated within a Nanocapsule with a Nitroxide in Bulk Aqueous Media

5.1 Background

The host molecule, octa acid (OA) in this study is a synthetic resorcinarene derivative capable of forming a dimeric capsular structure by self-assembly in an aqueous medium. Its structure and dimensions are shown in Figure 5.1. The synthesis of OA was reported

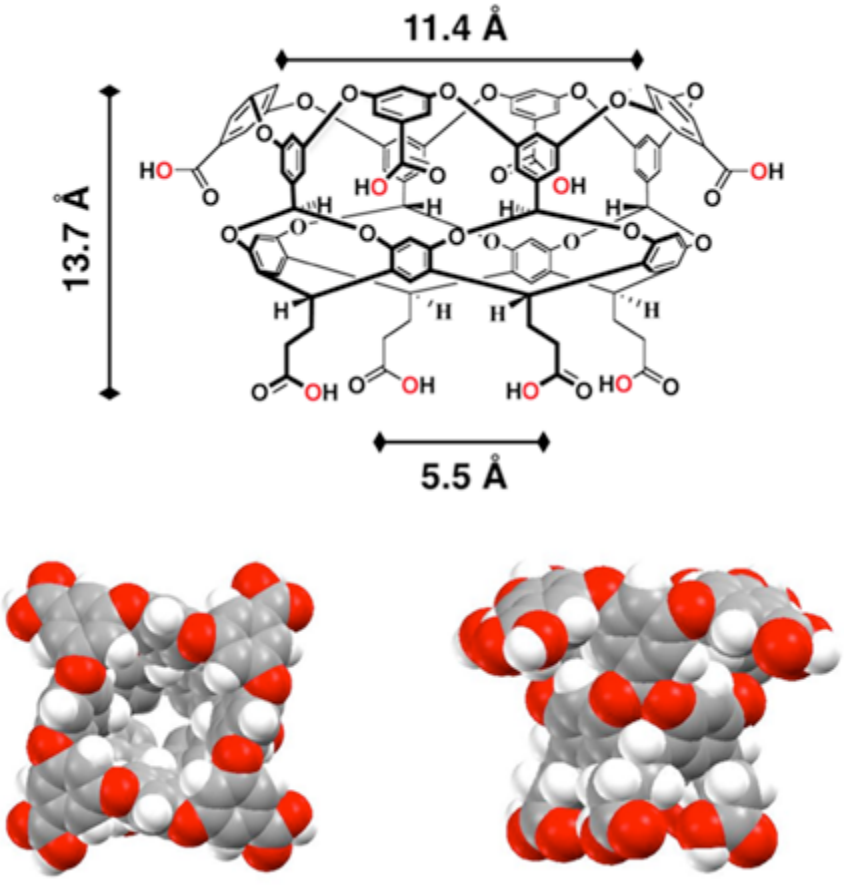

Figure 5.1: Top: Chemical structure, dimensions and pictorial representation of octa acid (OA). Bottom: Space filling molecular models of OA.

by Gibb in 2004.[1] The molecule has eight carboxylic acid groups, four on top and four on the bottom rims; hence the name octa acid. The carboxylic acid groups are on the *external* surface of the molecule and it is soluble in basic aqueous solutions (pH ≥ 9). The top rim and the interior of the cavity are hydrophobic. The major driving force for binding of guest(s) to OA in aqueous solutions is the solvophobic interaction[2] - the host provides a hydrophobic pocket for the guests. When a guest that is insoluble in water is added to an aqueous solution of OA, two OA molecules come together and enclose the guest to form a self-assembled hemicarceplex, or 2:1 OA:Guest complex, and depending on the size of the guest molecule, the hemicarceplex can also form a 2:2 complex with smaller guest molecules.

Previous binding studies involving naphthalene, anthracene and tetracene where two guest molecules of naphthalene and anthracene were incarcerated inside the OA cavity forming a 2:2 complex resulted in greatly enhanced excimer emission due to greater local concentration of the substrates. Only one molecule of the larger tetracene was accommodated inside the cavity forming a 2:1 complex (Figure 5.2).[3]

Now, instead of using the host, octa acid as a means to alter excited-state chemistry of aromatic guests[3] or in general, using the host as a means to bring about selectivity in a chemical[4,5] or photochemical[6,7,8,9] reaction of the guest, we used nitroxide guests as probes to investigate the changes in their local environment (Section 1.1) in the presence of octa acid by electron paramagnetic resonance (EPR) spectroscopy.

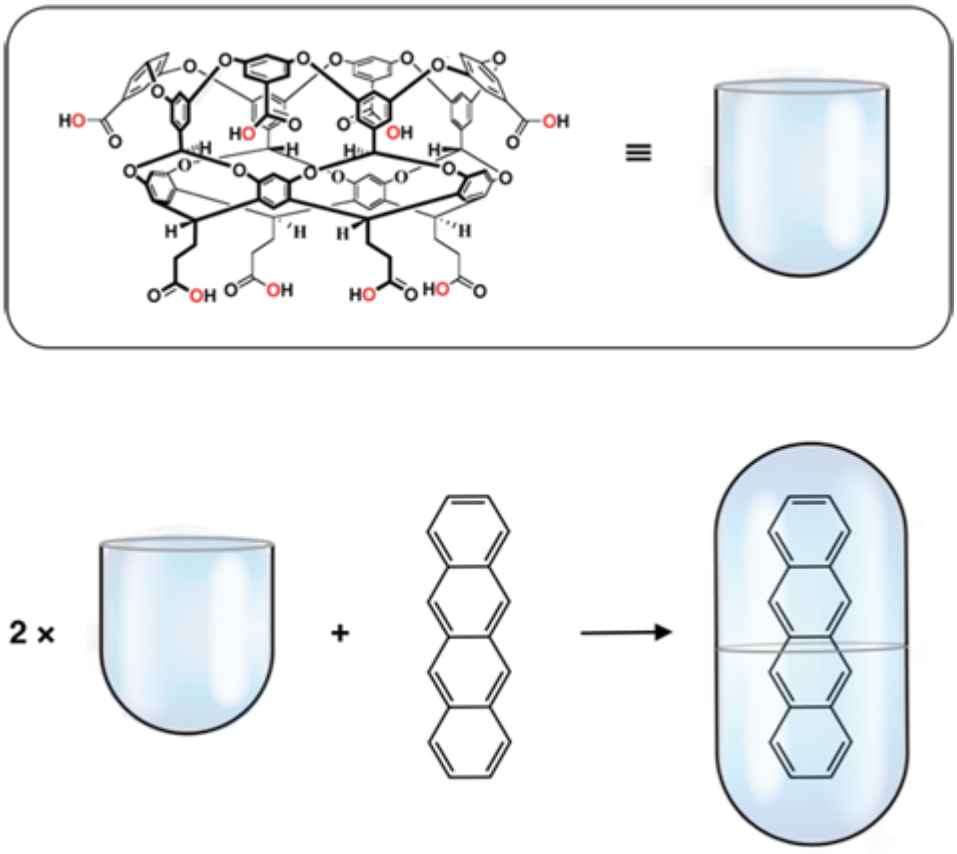

Figure 5.2: Top: Cartoon representation of octa acid cavity. Bottom: Illustration of formation of complex between OA and tetracene.

5.2 Scope of this work

The results presented in this chapter of the thesis are detailed analyses of the experimental EPR data of four combinations of nitroxide guests (Chart 5.1) with OA to give the following information: (a) the ability of OA to encapsulate internal guests of different polarity (Sections 5.3.1 and 0); (b) an analysis of the interacting properties of guests on the internal and external OA surface by Coulombic forces (Sections 5.3.1 and 0) as well as hydrophobic interactions (Section 5.3.1 and 0); (c) a characterization of the electron spin-spin exchange through the capsule's orbitals between the internal and the external guests of the OA capsuleplex by employing a ^{15}N-labeled incarcerated nitroxide and a ^{14}N-labeled free nitroxide in the external

aqueous phase (Section 5.3.2). This type of exchange, or electronic communication, in which interactions occur as a result of the overlap of the orbitals of the incarcerated guest with the orbitals of molecules present outside is termed “superexchange”. Finally, we will show that superexchange interactions can be controlled by Coulombic attraction and repulsion between a charged Guest@Host complex and charged molecules in the bulk aqueous phase (Section 5.3.2).

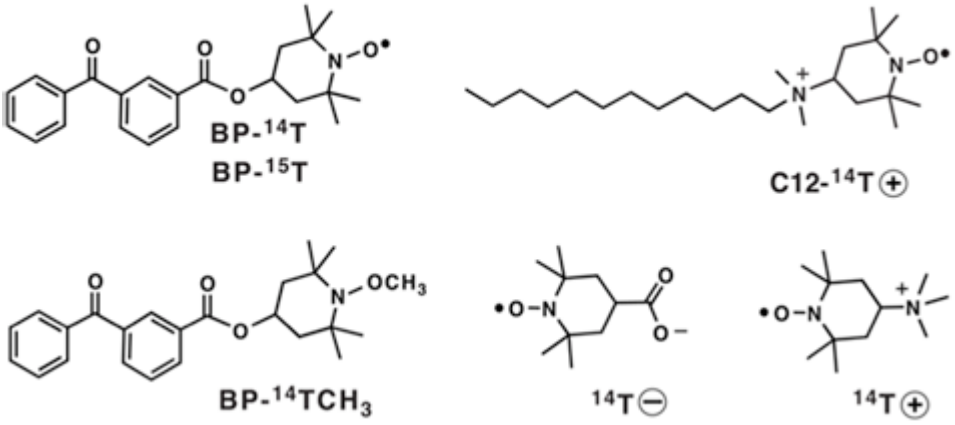

Chart 5.1: Chemical structures and corresponding abbreviations for the guest molecules.

Chart 5.1 shows the chemical structures of the different paramagnetic probes, as internal/external guests. They were selected based on their hydrophilic-hydrophobic nature and for the hydrophilic guests; we chose one with a positive charge and one with a negative charge. The structures in Chart 5.1 are accompanied by their corresponding abbreviations that will be referred to in the rest of this chapter. The superscripts 14 and 15 indicate the isotopic labeling on the nitrogen atom of the nitroxide moiety. The ^{14}N-labeled positively charged guest is denoted ^{14}T⊕, and the ^{14}N-labeled negatively charged guest is denoted ^{14}T⊖ (Chart 5.1). We will show that there is a Coulombic attraction and repulsion between the charged guests, ^{14}T⊕ and ^{14}T⊖ in the bulk aqueous phase with the negatively charged carboxylate groups (COO-) on the exterior of the OA (Figure 5.1 shows the protonated structure. Under our conditions, the pH ≥ 9 and some

of the carboxylic acid groups are deprotonated). C12-^{14}T⊕ in Chart 5.1 is a guest consisting of a twelve-carbon chain (C12) covalently linked to a positively charged trimethylammo-^{14}N-labeled TEMPO. It bears both hydrophilic and hydrophobic moieties. BP-T is a benzophenone derivative with TEMPO covalently linked by an ester functional group (Chart 5.1). It is a hydrophobic guest and from previous studies on benzophenone, it has been shown that the hydrophobic moiety is easily internalized by the OA cage to form a 2:1 OA:BP complex.[10] BP-^{14}TCH$_3$ in Chart 5.1 denotes the diamagnetic version of BP-T where the nitroxide radical is capped with a methyl group. These systems were analyzed by both NMR[11] and EPR spectroscopy. Information obtained from the nitroxide probes about the local environments and other relevant parameters were extracted from simulations of the experimental EPR spectrum by Dr. M. Francesca Ottaviani.

5.3 Results and Discussion

The EPR spectra of each probe in the presence of increasing concentration of OA were analyzed and discussed. A comparison between the different guests on their interacting abilities and localization at different interacting sites of OA are provided. Chart 5.2 is a simplified cartoon depiction of the relevant components for each of the nitroxide guests as well as octa acid and water molecule. This will be used later to help illustrate what the parameters mean in terms of the overall picture for the system.

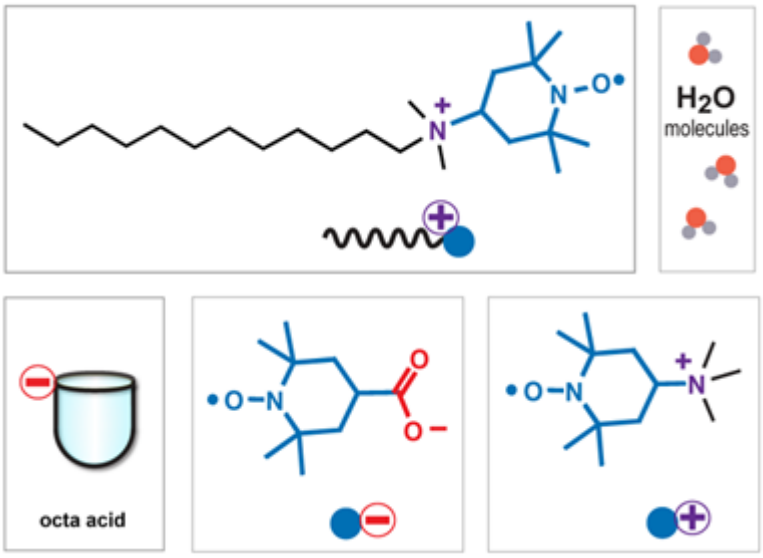

Chart 5.2: Cartoon depiction of the chemical structure for guest and host molecule.

5.3.1 ^{14}T⊕ and C12-^{14}T⊕ with increasing relative amounts of OA

Examples of the experimental spectra (normalized) obtained for the ^{14}T⊕@OA system at different OA/^{14}T⊕ ratios are shown in Figure 5.3.

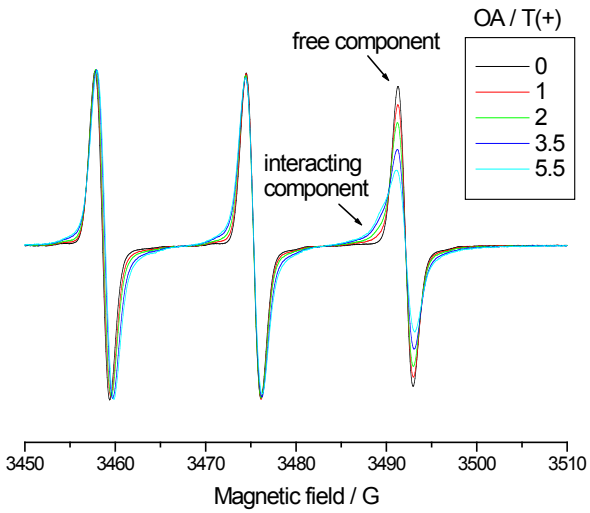

Figure 5.3: Experimental EPR spectra for the ^{14}T⊕@OA system at different OA/^{14}T⊕ ratios.

As indicated by the arrows in Figure 5.3, two components contributed to the EPR spectra, which were extracted by subtraction of the spectra at different OA/^{14}T⊕ ratios.

The computation,[12] by means of the well established procedure by Budil and Freed,[13] allowed to extract the following main magnetic and mobility parameters: g_{ii}, A_{ii} and τ (Section 1.1). (a) The electron spin main components of the tensor, g_{ii} for the coupling between the electron spin and the magnetic field were assumed to be 2.009, 2.006, 2.002, unless specified. (b) The nitrogen hyperfine main components of the tensor, A_{ii} for the coupling between the unpaired electron and the nuclear electron spin, ^{14}N(I=1) and ^{15}N(I=1/2). An increase in this parameter corresponds to an increase in the polarity of environment experienced by the probes.[14] The A_{xx} and A_{yy} components of the tensor for ^{14}N probes were assumed to be equal and 7 G unless otherwise specified. The parameter reported for the polarity variation is A_{zz}. (c) The correlation time for the rotational motion, τ corresponds to the strength of the interaction of the probe with its environment and unless otherwise specified, we assumed a Brownian rotational diffusional motion, with $\tau = 1/(6D)$, where D is the diffusion coefficient. By subtraction of the spectra, we extracted and computed the components mentioned above and provided the percentage of the components.

The two signals indicated with arrows in Figure 5.3 were characterized by different correlation of motion (mobility parameter) and different A_{zz} values (polarity parameter). The component characterized by slower mobility and lower polarity was denoted as “interacting”, since it reports on the interactions of ^{14}T⊕ with internal/external groups on the OA; the component characterized by faster mobility and higher polarity was designated as “free” component, since it reports on the probes which are free in solution or fast exchanging between

the OA surface and the bulk solution. Some examples of computation of the different components are reported in Figure 5.20 of Section 5.5.

The analysis of the spectra at different OA/^{14}T⊕ ratios from Figure 5.20 is summarized in Figure 5.4. The graph on the left plots the variation of the percentage of the interacting component as a function of the OA/^{14}T⊕ ratio. The graph on the right shows the correlation time for motion (both for the free and the interacting components) and the A_{zz} value (for the interacting component) as a function of the OA/^{14}T⊕ ratio.

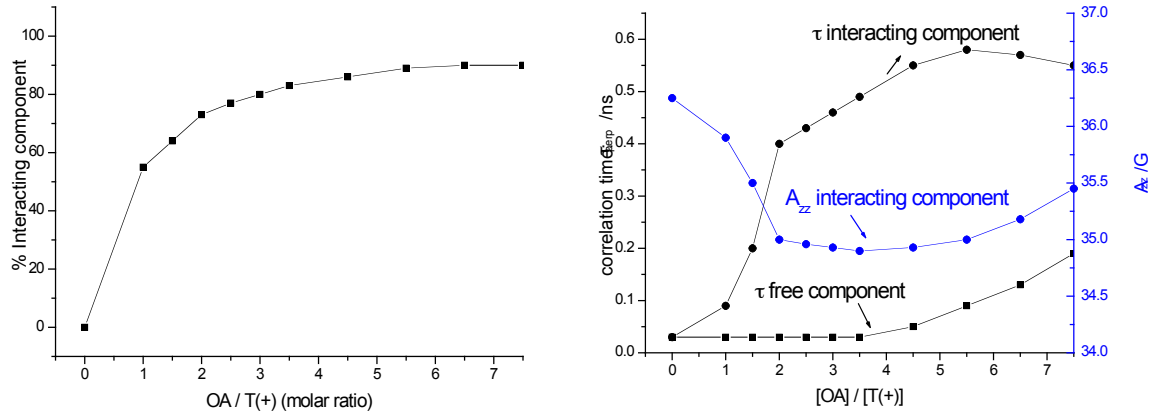

Figure 5.4: Left: Plot of the percent interacting component as a function of the OA/^{14}T⊕ molar ratio. Right: Correlation time, τ (ns) [left axis] for motion and hyperfine, A_{zz} (G) [right axis] for both the free and interacting components as a function of the OA/^{14}T⊕ molar ratio.

The results for C12-^{14}T⊕ (Chart 5.1) were different from ^{14}T⊕ despite the same positive charge and similar moiety. Only the interacting component was present for C12-^{14}T⊕ in the presence of OA. Its corresponding τ and A_{zz} parameters are reported in Figure 5.5.

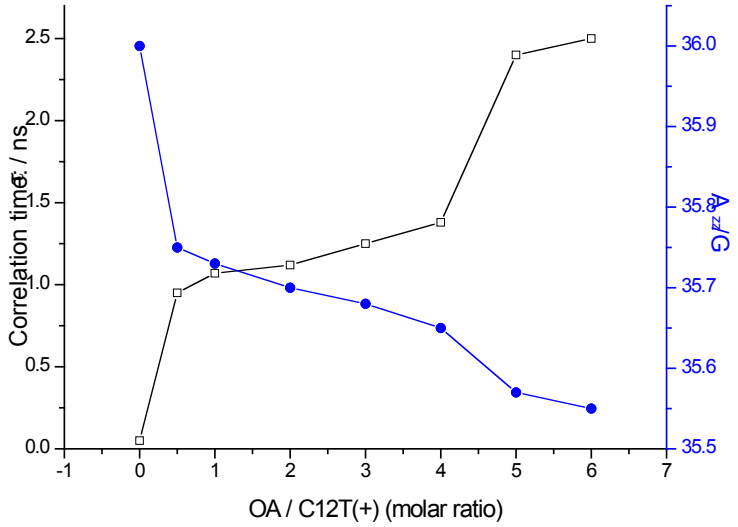

Figure 5.5: Correlation time, τ (ns) [left axis] and hyperfine, A_{zz} (G) [right axis] for interacting components as a function of the OA/ C12-^{14}T⊕ molar ratio.

On the basis of the data in Figure 5.4 and Figure 5.5, the observation on both the ^{14}T⊕@OA and C12-^{14}T⊕@OA systems are as follows:

1. The steep increase in the relative intensity of the interacting component of ^{14}T⊕ occurs from OA/^{14}T⊕ = 0 to 2 [Figure 5.6 (a) to (b)], which is in agreement with the complexation between ^{14}T⊕ and OA [Figure 5.6 (b)]. At OA/^{14}T⊕ > 2 the intensity slowly decreases and at OA/^{14}T⊕ = 6-7, the free component is barely detectable [Figure 5.6 (c)]. This we can assume that all ^{14}T⊕ are involved in the complexation

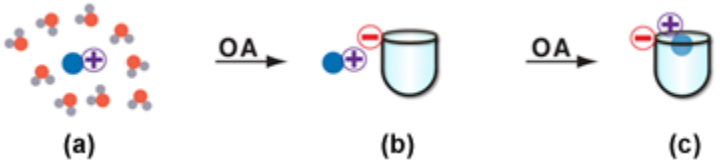

Figure 5.6: Cartoon depiction of interaction between ^{14}T⊕ and OA as a function of increasing concentration of OA. Cartoon in (a) is ^{14}T⊕ free in solution before addition of OA. (b) shows the senario where OA/^{14}T⊕ = 0 to 2. (c) illustrates the possible interacting site when the OA/^{14}T⊕ >2.

with OA either on its external surface of the OA cage and/or inside the OA cavity.

2. The free component of ^{14}T⊕ levels off at OA/^{14}T⊕ ~ 4, then its mobility slows down as shown by an increase in the correlation time for motion. This is because of an increase in the microviscosity as a result of an increased local concentration of OA felt by the probes. The decrease in τ is accompanied by a decrease in the hyperfine-coupling constant, which reflects a decrease in the environmental polarity of the probes indicating that the nitroxide groups are approaching the less polar (hydrophobic) parts of the OA. This is also in agreement with the cartoon in Figure 5.6).
3. The interacting component of both ^{14}T⊕ and C12-^{14}T⊕ is anisotropic; therefore, a tilt of the probe's main rotational axis is forced to shift with respect to the magnetic axis, which provides a different orientation of the NO moiety in probes@OA with respect to the free probes (Figure 5.20).
4. The correlation time of the interacting component increases with the increasing OA concentration at least up to OA/probe = 4 corresponding to a decrease in mobility of the probe when interacting with the OA cage.
5. The preferred complexation site between the guests and OA was determined based on the decrease in A_{zz} with an increase in τ corresponding to a less polar environment or a partially encapsulated probe inside the OA cavity. In the case of ^{14}T⊕, it may interact with both the hydrophilic surface and hydrophobic pocket of the OA (Figure 5.6). On the other hand, the C12 chain of C12-^{14}T⊕ is anchored inside the hydrophobic pocket of the OA (Figure 5.7), thus preventing exchange with a free C12-^{14}T⊕ resulting in a decrease in mobility relative to ^{14}T⊕. The NMR results are also in line with this picture.

6. A completely opposite behavior is observed for ^{14}T⊕ and C12-^{14}T⊕ at the highest OA/probe ratios (5-6): a slight increase in mobility and polarity was calculated for ^{14}T⊕, whereas a decrease in both mobility and polarity was calculated for C12-^{14}T⊕. This may be due to the formation of OA aggregates which partially expel ^{14}T⊕ from the OA internal surface thus increasing both parameters. C12-^{14}T⊕ cannot escape due to its hydrophobic tail and is squeezed into the OA capsules [Figure 5.7 (c)].

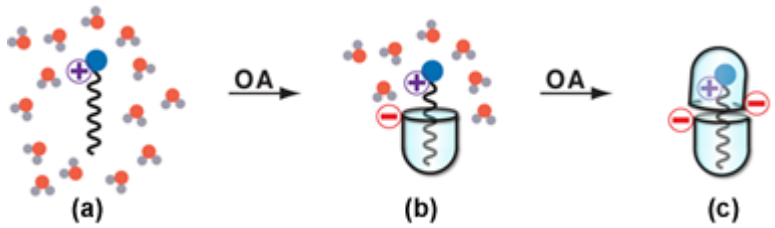

Figure 5.7: Cartoon depiction of interaction between C12-^{14}T⊕ and OA as a function of increasing concentration of OA. Cartoon in (a) is C12-^{14}T⊕ free in solution before addition of OA. (b) shows the senario where OA/ C12-^{14}T⊕ ratio is 1:1. (c) illustrates 2:1 ratio of OA/ C12-^{14}T⊕ to form C12-^{14}T⊕@$(OA)_2$ complex.

5.3.2 $^{14}T\ominus$ with increasing relative amounts of OA

Figure 5.8 are superposition of experimental spectra recorded for $^{14}T\ominus$ in the absence and in the presence of increasing concentration of OA.

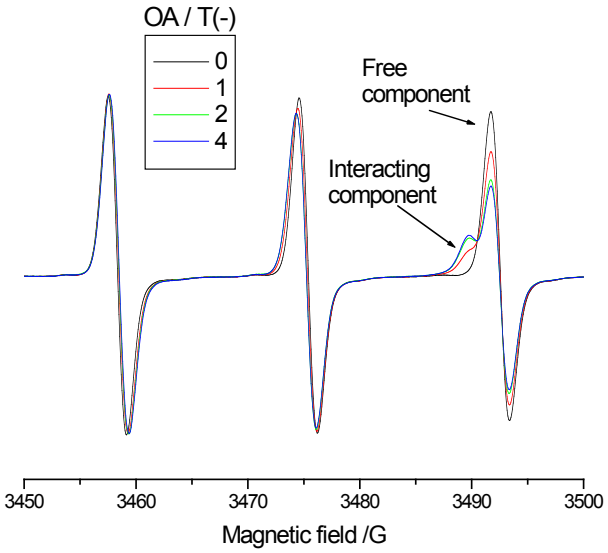

Figure 5.8: Experimental EPR spectra for the $^{14}T\ominus$@OA system at different OA/$^{14}T\ominus$ ratios.

The spectra are also composed of free and interacting components. These components were extracted by subtraction and were computed as shown in Figure 5.21 of Section 5.5. The parameters extracted from the computation, e.g., the relative percentage of the components, A_{zz} and τ (for the interacting component), are plotted as a function of the OA/$^{14}T\ominus$ molar ratio in Figure 5.9. The graph on the left is a plot of the percent interacting component as a function of the OA/$^{14}T\ominus$ molar ratio. The graph on the right is the correlation time, τ (ns) [left axis] for motion and hyperfine, A_{zz} (G) [right axis] for the interacting components as a function of the OA/$^{14}T\ominus$ molar ratio.

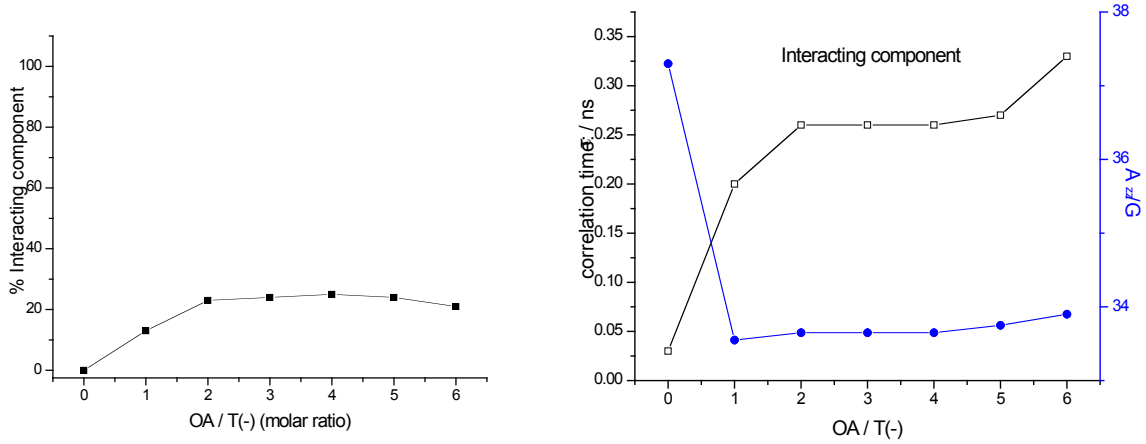

Figure 5.9: Left: Plot of the percent interacting component as a function of the OA/^{14}T⊖ molar ratio. Right: Correlation time, τ (ns) [left axis] for motion and hyperfine, A_{zz} (G) [right axis] for the interacting components as a function of the OA/^{14}T⊖ molar ratio.

On the basis of the data in Figure 5.9, the free component of ^{14}T⊖ is consistent and has no dependence on the concentration of OA [Figure 5.10 (b)] with a smaller contribution of the interacting component relative to ^{14}T⊕. In addition, ^{14}T⊖ has a higher mobility but a lower polarity which is indicative of its localization in less interacting and nonpolar sites: inside the OA hydrophobic pocket [Figure 5.10 (c)]. This can be explained on the basis of charge repulsion between the negatively charged COO^- groups on OA and ^{14}T⊖.

1. The main variation in the parameters τ and A_{zz} is from 0 to 1-2 OA/^{14}T⊖ ratios. Between 2 and 4, the variations in τ and A_{zz} are negligible, while the interacting component slightly increased.
2. At OA/^{14}T⊖ > 4, both the relative amount of the interacting component and the mobility decrease. This is because the OA is negatively charged at pH 9 and with increasing OA concentrations, forces of repulsion also increase. This forces the negatively charged ^{14}T⊖ to seek refuge in the internal hydrophobic pocket of OA. In the limit where the

OA: $^{14}T\ominus$ forms a 2:2 complex, the internal pocket is no longer available/capable to host additional $^{14}T\ominus$ probes (Figure 5.10).

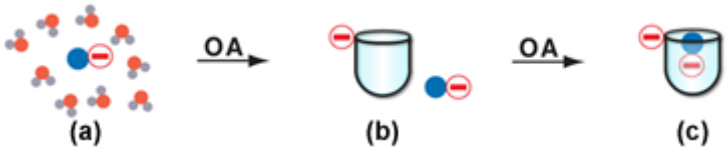

Figure 5.10: Cartoon depiction of the lack of interaction between $^{14}T\ominus$ and OA due to Coulombic repulsion between like charges. With increasing OA concentration, $^{14}T\ominus$ are forced to refuge into the internal hydrophobic pocket of OA as illustrated in (c).

5.3.1 BP-^{14}T with increasing relative amounts of OA

The BP-^{14}T probe is insoluble in water. But in the presence of OA, it forms a 2:1 OA:BP-^{14}T complex and renders the probe soluble. Figure 5.11 shows superimposition of experimental spectra (normalized to the same intensity) of OA / ^{14}BP-T at 1, 2, and 4

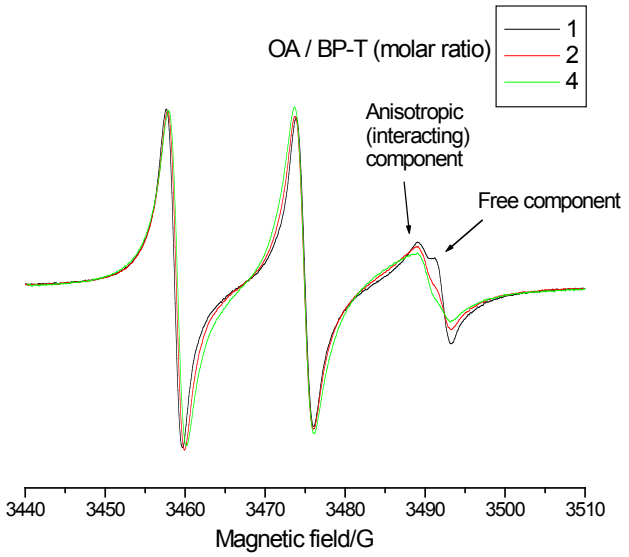

Figure 5.11: Experimental EPR spectra for the BP-^{14}T@OA system at different OA/ BP-^{14}T ratios.

molar ratios. The spectra indicate contributions from two main components, termed "free" and "anisotropic-interacting" (arrows in the Figure 5.11). The computations of the components from subtraction of the spectra at different OA / BP-^{14}T ratios, is shown in Figure 5.22 in Section 5.5. The intensity of the free component decreased with increasing OA concentration. The interacting-anisotropic component (black plot in Figure 5.12) and the solubility of BP-^{14}T, as determined by percentage from the absolute spectral intensity (green plot in Figure 5.12), reaches a maximum at OA/ BP-^{14}T = 2. At OA / BP-^{14}T > 2 a small amount (up to about 10 %) of a "slow" component also contributed to the overall EPR signal. This component is "slow" because an increased correlation time for motion with respect to the anisotropic component (bottom center of Figure 5.22).

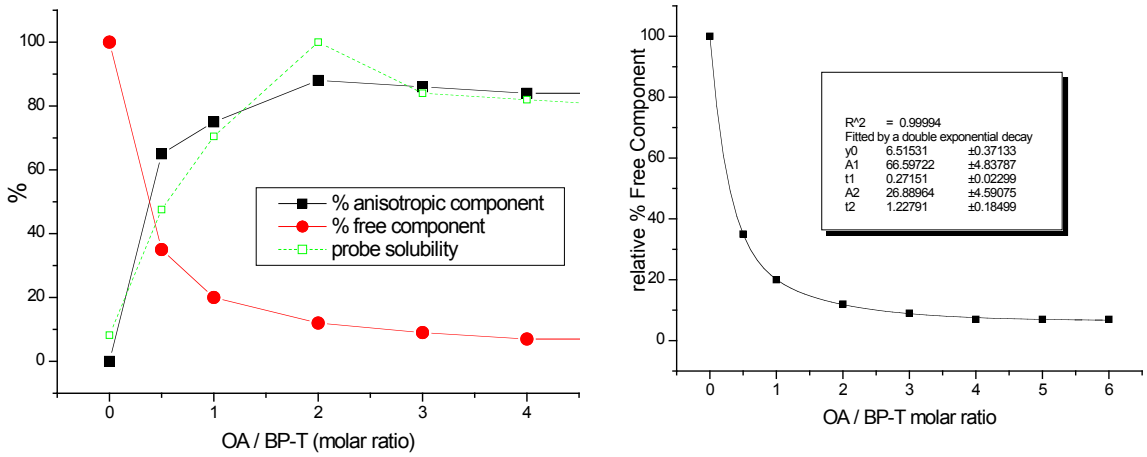

Figure 5.12: Left: Plot of the percent anisotropic-interacting and free components, as well as the percentage probe solubility as a function of the OA/BP-^{14}T molar ratio. Right: Percentage of free component as a function of the OA/ BP-^{14}T molar ratio.

The analysis of the relative intensities and the parameters extracted from computation suggests the following:

1. The free component corresponds to the probe, BP-T in water. It is at very low concentrations because BP-T is hydrophobic and insoluble in water as mentioned earlier.

2. The addition of OA solubilized BP-T due to encapsulation of the probe into the OA capsule forming a 2:1 complex of OA: BP-T or BP-T@$(OA)_2$ capsuleplex (Figure 5.13).

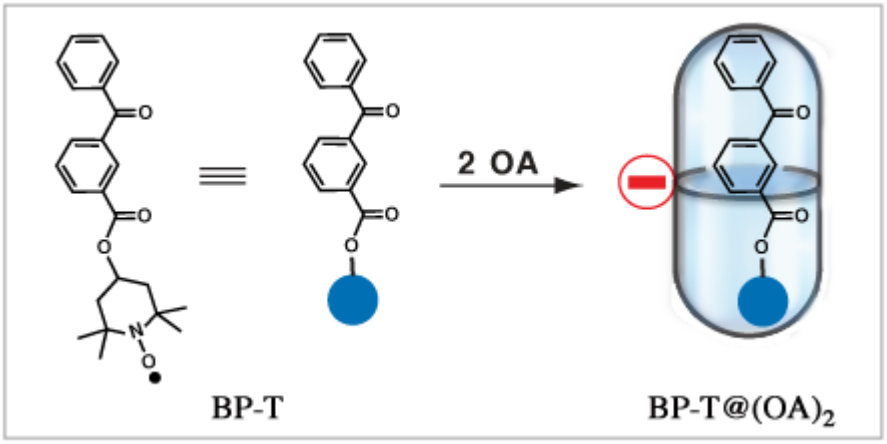

Figure 5.13: Cartoon depiction for the formation of 2:1 OA/BP-T complex, or BP-T@$(OA)_2$ capsuleplex.

3. The formation of the BP-T@$(OA)_2$ capsuleplex is also confirmed by the decrease of both the environmental polarity, A_{zz} and the probe mobility, τ.
4. The anisotropic character of the encapsulated probe determined by computation of the anisotropy of the g_{ii} values or tilt of the main rotational axis, indicated that a self-assembly of the 2:1 complex was favored and that the probe is forced to sit at an incline inside the capsule as two OAs come together and close on itself.
5. The OA / BP-T = 2 molar ratio corresponds to maximum solubility and maximum relative amount of the anisotropic-interacting component, in agreement with the formation of BP-T@$(OA)_2$ capsuleplex (Figure 5.13).
6. The slow component, which was formed in small amounts at the highest OA / BP-T ratios, has the same polarity, A_{ii} as the anisotropic component, yet with a slower mobility. In addition, the anisotropic-interacting component is almost lost. We ascribe this slow component to the compression felt by the probes as they are squeezed into the capsule

due to the high OA concentration. In other words, the excess empty OA exert a pressure onto the BP-T@$(OA)_2$ capsules by means of collisions, thus also increasing the ionic character of the solution.

7. The variations in the free component are fitted by a biexponential decay. The resulting kinetic constant for the formation of the BP-T@$(OA)_2$ complex is ~3.7 sec^{-1}.

5.3.2 BP-T@$(OA)_2$ in the presence of $^{14}T\oplus$ or $^{14}T\ominus$

After analyzing the two component systems between BP-T and OA, we introduced a three component system, using BP-T guest inside the OA capsule forming a 2:1 complex, denoted BP-T@$(OA)_2$ and either $^{14}T\oplus$ or $^{14}T\ominus$ guest in the bulk solvent. The notation for each system is denoted as follows: [$^{14}T\oplus$ + BP-T@$(OA)_2$] and [$^{14}T\ominus$ + BP-T@$(OA)_2$].

To better differentiate between the host and the guest nitroxides in our EPR analysis, we used the ^{15}N-labeled BP-^{15}T as the probe inside the OA host (Figure 5.14) and maintained the ^{14}N-labeled $^{14}T\oplus$ or $^{14}T\ominus$ as the guest outside. As a control, we used the

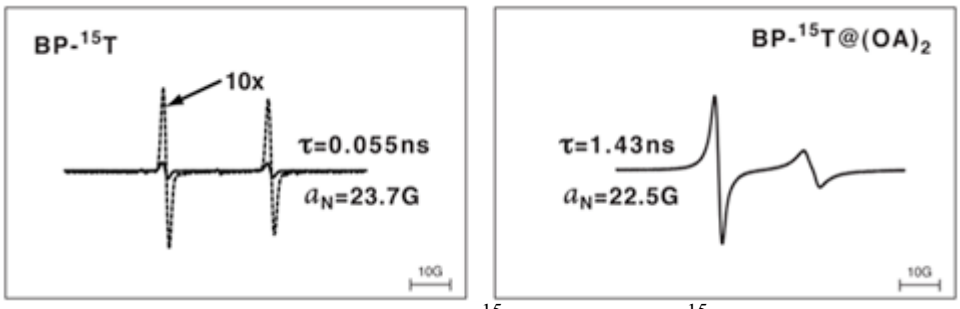

Figure 5.14: Experimental spectra of ^{15}N-labeled BP-^{15}T free in solution (Left) and BP-^{15}T@$(OA)_2$ (Right) with its corresponding extrapolated correlation times τ and hyperfine coupling constant, $a_N = A_{ii}$.

diamagnetic analog BP-TCH_3 as internal guest, BP-TCH_3@$(OA)_2$ to extract the interactions between the external guests with the $(OA)_2$ capsule in the absence of a paramagnetic internal

guest. From here forward, when the word "guest" is capitalized and expressed with "@$(OA)_2$", Guest@$(OA)_2$, it means that it is the *internal* guest which may either be the paramagnetic BP-^{15}T or the diamagnetic analog BP-TCH_3. When the guest is just "guest", it refers to the external guest in the bulk solvent.

Figure 5.15 compares the spectra obtained for Guest@$(OA)_2$ for both BP-^{15}T and BP-TCH_3 in the presence of ^{14}T⊕ (Figure 5.15 **a** and **c**) and ^{14}T⊖ (Figure 5.15 **b** and **d**) at [guest]/[Guest@$(OA)_2$] molar ratios of 1, 2, and 3. The ^{14}T⊕ spectrum is slightly broadened due to positive interactions with the capsules. In the case of the paramagnetic BP-^{15}T$(OA)_2$ capsule, the intensity of the spectrum corresponding to both the external ^{14}T⊕ and internal BP-^{15}T decreases and is ascribed to strong spin-spin interactions between the internal and the external probes. In other words, the two paramagnetic moieties are magnetically communicating, by spin exchange, through the OA-capsule wall or superexchange.

The spectra with decreasing intensity of the external and internal probes were divided by the intensity of the control spectra and plotted against increasing concentrations of guest/Guest@$(OA)_2$ ratio, denoted as [T]/[capsule] in Figure 5.16. The plot on the left showed that the decrease in intensity of the ^{14}T⊕ signal is inversely proportional to the

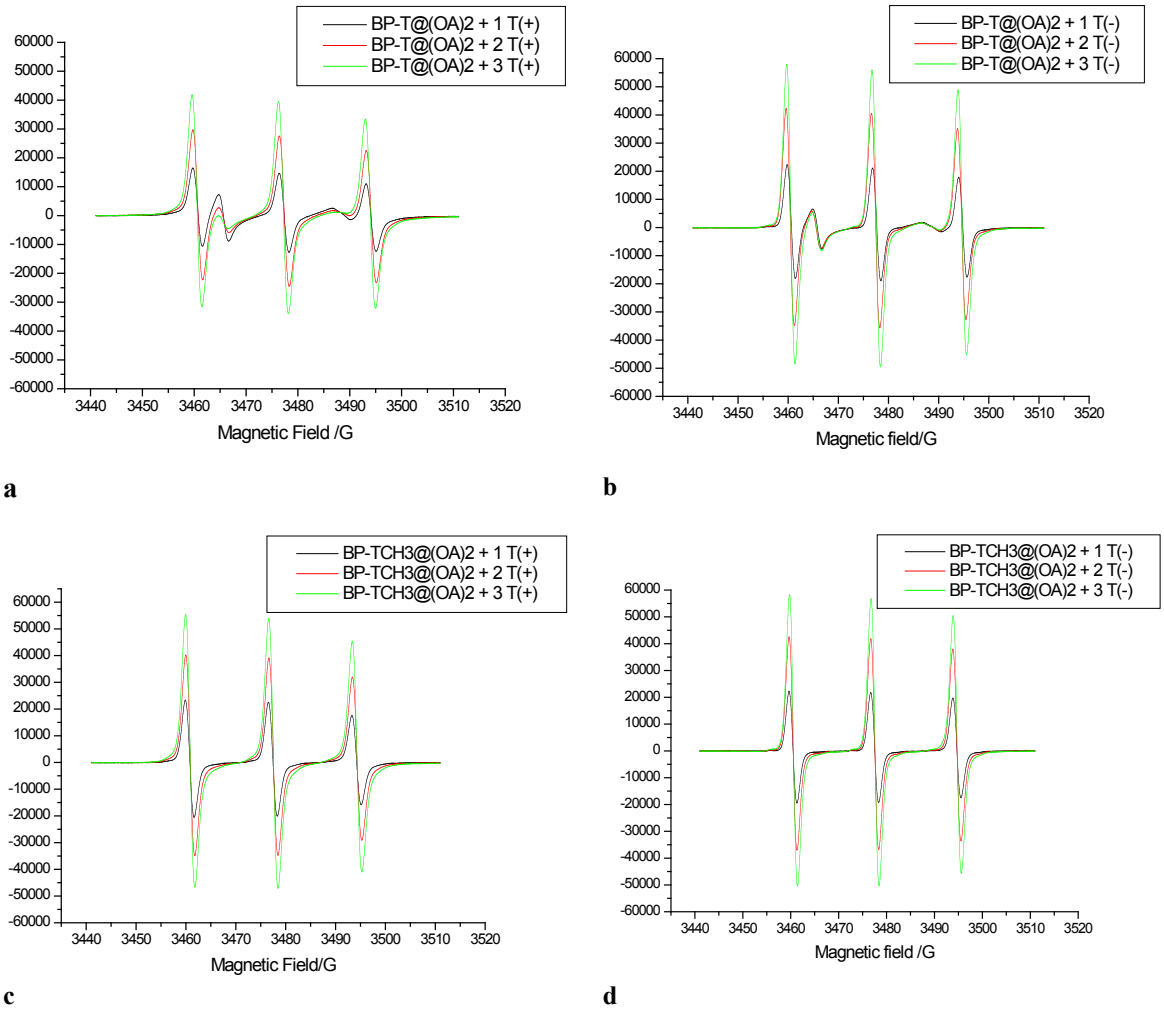

Figure 5.15: EPR spectrum of three component system. Top row (**a**, **b**): internal Guest is ^{15}N-labeled BP-^{15}T. Bottom row (**c**, **d**): internal Guest is the diamagnetic analog, BP-TCH$_3$. Left column (**a**, **c**): guest is ^{14}T$\oplus$. Right column (**b**, **d**): guest is ^{14}T$\ominus$.

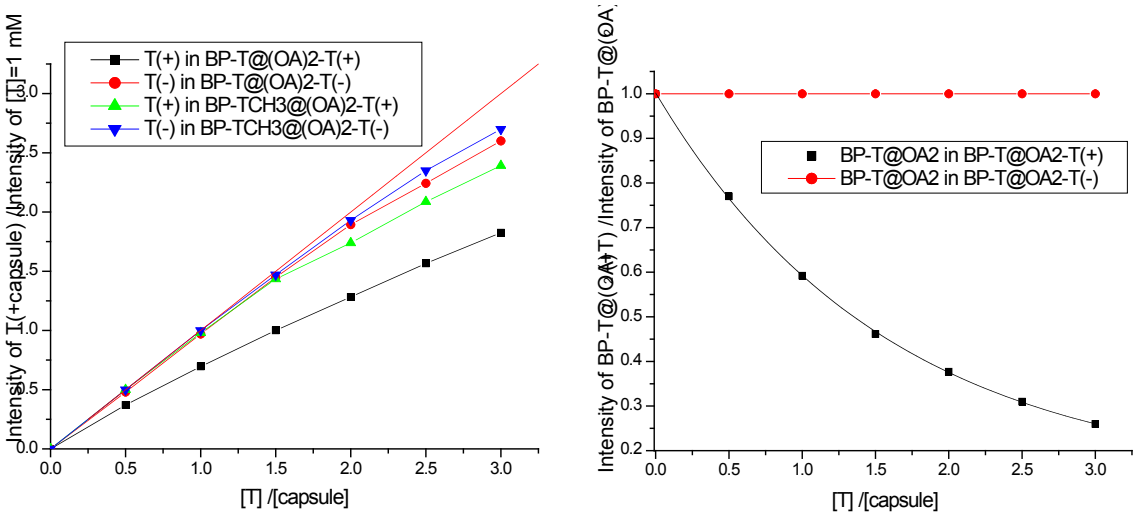

Figure 5.16: Left: Normalized external guest, $^{14}T\oplus$ or $^{14}T\ominus$ as a function of the external guest, [T] / BP-T@$(OA)_2$ or BP-TCH_2@$(OA)_2$, [capsule] ratio. Right: Normalized internal guest, BP-^{15}T as a function of the external guest, [T] / BP-T@$(OA)_2$, [capsule] ratio.

[$^{14}T\oplus$/[BP-^{15}T@$(OA)_2$] up to [T]/[capsule] = 3 (higher $^{14}T\oplus$ concentrations do not provide reliable information due to spin-spin interactions among the $^{14}T\oplus$ radicals). At [T]/[capsule] the ratio between 2-3, a small intensity variation was found mainly for the [$^{14}T\oplus$ + BP-^{15}T@$(OA)_2$] system as a result of Coulombic attraction between the positively charged guest and negatively charged host thus enhancing the spin-spin interactions at the capsule surface. The spectral intensity of BP-^{15}T of BP-^{15}T@$(OA)_2$ also show a decrease in the presence of increasing amounts of $^{14}T\oplus$ (Figure 5.16, graph on the right) in agreement with strong spin-spin interactions between BP-^{15}T and $^{14}T\oplus$.

The analysis of the spectra in Figure 5.15 **a** and **b** was performed by subtracting the signals at different $^{14}T\oplus$/$^{14}T\ominus$ concentrations to extract the individual $^{14}T\oplus$/$^{14}T\ominus$ and BP-T@$(OA)_2$ components. Then each was computed as shown in Section 5.5: Figure 5.23 for $^{14}T\oplus$ and Figure 5.24 for $^{14}T\ominus$. In these figures the computations of each of the individual components, $^{14}T\oplus$, $^{14}T\ominus$ and BP-^{15}T@$(OA)_2$ were also shown for comparison with corresponding parameters.

Figure 5.25 shows computations for $^{14}T\oplus$ and $^{14}T\ominus$, respectively, in the presence of the diamagnetic analog BP-TCH_3@$(OA)_2$. The results from the aforementioned computations are as follows:

1. For the [$^{14}T\oplus$ + BP-^{15}T@$(OA)_2$] system, a 4X decrease in mobility was observed for $^{14}T\oplus$ with the addition of Guest@$(OA)_2$. A slight increase in line width (ΔH) was observed for $^{14}T\oplus$ in the presence of paramagnetic BP-^{15}T@$(OA)_2$ indicating weak but positive interaction between $^{14}T\oplus$ and the OA surface and exchange between the OA surface and the bulk solution.
2. Two interacting sites on the surface of the OA were determined for $^{14}T\oplus$: **(a)** carboxylate sites on the OA surface that are farther away from the nitroxide group of the internal guest, BP-^{15}T. A slight broadening in the EPR spectrum of $^{14}T\oplus$ is evident for the proximity of the nitroxide group of BP-^{15}T@$(OA)_2$ relative to $^{14}T\oplus$. **(b)** carboxylate sites on the OA surface that are in the vicinity of the nitroxide group of the internal guest, BP-^{15}T. The fraction of $^{14}T\oplus$ interacting with these sites is responsible for the decrease in spectral intensity of both $^{14}T\oplus$ and BP-^{15}T as described in Figure 5.15. These interacting sites determined by simulations of experimental EPR spectrum are in agreement with independent analysis of similar systems via NMR[11] and a cartoon illustrating the interaction between the OA surface and $^{14}T\oplus$ nitroxide is shown in Figure 5.17. The fraction of $^{14}T\oplus$ interacting at site **(b)** is 30-40 % of the total $^{14}T\oplus$ probes. Moreover, BP-^{15}T gains mobility (decrease in τ_{perp}) inside the OA capsule when $^{14}T\oplus$ is interacting. We suspect that $^{14}T\oplus$ perturbs the capsule structure which allows partial opening of the capsule.

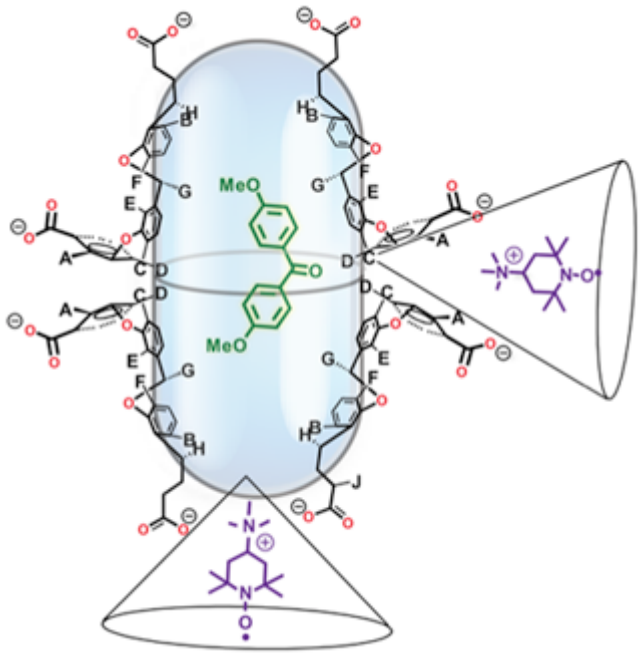

Figure 5.17: Cartoon depiction of the interacting sites between $^{14}T\oplus$ and the OA hemicarceplex determined by ^{1}H NMR. The chemical structures are explicitly shown for only the interacting sites on the OA. The locations of $^{14}T\oplus$ are in agreement with independent simulations from experimental EPR spectra. Internal guest is diamagnetic 4,4'-Dimethoxybenzophenone (DMBP).

3. For the [$^{14}T\ominus$ + BP-^{15}T@$(OA)_2$] system, Coulombic repulsion between $^{14}T\ominus$ and the carboxylate groups on the surface of OA is evident by the very slight decrease in mobility due to collisions by diffusion. In the case of BP-^{15}T, its mobility inside the OA capsule is *decreased* in the presence of $^{14}T\ominus$. Thus, in the Coulombic repulsion case involving $^{14}T\ominus$, the mobility of BP-^{15}T decreases inside the OA cavity due to collisions between capsules. Whereas in the Coulombic attraction case involving $^{14}T\oplus$, BP-^{15}T's mobility increases inside the OA cavity as a result of probe-capsule interaction.

5.4 Summary of the three component systems with BP-T@(OA)$_2$ in the presence of ^{14}T⊕ or ^{14}T⊖

Figure 5.18 is a summary of the experiments described in Section 5.3.2. The top row is the original EPR spectra and the bottom row is the integrated EPR spectra for purpose of familiarity with interpreting a typical NMR spectrum. The dashed black lines are the mathematical sum of each individual BP-^{15}T@(OA)$_2$ and ^{14}T⊕ or ^{14}T⊕ EPR spectrum and serves as the baseline for the three component systems. If there is an effective spin-spin interaction between the internal and external nitroxide guests, then the EPR spectrum of the three component system (in red) will deviate from the black dotted line. Column (a) of Figure 5.18 show the spectra for [^{14}T⊕+ BP-^{15}T@(OA)$_2$] system (in red) and the sum of ^{14}T⊕ and BP-^{15}T@(OA)$_2$ spectra (dashed black lines). Column (b) of Figure 5.18 show the spectra for [^{14}T⊖+ BP-^{15}T@(OA)$_2$] system (in red) and the sum of ^{14}T⊖ and BP-^{15}T@(OA)$_2$ spectra (dashed black lines)

It can be seen in Figure 5.19(a) that the spectrum of the [^{14}T⊕+ BP-^{15}T@(OA)$_2$] system has significantly more broadening than the sum of the individual spectra, which is indicative of electron-spin-electron-spin interaction. This result is in contrast with the spectra in Figure 5.18(b), which show the system with the negatively charged external guest (^{14}T⊖). In this case, both spectra are superimposible on the sum of the individual spectra, indicating no significant spin-spin interaction occurred.

Figure 5.19 is a cartoon that illustrates the two scenarios described in Figure 5.18: (a) positive spin-spin interaction as a result of Coulombic attraction between the positively charged external nitroxide guest and the negatively charged surface of an octa acid as a result of the ionization of the carboxylic acid groups at pH = 9 and (b) the lack of spin-

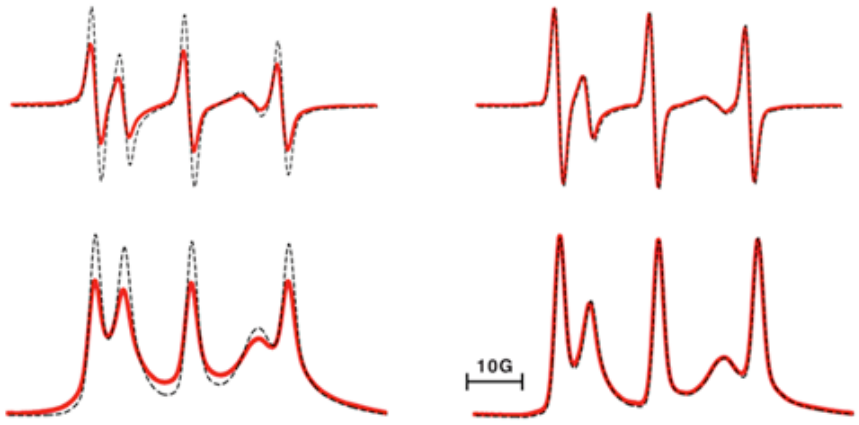

Figure 5.18: Summary EPR spectra of BP-^{15}T@$(OA)_2$ in the presence of external guests. Top row are the original EPR spectra and the bottom row are the integrated EPR spectra for purpose of familiarity with a typical NMR spectrum. The dashed black lines are the mathematical sum of each individual BP-^{15}T@$(OA)_2$ and ^{14}T⊕ or ^{14}T⊕ EPR spectrum and serves as the baseline for the three component systems. If there is an effective spin-spin interaction between the internal and external guests then the EPR spectrum of the three component system (in red) will deviate from the black dotted line. Spectra shown in (a) corresponds to the three component system in Figure 5.19 (a) and spectra shown in (b) corresponds to the three component system in Figure 5.19 (b).

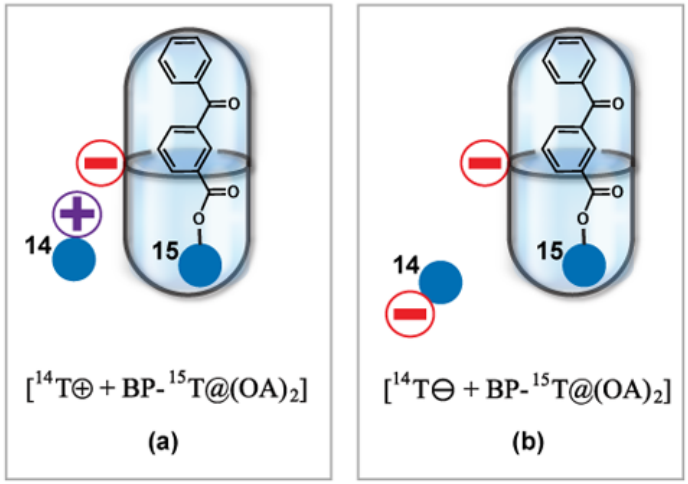

Figure 5.19: Summary cartoon depiction of BP-^{15}T@$(OA)_2$ in the presence of external guests. (a) shows a Coulombic attraction between the host and external guest of the [^{14}T⊕+ BP-^{15}T@$(OA)_2$] system and (b) shows a Coulombic repulsion between the host and external guest of the [^{14}T⊖+ BP-^{15}T@$(OA)_2$] system.

spin interaction as a result of Coulombic repulsion between like charges on the external nitroxide guest and the surface of octa acid.

This set of steady-state EPR experiments of the three-component system was followed-up with a more direct method to investigate spin-spin interaction by time-resolved EPR spectroscopy[15] but this is outside the scope of this thesis.

5.5 Simulations

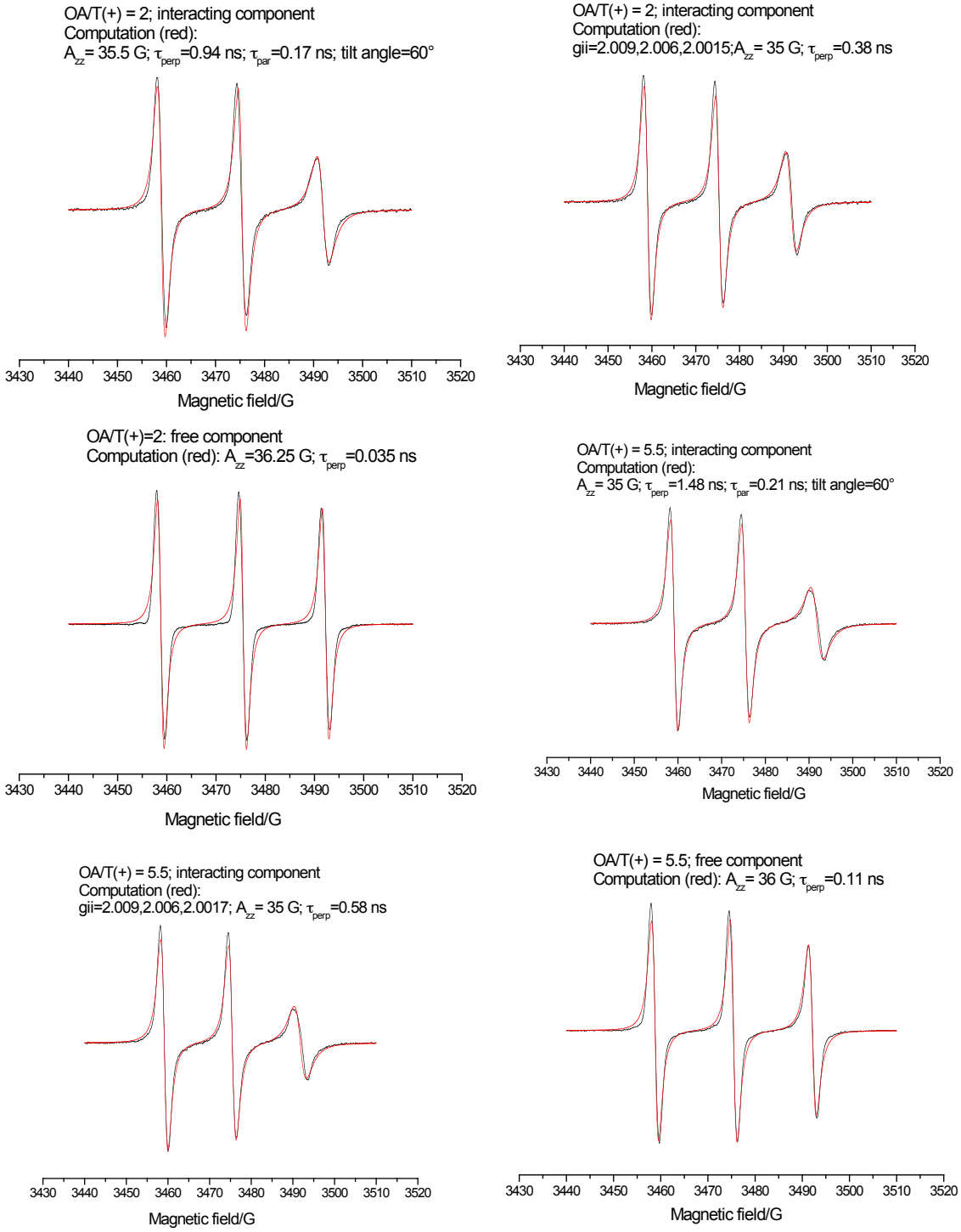

Figure 5.20: EPR spectrum of OA / ^{14}T⊕. Black spectrum: experimental. Red spectrum: simulated. Computation of g_{ii}, A_{zz} and τ for different ratios of OA / ^{14}T⊕.

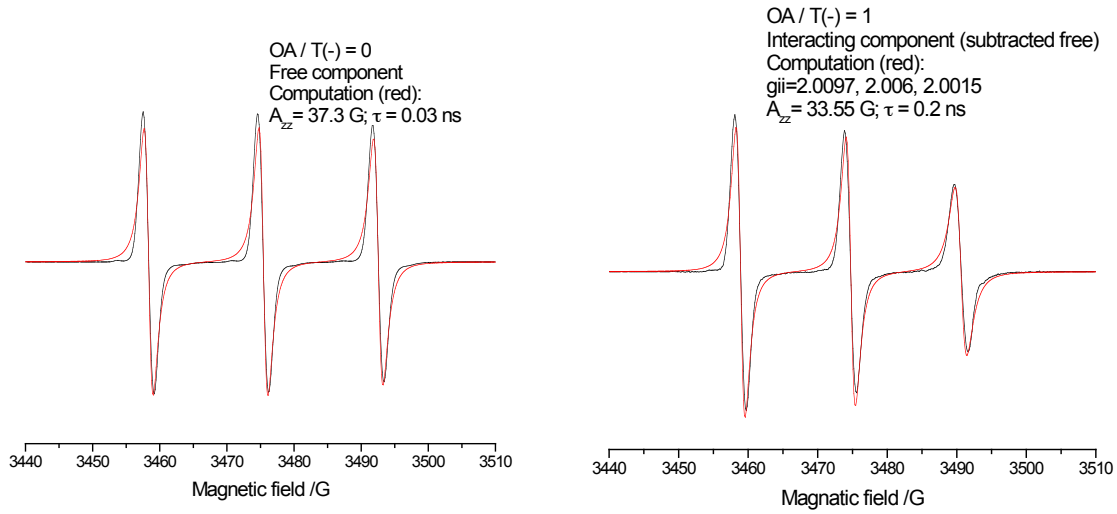

Figure 5.21: EPR spectrum of OA / ^{14}T⊖. Black spectrum: experimental. Red spectrum: simulated. Computation of g_{ii}, A_{zz} and τ for different ratios of OA / ^{14}T⊖.

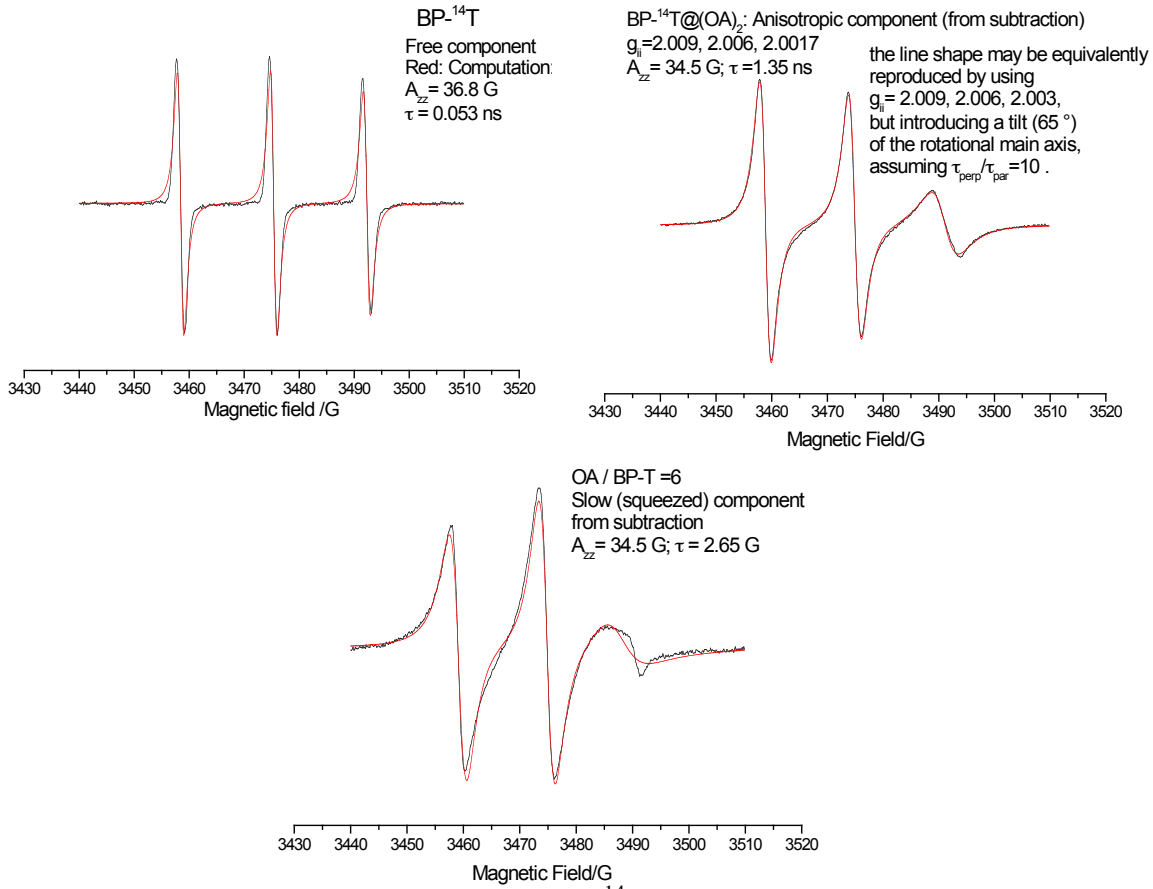

Figure 5.22: EPR spectrum of OA / BP-^{14}T. Black spectrum: experimental. Red spectrum: simulated. Computation of g_{ii}, A_{zz} and τ for different ratios of OA / BP-^{14}T. Top left: Free BP-^{14}T. Top right: BP-^{14}T@$(OA)_2$ complex. Bottom center: OA / BP-^{14}T = 6, excess OA.

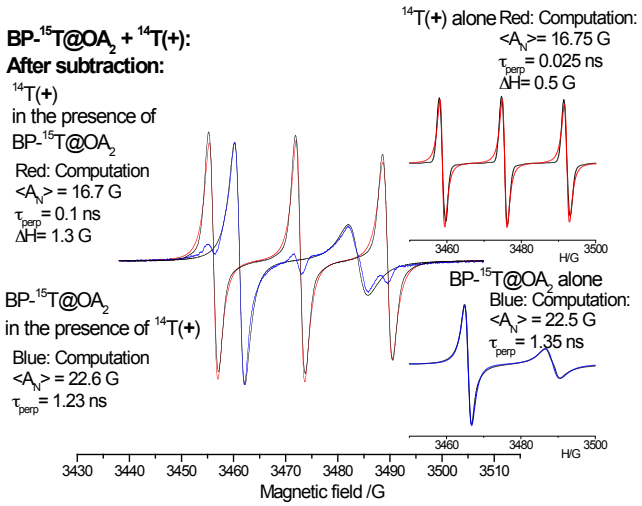

Figure 5.23: Analysis of [^{14}T⊕ + BP-^{15}T@(OA)$_2$] system {center spectrum} and its respective individual components, ^{14}T⊕ and BP-T@(OA)$_2$ {insets}.

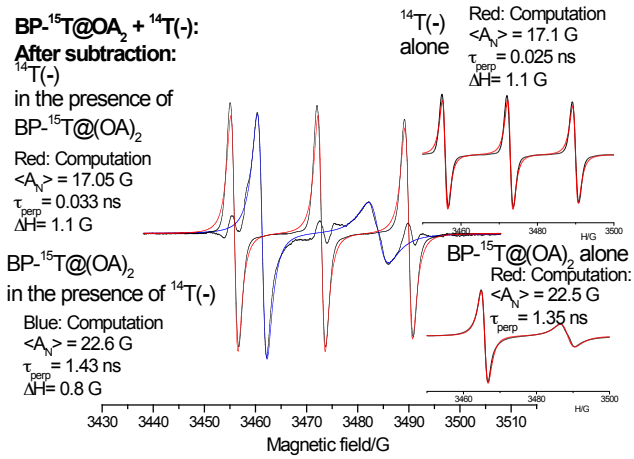

Figure 5.24: Analysis of [^{14}T⊖ + BP-^{15}T@(OA)$_2$] system {center spectrum} and its respective individual components, ^{14}T⊖ and BP-T@(OA)$_2$ {insets}.

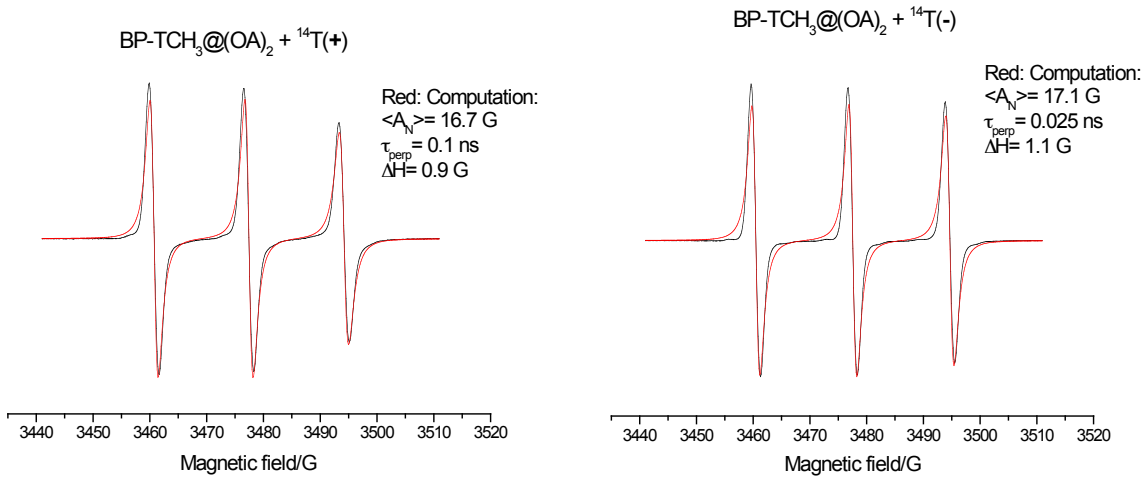

Figure 5.25: EPR spectrum of [^{14}T⊕ + BP-TCH$_3$@(OA)$_2$] system {Left} and [^{14}T⊖ + BP-TCH$_3$@(OA)$_2$] system {Right}. Black spectrum: experimental. Red spectrum: simulated.

5.6 References

(1) Gibb, C. L. D.; Gibb, B. C. Well-defined, organic nanoenvironments in water: the hydrophobic effect drives a capsular assembly. *J. Am. Chem. Soc.* **2004**, *126*, 11408-9.

(2) Yaacobi, M.; Ben-Naim, A. Solvophobic interaction. *J. Phys. Chem.* **1974**, *78*, 175-178.

(3) Kaanumalle, L. S. Gibb, C. L. D. Gibb, B. C.; Ramamurthy, V. A hydrophobic nanocapsule controls the photophysics of aromatic molecules by suppressing their favored solution pathways. *J. Am. Chem. Soc.* **2005**, *127*, 3674-5.

(4) Kang, J. Santamaría, J. Hilmersson, G.; Rebek, J. Self-Assembled Molecular Capsule Catalyzes a Diels−Alder Reaction. *J. Am. Chem. Soc.* **1998**, *120*, 7389-7390.

(5) Chen, J. Körner, S. Craig, S. L. Rudkevich, D. M.; Rebek, J. Amplification by compartmentalization. *Nature* **2002**, *415*, 385-6.

(6) Weiss, R. G. Ramamurthy, V.; Hammond, G. S. Photochemistry in organized and confining media: a model. *Acc. Chem. Res.* **1993**, *26*, 530-536.

(7) Ramamurthy, V.; Eaton, D. F. Photochemistry and photophysics within cyclodextrin cavities. *Acc. Chem. Res.* **1988**, *21*, 300-306.

(8) Tung, C.-H. Wu, L.-Z. Zhang, L.-P.; Chen, B. Supramolecular systems as microreactors: control of product selectivity in organic phototransformation. *Acc. Chem. Res.* **2003**, *36*, 39-47.

(9) Turro, N. J.; Kraeutler, B. Magnetic field and magnetic isotope effects in organic photochemical reactions. A novel probe of reaction mechanisms and a method for enrichment of magnetic isotopes. *Acc. Chem. Res.* **1980**, *13*, 369-377.

(10) Kaanumalle, L. S. Gibb, C. L. D. Gibb, B. C.; Ramamurthy, V. Controlling photochemistry with distinct hydrophobic nanoenvironments. *J. Am. Chem. Soc.* **2004**, *126*, 14366-7.

(11) Chen, J. Y.-C. Jayaraj, N. Jockusch, S. Ottaviani, M. F. Ramamurthy, V.; Turro, N. J. An EPR and NMR Study of Supramolecular Effects on Paramagnetic Interaction between a Nitroxide incarcerated within a Nanocapsule with a Nitroxide in Bulk Aqueous Media. . *J. Am. Chem. Soc.* **2008**, *130*, 7206-7207.

(12) Dr. Ottaviani, M. F. Collaboration.

(13) Budil, D. Nonlinear-Least-Squares Analysis of Slow-Motion EPR Spectra in One and Two Dimensions Using a Modified Levenberg–Marquardt Algorithm. *Journal of Magn. Res., Series A* **1996**, *120*, 155-189.

(14) Dodd, G. Barratt, M.; Rayner, L. Spin probes for binding site polarity. *FEBS Lett.* **1970**, *8*, 286-288.

(15) Jockusch, S. Zeika, O. Jayaraj, N. Ramamurthy, V.; Turro, N. J. Electron Spin Polarization Transfer from a Nitroxide Incarcerated within a Nanocapsule to a Nitroxide in the Bulk Aqueous Solution. *J. Phys. Chem. Lett.* **2010**, *1*, 2628-2632.